MULTIDISCIPLINARY CENTER FOR EARTHQUAKE ENGINEERING RESEARCH
A National Center of Excellence in Advanced Technology Applications

ISSN 1520-295X

Further Development of Tubular Eccentrically Braced Frame Links for the Seismic Retrofit of Braced Steel Truss Bridge Piers

by

Jeffrey W. Berman and Michel Bruneau
University at Buffalo, State University of New York
Department of Civil, Structural and Environmental Engineering
Ketter Hall
Buffalo, New York 14260

Technical Report MCEER-06-0006

March 27, 2006

This research was conducted at the University at Buffalo, State University of New York and was supported by the Federal Highway Administration under contract number DTFH61-98-C-00094.

NOTICE

This report was prepared by the University at Buffalo, State University of New York as a result of research sponsored by the Multidisciplinary Center for Earthquake Engineering Research (MCEER) through a contract from the Federal Highway Administration. Neither MCEER, associates of MCEER, its sponsors, the University at Buffalo, State University of New York, nor any person acting on their behalf:

a. makes any warranty, express or implied, with respect to the use of any information, apparatus, method, or process disclosed in this report or that such use may not infringe upon privately owned rights; or

b. assumes any liabilities of whatsoever kind with respect to the use of, or the damage resulting from the use of, any information, apparatus, method, or process disclosed in this report.

Any opinions, findings, and conclusions or recommendations expressed in this publication are those of the author(s) and do not necessarily reflect the views of MCEER or the Federal Highway Administration.

MULTIDISCIPLINARY CENTER FOR EARTHQUAKE ENGINEERING RESEARCH
A National Center of Excellence in Advanced Technology Applications

Further Development of Tubular Eccentrically Braced Frame Links for the Seismic Retrofit of Braced Steel Truss Bridge Piers

by

Jeffrey W. Berman[1] and Michel Bruneau[2]

Publication Date: March 27, 2006
Submittal Date: March 20, 2006

Technical Report MCEER-06-0006

Task Number 094-C-3.3

FHWA Contract Number DTFH61-98-C-00094

1 Post-Doctoral Research Associate, Department of Civil, Structural and Environmental Engineering, University at Buffalo, State University of New York
2 Professor, Department of Civil, Structural and Environmental Engineering, University at Buffalo, State University of New York

MULTIDISCIPLINARY CENTER FOR EARTHQUAKE ENGINEERING RESEARCH
University at Buffalo, State University of New York
Red Jacket Quadrangle, Buffalo, NY 14261

Preface

The Multidisciplinary Center for Earthquake Engineering Research (MCEER) is a national center of excellence in advanced technology applications that is dedicated to the reduction of earthquake losses nationwide. Headquartered at the University at Buffalo, State University of New York, the Center was originally established by the National Science Foundation in 1986, as the National Center for Earthquake Engineering Research (NCEER).

Comprising a consortium of researchers from numerous disciplines and institutions throughout the United States, the Center's mission is to reduce earthquake losses through research and the application of advanced technologies that improve engineering, pre-earthquake planning and post-earthquake recovery strategies. Toward this end, the Center coordinates a nationwide program of multidisciplinary team research, education and outreach activities.

MCEER's research is conducted under the sponsorship of two major federal agencies, the National Science Foundation (NSF) and the Federal Highway Administration (FHWA), and the State of New York. Significant support is also derived from the Federal Emergency Management Agency (FEMA), other state governments, academic institutions, foreign governments and private industry.

The Center's Highway Project develops improved seismic design, evaluation, and retrofit methodologies and strategies for new and existing bridges and other highway structures, and for assessing the seismic performance of highway systems. The FHWA has sponsored three major contracts with MCEER under the Highway Project, two of which were initiated in 1992 and the third in 1998.

Of the two 1992 studies, one performed a series of tasks intended to improve seismic design practices for new highway bridges, tunnels, and retaining structures (MCEER Project 112). The other study focused on methodologies and approaches for assessing and improving the seismic performance of existing "typical" highway bridges and other highway system components including tunnels, retaining structures, slopes, culverts, and pavements (MCEER Project 106). These studies were conducted to:

- assess the seismic vulnerability of highway systems, structures, and components;
- develop concepts for retrofitting vulnerable highway structures and components;
- develop improved design and analysis methodologies for bridges, tunnels, and retaining structures, which include consideration of soil-structure interaction mechanisms and their influence on structural response; and
- develop, update, and recommend improved seismic design and performance criteria for new highway systems and structures.

The 1998 study, "Seismic Vulnerability of the Highway System" (FHWA Contract DTFH61-98-C-00094; known as MCEER Project 094), was initiated with the objective of performing studies to improve the seismic performance of bridge types not covered under Projects 106 or 112, and to provide extensions to system performance assessments for highway systems. Specific subjects covered under Project 094 include:

- development of formal loss estimation technologies and methodologies for highway systems;
- analysis, design, detailing, and retrofitting technologies for special bridges, including those with flexible superstructures (e.g., trusses), those supported by steel tower substructures, and cable-supported bridges (e.g., suspension and cable-stayed bridges);
- seismic response modification device technologies (e.g., hysteretic dampers, isolation bearings); and
- soil behavior, foundation behavior, and ground motion studies for large bridges.

In addition, Project 094 includes a series of special studies, addressing topics that range from non-destructive assessment of retrofitted bridge components to supporting studies intended to assist in educating the bridge engineering profession on the implementation of new seismic design and retrofitting strategies.

This report is a continuation of research on eccentrically braced frames with self-stabilizing tubular links for use as both a retrofit alternative and seismic load resisting system for new bridges (see Technical report MCEER-05-0004). A finite element parametric study was performed to investigate the effects of key design parameters for rectangular link cross-sections on link rotation capacity, energy dissipation, and overstrength. Results from this parametric study were used to develop proposed design recommendations and provide insight into the behavior of tubular links. An experimental program was developed to test fourteen links with cross-sections that were at the revised limits for web and flange compactness and four different link lengths. Results indicate that the design recommendations are successful in achieving links that can sustain their target rotation prior to strength degradation from local buckling. Further comparisons with finite element analysis results indicates that models used in the parametric study adequately represented the behavior of links, with the exception of degradation due to fracture. Recommendations for design requirements for tubular links for implementation in bridge and building seismic design codes are provided.

ABSTRACT

There are many steel truss bridges in the United States and other countries that were constructed prior to 1940, when seismic demands on structures were not well understood. Many of these bridges are now considered seismically vulnerable. Contributing significantly to their undesirable seismic performance are the steel piers that support the superstructure. These piers typically have bracing members that are made up of channels or angles that are tied together with steel lacings and rivets. Recent experimental investigations have shown that such structural members can suffer severe local buckling, rapid strength degradation, and limited ductility, when subjected to cyclic loading. Therefore, it is necessary to develop retrofit strategies for these piers that focus on protecting, strengthening, or increasing the ductility of the existing brace members.

Previous research has proposed the use of eccentrically braced frames with self-stabilizing tubular links as both a retrofit alternative and seismic load resisting system for new bridges (Berman and Bruneau, 2005a). That research showed, via analytical development and a proof-of-concept experiment, that these types of links can provide ductile and stable hysteretic energy dissipation without any lateral bracing, which can be difficult to provide in bridge piers. This report is a continuation of that research, with the objective of proposing design requirements for tubular links for eccentrically braced frames.

First, a finite element model of the link from the proof-of-concept test described in Berman and Bruneau (2005a) was developed. Mesh refinements, elements, boundary conditions, and comparison with experimental results are all described. After the model is shown to have adequate agreement with the experimental results it is used as the base model for the development of a finite element parametric study of tubular links.

The finite element parametric study was performed to investigate the effects of key design parameters for rectangular link cross-sections on link rotation capacity, energy dissipation, and overstrength. Results of this parametric study are used to revise the proposed design recommendations and provide insight into the behavior of tubular links. The proposed

design recommendations aim to establish compactness and stiffener spacing requirements for links with various lengths and target rotation capacities.

A second experimental program was then developed. This program tests fourteen links with cross-sections that were at the revised limits for web and flange compactness and four different link lengths. Results indicate that the design recommendations are successful in achieving links that can sustain their target rotation prior to strength degradation from local buckling. Further comparisons with finite element analysis results indicates that models used in the parametric study adequately represented the behavior of links, with the exception of degradation due to fracture. Conclusions and recommendations for future research are then given, including recommendations for design requirements for tubular links for implementation in bridge and building seismic design codes.

ACKNOWLEDGMENTS

Sincere thanks to the staff of the Structural Engineering and Earthquake Simulation Laboratory and George E. Brown Network for Earthquake Engineering Research node at the University of Buffalo, Duane Kozlowski, Scot Weinreber, Dick Cizdziel, Robert Staniszewski, Christopher Budden, Jason Hanley, Goran Josipovic, and Mark Pitman for their assistance and expertise.

The authors also thank Dr. Andrew Whittaker, and Dr. Andrei Reinhorn both of the University at Buffalo, and Dr. Ahmad Itani of the University of Nevada, Reno for making time in their busy schedules to review this work. Their input and suggestions have helped make this a successful research endeavor.

This research was conducted by the State University of New York at Buffalo and was supported by the Federal Highway Administration under contract number DTFH61-98-C-00094 to the Multidisciplinary Center for Earthquake Engineering Research. However, any opinions, findings, conclusions, and recommendations presented in this paper are those of the authors and do not necessarily reflect the views of the sponsors.

TABLE OF CONTENTS

SECTION 1

INTRODUCTION

1.1 Statement of Problem and Objectives 1

1.2 Scope of Work 2

1.3 Organization 3

SECTION 2

FINITE ELEMENT MODELING OF THE PROOF-OF-CONCEPT LINK

2.1 General 5

2.2 Review of Finite Element Study of WF Links 5

2.3 Development of the Proof-of-Concept Link Model 10

2.3.1 Materials 12

2.3.2 Boundary Conditions and Loading 14

2.3.2 Elements and Mesh 14

2.4 Comparison with Experimental Results 17

SECTION 3

FINITE ELEMENT PARAMETRIC STUDY OF HYBRID RECTANGULAR LINKS

3.1 General 27

3.2 Parameter Selection - Part 1 28

3.2.1 Non-Dimensional Parameters 28

3.2.2 Resulting Dimensional Parameters 30

3.3 Differences from the Proof-of-Concept Model 35

3.4 Evaluation of the Limit Plastic Link Rotation 38

3.5 Results of Parametric Study - Part 1 39

3.5.1 Presentation of Results 39

3.5.2 Effect of Stiffeners and Web Compactness 40

3.5.3 Effect of Flange Compactness 46

3.5.4 Revised Design Requirements 51

3.6 Parameter Selection - Part 2 53

TABLE OF CONTENTS (CONT'D)

3.7 Results of Parametric Study - Part 2 61
3.8 Energy Dissipation of Link 66
3.8.1 Normalized Energy Observations - Part 1 Shear Links 68
3.8.2 Normalized Energy Observations - Part 1 Intermediate and Flexural Links 69
3.8.3 Energy Observations - Part 2 Links 69
3.8.4 Energy Observations - Energy Dissipated per Cycle 74
3.9 Link Overstrength 77
3.10 Summary 83

SECTION 4

DESIGN AND SETUP OF LINK TESTING

4.1 General 85
4.2 Link Selection 87
4.2.1 Cross-Section 1 (X1) 88
4.2.2 Cross-Section 2 (X2) 91
4.2.3 Cross-Section 3 (X3) 93
4.2.4 Link Material Testing 94
4.2.5 Haunch Design 98
4.2.6 Link End-Plates 100
4.3 Test Setup Design 101
4.3.1 Foundation Beam (FB) 102
4.3.2 Loading Beam (LB) 109
4.3.3 Pantograph 112
4.3.4 Lateral Bracing 116
4.4 Instrumentation 119
4.4.1 Strain Gages 120
4.4.2 String Displacement Potentiometers 121
4.4.3 Krypton Dynamic Measurement Machine 122
4.4.3 Video Recording 123

TABLE OF CONTENTS (CONT'D)

4.5 Supplementary Link Specimens 123

SECTION 5

LINK TESTING OBSERVATIONS

5.1 General 127
5.2 Loading Protocol 127
5.3 Experimental Observations 128
5.3.1 Specimen X1L1.2 129
5.3.2 Specimen X2L1.2 132
5.3.3 Specimen X3L1.2 136
5.3.4 Specimen X1L1.6 140
5.3.5 Specimen X2L1.6 143
5.3.6 Specimen X3L1.6 146
5.3.7 Specimen X1L2.1 149
5.3.8 Specimen X2L2.1 153
5.3.9 Specimen X3L2.1 156
5.3.10 Specimen X1L3.0 159
5.3.11 Specimen X2L3.0 163
5.3.12 Specimen X3L3.0 166
5.3.13 Specimen AX1L1.6 170
5.3.14 Specimen AX2L1.6 176
5.4 Summary 180

SECTION 6

LINK TESTING RESULTS AND ANALYSIS

6.1 General 183
6.2 Rotation Results 184
6.2.1 Limit Total Rotation and Limit Plastic Rotation 184
6.2.2 Discussion of Links with $\rho = 1.6$ 187
6.3 Energy Dissipation Results 189

TABLE OF CONTENTS (CONT'D)

6.4 Extrapolation to Updated Loading Protocol 191
6.4.1 Bounding Surface Model 192
6.4.2 Estimation of Limit Rotation for the 2005 Loading Protocol . . 195
6.5 Supplementary Link Test Results 200
6.6 Overstrength Results 207
6.7 Flange Strains 210
6.8 Comparison with Finite Element Results 213
6.9 Impact of Proposed Design Requirements 217
6.10 Summary 218

SECTION 7

SUMMARY, CONCLUSIONS, AND RECOMMENDATIONS FOR FURTHER RESEARCH

7.1 Summary 221
7.1.1 Link Strength 224
7.1.2 Link Length and Maximum Rotations 224
7.1.3 Compactness and Stiffener Requirements 225
7.1.4 Link Overstrength 226
7.1.5 Link Connections 227
7.2 Conclusions 227
7.3 Recommendations for Further Research 228
7.3.1 Laterally Stable Links for EBFs 228
7.3.2 Seismic Retrofit of Braced Steel Truss Bridge Piers 229

SECTION 8

REFERENCES 231

APPENDIX A

LINK HYSTERESIS CURVES FROM THE FINITE ELEMENT PARAMETRIC STUDY

A.1 General 235
A.2 Part 1 Link Hysteresis Curves 237

TABLE OF CONTENTS (CONT'D)

A.3 Part 2 Link Hysteresis Curves 253

APPENDIX B

ALTERNATIVE RECOMMENDED DESIGN REQUIREMENTS FOR HYBRID RECTANGULAR LINK 263

LIST OF FIGURES

FIGURE	TITLE	PAGE
2-1	Link Boundary Conditions (a) Initial Position (b) Deformed Configuration (Adapted from Richards and Uang, 2002)	7
2-2	Comparison of Experimental and Analytical Hystereses (Richards and Uang, 2002)	9
2-3	Comparison of Deformed Geometry for Specimen UTA 6 (Richards and Uang, 2002)	10
2-4	Link and Stiffener Cross-Sections (Berman and Bruneau 2005a)	11
2-5	Link and Stiffener Detail (Berman and Bruneau 2005a)	11
2-6	Cyclic Stress-Strain Curve for Steel C (Adapted from Kaufmann et al., 2001)	12
2-7	Engineering Stress-Strain Curves: (a) Web Material; and (b) Flange Material	13
2-8	Mesh 1	15
2-9	Mesh 2	16
2-10	Mesh 3	16
2-11	Link Shear vs. Link Rotation for Monotonic Analyses and Experimental Results	17
2-12	Mid-Width Flange Stress vs. Link Rotation for Various FE Model Refinements	18
2-13	Mid-Depth Web Shear Stress vs. Link Rotation for Various FE Model Refinements	18
2-14	Comparison of Model 1 and Experimental Link Shear vs Link Rotation Hystereses	19
2-15	Comparison of Model 2 and Experimental Link Shear vs Link Rotation Hystereses	20
2-16	Comparison of Model 4 and Experimental Link Shear vs Link Rotation Hystereses	20
2-17	Deformed Link in Model 1	21
2-18	Deformed Link in Model 2	21
2-19	Deformed Link and Stiffener Curl at $6\delta_y$, 2.3% Drift, 0.140 rads Rotation, Cycle 20	22
2-20	Longitudinal Stresses at End of Cyclic Analysis for Model 1	23

LIST OF FIGURES (CONTINUED)

FIGURE	TITLE	PAGE
2-21	Longitudinal Stresses at End of Cyclic Analysis for Model 2	23
2-22	Longitudinal Stresses at End of Cyclic Analysis for Model 4	24
2-23	Shear Stresses at End of Cyclic Analysis for Model 1	24
2-24	Shear Stresses at End of Cyclic Analysis for Model 2	25
2-25	Shear Stresses at End of Cyclic Analysis for Model 4	25
3-1	Hollow Hybrid Rectangular Cross-Section	27
3-2	True Stress vs. True Strain Curves for Materials in Parametric Study Models	36
3-3	Example of Limit Plastic Rotation Determination	39
3-4	Limit Plastic Rotation vs. Normalized Link Length for Unstiffened Links with $b'/t_f \leq 17.0$	44
3-5	Limit Plastic Rotation vs. Normalized Link Length for Stiffened Links with $b'/t_f \leq 17.0$	44
3-6	Hysteresis for Link S-17-36-1.2	46
3-7	Hysteresis for Link N-17-36-1.2	46
3-8	Limit Plastic Rotation vs. Normalized Link Length for Unstiffened Links with $b'/t_f > 17.0$	47
3-9	Limit Plastic Rotation vs. Normalized Link Length for Stiffened Links with $b'/t_f > 17.0$	47
3-10	Normalized Limit Plastic Rotation vs. Flange Compactness for Shear Links	49
3-11	Normalized Limit Plastic Rotation vs. Flange Compactness for Intermediate Links	49
3-12	Normalized Limit Plastic Rotation vs. Flange Compactness for Flexural Links	50
3-13	Limit Plastic Rotation vs. Normalized Link Length for Unstiffened Part 2 Links - Sorted by Web Yield Stress	65
3-14	Limit Plastic Rotation vs. Normalized Link Length for Stiffened Part 2 Links - Sorted by Web Yield Stress	65
3-15	Limit Plastic Rotation vs. Normalized Link Length for Unstiffened Part 2 Links - Sorted by Flange Yield Stress	66

LIST OF FIGURES (CONTINUED)

FIGURE	TITLE	PAGE
3-16	Limit Plastic Rotation vs. Normalized Link Length for Stiffened Part 2 Links - Sorted by Flange Yield Stress	66
3-17	Cumulative Energy Dissipation for Part 1 Links - Summed to the Limit Plastic Rotation for Each Link	70
3-18	Normalized Cumulative Energy Dissipation for Part 1 Links - Summed to the Limit Plastic Rotation for Each Link	71
3-19	Cumulative Energy Dissipation for Part 2 Links - Summed to the Limit Plastic Rotation for Each Link	72
3-20	Normalized Cumulative Energy Dissipation for Part 2 Links - Summed to the Limit Plastic Rotation for Each Link	73
3-21	Energy Dissipated per Cycle for a Unstiffened and Stiffened Link of the Same Cross-Section	74
3-22	Energy Dissipated per Cycle for Two Links with Differing Flange Compactnesses	76
3-23	Energy Dissipated per Cycle for a Shear and a Flexural Link	76
3-24	V_{max}/V_p for Unstiffened Part 1 Links	78
3-25	V_{max}/V_p for Stiffened Part 1 Links	78
3-26	M_{max}/M_p for Unstiffened Part 1 Links	79
3-27	M_{max}/M_p for Stiffened Part 1 Links	79
3-28	V_{max}/V_{ult} for Unstiffened Part 1 Links	82
3-29	V_{max}/V_{ult} for Stiffened Part 1 Links	83
4-1	Test Setup for Specimens with a Normalized Link Length of 3.0	86
4-2	Link Specimen Cross-Section Details	88
4-3	X1 Link Specimen	90
4-4	Stiffener Details for X2 Links	91
4-5	X2 Link Specimens	92
4-6	X3 Link Specimens	93
4-7	Tension Coupon Test Results for Web Materials	95
4-8	Tension Coupon Test Results for Flange Materials	95

LIST OF FIGURES (CONTINUED)

FIGURE	TITLE	PAGE
4-9	Cyclic Stress-Strain Curves for Link Materials	97
4-10	Cyclic Coupon Schematics	98
4-11	General Haunch Cross-Section	99
4-12	Link End-Plates	100
4-13	Test Setup for Specimens with a Normalized Link Length of 1.2 and 1.6	103
4-14	Test Setup for Specimens with a Normalized Link Length of 2.1	104
4-15	Foundation Beam (FB) Schematic	106
4-16	Foundation Beam Stiffeners A and B	106
4-17	Foundation Beam Stiffeners C and D	107
4-18	FB Actuator Beam and Brace and Connection to Foundation Beam	107
4-19	Foundation Beam-to-Link Connection	108
4-20	Loading Beam (LB) Schematic	110
4-21	LB Actuator Beam and Brace and Connection to Loading Beam	111
4-22	Loading Beam-to-Link Connection	111
4-23	Free Body Diagram of Loading Beam and Link (Cut at Midpoint)	113
4-24	Pantograph Center Member Free Body Diagram	113
4-25	Pantograph Deformation Kinematics	114
4-26	Pantograph Connections to Foundation and Loading Beams	115
4-27	Pantograph Connection Details and Center Member	116
4-28	Lateral Bracing of FB Brace	117
4-29	Elevation of Loading Beam Lateral Bracing	118
4-30	Cross-Section of Setup at Loading Beam Lateral Bracing	119
4-31	Instrumentation for Shear Links	120
4-32	Instrumentation for Intermediate and Flexural Links	121
4-33	Instrumentation Outside the Links	122
4-34	Supplementary Links and Details	125
5-1	Link Shear vs. Rotation Hysteresis for Specimen X1L1.2	130
5-2	Whitewash Flaking from Flange of Specimen X1L1.2 During Sequence 6	131

LIST OF FIGURES (CONTINUED)

FIGURE	TITLE	PAGE
5-3	Flange Fracture of Specimen X1L1.2 During: (a) Sequence 14; and (b) Sequence 15	132
5-4	Link Shear vs. Rotation Hysteresis for Specimen X2L1.2	133
5-5	Deformed Specimen X2L1.2 During: (a) the Negative Peak of Cycle 1 of Sequence 11; and (b) the Positive Peak of Cycle 2 of Sequence 11	134
5-6	Fracture Propagation From: (a) Near the Midpoint of the Negative Excursion of Cycle 1 of Sequence 13; (b) and (c) the End of the Negative Excursion of the First Cycle of Sequence 13; and (d) the Subsequent Positive Excursion of the First Cycle of Sequence 13	135
5-7	Bottom West Flange Fracture Surface and Fatigue Striations	136
5-8	Link Shear vs. Rotation Hysteresis for Specimen X3L1.2	137
5-9	Specimen X3L1.2 at 0.10 rads of Cycle 1 of Sequence 13	138
5-10	Fractures Developing in Specimen X3L1.2 During: (a) the Negative Excursion of Cycle 1 of Sequence 14; and (b) the Positive Excursion of Cycle 2 of Sequence 14	139
5-11	Fracture Surface of Top East Flange of Specimen X3L1.2	139
5-12	Link Shear vs. Rotation Hysteresis for Specimen X1L1.6	140
5-13	Specimen X1L1.6 at -0.055 rads During Cycle 1 of Sequence 8	141
5-14	Flange Fracture of Specimen X1L1.6 During Cycle 1 of Sequence 10	142
5-15	Fracture Surface of Top East Flange of Specimen X1L1.6	142
5-16	Link Shear vs. Rotation Hysteresis for Specimen X2L1.6	143
5-17	Specimen X2L1.6 at 0.058 rads During Cycle 2 of Sequence 8	144
5-18	Fracture of Flange Extending to Web in Specimen X2L1.6	145
5-19	Close-up of Flange and Web Fracture of Specimen X2L1.6	145
5-20	Fatigue Striations in Fracture Surface of Specimen X2L1.6	147
5-21	Link Shear vs. Rotation Hysteresis for Specimen X3L1.6	147
5-22	Specimen X3L1.6 at -0.064 rads During Cycle 2 of Sequence 9	148
5-23	Flange Fracture in Specimen X3L1.6 During the Negative Excursion of Cycle of Sequence 10	148

LIST OF FIGURES (CONTINUED)

FIGURE	TITLE	PAGE
5-24	Fatigue Striations and Chevron Markings in Fracture Surface of Specimen X3L1.6	149
5-25	Link Shear vs. Rotation Hysteresis for Specimen X1L2.1	150
5-26	Specimen X1L2.1 at 0.056 rads During Cycle 2 of Sequence 8	151
5-27	Magnitude of Flange Buckling After Testing of Specimen X1L2.1 Relative to a Straight Edge	151
5-28	Fracture of Bottom West Flange Extending Into Web of Specimen X1L2.1	152
5-29	Fracture Surface of Bottom East Flange of Specimen X1L2.1	152
5-30	Link Shear vs. Rotation Hysteresis for Specimen X2L2.1	153
5-31	Specimen X2L2.1 at 0.042 rads During Cycle 1 of Sequence 7	154
5-32	Flange Buckling of Specimen X2L2.1 After Testing	155
5-33	West Flange Fracture Extending into North Web of Specimen X2L2.1	155
5-34	Fracture of Bottom East Flange of Specimen X2L2.1	156
5-35	Link Shear vs. Rotation Hysteresis for Specimen X3L2.1	157
5-36	Specimen X3L2.1 at 0.056 rads During Cycle 2 of Sequence 8	160
5-37	Fracture of the Bottom East Flange of Specimen X3L2.1 After Testing	160
5-38	Fracture Surface of Bottom East Flange of Specimen X3L2.1	159
5-39	Link Shear vs. Rotation Hysteresis for Specimen X1L3.0	160
5-40	Specimen X1L3.0 at -0.058 rads During Cycle 1 of Sequence 8	161
5-41	Buckling Magnitude of Bottom East Flange of Specimen X1L3.9 Relative to a Straight Edge After Testing	161
5-42	Fracture of Top East Flange Beginning in the Web-to-Flange Weld of Specimen X1L3.0	162
5-43	Fracture Surface of Top East Flange of Specimen X1L3.0	162
5-44	Link Shear vs. Rotation Hysteresis for Specimen X2L3.0	163
5-45	Specimen X2L3.0 at -0.044 rads During Cycle 2 of Sequence 7	164
5-46	Buckling Magnitude of Lower North Web Relative to a Straight Edge After Testing of Specimen X2L3.0	165

LIST OF FIGURES (CONTINUED)

FIGURE	TITLE	PAGE
5-47	Buckling Magnitude of Top West Flange Relative to a Straight Edge After Testing of Specimen X2L3.0	165
5-48	Web and Flange Fracture at Top of Specimen X2L3.0 During Cycle 2 of Sequence 8	166
5-49	Link Shear vs. Rotation Hysteresis for Specimen X2L3.0	167
5-50	Specimen X3L3.0 at -0.059 rads During Cycle 2 of Sequence 8	168
5-51	Fracture of Top East Flange of Specimen X3L3.0 During Cycle 1 of Sequence 9	169
5-52	Top East Flange Fracture of Specimen X3L3.0 After Testing	169
5-53	Link Shear vs. Rotation Hysteresis for Specimen AX1L1.6	171
5-54	Whitewash Flaking off of Gusset Stiffener of AX1L1.6 After Sequence 8	172
5-55	Specimen AX1L1.6 at -0.06 rads of Rotation During Cycle 1 of Sequence 9	173
5-56	Initial Cracking of Bottom Gusset Stiffener and Weld on Specimen AX1L1.6 After Sequence 9	174
5-57	Fracture of Gusset Stiffener of AX1L1.6 During Cycle 1 of Sequence 10	174
5-58	Gusset Stiffener Fracture and Plastic Hinge Movement During Cycle 1 of Sequence 10 for AX1L1.6	175
5-59	Complete Gusset Stiffener Fracture of AX1L1.6 During Cycle 1 of Sequence 11	175
5-60	Link Shear vs. Rotation Hysteresis for Specimen AX2L1.6	177
5-61	Whitewash Flaking on End Connection of AX2L1.6 After Sequence 5	178
5-62	Specimen AX2L1.6 at 0.098 rads of Rotation During Cycle of Sequence 11	178
5-63	Flange Fracture of Specimen AX2L1.6 Near End Connection During Cycle 1 of Sequence 13	179
5-64	Flange Buckling of Specimen AX2L1.6 Near Bottom End Connection During Cycle 1 of Sequence 10	179
5-65	Flange and Stiffener Buckling of Specimen AX2L1.6 After Testing	180
6-1	Total Rotation vs. Link Length for Link Test Specimens with Haunch End Connections	185

LIST OF FIGURES (CONTINUED)

FIGURE	TITLE	PAGE
6-2	Plastic Rotation vs. Link Length for Link Test Specimens with Haunches	187
6-3	Cumulative Plastic Rotation vs. Link Length for Link Test Specimens with Haunches	188
6-4	Energy Dissipation vs. Link Length for Link Test Specimens with Haunches	190
6-5	Normalized Energy Dissipation for Link Test Specimens with Haunches Using Design V_p and M_p Values	190
6-6	Comparison of the 2002 and 2005 AISC Loading Protocols for EBF Links	192
6-7	Bounding Surface Model (Adapted from Chen et al. 1996)	194
6-8	Comparison of Bounding Surface Model to Experimental Results for X1 Specimens	196
6-9	Cumulative Energy Dissipation for Both Experimental and Projected Results versus Half Cycle Number for Specimen X1L1.6	197
6-10	Cumulative Plastic Rotation for Both Experimental and Projected Results versus Half Cycle Number for Specimen X1L1.6	197
6-11	Projected Limit Rotation vs. Link Length for the 2005 Loading Protocol Considering Equal Cumulative Energy Dissipation - Links with Haunch End Connections	199
6-12	Projected Limit Rotation vs. Link Length for the 2005 Loading Protocol Considering Equal Cumulative Plastic Rotation - Links with Haunch End Connections	199
6-13	Limit Rotation vs. Link Length for All Link Specimens	202
6-14	Cumulative Plastic Rotation vs. Link Length for All Link Specimens	202
6-15	Normalized Energy Dissipation for All Link Specimens Using Design V_p and M_p Values	203
6-16	Projected Limit Rotation vs. Link Length for the 2005 Loading Protocol Considering Equal Cumulative Energy Dissipation - All Link Specimens	205
6-17	Projected Limit Rotation vs. Link Length for the 2005 Loading Protocol Considering Equal Cumulative Plastic Rotation - All Link Specimens	205

LIST OF FIGURES (CONTINUED)

FIGURE	TITLE	PAGE
6-18	Link Shear Overstrength vs. Normalized Link Length for All Link Specimens	207
6-19	Link Flexural Overstrength vs. Normalized Link Length for All Link Specimens	208
6-20	Link Shear Overstrength vs. Normalized Link Length for All Link Specimens - with Cyclic Hardening Factor	209
6-21	Link Shear Overstrength vs. Normalized Link Length for All Link Specimens - with Revised Cyclic Hardening Factor	210
6-22	Approximate Cumulative Plastic Strain at Bottom of West Flange for All Link Specimens (Data Incomplete for Specimen X2L3.0 Due to Flange Buckling)	212
6-23	Comparison of Finite Element Models to Experimental Results for X1 Specimens	214
6-24	Comparison of Finite Element Models to Experimental Results for X2 Specimens	215
6-25	Comparison of Finite Element Models to Experimental Results for X3 Specimens	216

LIST OF TABLES

TABLE	TITLE	PAGE
2-1	Loading Protocol for FE Models of Proof-of-Concept Link	14
3-1	Cross-Section Dimensions for Part 1 Links	30
3-2	*b*/*d* Ratios for Part 1 Links	31
3-3	Resulting Link Properties for Cross-Sections Chosen	32
3-4	Link Lengths, mm (in)	33
3-5	Required Stiffener Spacing, mm (in)	34
3-6	Spacings Between Stiffeners (in)	35
3-7	Limit Plastic Rotations for Part 1 Links (rads)	41
3-8	Maximum Link Shear Normalized by V_p	42
3-9	Maximum Link End Moment Normalized by M_p	43
3-10	Maximum Link End Moment Normalized by M_p	52
3-11	Limit Compactness and Used Compactness Ratios for Part 2 Links	54
3-12	Cross-Section Dimensions for Part 2 Links	55
3-13	*b*/*d* Ratios for Part 2 Links	56
3-14	Resulting Link Properties for Part 2 Models	58
3-15	Link Lengths Used - Part 2 Models, mm (in)	59
3-16	Required Stiffener Spacing, mm (in)	60
3-17	Stiffener Layout Used for Part 2 Stiffened Links (in)	60
3-18	Limit Plastic Rotations for Part 2 Links (rads)	62
3-19	Maximum Link Shear Normalized by V_p for Part 2 Links	63
3-20	Maximum Link End Moment Normalized by M_p for Part 2 Links	64
4-1	Link Specimen Cross-Section Geometries and Properties	88
4-2	Link Lengths for Specimen	89
4-3	Material Test Results	96
5-1	Loading History for Specimen X1L1.2	131
5-2	Loading History for Specimen X2L1.2	134
5-3	Loading History for Specimen X3L1.2	137
5-4	Loading History for Specimen X1L1.6	141
5-5	Loading History for Specimen X2L1.6	144

LIST OF TABLES (CONTINUED)

TABLE	TITLE	PAGE
5-6	Loading History for Specimen X3L1.6	147
5-7	Loading History for Specimen X1L2.1	150
5-8	Loading History for Specimen X2L2.1	154
5-9	Loading History for Specimen X3L2.1	157
5-10	Loading History for Specimen X1L3.0	160
5-11	Loading History for Specimen X2L3.0	164
5-12	Loading History for Specimen X3L3.0	167
5-13	Loading History for Specimen AX1L1.6	171
5-14	Loading History for Specimen AX2L1.6	176
6-1	Summary of Experimental Results for Link Specimens with Haunch End Connections	184
6-2	Bounding Surface Model Parameters Used for Links with Haunch End Connections	195
6-3	Projected Limit Rotations Considering the 2005 Loading Protocol and Parameter Values Used to Approximate Them	198
6-4	Summary of Experimental Results for Supplementary Link Specimens and Similar Haunch Specimens	201
6-5	Parameter Values Used for the Bounding Surface Models for the Supplementary and Proof-of-Concept Specimens	204
6-6	Projected Limit Rotations Considering the 2005 Loading Protocol for the Supplementary and Proof-of-Concept Specimens	204

NOTATIONS

a	Stiffener spacing
b	Flange width
b'	Clear flange width
C_B	Factor for stiffener spacing equation
d	Section depth
d'	Clear section depth
e	Link length
e^*	Balanced link length
E	Young's modulus of elasticity
E_s	Young's modulus of elasticity for steel
E_H	Cumulative energy dissipation
E_{HN}	Normalized energy dissipation
F_u	Ultimate stress
F_{uf}	Ultimate stress of flanges
F_{uw}	Ultimate stress of web
F_y	Yield stress
F_{yf}	Yield stress of flange
F_{yst}	Yield stress of stiffeners
F_{yw}	Yield stress of webs
h	Hardening parameter (bounding surface model)
K_e	Elastic stiffness
k_{li}	Initial elastic stiffness of link
L_{p2}	Distance between pantograph diagonals
$L_{p\mathrm{d}}$	Length of pantograph diagonals
M	Applied moment
M_{max}	Maximum experimentally obtained link end moment
M_p	Plastic moment
M_{pr}	Plastic moment reduced for full plastic shear force
M_p^f	Local flange plastic moment considering flange axial force
$M_{po}^{\ f}$	Local flange plastic moment without considering flange axial force

NOTATIONS (CONTINUED)

M_p^V	Plastic moment reduced for plastic shear force V_p^M
N_f	Number of cycles to failure
P_{pl}	Lower pantograph diagonal axial force
P_{ph}	Horizontal pantograph member axial force
P_{pt}	Upper pantograph diagonal axial force
R_b	Slope of bound line (bounding surface model)
R_{ki}	Initial stiffness (bounding surface model)
R_{kp}	Tangent plastic stiffness (bounding surface model)
R_{kt}	Tangent stiffness at current displacement (bounding surface model)
R_y	Ratio of expected to specified yield stress
t_f	Flange thickness
t_f	Stiffener thickness
t_w	Web thickness
V	Applied shear force
V_a	Applied actuator load
V_f	Shear force carried by the flanges
V_L	Applied link shear force
V_{lmax}	Maximum link shear force (finite element result)
V_{max}	Experimentally obtained maximum link shear
V_p	Plastic shear force
V_{ult}	Ultimate (upper bound) shear force
w	Stiffener width
α	Stiffener spacing over clear web depth and pantograph diagonal inclination angle
β	Section depth over web thickness
Δ	Frame displacement
Δ_{p2}	Displacement recording from string-pot P2
Δ_{p3}	Displacement recording from string-pot P3
$\Delta\varepsilon_p$	Plastic strain amplitude
$\delta\alpha$	Change in pantograph diagonal inclination angle

NOTATIONS (CONTINUED)

ϵ	Engineering strain
ϵ_t	True strain
ϵ_{tp}	True plastic strain
γ	Link rotation angle
γ_{lim}	Limit link rotation angle
γ_{limEH}	Limit link rotation angle projected from cumulative energy dissipation
γ_{limRP}	Limit link rotation angle projected from cumulative plastic rotation
γ_p	Plastic link rotation angle
γ_{pcum}	Cumulative plastic link rotation angle
γ_{plim}	Limit plastic link rotation angle
γ_t	Total or target link rotation angle
γ_{targ}	Target link rotation angle
γ_u	Design or ultimate link rotation angle
γ_y	Yield link rotation angle
ρ	Normalized link length
ρ_{targ}	Target normalized link length
σ	Normal stress
σ_t	True normal stress
Ω	Cyclic hardening factor

ABBREVIATIONS

AISC	American Institute of Steel Construction
ASTM	American Society for Testing and Materials
ATC	Applied Technology Council
EBF	Eccentrically Braced Frame
FE	Finite Element
FEA	Finite Element Analysis
HSS	Hollow Structural Section
LRFD	Load and Resistance Factored Design
MCEER	Multidisciplinary Center for Earthquake Engineering Research
MTS	Material Testing Systems, Inc.
SEESL	Structural Engineering and Earthquake Simulation Laboratory
UB	University at Buffalo or Unbonded Brace
UTM	Universal Testing Machine
WF	Wide-flange

SECTION 1

INTRODUCTION

1.1 Statement of Problem and Objectives

There are many bridges in the United States and other countries that are considered to be seismically vulnerable (Ritchie et al., 1995). Steel truss bridges, which are often long span bridges and might carry critical transportation lifelines, are one such category of bridges. The piers of these bridges, and particularly the pier brace members, have been identified in previous studies as elements which may contribute significantly to their poor seismic performance. Typically, the brace members are composed of angles or channels tied together with steel lacings and rivets. Experimental studies have shown these members are subject to local buckling, leading to rapid strength degradation and limited ductility when subjected to large cyclic loads (Astaneh et al., 1994, Uang and Keiser, 1997, Astaneh et al., 1998, Itani et al., 1998, and Lee and Bruneau, 2004).

The retrofit of these piers and bracing members is often undertaken to ensure the adequate seismic performance of steel bridges. Previous research has proposed the use of eccentrically braced frames with self-stabilizing tubular links as both a retrofit alternative and seismic load resisting system for new bridges (Berman and Bruneau, 2005a). That research showed, via analytical development and a proof-of-concept experiment, that these types of links can provide ductile and stable hysteretic energy dissipation without any lateral bracing. This report is a continuation of that research, with the objective of proposing design requirements for tubular links for eccentrically braced frames. Additionally, Berman and Bruneau (2005b) investigated the use of supplemental systems for the retrofit of braced bridge piers, which was another alternative presented in Berman and Bruneau (2005a).

First, a finite element model of the link from the proof-of-concept test described in Berman and Bruneau (2005a) is developed utilizing shell elements. Refinement of the finite element mesh and selection of the element type is discussed in the context of achieving convergence and good agreement with the experimental results.

Using the finite element model of the proof-of-concept link as a basis, a parametric study of hybrid rectangular links is performed (hybrid meaning that webs and flanges may have different yield stresses). This parametric study is divided into two parts, the first examines links with various web and flange compactness ratios and link lengths, and the results are used to formulate proposed design recommendations. The second part of the parametric study examines links with webs and flanges near the revised compactness ratio limits, but having different yield stresses, to verify that those revised limits are acceptable for a common range of available steel grades.

Finally, a testing program is conducted on fourteen different links. Three different cross-sections are developed for this testing, two that have webs and flanges near the revised compactness ratio limits, and one with much stockier cross-section elements. Four link lengths are used for each cross-section. Two of the links are also fabricated and tested with different end connections. The design of a large, reconfigurable, test frame to conduct these experiments is presented. Results of this testing are presented and further design recommendations for hybrid rectangular links are given.

1.2 Scope of Work

The research conducted and reported herein is outlined below:

- Develop a finite element model of the link from the proof-of-concept test described in Berman and Bruneau (2005a).
- Conduct a finite element parametric study using links with a range of web and flange compactness ratios and use the results to revise the proposed design requirements.
- Conduct a second finite element parametric study to investigate the appropriateness of the revised recommendations for links having webs and flanges with differing yield stresses.

- Design and conduct an experimental program to validate the design recommendations and finite element results.
- Recommend additional research needs for the retrofit strategy of laterally stable eccentrically braced frames.

1.3 Organization

Section 2 describes the finite element modeling of the link from the proof-of-concept testing. Comparison with the experimental results is provided, as is a mesh refinement study.

Section 3 describes the development and results of the finite element parametric study. This study is composed of two parts. The first part investigates a range link geometries and the results are used to revise the design recommendations for hollow rectangular link. The second part investigates the effects of webs and flanges with different yield stresses on links with geometries near the revised compactness limits.

Section 4 describes the design of fourteen different links for experimental verification of the revised design recommendations and finite element results. Also described is the design of the setup to carry out this testing.

Section 5 describes the loading protocol and observations made for the testing of the fourteen link specimens described in Section 9. The failure mode of each link is documented and link shear force versus rotation hysteresis curves are presented.

Section 6 presents the analysis of the link testing data, including, maximum rotations, energy dissipation, overstrength, flange strains, and comparison with finite element models.

Section 7 presents conclusions and recommendations for further research. Included in this section are proposed rules for the design of hybrid rectangular links for eccentrically braced frames considering the results of all presented work. Recommendations for future research are also given for eccentrically braced frames having links with hybrid rectangular cross-sections.

SECTION 2
FINITE ELEMENT MODELING OF THE PROOF-OF-CONCEPT LINK

2.1 General

In this section, the development of a finite element analysis (FEA) model of the link from the proof-of-concept experiment described in Berman and Bruneau (2005a) is presented. This model provides the basis for a parametric study of tubular links to investigate the design equations and requirements formulated in that same report. Some modeling assumptions were made consistently with a previous finite element study of WF links by others calibrated to experimental data. Material properties, boundary conditions, loading, elements, and mesh used to model the proof-of-concept link are also described . Finally, the results of the FEA are compared with the experimental results.

2.2 Review of Finite Element Study of WF Links

Richards and Uang (2002) performed a comprehensive finite element study to evaluate the rotation capacity and overstrength of WF links as a function of flange compactness. They correlated three base models in ABAQUS (HKS, 2001) with experimental results for three WF link specimens (Arce, 2002). These models were then extrapolated to various link geometries. In all cases, only the link was modeled and no attempt to account for the flexibility of framing used in the experimental investigation was made. A review of this work is significant, as finite element analysis results were "calibrated" to accurately replicate experimental results, which can help define many modeling parameters for the current study.

Loading was consistent with that given in the American Institute of Steel Construction Seismic Provisions (AISC, 2002) for link-to-column connections, which specifies three cycles at each total link rotation level of 0.0025, 0.005, and 0.01 radians, followed by two cycles at 0.01 radian increments up to the maximum code specified rotation.

Richards and Uang used the reduced integration, 4-noded, 6 degree of freedom, shell element S4R to model the webs, flanges, and stiffeners of their WF links. Mesh refinement studies were conducted to determine the adequate level of refinement. The final mesh density resulted in elements with edge lengths of approximately 25.4 mm (1 in) and edge length-to-thickness ratios of 2 to 4.

The elasto-plastic material model with nonlinear kinematic hardening was selected for the web and flanges of the links. Data from cyclic coupon testing of ASTM A572 Grade 50 steel performed at Lehigh University (Kaufmann et al. 2001) was used to calibrate the material model. Experimental data was taken from cycles at strains of ±0.04%, since strains near that level were expected. It should be noted that at this strain level there was negligible isotropic hardening in the cyclic coupon test results, which is typical for mild steels cycled at large strains, which justified use of a nonlinear kinematic hardening material model without an isotropic hardening component for that study. The flange material was also used for the stiffeners in the link models.

Boundary conditions were specified as illustrated in figure 2-1. Nodal rotations at each link end were restrained and loads were applied by imposing vertical displacements on the right end nodes, which were fixed against all other translations. Nodes on the left end were allowed to translate in the horizontal in-plane direction to prevent the development of axial force in the link, and were restrained against all other translations.

Comparisons of experimental and finite element analysis results are shown in figures 2-2 and 2-3. The former compares the obtained analytical and experimental link shear versus plastic rotation hystereses for the UTA 6 specimen, and the latter compares the deformed geometry for the same specimen. The behavior of the link, as shown in figure 2-2, consists of several

elastic cycles, followed by the development of the link plastic shear strength (or plastic moment for the case of flexural links). Increases in link strength following the development of the plastic shear are primarily due to strain hardening, and appropriately detailed links can achieve large rotations without loss of link plastic shear strength. Degradation begins, in most cases, with web, flange, or lateral torsional buckling as shown in figure 2-3. Similar agreement was obtained for the modeling of the two other reference specimens. Following the development and verification of the base models, link geometries were extrapolated to various link lengths, flange thicknesses, and stiffener spacings. Approximately 70 links were analyzed in total.

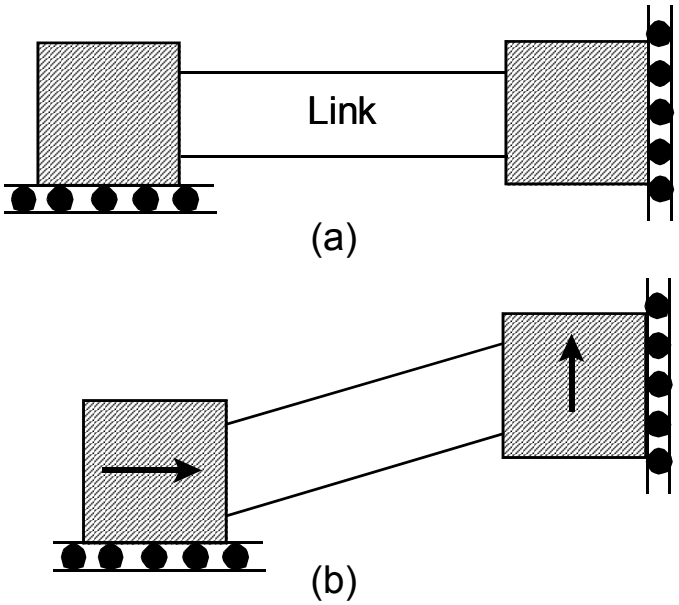

FIGURE 2-1 Link Boundary Conditions (a) Initial Position (b) Deformed Configuration (Adapted from Richards and Uang, 2002)

The finite element study of WF links by Richards and Uang showed that shear and flexural links with flange compactnesses up to $0.38\sqrt{E_s/F_{yf}}$ can achieve their target maximum rotations. They also observed that some intermediate length links with flanges meeting both the AISC seismic flange compactness limits for WF sections $b_f/t_f<0.30\sqrt{E_s/F_{yf}}$ and $b_f/t_f<0.38\sqrt{E_s/F_{yf}}$ did not achieve their target rotation, leading them to the conclusion that factors other than flange compactness were effecting the rotation capacity of the intermediate links considered. Therefore, they proposed that the current WF flange compactness limit

($b_f/t_f<0.30\sqrt{E_s/F_{yf}}$) be changed to $b_f/t_f<0.38\sqrt{E_s/F_{yf}}$, since this limit worked for all shear and flexural links considered (i.e., they all met the target rotation), and in the case of intermediate links resulted in no fewer links not reaching the target rotation than was the case for the current flange limit. As a result of this change, nearly all WF shapes available in the AISC Manual could be used as links in eccentrically braced frames.

Richards and Uang determined that stiffener spacing and link length were the primary factors affecting maximum link rotation. Certain intermediate links in the study did not achieve the code specified maximum rotations, even though they met the code criteria for stiffener spacing, which is based on link length and target maximum rotation. They attributed this to the fact that the stiffener spacing requirements derived by Kasai and Popov (1986) for shear links were extrapolated to intermediate links without significant experimental or analytical supporting evidence. Although they explored several alternatives for modifying the stiffener spacing requirements and/or the calculation of maximum link rotations for intermediate links, no such changes were recommended on the basis that the complexity of the alternative equations could not be justified given that intermediate links are seldom used, and because stiffener spacing is usually less than the maximum allowed by the code (for the practical reason of achieving equal stiffener spacing).

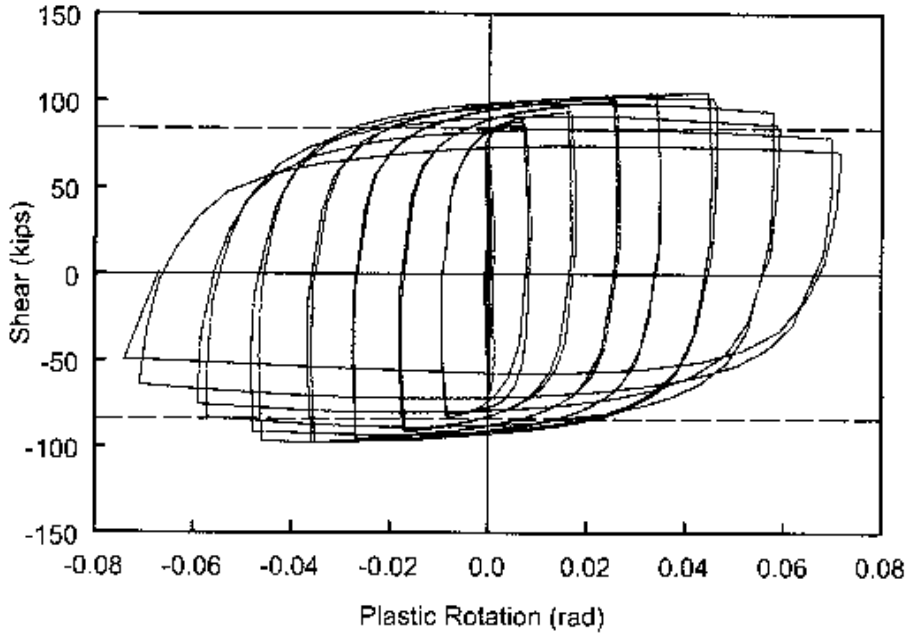

(a) Test

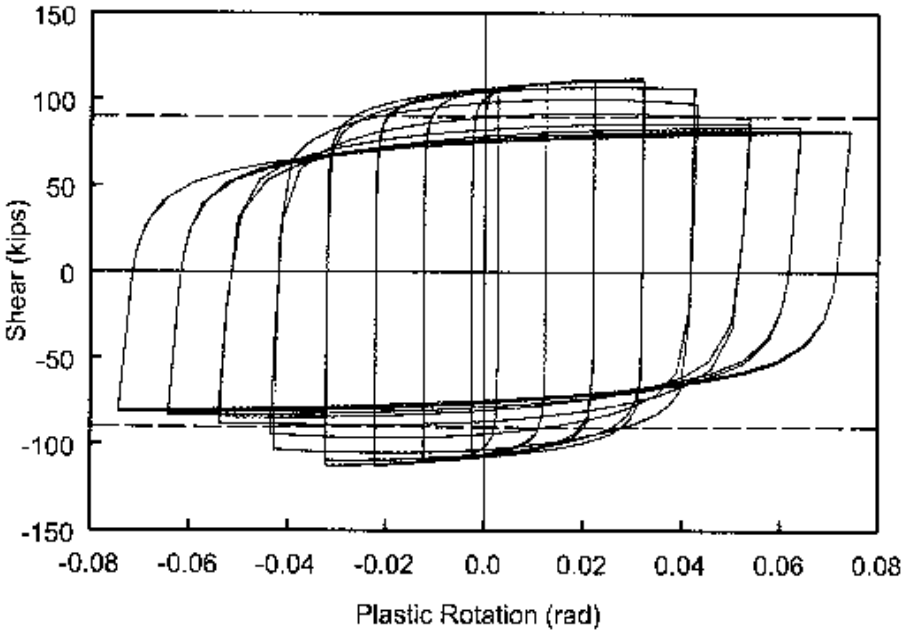

(b) ABAQUS Model

FIGURE 2-2 Comparison of Experimental and Analytical Hystereses (Richards and Uang, 2002)

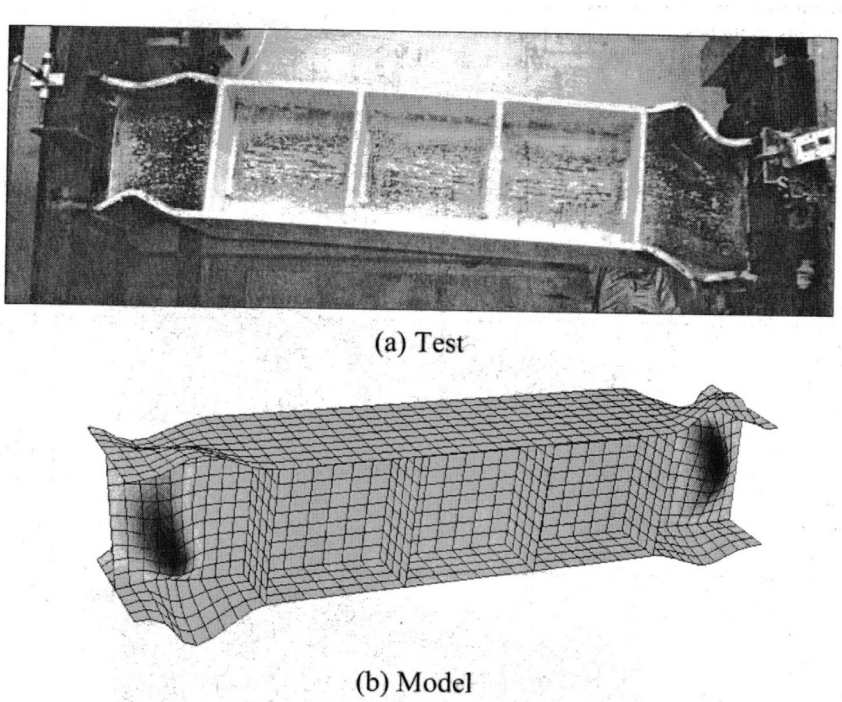

FIGURE 2-3 Comparison of Deformed Geometry for Specimen UTA 6 (Richards and Uang, 2002)

2.3 Development of the Proof-of-Concept Link Model

Using the link from the proof-of-concept test described in Berman and Bruneau (2005a), a FE model was developed in ABAQUS. Some preliminary analyses were conducted to study the effect of mesh refinement and to determine whether reduced integration elements could be used to improve computational time without loss of significant accuracy. The cross-section and details for the link from the proof-of-concept testing are shown in figures 2-4 and 2-5. Centerline dimensions were modeled in ABAQUS resulting in a modeled web depth of d-t_f, or 136.5 mm (5.375 in), and flange width of b-t_w, or 144 mm (5.6875 in).

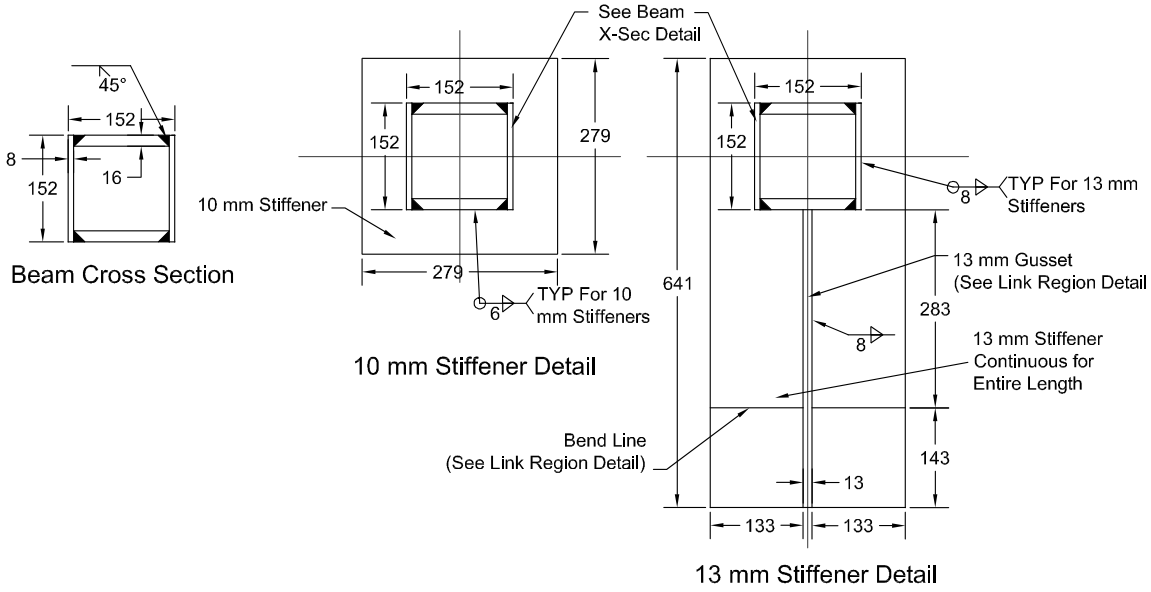

FIGURE 2-4 Link and Stiffener Cross-Sections (Berman and Bruneau 2005a)

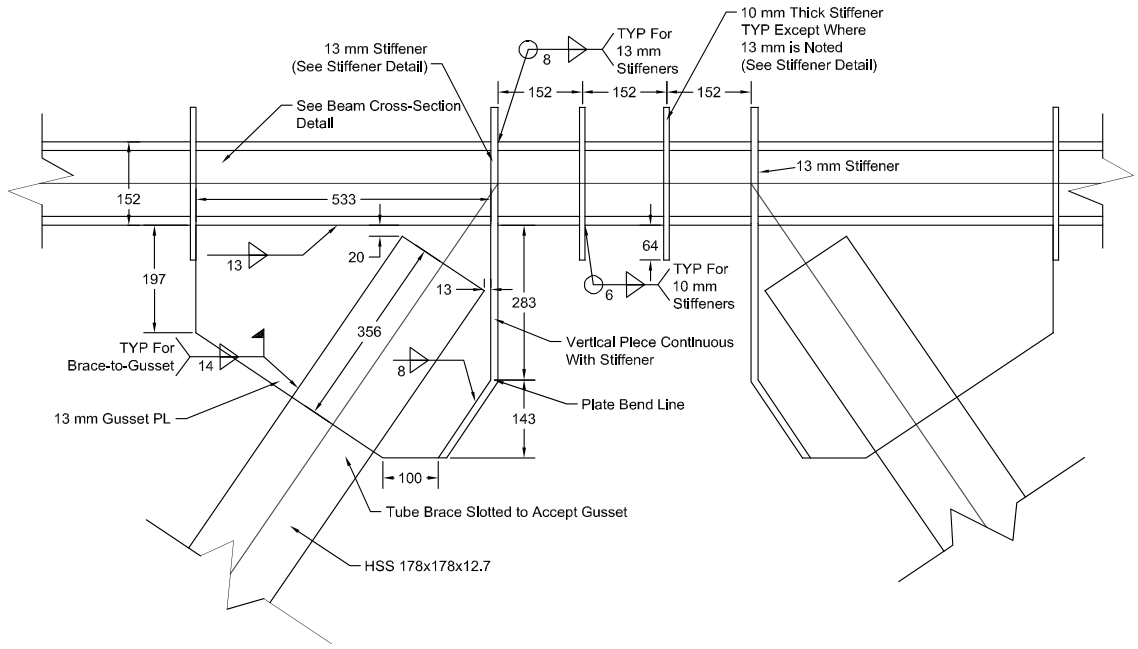

FIGURE 2-5 Link and Stiffener Detail (Berman and Bruneau 2005a)

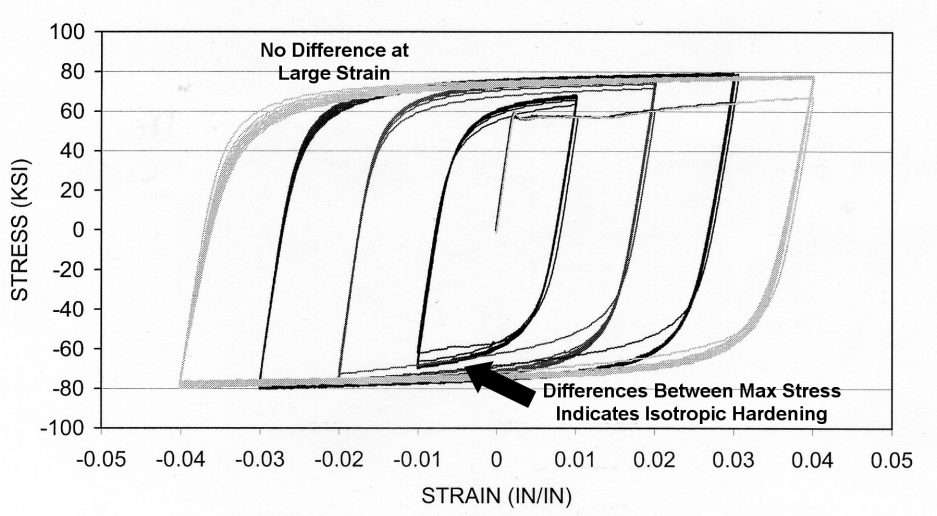

FIGURE 2-6 Cyclic Stress-Strain Curve for Steel C (Adapted from Kaufmann et al., 2001)

2.3.1 Materials

The material model chosen for this study is the nonlinear kinematic hardening plasticity model available in ABAQUS. Since high strains are expected to develop in the flanges and webs of the proposed tubular link, no isotropic hardening component was considered because at large cyclic strains the effect of this component is negligible (see figure 2-6). The stress-strain curves for both the web and flange material are shown in figures 2-7a and 2-7b respectively. Several methods for input of the stress-strain behavior are available for the nonlinear kinematic hardening plasticity model in ABAQUS. Since only monotonic curves for the material used in the proof-of-concept test were available, the "half cycle data" option of ABAQUS was selected. This option requires knowledge of only a stabilized half cycle (being defined as the stress-strain curve for a half cycle of a unidirectional tension experiment at a given strain amplitude), which in this case was derived from the monotonic tension coupon test results for the web and flange material (also shown in figures 2-7a and 7b). ABAQUS requires that stress and strain data are input in terms of true stress, σ_t, and corresponding true plastic strain, ϵ_{tp}, which can be found in terms of engineering stress, σ, and strain, ϵ, as:

$$\epsilon_t = \ln(1+\epsilon) \qquad \textit{and} \qquad \epsilon_{tp} = \epsilon_t - \frac{\sigma}{E} \tag{2-1}$$

$$\sigma_t = \sigma(1+\epsilon) \tag{2-2}$$

where ϵ_t is the true total stain. The material used for the stiffeners is based on Steel C from Kaufman et al. (2001), which is an A572 Gr. 50 steel. All materials used had isotropic linear elastic portions up to their respective yield stresses with modulus of elasticity, E, of 2 x 10^6 MPa (29000 ksi).

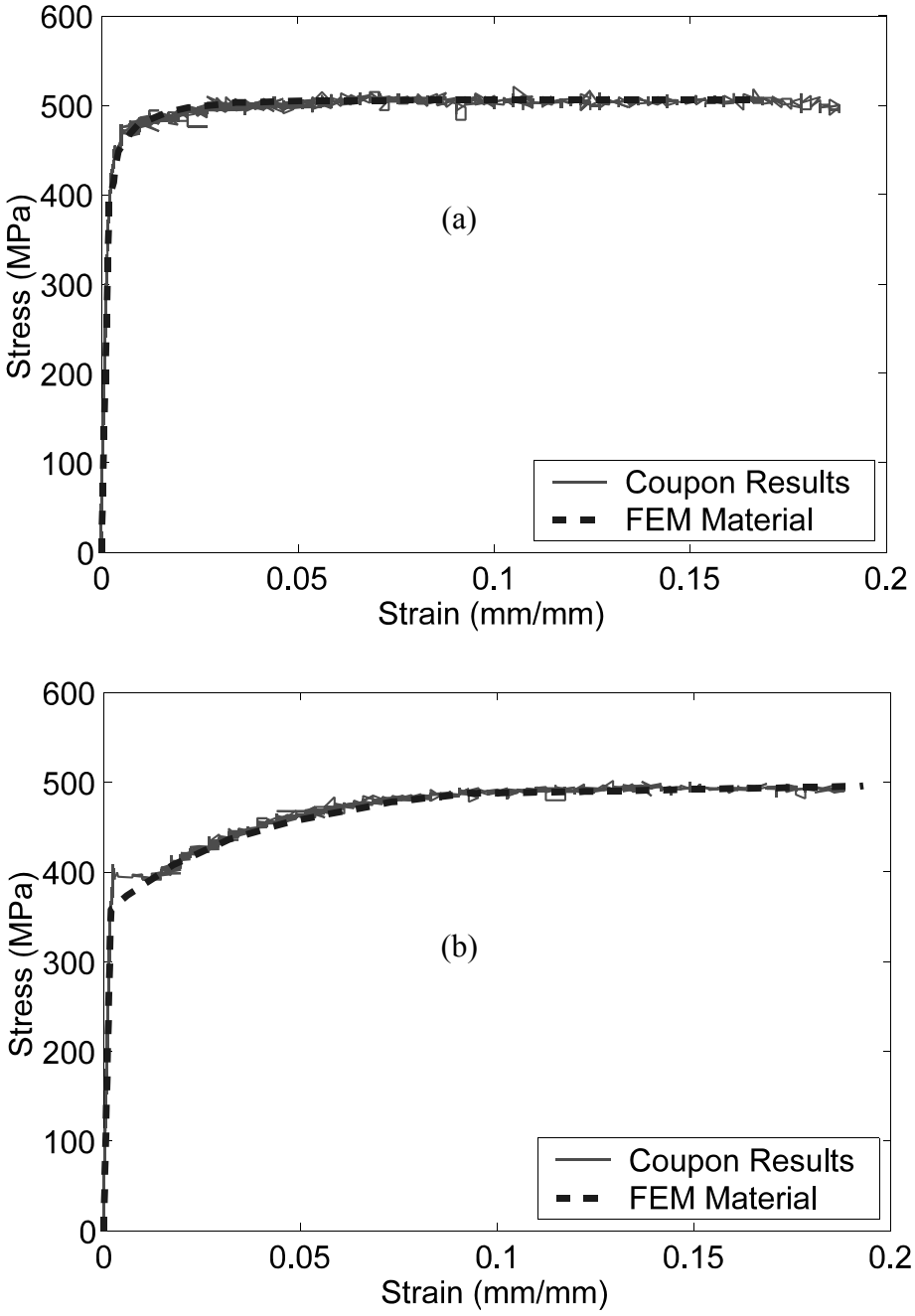

FIGURE 2-7 Engineering Stress-Strain Curves: (a) Web Material; and (b) Flange Material

2.3.2 Boundary Conditions and Loading

Boundary conditions were applied by constraining all degrees of freedom of the nodes at each end of the link to master nodes placed at the center of the cross-section at each link end. The left end master node was then restrained against all displacements and rotations except translation in the link's axial direction. The right end master node was restrained against all displacements and rotations except the vertical translation. These boundary conditions are the same as those in figure 2-3.

Loading was applied through the vertical translation of the right end master node. The same loading history as that recorded in the proof-of-concept testing was used, as summarized in table 2-1. A monotonic load up to a rotation of 0.15 rads was also run for the purposes of mesh refinement comparisons.

TABLE 2-1 Loading Protocol for FE Models of Proof-of-Concept Link

Number of Cycles	Link Rotation (rad)	End Displacement (mm)	Percent of Maximum
3	±0.002	±0.9	1.36
3	±0.004	±1.8	2.86
3	±0.007	±3.2	5.00
3	±0.029	±13.5	20.70
3	±0.056	±25.6	40.00
2	±0.085	±38.9	60.71
2	±0.113	±51.7	80.71
2	±0.140	±64.0	100.00

2.3.3 Elements and Mesh

Using the geometry and materials defined above, the link model was developed with a mesh with element edge lengths of approximately 50 mm (2 in), corresponding to element edge length-to-thickness ratios ranging from 3.2 to 6.4, as shown in figure 2-8 and denoted Mesh 1. This model used S4 elements, which are general purpose, 4-noded shell elements

with 6 degrees of freedom per node, large strain capabilities, and formulations that allow thick shell elements which reduce to Kirchhoff shell elements as the thickness decreases. They also use 3 Gauss Integration points through the thickness of the shell, are not subject to shear locking because they are reduced integration elements, and have an artificial hour-glass stiffness to prevent the propagation of hour-glass modes through the model.

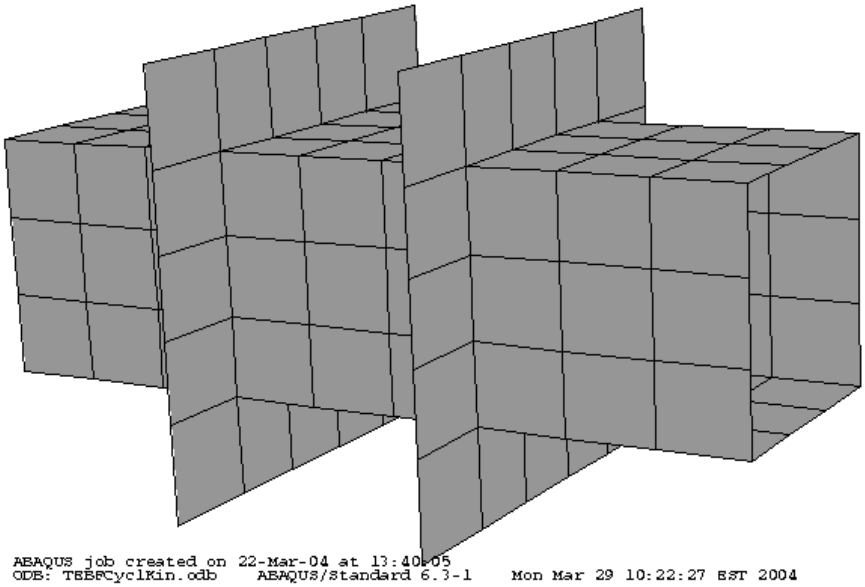

FIGURE 2-8 Mesh 1

The mesh of figure 2-8 was then refined by halving all the elements to obtain the mesh of figure 2-9 (denoted Mesh 2). This model used the same S4 shell elements and had element edge length-to-thickness ratios of 1.6 to 3.2. A third model was developed by halving all the elements of Mesh 2, to obtain Mesh 3 (figure 2-10) which had element edge length-to-thickness ratios ranging from 0.8 to 1.6. Only monotonic loading was considered with the third mesh. Finally, a fourth model using Mesh 2 was developed using S4R, reduced integration shell elements. Analysis results from these four models are discussed in following section. From those results it appears that Mesh 2 is adequate (element edge length to thickness ratios of 1.6 to 3.5), and that the reduced integration elements should provide reasonable results.

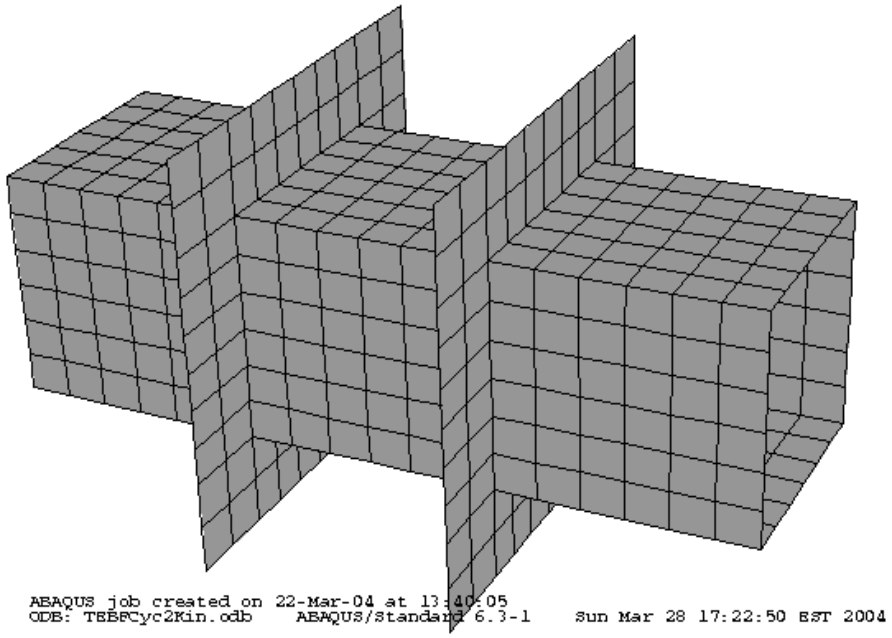

FIGURE 2-9 Mesh 2

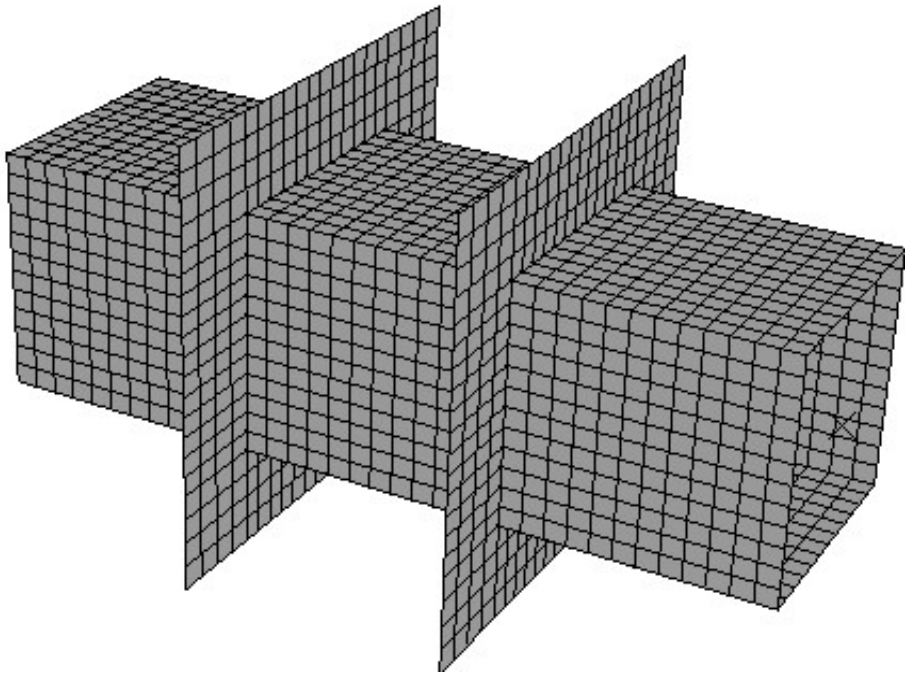

FIGURE 2-10 Mesh 3

2.4 Comparison with Experimental Results

Monotonic analyses were run for each of the models described above (Model 1 = Mesh 1, Model 2 = Mesh 2, Model 3 = Mesh 3, Model 4 = Mesh 2 with S4R elements). Results for link shear versus link rotation are given in figure 2-11. All models agree well with experimental results, and the difference between Models 2 and 4 is indistinguishable. Presented in figures 2-12 and 2-13 are the mid-width flange stresses at the link end and mid-depth web shear stress for each of the models respectively. Since the difference in the stress magnitudes between the three mesh refinements are small, it was determined that the second mesh density was adequate. Furthermore, since the difference in flange and web stress between Models 2 and 4 is small (essentially zero), it appears that S4R elements can be used. Following these analyses, cyclic analyses of Models 1, 2, and 4 were performed and are discussed below.

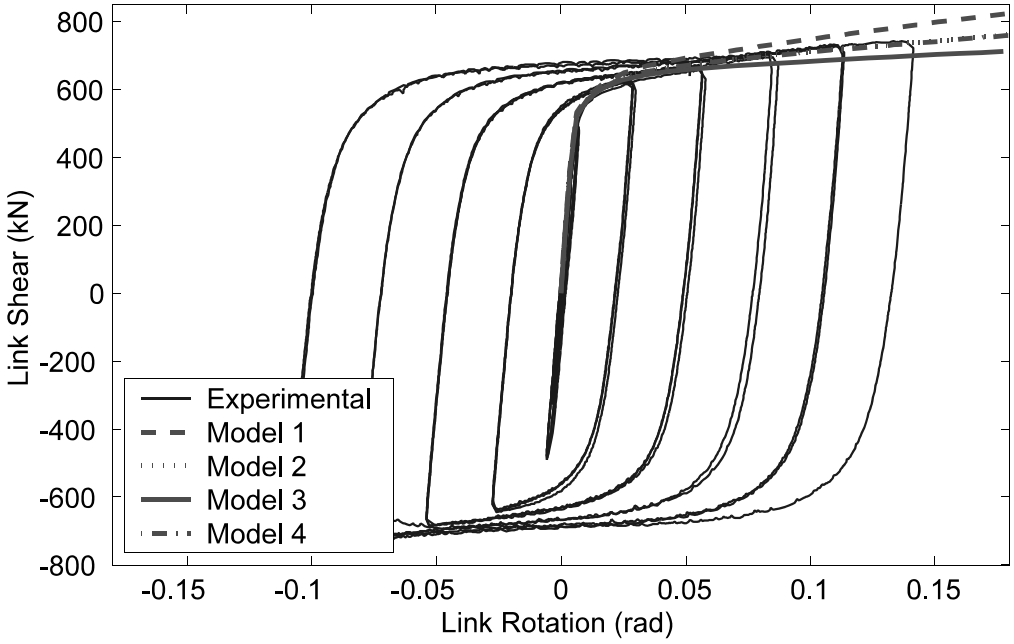

FIGURE 2-11 Link Shear vs. Link Rotation for Monotonic Analyses and Experimental Results

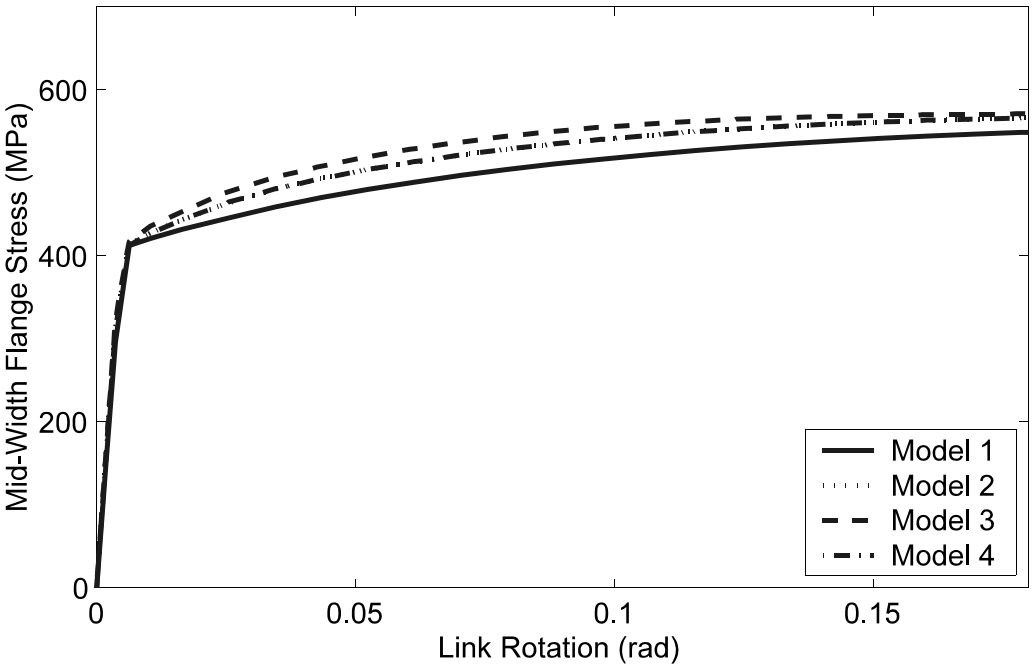

FIGURE 2-12 Mid-Width Flange Stress vs. Link Rotation for Various FE Model Refinements

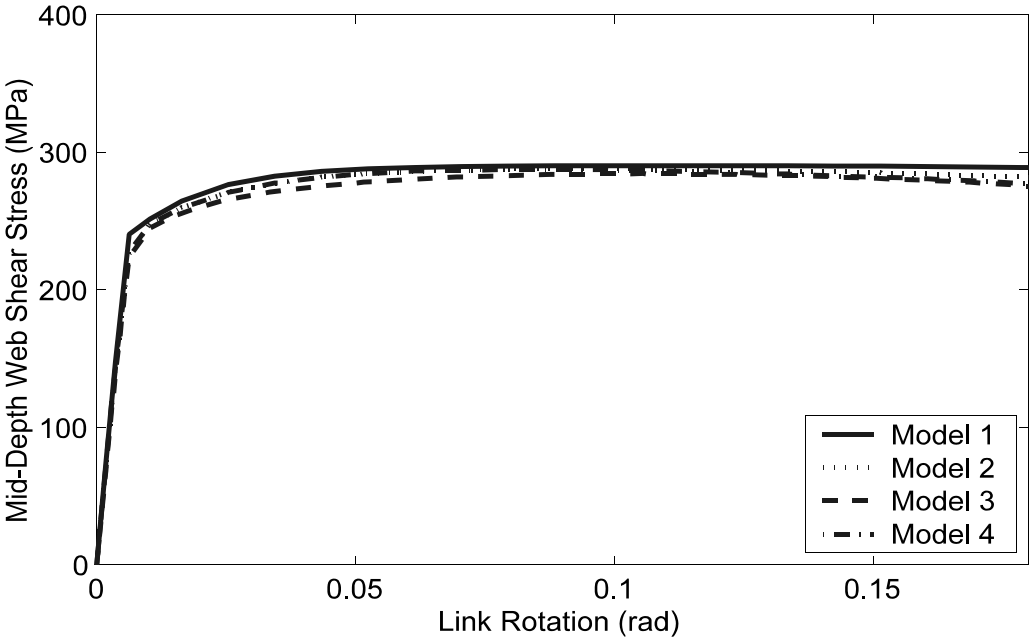

FIGURE 2-13 Mid-Depth Web Shear Stress vs. Link Rotation for Various FE Model Refinements

Figures 2-14, 2-15, and 2-16 show the obtained link shear vs. link rotation hystereses for the cyclic analyses of Models 1, 2, and 4. Comparison of the experimental and analytical results for each of these models in these figures all show good agreement in the hysteretic results for the various mesh refinements and type of elements used for the refined mesh. Figures 2-17 and 2-18 show the deformed link for Model 1 and Model 2 (the deformation of Model 4 was indistinguishable from that of Model 2). There are some small differences, such as the magnitude of the stiffener deformation, but both agree well with the experimentally obtained link deformation shown in figure 2-19.

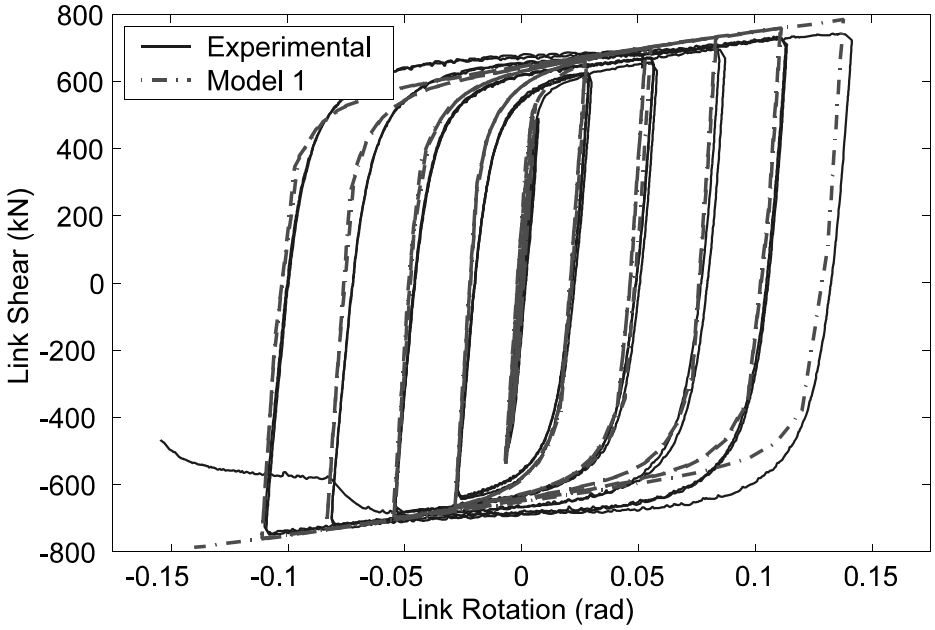

FIGURE 2-14 Comparison of Model 1 and Experimental Link Shear vs Link Rotation Hystereses

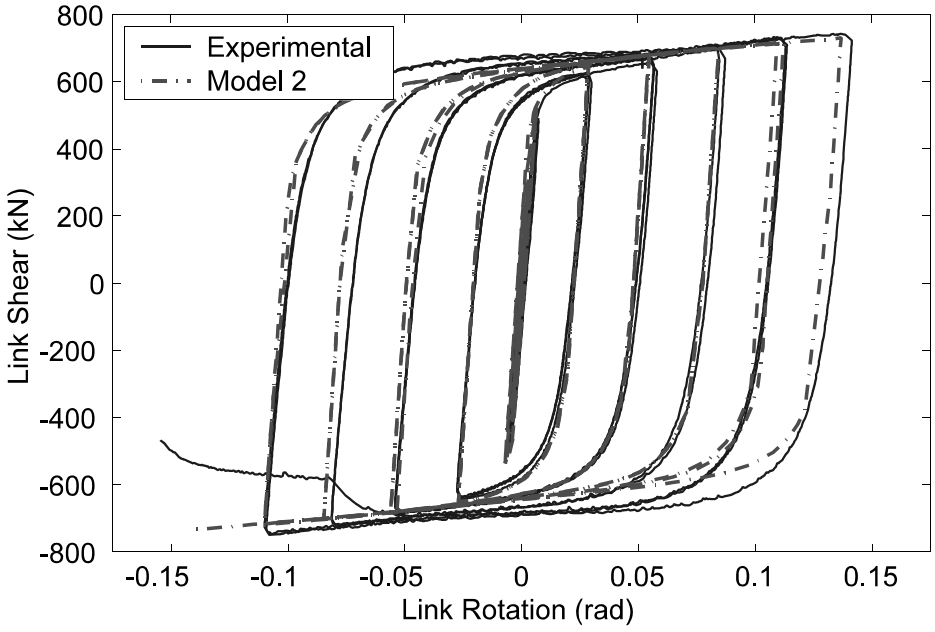

FIGURE 2-15 Comparison of Model 2 and Experimental Link Shear vs Link Rotation Hystereses

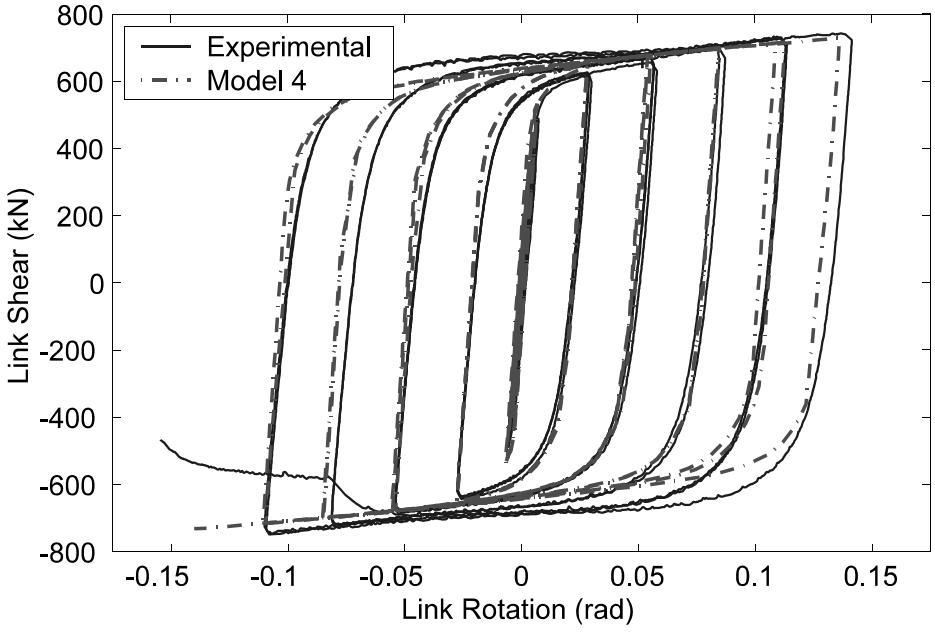

FIGURE 2-16 Comparison of Model 4 and Experimental Link Shear vs Link Rotation Hystereses

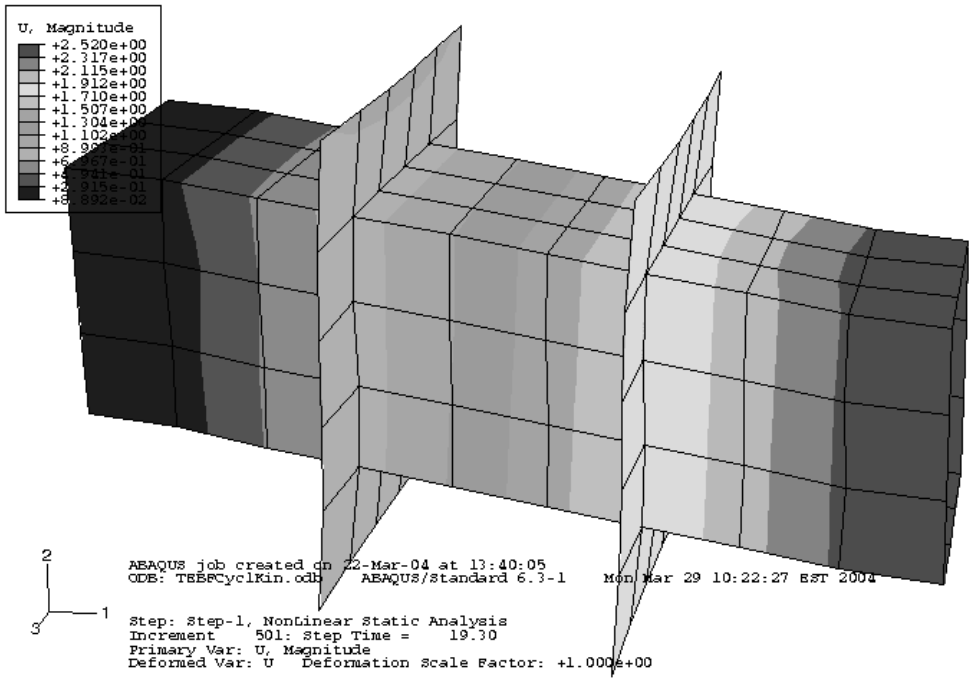

FIGURE 2-17 Deformed Link in Model 1

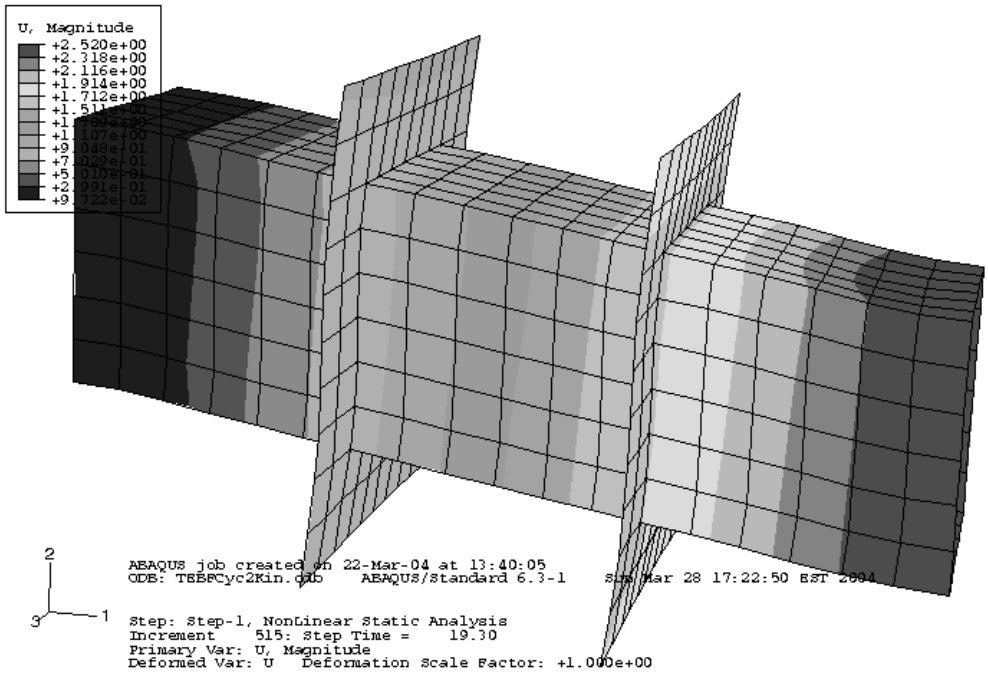

FIGURE 2-18 Deformed Link in Model 2

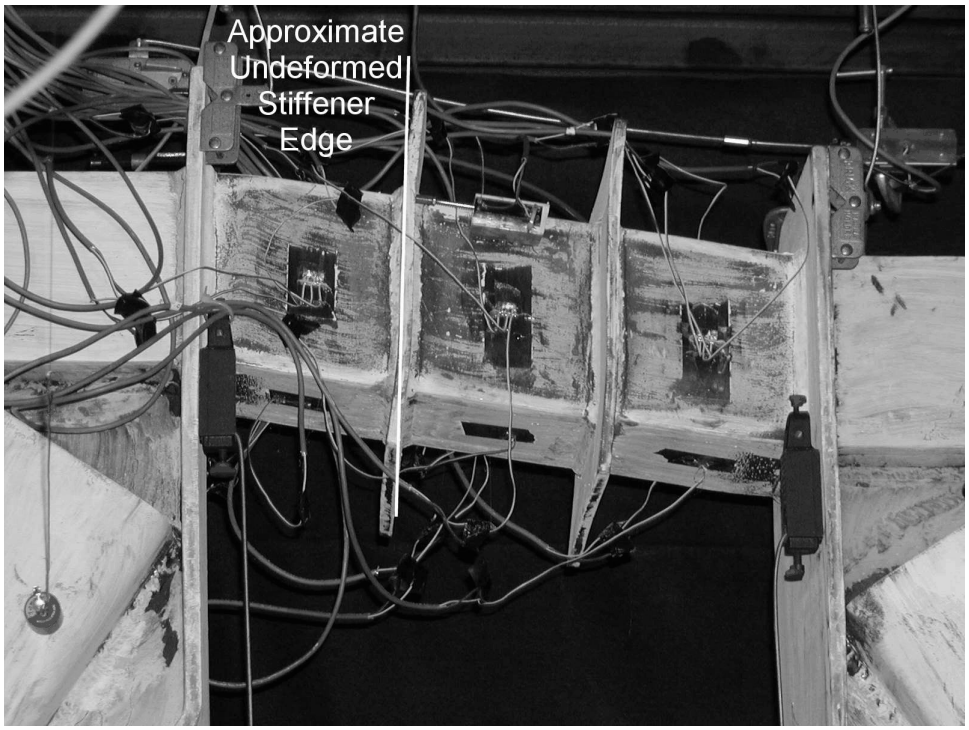

FIGURE 2-19 Deformed Link and Stiffener Curl at $6\delta_y$, 2.3% Drift, 0.140 rads Rotation, Cycle 20

Figures 2-20, 2-21, and 2-22 show element stresses in the longitudinal link direction at the end of the cyclic analysis. For Models 2 and 4 the maximum longitudinal stress in the mid-width of the top flange at the link end is in the range of 550 MPa to 607 MPa (80 to 88 ksi, note that the contour values are shown in ksi) while for Model 1 it is around 669 MPa (97 ksi). Furthermore, the pattern of the longitudinal stresses is similar in all 3 cyclic models and is especially similar when comparing Models 2 and 4. Shown in figures 2-23, 2-24, and 2-25 are the element shear stresses for Models 1, 2, and 4 respectively. While there is a slight change in the shear stress magnitudes near the web-stiffener intersections (these differences are not distinguishable in the figures presented here but are when investigated more closely in ABAQUS), the magnitude of the shear stresses for the majority of the web are the same for the three models and in the range of 276 MPa to 310 MPa (40 to 45 ksi). The differences in the stresses at both the web-flange intersections at the link endpoints and at the web-stiffener intersections is expected since this a region of some stress concentration. Considering the overall good agreement between the experimental results and the results using the second mesh with both S4 and S4R elements, as well as the significant

computational savings achieved with the S4R elements, the second level of mesh refinement with S4R elements is selected for use in the parametric study.

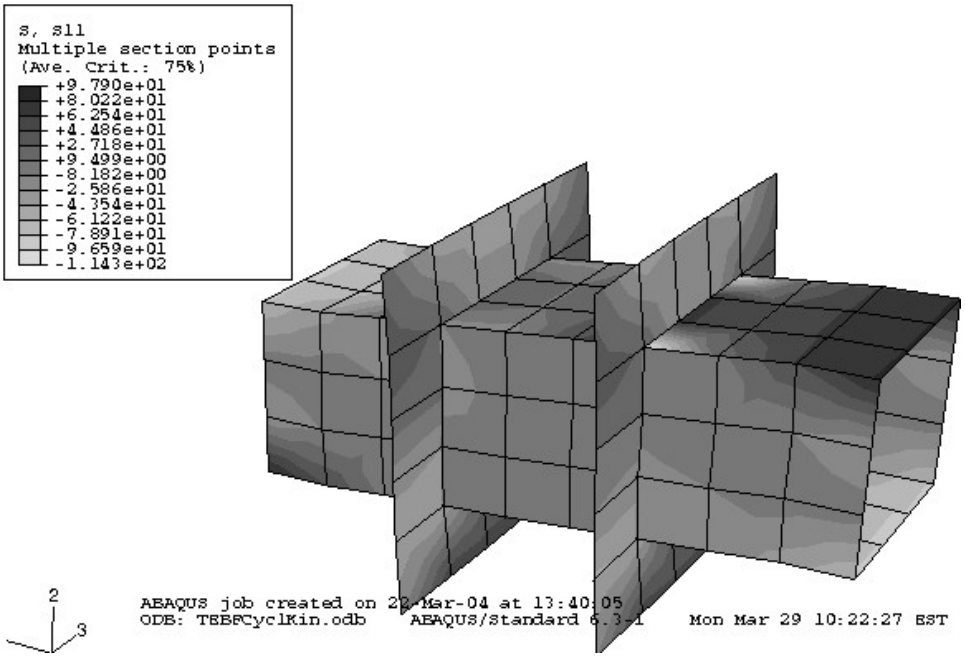

FIGURE 2-20 Longitudinal Stresses at End of Cyclic Analysis for Model 1

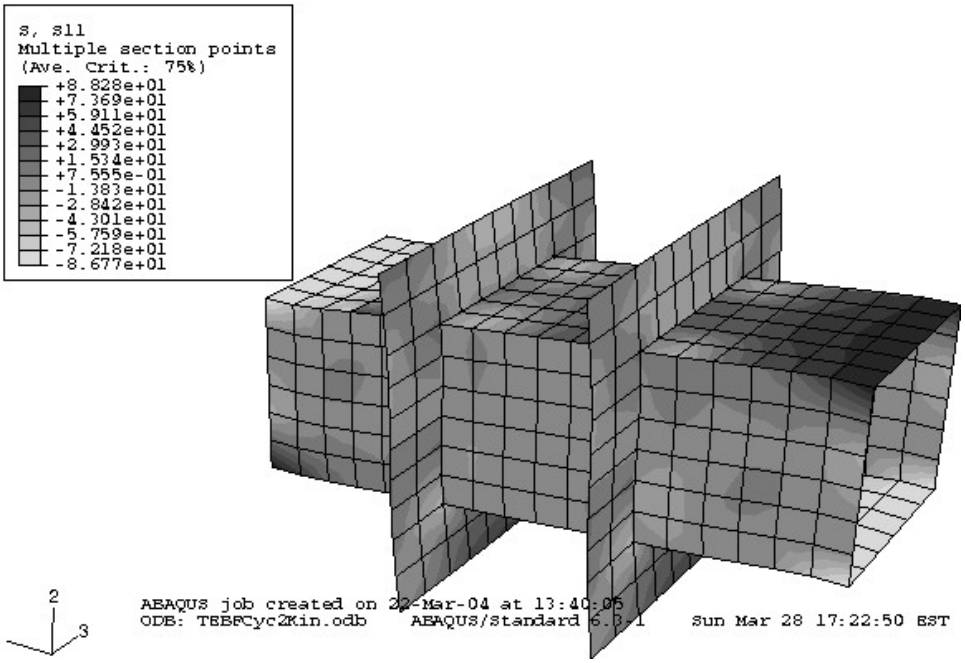

FIGURE 2-21 Longitudinal Stresses at End of Cyclic Analysis for Model 2

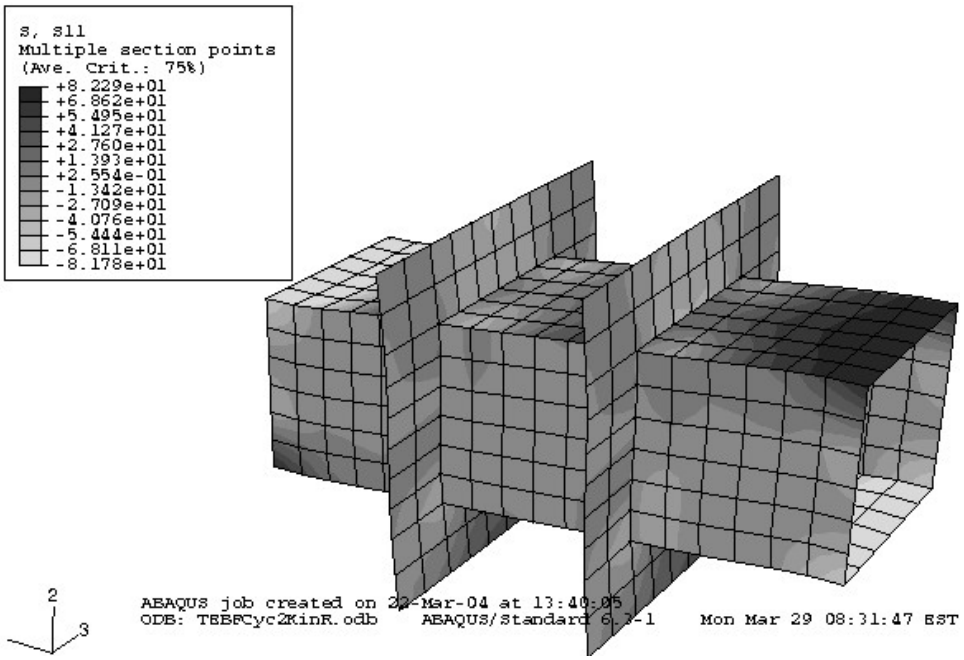

FIGURE 2-22 Longitudinal Stresses at End of Cyclic Analysis for Model 4

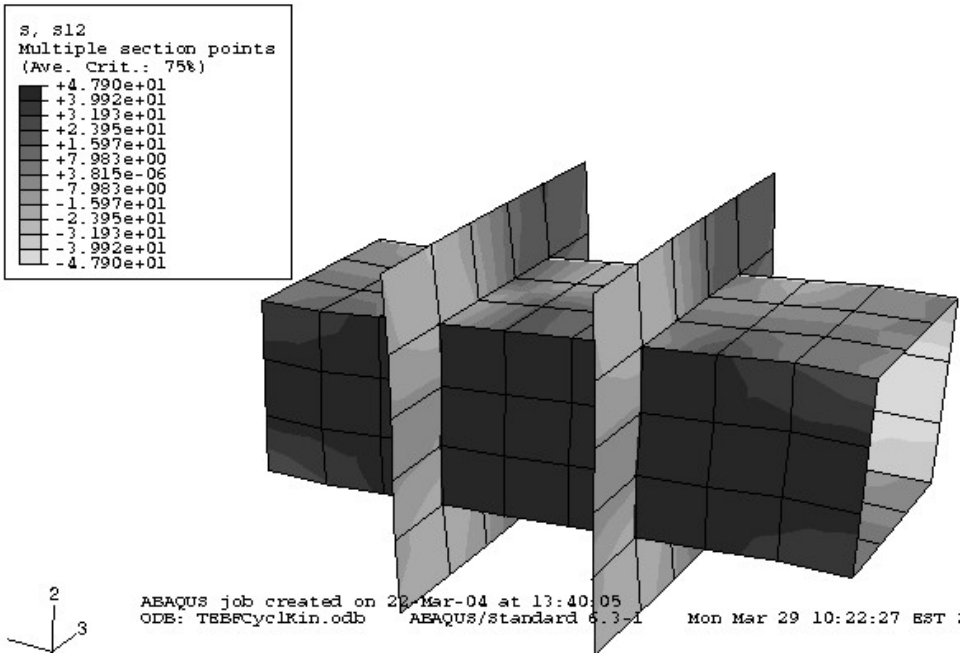

FIGURE 2-23 Shear Stresses at End of Cyclic Analysis for Model 1

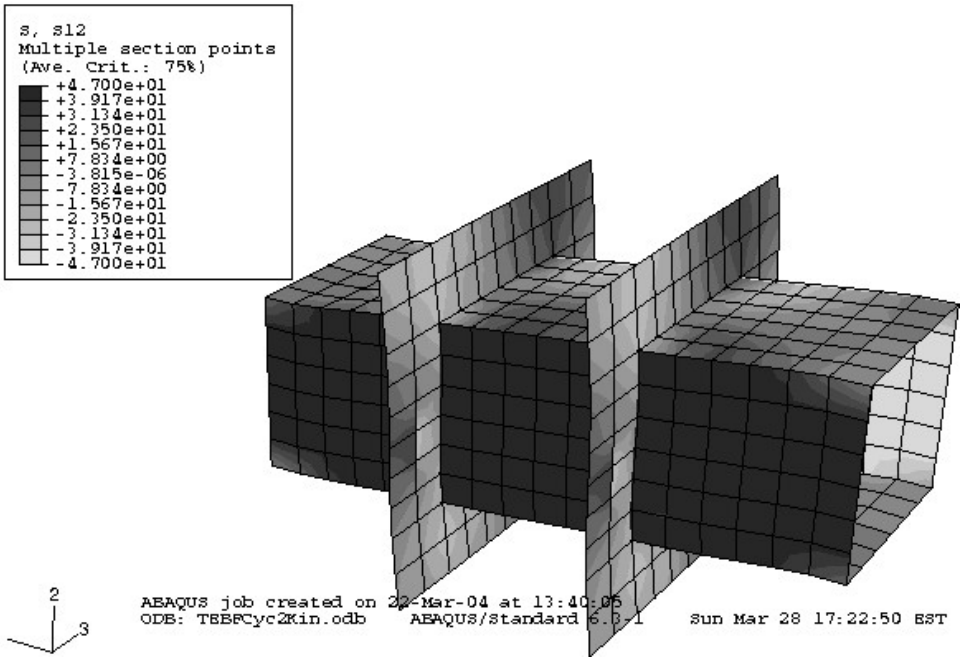

FIGURE 2-24 Shear Stresses at End of Cyclic Analysis for Model 2

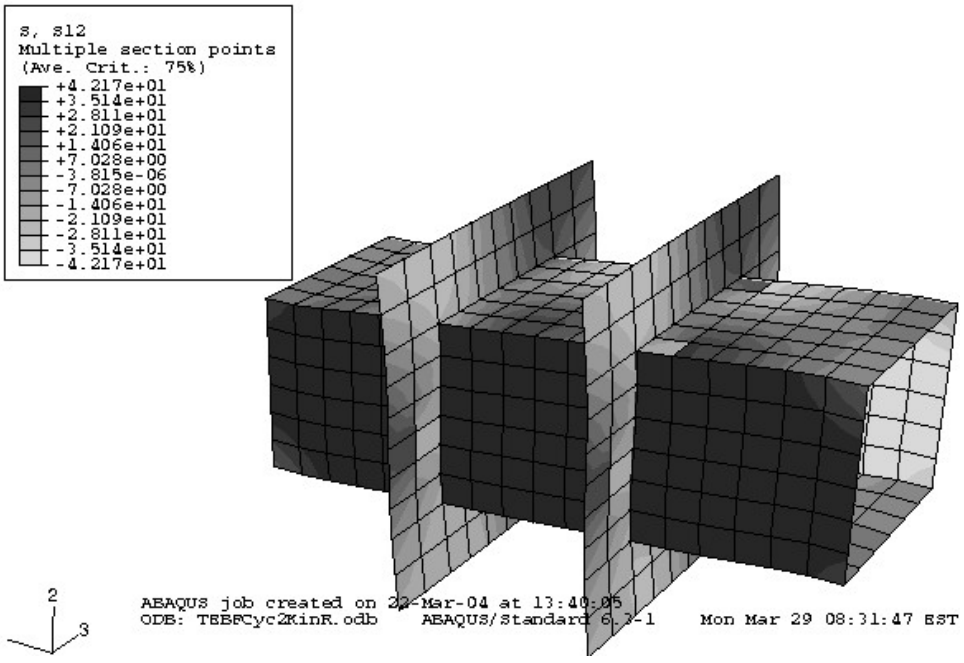

FIGURE 2-25 Shear Stresses at End of Cyclic Analysis for Model 4

SECTION 3

FINITE ELEMENT PARAMETRIC STUDY OF HYBRID RECTANGULAR LINKS

3.1 General

This section describes the development and results of a finite element parametric study of hybrid rectangular links, involving over 200 combinations of geometries and properties. The parametric study is divided into two parts. Part 1 considers a wide range of compactnesses and link lengths to examine the difference in behavior between links satisfying and not satisfying the proposed design requirements in Berman and Bruneau (2005a). Results of Part 1 are then used to revise the proposed design rules. Part 2 of the study involves models developed with flange compactness, web compactness, and stiffener spacings near the revised design limits, and also examines links having webs and flanges with different yield stresses (hybrid links). Results from both parts of the study are also used to investigate link overstrength, energy dissipation, and the general behavior of hybrid links with hollow rectangular cross-sections (shown schematically in figure 3-1).

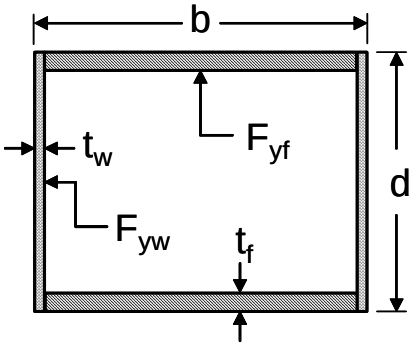

FIGURE 3-1 Hollow Hybrid Rectangular Cross-Section

3.2 Parameter Selection - Part 1

3.2.1 Non-Dimensional Parameters

Four parameters were used to develop the links in Part 1 of the parametric study: the normalized link length, ρ (defined as $e/(M_p/V_p)$), the flange compactness ratio, b'/t_f (where $b' = b - 2t_w$), the web compactness ratio, d'/t_w (where $d' = d - 2t_f$), and the stiffener spacing (where cases with stiffeners satisfying the spacing and sizing requirements derived in Berman and Bruneau (2005a) were considered). A total of 64 stiffened and 64 unstiffened links with cross-sections and lengths were analyzed, as described below. For the purpose of nomenclature, links will be labeled using S or N (for stiffened or unstiffened) followed by the numerical values for the parameters b'/t_f, d'/t_w, and ρ. For example, the name N-8-12-1.6 refers to an unstiffened link with a flange compactness of 8, web compactness of 12 and normalized length of 1.6.

Normalized link lengths representative of each yielding type, shear, intermediate, and flexural were selected. As assumed in Berman and Bruneau (2005a), the transition from shear to intermediate links occurs at ρ = 1.6 and the transition from intermediate to flexural links occurs at ρ = 2.6. Therefore, ρ = 1.2, 2.1, and 3.0 were selected as they represent evenly spaced values of normalized link lengths well within all three ranges of expected behavior. In addition, the length ρ = 1.6 was selected to verify that the proposed design rules work at this important transition length (i.e., the limit defining shear links). The target plastic rotation, denoted the target rotation, γ_t, for the links considered are 0.08 rads for ρ = 1.2 and 1.6, and 0.05 rads and 0.02 rads for links with ρ = 2.1 and 3.0 respectively. These values are used for consistency with the AISC seismic provisions for WF links and may warrant future research.

Flange compactness ratios were selected so that the applicability of the limit derived in Berman and Bruneau ($b'/t_f \leq 1.02\sqrt{E_s/F_{yf}}$) and the limit in the AISC seismic provisions ($b'/t_f \leq 0.64\sqrt{E_s/F_{yf}}$) could be evaluated. For a flange yield strength, F_{yf}, of 345 MPa (50 ksi) and a modulus of elasticity, E_s, of 2 x 10^6 MPa (29,000 ksi), which are the values used in the Part 1 models (See Section 3.3), the limit derived in Berman and Bruneau (2005a) is

24.5 and the AISC limit is 15.4. It is also desirable to have information on links with relatively stocky and slender flanges to examine the effect of link overstrength and the general effect of flange compactness on link behavior. Therefore, flange compactness ratios of 8.0, 17.0, 24.0, and 40.0 were selected, the first being well below both limits, the second near the AISC limit, the third near the limit derived in Berman and Bruneau (2005a), and the fourth well above both limits.

Limits for webs of hollow structural sections (HSS) shapes in the AISC seismic provisions are the same as those for the flanges ($d'/t_w \le 0.64\sqrt{E_s/F_{yw}}$). However, as discussed in Berman and Bruneau (2005a), the theoretical stiffener spacing equation derived in that report indicates that stiffeners are not required for webs meeting that compactness limit and that larger compactness ratios may be used if stiffeners are used. Therefore, webs compactness ratios below and well above that limit were selected and both stiffened (with stiffeners satisfying the criteria of Sections 3.4 and 3.5 in Berman and Bruneau, 2005a) and unstiffened cases were considered. The web compactness ratios selected were 12.0, 16.0, 24.0, and 36.0. Note that for a web compactness ratio of 36, the required stiffener spacing, *a*, found from the proposed stiffener spacing equation in Berman and Bruneau (2005a) is 0.43 times the web depth *d*, which is near a practical lower bound on stiffener spacing. For convenience, that equation is repeated here:

$$\frac{a}{t_w} + \frac{1}{8}\frac{d}{t_w} = C_B \qquad (a \le d) \tag{3-1}$$

where C_B is 20 and 37 for ultimate link rotations of 0.08 rads (which is the maximum allowed for WF links in the AISC LRFD seismic provisions) and 0.02 rads respectively.

Note that all combinations of the parameters described above will be analyzed. Therefore, in the context of factorial experimental design (Mason et al., 2003), this is considered to be a full block design with three factors at four levels (i.e., link length, flange compactness, and web compactness) and a fourth, categorical factor, at two levels (i.e, stiffened or unstiffened).

3.2.2 Resulting Dimensional Parameters

For all link models in Part 1 of the parametric study the thicknesses of the webs and flanges were 8 mm (5/16 in) and 16 mm (5/8 in) respectively. Using these thicknesses, the compactness ratios discussed above, and nominal yield stresses and moduli of elasticity for both the webs and flanges of 345 MPa and 2 x 10^6 MPa respectively, the link cross-section dimensions given in table 3-1 were calculated. The resulting cross-section aspect ratios, b/d, are shown in table 3-2.

After determining these cross-section dimensions, the plastic moment, M_p, fully reduced plastic moment, M_{pr}, the plastic shear, V_p, and the balanced link length, $e^* = 2M_p/V_p$, were calculated for each of the 16 cross-section combinations using the formulations from Berman and Bruneau (2005a). The results are shown in table 3-3, for a web and flange nominal yield stress of 345 MPa (50 ksi).

TABLE 3-1 Cross-Section Dimensions for Part 1 Links

b'/t_f	8.0	17.0	24.0	40.0
b' (mm)	127	270	381	635
b (mm)	143	286	397	651
No. Elements	5	11	15	25
El. Edge-to-Thickness [a]	1.6	1.5	1.6	1.6
d'/t_w	12.0	16.0	24.0	36.0
d' (mm)	95	127	191	286
d (mm)	127	159	222	318
No. Elements	4	6	8	12
El. Edge-to-Thickness [a]	3.0	2.7	3.0	3.0

[a] The mesh refinement study of Section 2 indicated values between 1.6 and 3.2 gave acceptable results.

TABLE 3-2 *b*/*d* Ratios for Part 1 Links

d'/t_w \ b'/t_f	8.0	17.0	24.0	40.0
12.0	1.13 	2.25 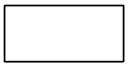	3.13 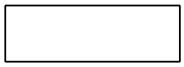	5.13 
16.0	0.90 	1.80 	2.50 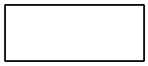	4.10 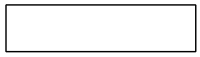
24.0	0.64 	1.29 	1.79 	2.93 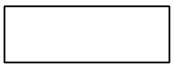
36.0	0.45 	0.90 	1.25 	2.05 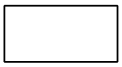

As mentioned in Section 2, the optimal finite element size from a mesh density analysis, considering both convergence of shear and rotation and computation time, was found to be approximately 25.4 mm (1 in). This corresponds to element edge length-to-thickness ratios of 1.6 to 3.2 and utilized the S4R elements. Since some of the web and flange widths selected above are not evenly divisible by this element size, some adjustment in element sizes was necessary for each case. Table 3-1 gives the number of elements along the cross-section edges for the flanges and webs as a function of the compactness of the cross-section. Conversely, in the longitudinal direction of the link, the link length was rounded to achieve a length divisible by 25.4 mm as this causes only a slight difference between the actual and target normalized link length. Table 3-4 gives the resulting actual length used for each link.

TABLE 3-3 Resulting Link Properties for Cross-Sections Chosen

b'/t_f	d'/t_w	M_p (kN-m)	M_{pr} (kN-m)	V_p (kN)	e^* (mm)
8.0	12.0	99	87	301	660
8.0	16.0	134	112	401	667
8.0	24.0	211	161	602	701
8.0	36.0	348	236	903	770
17.0	12.0	186	174	301	1237
17.0	16.0	246	223	401	1224
17.0	24.0	372	323	602	1237
17.0	36.0	583	472	903	1292
24.0	12.0	254	241	301	1686
24.0	16.0	332	310	401	1657
24.0	24.0	498	448	602	1654
24.0	36.0	767	655	903	1699
40.0	12.0	408	396	301	2713
40.0	16.0	531	509	401	2647
40.0	24.0	785	735	602	2608
40.0	36.0	1186	1074	903	2627

TABLE 3-4 Link Lengths, mm (in)

b'/t_f	d'/t_w	ρ = 1.2	ρ = 1.6	ρ = 2.1	ρ = 3.0
8.0	12.0	406.4 (16)	533.4 (21)	685.8 (27)	990.6 (39)
8.0	16.0	406.4 (16)	533.4 (21)	711.2 (28)	990.6 (39)
8.0	24.0	431.8 (17)	558.8 (22)	736.6 (29)	1041.4 (41)
8.0	36.0	457.2 (18)	609.6 (24)	812.8 (32)	1143.0 (45)
17.0	12.0	736.6 (29)	990.6 (39)	1295.4 (51)	1854.2 (73)
17.0	16.0	736.6 (29)	990.6 (39)	1295.4 (51)	1828.8 (72)
17.0	24.0	736.6 (29)	990.6 (39)	1295.4 (51)	1854.2 (73)
17.0	36.0	787.4 (31)	1041.4 (41)	1346.2 (53)	1930.4 (76)
24.0	12.0	1016.0 (40)	1346.2 (53)	1778.0 (70)	2540.0 (100)
24.0	16.0	990.6 (39)	1320.8 (52)	1727.2 (68)	2489.2 (98)
24.0	24.0	990.6 (39)	1320.8 (52)	1727.2 (68)	2489.2 (98)
24.0	36.0	1016.0 (40)	1371.6 (54)	1778.0 (70)	2540.0 (100)
40.0	12.0	1625.6 (64)	2159.0 (85)	2844.8 (112)	4064.0 (160)
40.0	16.0	1600.2 (63)	2108.2 (83)	2768.6 (109)	3962.4 (156)
40.0	24.0	1574.8 (62)	2082.8 (82)	2743.2 (108)	3911.6 (154)
40.0	36.0	1574.8 (62)	2108.2 (83)	2768.6 (109)	3937.0 (155)

The required stiffener spacings for the stiffened links were calculated from the proposed design equation (3-1) for the shear and intermediate links. Table 3-5 gives these required stiffener spacings for the selected web compactness ratios and link lengths. Note that for flexural links, the table shows "N.A." as an entry because flexural links had stiffeners added only at 1.5*b* from each end (in accordance with the AISC requirements for WF flexural links). Also shown in table 3-5 are the stiffener spacings required using the theoretical equation (Berman and Bruneau, 2005a):

$$\alpha = \sqrt{\frac{5.34}{\left(\frac{\gamma_u \beta^2}{4.35}\right) - 4}} \qquad (3\text{-}2)$$

where α, is defined as the stiffener spacing, a, over the web depth, d-$2t_f$. As shown, some of the compact links that have stiffeners required by the proposed design equation are not required to have stiffeners according to the theoretical equation. Note that it was not always possible to achieve equal stiffener spacing due to the link length not being evenly divisible by the stiffener spacing, therefore, many unequal spacings were used. Three constraints drove the stiffener spacing selections: (i) the space between any two stiffeners was to be kept, for the most part, slightly larger than the required spacing in table 3-5; (ii) the spacing between adjacent stiffeners was to be kept as similar as possible (except for flexural links as noted above); and (iii) all stiffener layouts were to be symmetric. In a few instances it was necessary to use a spacing that was slightly less than that given in table 3-5, however, this was never done at the link ends, which is the critical location where buckling initiated in all models. The selected stiffener spacings for the links are given in table 3-6 in units of inches for simplicity.

TABLE 3-5 Required Stiffener Spacing, mm (in)

d'/t_w	$\rho = 1.2$	$\rho = 1.6$	$\rho = 2.1$	$\rho = 3.0$
Proposed Design Equation (3-1)				
12.0	143.0 (5.63)	143.0 (5.63)	210.3 (8.28)	N.A.
16.0	138.9 (5.47)	138.9 (5.47)	206.5 (8.13)	N.A.
24.0	131.1 (5.16)	131.1 (5.16)	198.4 (7.81)	N.A.
36.0	119.1 (4.69)	119.1 (4.69)	186.4 (7.34)	N.A.
Theoretical Equation (3-2)				
12.0	∞	∞	∞	N.A.
16.0	200.2 (7.88)	200.2 (7.88)	∞	N.A.
24.0	159.0 (6.26)	159.0 (6.26)	231.9 (9.13)	N.A.
36.0	145.5 (5.73)	145.5 (5.73)	193.3 (7.61)	N.A.

Stiffener thicknesses were 10 mm (3/8 in) for links with flange compactnesses of 8.0 and 17.0, and were 13 mm (1/2 in) for all other links. The stiffeners were assumed to be continuous around the perimeter of the link cross-sections (see figure 3-10). Their dimensions were slightly less than those required by (3-60), (3-53), and (3-54) as they were reduced as necessary to the nearest multiple of 25.4 mm (1 in) for simplicity in modeling.

TABLE 3-6 Spacings Between Stiffeners (in)

b'/t_f	d'/t_w	ρ = 1.2	ρ = 1.6	ρ = 2.1	ρ = 3.0
8.0	12.0	8-8	7-7-7	9-9-9	9-21-9
8.0	16.0	8-8	7-7-7	9-10-9	9-21-9
8.0	24.0	6-5-6	7-8-7	10-9-10	9-23-9
8.0	36.0	6-6-6	6-6-6-6	8-8-8-8	9-27-9
17.0	12.0	6-6-5-6-6	6-6-5-5-5-6-6	9-11-11-11-9	17-39-17
17.0	16.0	6-6-5-6-6	6-6-5-5-5-6-6	9-11-11-11-9	17-38-17
17.0	24.0	6-6-5-6-6	6-6-5-5-5-6-6	9-11-11-11-9	17-39-17
17.0	36.0	6-6-7-6-6	6-6-6-5-6-6-6	8-8-7-7-7-8-8	17-42-17
24.0	12.0	7-7-6-6-7-7	4@6-5-4@6	7@10	24-52-24
24.0	16.0	6-6-5-5-5-6-6	7-7-4@6-7-7	3@10-8-3@10	24-50-24
24.0	24.0	8-8-7-8-8	7-7-4@6-7-7	9-9-4@8-9-9	24-50-24
24.0	36.0	8@5	9@6	8-8-3@9-8-8	24-52-24
40.0	12.0	7-7-6@6-7-7	3@6-7@7-3@6	2@10-8@9-2@10	39-82-39
40.0	16.0	3@6-3@5-3@6	5@6-8-7-8-5@6	5@10-9-5@10	39-78-39
40.0	24.0	7-8@6-7	7-7-9@6-7-7	9-9-9@8-9-9	39-76-39
40.0	36.0	6-10@5-6	4@6-5@7-4@6	4@8-5@9-4@8	39-77-39

3.3 Differences from the Proof-of-Concept Model

In Section 2 the finite element model of the proof-of-concept test specimen, which forms the basis for the models of this parametric study, was described in detail. Included there was a

discussion on element selection, mesh refinement, boundary conditions, and material specification. This section describes the few differences between that base model and the models developed for this parametric study.

Other than the geometries, there were two additional differences between the links modeled in the parametric study and the model of the proof-of-concept link; the material definition and the loading history. In order to keep the parametric study consistent with the study of WF links by Richards and Uang (2002), the material data for the webs, flanges and stiffeners in Part 1 of this parametric study was adapted from Steel C from Kaufmann et al. (2001), which was ASTM A572 Grade 50. The true stress versus true strain curve for this steel is the solid line in figure 3-2. The same nonlinear plasticity model with kinematic hardening as used for the proof-of-concept model and by Richards and Uang was utilized along with the stabilized half cycle data option to input the experimental data from Kaufmann.

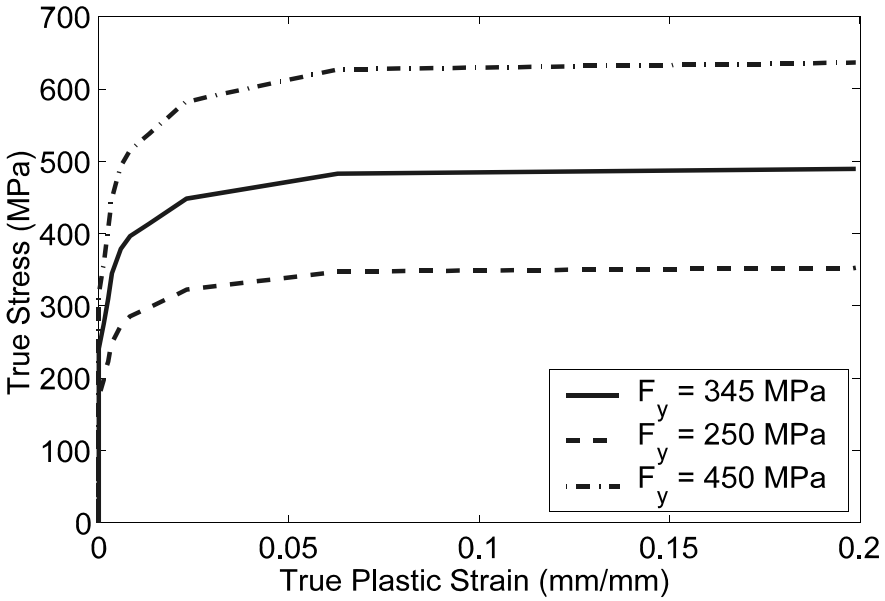

FIGURE 3-2 True Stress vs. True Strain Curves for Materials in Parametric Study Models

Recall that Part 2 of this parametric study will investigate links having webs and flanges with differing yield stresses. Figure 3-2 shows the piece-wise linear true stress versus true strain curve for the material used in Part 1 (yield stress of 372 MPa, 54 ksi) as well as the curves scaled to yield stresses of 268 MPa (39 ksi), and 484 MPa (70 ksi), which will be used in Part 2 of the parametric study. Note that the nominal yield strengths, which are used

in design and in the compactness equations, are 345 MPa (50 ksi), 248 MPa (36 ksi), and 448 MPa (65 ksi) respectively, and that there is a constant ratio between actual and nominal yield stress of 1.08, which is close to the R_y of 1.1 used for A572 Gr. 50 steel in the current AISC Seismic Provisions. To obtain actual link plastic shear force, $V_p{}^a$, and plastic moment , $M_p{}^a$, capacities, the values in table 3-3 may be multiplied by R_y = 1.08.

Since buckling is expected to develop in many of the models at large rotations, and because the mesh refinement study in Section 2 was performed on the proof-of-concept link model which did not buckle, another mesh refinement study was performed, this time using a more slender cross-section, namely S-24-24-2.1 (i.e., stiffened link with flange compactness of 24, web compactness of 24, and normalized length of 2.1). The element size was reduced to half the values previously considered (to element edge lengths of approximately 12.7 mm) and the link was re-analyzed. Results obtained were nearly identical to those obtained for the coarser mesh. Buckling occurred at the same rotation level and was initiated by flange buckling in both analyses. These results, and the good correlation Richards and Uang obtained for WF links when comparing their experimental results with finite element analysis results using a mesh of elements with edge lengths of approximately 25.4 mm and corresponding edge length-to-thickness ratios between 2 and 4, indicate that the final mesh density from the refinements of Section 2 is adequate.

In this parametric study, the rotation magnitudes and number of cycles corresponding to the AISC requirements for testing of link-to-column connections were used (this loading protocol was also used by Richards and Uang for some models, but differs from the ATC protocol used for the proof-of-concept test and model in Section 2). This loading protocol specifies three cycles at each total link rotation level of 0.0025, 0.005, and 0.01 radians, followed by two cycles at 0.01 radian increments up to the maximum code specified rotation. However, for the current research purposes, loading was continued with two cycles at 0.01 radian increments up to 0.2 radians of total rotation or convergence failure due to very large buckling displacements, whichever happened first.

3.4 Evaluation of the Limit Plastic Link Rotation

For the purpose of this parametric study, the limit plastic rotation, γ_{lim}, is defined as the inelastic rotation at which the backbone curve of the link shear force hysteresis drops below 80% of the maximum link shear force obtained for a given link. This definition is selected because it represents a degradation that may be neglected so that a bilinear macro model for links may used and it is consistent with what has been done for WF links. The procedure used here to determine the limit rotation is similar to that used by Richards and Uang and can be described as follows:

First, the plastic rotation versus normalized shear force hysteresis curve was calculated using MATLAB (Math Works, 1999) and the results from ABAQUS. For each link, the initial link stiffness, k_{li}, was determined by fitting a line through the first three points of the link shear versus total rotation hysteresis curve. The plastic rotation, γ_p, is then determined from:

$$\gamma_p = \gamma_t - \frac{V_l}{k_{li}} \tag{3-3}$$

where γ_t is the total rotation and V_l is the link shear. The shear force, V_l, is then normalized by the maximum link shear, V_{lmax}, obtained for each link.

From the normalized link shear versus plastic rotation hysteresis, the backbone curve is constructed and a simple search algorithm is used to find the limit plastic rotation, γ_{lim}, where the link shear force drops below 80% of the maximum. An example is shown in figure 3-3 for link N-24-24-2.1, for which the limit plastic rotation was found to be 0.0325 rads.

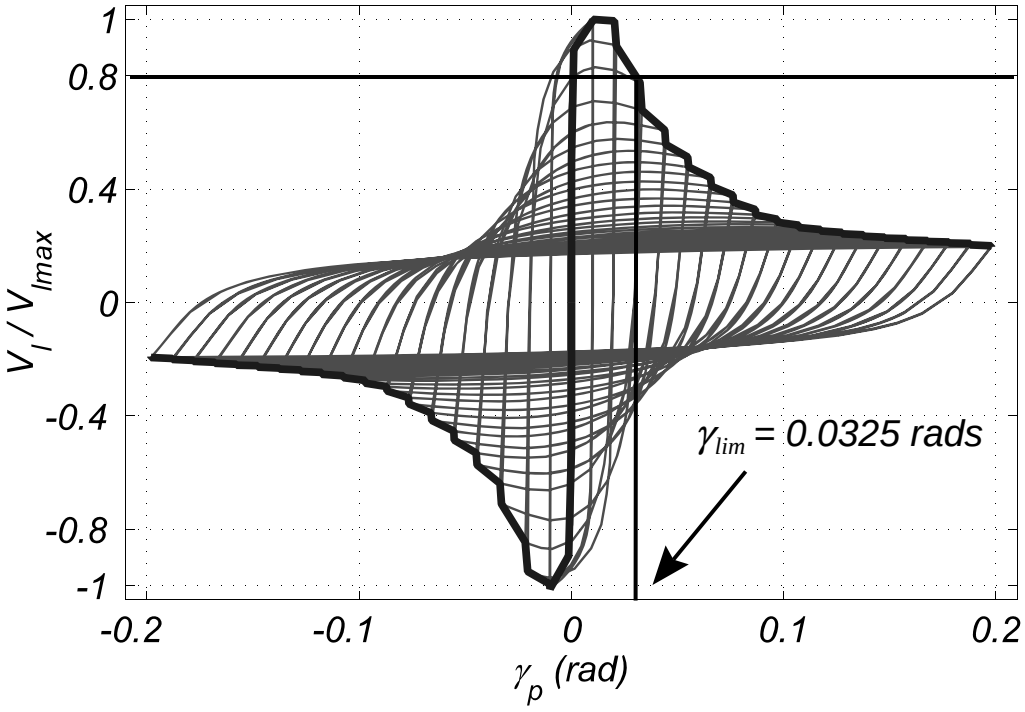

FIGURE 3-3 Example of Limit Plastic Rotation Determination

3.5 Results of Parametric Study - Part 1

Appendix A contains the link shear versus plastic rotation hysteresis for each link analysis performed in Part 1 of the parametric study. The following subsections present the results (limit plastic rotations, maximum shear force, and maximum end-moments) and investigate the issues related to the effect of stiffeners and web compactness and the effect of flange compactness. Revised design rules are proposed as a result of these observations. It should be noted that in certain cases involving stiffened links with large web compactness ratios, numerical convergence as part of the finite element analysis became difficult after the onset of severe buckling and significant strength degradation. However, in all cases the limit plastic rotation was obtained since the convergence problems began after the link shear had degraded to below 80% of the maximum obtained.

3.5.1 Presentation of Results

The limit plastic rotation obtained for the link analyses in Part 1 of the parametric study are given in table 3-7 for both unstiffened and stiffened links. Recall that no attempt to model fracture was made and therefore some of the links that have large limit plastic rotations

might in practice, fracture prior to reaching those plastic rotations. For example, the proof-of-concept specimen fractured at a total rotation of 0.15 rads yet the finite element results for that specimen would indicate that a plastic rotation greater than 0.2 rads could be achieved prior to strength degradation from buckling. Tables 3-8 and 3-9 respectively give the maximum link shear force and end-moment obtained in the analyses normalized by the V_p and M_p values given in table 3-3 (calculated assuming a nominal yield stress of 345 MPa (50 ksi)).

3.5.2 Effect of Stiffeners and Web Compactness

Several observations can be made regarding the effect of stiffeners and web compactness on a link's ability to reach the target rotation by plotting the data from table 3-7 as a function of normalized link length for all data for which $b'/t_f \leq 17.0$ and grouping results in terms of d'/t_w values (figures 3-4 and 3-5). For reference, these figures also have a solid line indicating the AISC specified maximum rotation (also referred to as the target rotation). First, it appears that links with $d'/t_w \leq 16.0$ and $b'/t_f \leq 17.0$ can achieve their target rotation without stiffeners. These are shown as the squares ($d'/t_w = 12.0$) and circles ($d'/t_w = 16.0$) of figure 3-4. Recall it was shown in Berman and Bruneau (2005a), from the theoretical stiffener spacing equation (3-2), that no stiffeners would be required for webs with compactness less than 17.0 (the current AISC compactness limit is 15.4 for rectangular HSS with $F_{yw} = 345$ MPa). Therefore, the results of the analyses seem to validate this prediction, as long as the flange compactness ratio is also kept less than or equal to 17.0. There are three exceptions to this, namely, N-17-16-1.6, N-17-12-2.1, and N-17-16-2.1, which are discussed in the next section.

TABLE 3-7 Limit Plastic Rotations for Part 1 Links (rads)

b'/t_f	d'/t_w	Unstiffened				Stiffened			
		$\rho = 1.2$ $\gamma_t = 0.08$	$\rho = 1.6$ $\gamma_t = 0.08$	$\rho = 2.1$ $\gamma_t = 0.05$	$\rho = 3.0$ $\gamma_t = 0.02$	$\rho = 1.2$ $\gamma_t = 0.08$	$\rho = 1.6$ $\gamma_t = 0.08$	$\rho = 2.1$ $\gamma_t = 0.05$	$\rho = 3.0$ $\gamma_t = 0.02$
8.0	12.0	0.193	0.176	0.107	0.132	0.193	0.154	0.105	0.132
8.0	16.0	0.195	0.195	0.104	0.114	0.194	0.174	0.103	0.113
8.0	24.0	0.086	0.072	0.097	0.084	0.195	0.195	0.095	0.084
8.0	36.0	0.036	0.036	0.046	0.055	0.196	0.136	0.076	0.055
17.0	12.0	0.178	0.083	0.049	0.048	0.182	0.081	0.050	0.048
17.0	16.0	0.158	0.078	0.049	0.040	0.184	0.083	0.048	0.040
17.0	24.0	0.065	0.064	0.044	0.032	0.194	0.083	0.044	0.032
17.0	36.0	0.033	0.027	0.035	0.024	0.195	0.085	0.035	0.024
24.0	12.0	0.122	0.050	0.040	0.044	0.117	0.059	0.043	0.036
24.0	16.0	0.123	0.051	0.030	0.028	0.119	0.071	0.035	0.028
24.0	24.0	0.058	0.049	0.033	0.027	0.154	0.056	0.034	0.027
24.0	36.0	0.026	0.032	0.024	0.021	0.194	0.064	0.024	0.020
40.0	12.0	0.067	0.026	0.033	0.019	0.092	0.044	0.022	0.020
40.0	16.0	0.060	0.030	0.017	0.028	0.107	0.047	0.033	0.030
40.0	24.0	0.063	0.033	0.023	0.019	0.100	0.044	0.020	0.019
40.0	36.0	0.032	0.024	0.013	0.011	0.118	0.054	0.023	0.013

TABLE 3-8 Maximum Link Shear Normalized by V_p

b'/t_f	d'/t_w	Unstiffened				Stiffened			
		ρ = 1.2	ρ = 1.6	ρ = 2.1	ρ = 3.0	ρ = 1.2	ρ = 1.6	ρ = 2.1	ρ = 3.0
8.0	12.0	1.90	1.71	1.45	1.00	1.97	1.74	1.45	1.00
8.0	16.0	1.68	1.61	1.39	1.01	1.75	1.66	1.39	1.01
8.0	24.0	1.53	1.52	1.36	1.00	1.67	1.55	1.35	1.00
8.0	36.0	1.41	1.40	1.28	0.98	1.56	1.49	1.29	0.98
17.0	12.0	1.76	1.63	1.33	0.91	1.92	1.70	1.33	0.92
17.0	16.0	1.65	1.57	1.31	0.92	1.80	1.63	1.31	0.92
17.0	24.0	1.53	1.50	1.31	0.93	1.73	1.59	1.31	0.93
17.0	36.0	1.39	1.37	1.28	0.93	1.59	1.51	1.29	0.93
24.0	12.0	1.72	1.58	1.24	0.85	1.86	1.68	1.25	0.85
24.0	16.0	1.63	1.54	1.26	0.86	1.72	1.64	1.27	0.86
24.0	24.0	1.53	1.49	1.23	0.86	1.62	1.56	1.26	0.86
24.0	36.0	1.39	1.37	1.22	0.88	1.66	1.51	1.23	0.88
40.0	12.0	1.64	1.41	1.10	0.76	1.84	1.64	1.19	0.76
40.0	16.0	1.57	1.36	1.09	0.74	1.76	1.61	1.19	0.76
40.0	24.0	1.51	1.39	1.12	0.77	1.67	1.54	1.19	0.77
40.0	36.0	1.39	1.34	1.11	0.78	1.64	1.52	1.21	0.78

TABLE 3-9 Maximum Link End Moment Normalized by M_p

b'/t_f	d'/t_w	Unstiffened				Stiffened			
		ρ = 1.2	ρ = 1.6	ρ = 2.1	ρ = 3.0	ρ = 1.2	ρ = 1.6	ρ = 2.1	ρ = 3.0
8.0	12.0	1.16	1.38	1.51	1.51	1.21	1.41	1.51	1.51
8.0	16.0	1.02	1.28	1.48	1.51	1.06	1.33	1.48	1.51
8.0	24.0	0.94	1.20	1.42	1.49	1.03	1.24	1.42	1.49
8.0	36.0	0.83	1.11	1.35	1.45	0.93	1.18	1.36	1.45
17.0	12.0	1.05	1.31	1.39	1.37	1.14	1.36	1.39	1.37
17.0	16.0	0.99	1.27	1.38	1.38	1.07	1.32	1.39	1.38
17.0	24.0	0.91	1.20	1.37	1.40	1.02	1.27	1.37	1.40
17.0	36.0	0.85	1.11	1.34	1.39	0.97	1.22	1.35	1.39
24.0	12.0	1.04	1.26	1.31	1.27	1.11	1.34	1.32	1.27
24.0	16.0	0.97	1.23	1.31	1.29	1.03	1.33	1.33	1.29
24.0	24.0	0.91	1.19	1.28	1.30	0.97	1.24	1.32	1.30
24.0	36.0	0.83	1.10	1.28	1.32	0.99	1.22	1.28	1.32
40.0	12.0	0.98	1.12	1.16	1.13	1.10	1.30	1.24	1.13
40.0	16.0	1.00	1.13	1.15	1.13	1.06	1.28	1.25	1.13
40.0	24.0	0.91	1.11	1.17	1.15	1.00	1.23	1.25	1.15
40.0	36.0	0.83	1.08	1.17	1.16	0.98	1.22	1.27	1.16

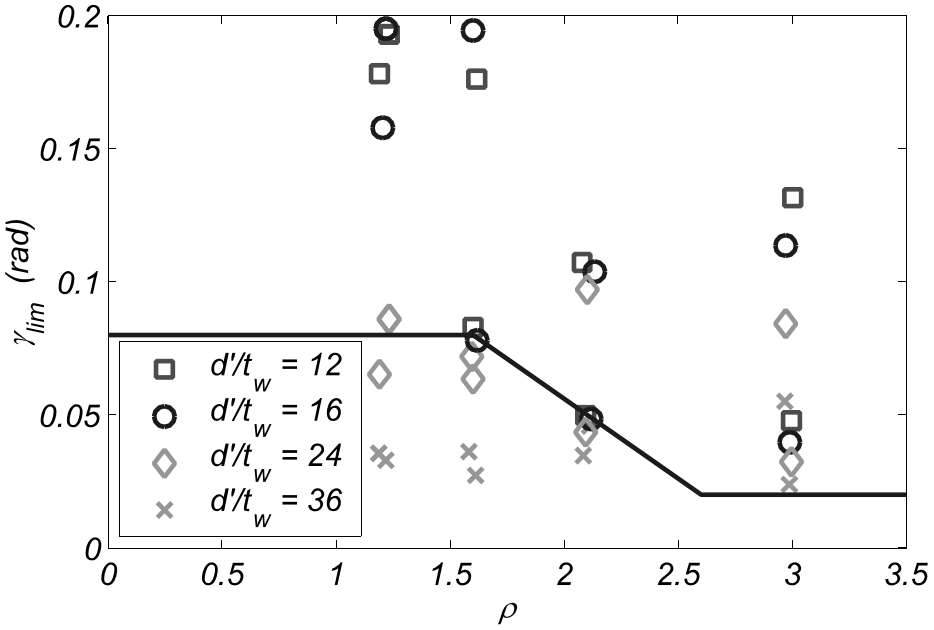

FIGURE 3-4 Limit Plastic Rotation vs. Normalized Link Length for Unstiffened Links with $b'/t_f \leq 17.0$

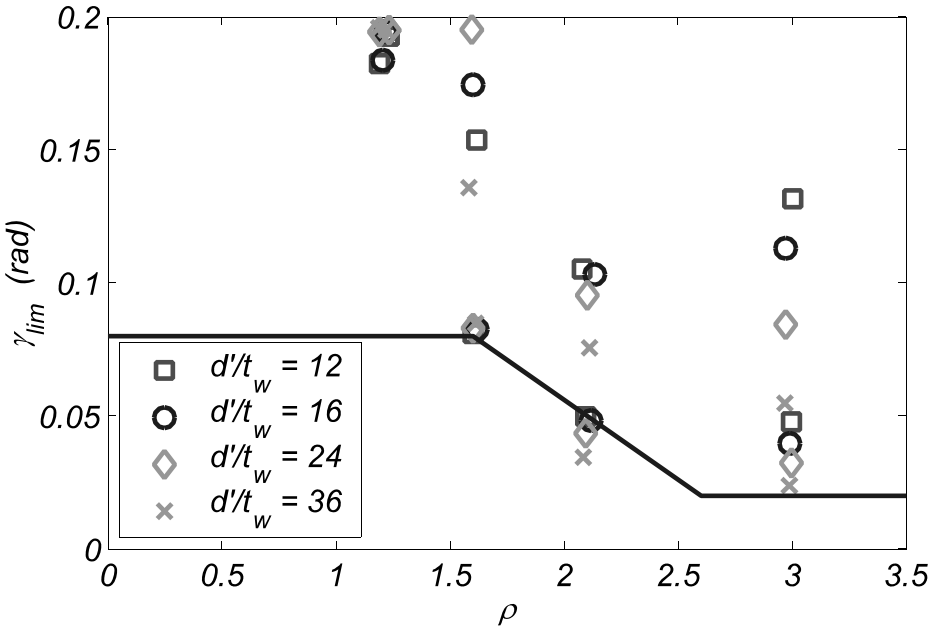

FIGURE 3-5 Limit Plastic Rotation vs. Normalized Link Length for Stiffened Links with $b'/t_f \leq 17.0$

The results in table 3-7 also indicate that stiffeners were effective in helping shear links with web compactness up to 36.0 and flange compactness less than or equal to 17.0 achieve the target rotation. For instance, the limit plastic rotation for S-17-36-1.2 was 0.195 rads and the hysteresis was full and stable as shown in figure 3-6, while without stiffeners the limit plastic rotation for that same link (N-17-36-1.2) was 0.033 rads and the hysteresis showed rapid strength degradation following web buckling at small plastic rotations as shown in figure 3-7. This is demonstrated further in figures 3-4 and 3-5, which show limit plastic rotations versus normalized link length for unstiffened and stiffened links respectively, both for $b'/t_f \leq 17.0$. Stiffeners improved the rotation capacity of all shear links, however, only for links with $b'/t_f \leq 17.0$ was that improvement enough to reach the target rotation of 0.08 rads for both ρ = 1.2 and 1.6. Note that the web compactness of 36.0 corresponds to $d'/t_w = 1.50\sqrt{E_s/F_{yw}}$ with F_{yw} = 345 MPa and E_s = 2 x 10^6 MPa which will be used later to develop non-dimensional compactness limits.

For intermediate and flexural links, there was little difference in limit plastic rotation obtained between stiffened and unstiffened links. N-8-36-2.1 was the only intermediate link for which the addition of stiffeners was found to help it reach and exceed the target rotation. Since this link had a low flange compactness ratio and high web compactness ratio, web buckling was the trigger for strength degradation. When stiffeners were added, web buckling (and the corresponding strength degradation due to web buckling) was delayed and the link achieved a 0.076 rads rotation prior to a 20% strength degradation that was initiated by flange buckling. For the other intermediate and flexural links considered, flange buckling was the trigger for strength degradation and the addition of stiffeners did not effectively delay this buckling mode. However, intermediate and flexural links with a given value of flange compactness exhibited decreasing limit plastic rotations with increasing web compactness ratios, indicating that the stabilizing effect of the web against flange buckling decreases with increasing web compactness ratios. It also appears from the case considered that flexural links with web compactness up to 36.0 can reach their target rotation as long as the flange compactness is less than or equal to 24.0.

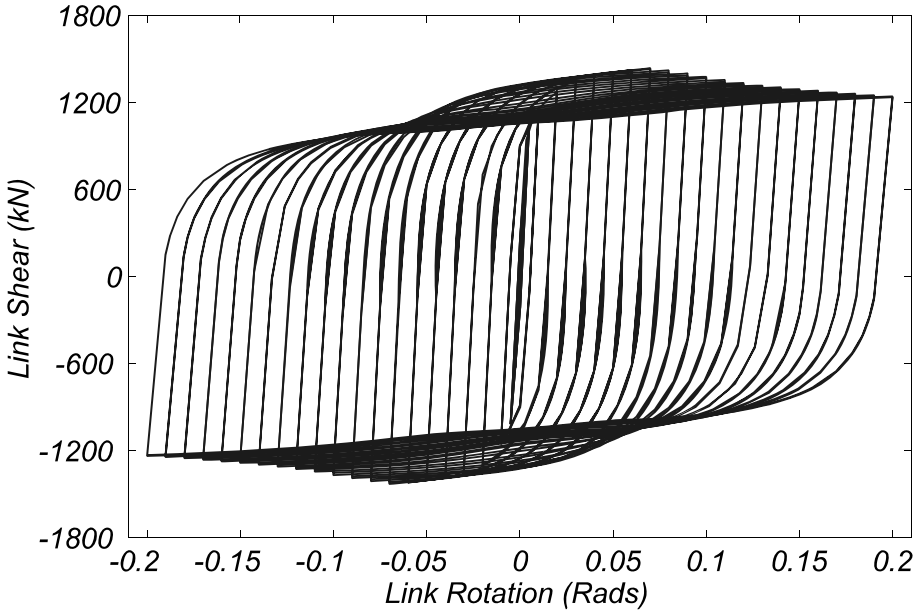

FIGURE 3-6 Hysteresis for Link S-17-36-1.2

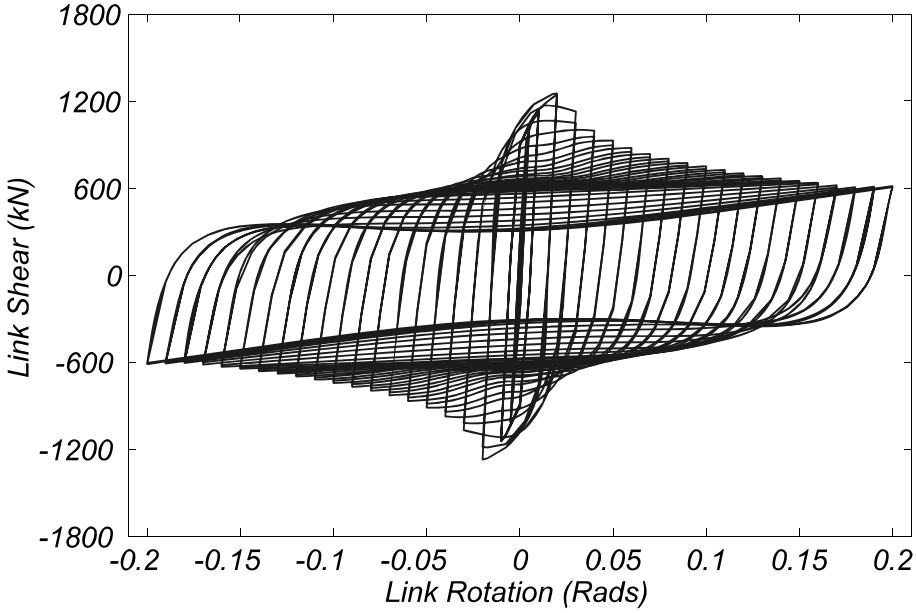

FIGURE 3-7 Hysteresis for Link N-17-36-1.2

3.5.3 Effect of Flange Compactness

Figures 3-8 and 3-9 show limit plastic rotation versus link length for stiffened and unstiffened links respectively, both with $b'/t_f > 17.0$. When comparing these with figures 3-4 and 3-5, which showed the same information for links with $b'/t_f \leq 17.0$, it is observed that many links with larger flange compactness ratios did not achieve their target rotation.

Only stiffened shear links with ρ = 1.2 were able to consistently meet their target rotation when $b'/t_f > 17.0$. At the transition length from shear to intermediate links, ρ = 1.6, and at the intermediate length of ρ = 2.1, no links with $b'/t_f > 17.0$ achieved the target rotation, even when stiffened.

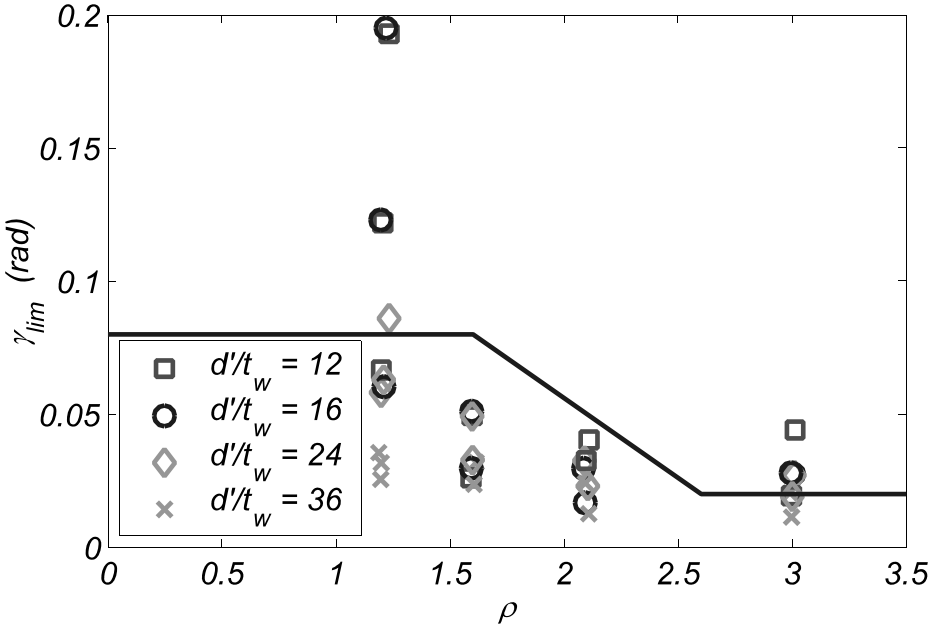

FIGURE 3-8 Limit Plastic Rotation vs. Normalized Link Length for Unstiffened Links with $b'/t_f > 17.0$

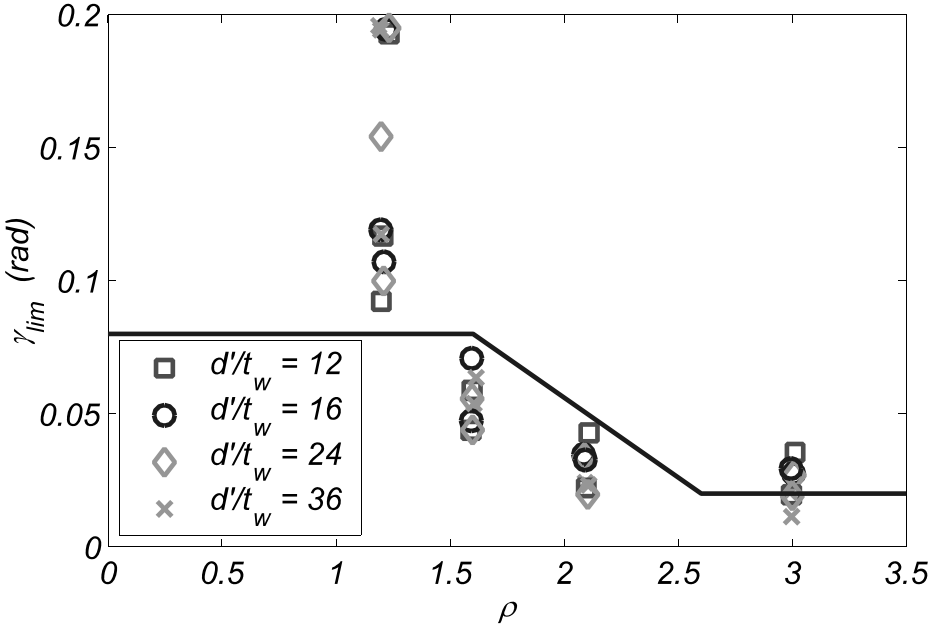

FIGURE 3-9 Limit Plastic Rotation vs. Normalized Link Length for Stiffened Links with $b'/t_f > 17.0$

This trend may be examined further using figures 3-10, 3-11, and 3-12, which show the limit plastic rotation, normalized by the target rotation, versus the flange compactness for the shear, intermediate, and flexural links, respectively. Figure 3-10 groups the shear links into two categories: unstiffened shear links with $d'/t_w > 16.0$ and all other shear links (which includes unstiffened and stiffened shear links with $d'/t_w \leq 16.0$ and stiffened shear links with $d'/t_w > 16.0$). Results show that for the latter category the links require $b'/t_f \leq 17.0$ to achieve their target rotation, while links in the former category do not consistently achieve their target rotation regardless of the flange compactness ratio. An exception to this trend was observed with N-17-16-1.6, which failed to reach its' target rotation by 0.002 rads. This is investigated further in the next paragraph. Figure 3-11 groups the intermediate links into two categories: intermediate links with $d'/t_w > 16.0$ and intermediate links with $d'/t_w \leq 16.0$, since it was shown above that stiffening the intermediate links had little influence on limit plastic rotation. From this figure it appears that intermediate links (like shear links) require that $b'/t_f \leq 17.0$ to reach their target rotation. Links N-17-12-2.1 and N-17-16-2.1, which missed their target rotations by 0.001 rads are also reviewed in the next paragraph. Finally, figure 3-12 groups the flexural links into stiffened and unstiffened categories, although no appreciable difference in results is discernable. The figure indicates a trend between maximum plastic rotation and flange ratio for flexural links, which is to be expected since the inelastic behavior occurs mostly in the flanges of flexural links. Figure 3-12 also shows that flexural links with $b'/t_f \leq 24.0$ all achieved their target rotation.

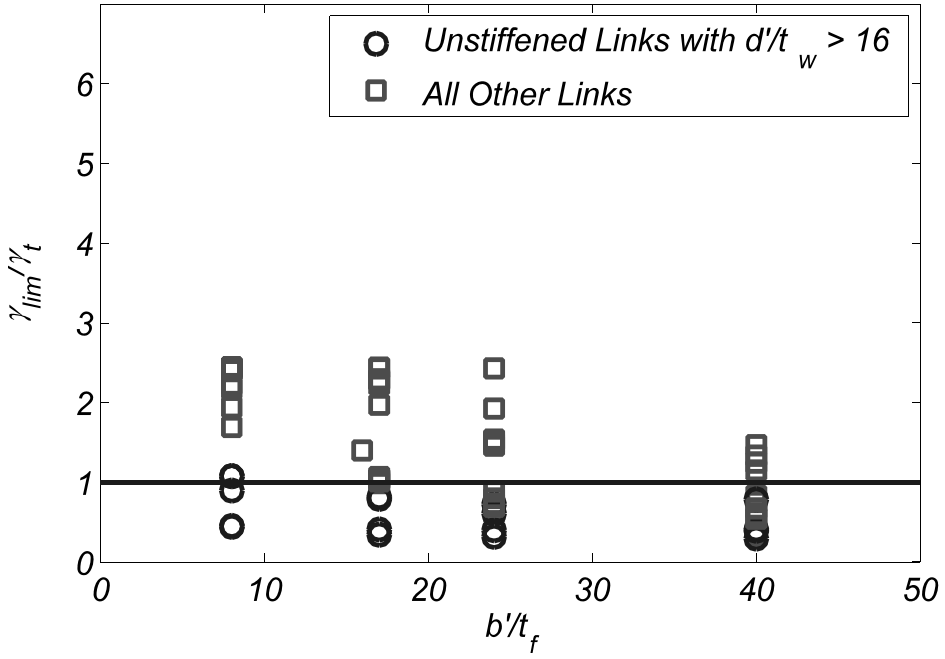

FIGURE 3-10 Normalized Limit Plastic Rotation vs. Flange Compactness for Shear Links

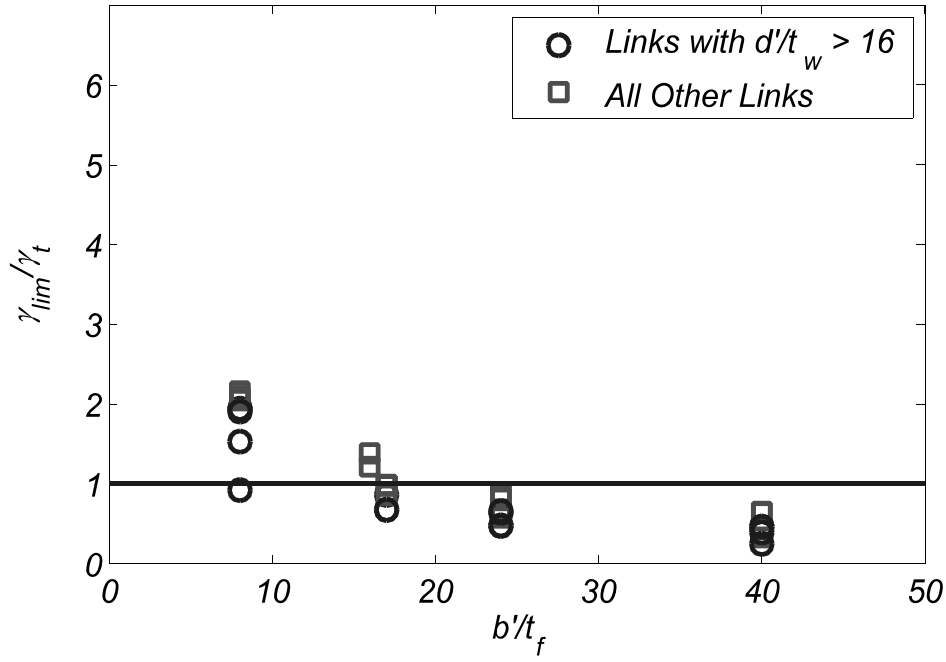

FIGURE 3-11 Normalized Limit Plastic Rotation vs. Flange Compactness for Intermediate Links

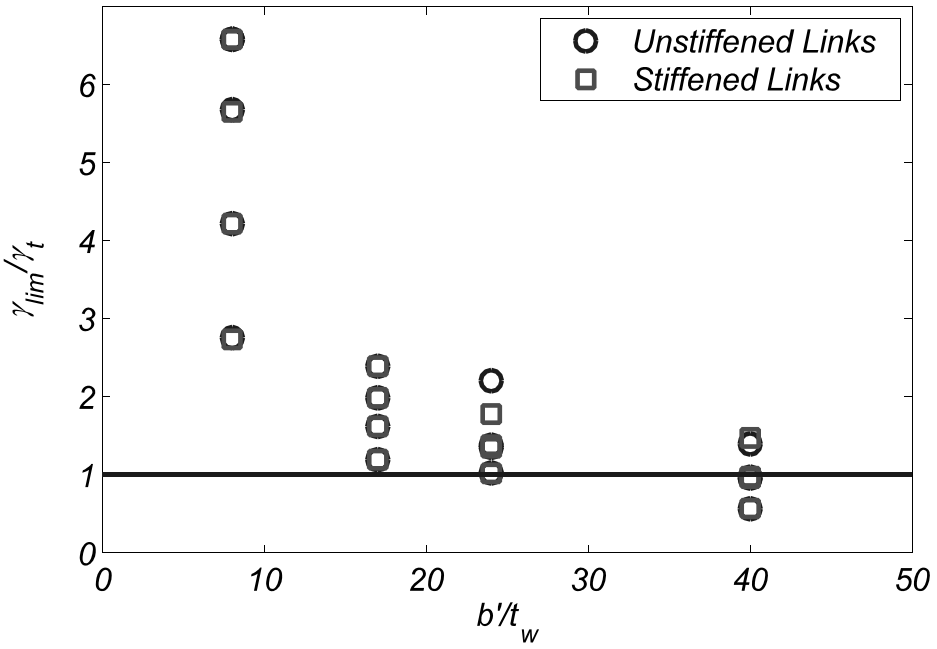

FIGURE 3-12 Normalized Limit Plastic Rotation vs. Flange Compactness for Flexural Links

The three unstiffened links, namely, N-17-12-2.1, N-17-16-1.6, and N-17-16-2.1, that had $b'/t_f \leq 17.0$ along with $d'/t_w \leq 16.0$ and did not reach their target rotation were investigated in more detail. Flange buckling was the trigger for strength degradation and they all came to within 3% of their target rotations. This difference could be considered insignificant for engineering purposes. However, for completeness, since the AISC limit for flange compactness is actually 15.4 for F_{yf} = 345 MPa (50 ksi) and a value of 17.0 had been used to develop the models, these three links were re-analyzed with a modified flange thickness corresponding to a flange compactness of 15.9 (a value slightly larger than 15.4 was selected to be conservative). The limit plastic rotations for these modified links were found to be 0.051 rads, 0.083 rads, and 0.050 rads, respectively, which are greater than or equal to their target rotations. Results for these links are also included in figures 3-10 through 3-12.

On the basis of the above results, it is found that for rectangular shear and intermediate links, the current AISC seismic limit for flange compactness of HSS shapes is appropriate when used in combination with a web compactness limit and/or stiffeners as described in the next section, while for flexural links it may be increased to allow flange compactnesses of up to 24.0. Furthermore, results presented together in figures 3-5 and 3-9, suggest that it may be

possible to relate the limit displacement for shear and intermediate links to not only normalized link length but also flange compactness, for links with flange compactness greater than 17.0. This would allow engineers to design a shear or intermediate link with a flange compactness exceeding 17.0 as long as the anticipated plastic rotation demand is kept below a value that depends on both link length and flange compactness. This idea is explored further in later sections.

3.5.4 Revised Design Requirements

Based on the results of Part 1 of the finite element parametric study and the above discussion, the recommended compactness ratio limits for hybrid rectangular links are revised and compared to AISC limits for rectangular HSS shapes and the limits derived in Berman and Bruneau (2005a) as shown in table 3-10. Note that the recommended stiffened web compactness ratio limit for shear links is $1.67\sqrt{E_s/F_{yw}}$. In Part 1 of the parametric study a web yield stress of 345 MPa and d'/t_w of 36 were used. This d'/t_w value was determined based on limiting the minimum stiffener spacing, a, to approximately $0.4d'$, considered to be a practical minimum. Substituting this stiffener spacing (3-1) with C_B equal to 20, which is the value for shear links with an anticipated rotation of 0.08 rads, gives the d'/t_w value of 36. The web compactness ratio that corresponds to this yield strength and d'/t_w value is $1.50\sqrt{E_s/F_{yw}}$. The larger value of $1.67\sqrt{E_s/F_{yw}}$ recommended in table 3-10 has been determined from ancillary models not presented here that considered a web yield stress of 1.25 times the 345 MPa yield stress used in Part 1. These case studies revealed that stiffened shear links with this web compactness ratio and web yield stress could achieve their target rotation. Part 2 of the parametric study will focus on investigating the appropriateness of the proposed limit for various steel yield strengths.

Another revision to the design recommendations based on results of Part 1 of the parametric study is that the web compactness ratios for intermediate and flexural links be limited to that for unstiffened shear links. This results from the observation that stiffeners do not enhance the performance of intermediate or flexural links because flange buckling typically occurs prior web buckling. The stiffener spacing equation remains unchanged from that proposed

in Berman and Bruneau (2005a) and repeated as (3-1), although it is only recommended for shear links with web compactness values between $0.64\sqrt{E_s/F_{yw}}$ and $1.67\sqrt{E_s/F_{yw}}$.

TABLE 3-10 Maximum Link End Moment Normalized by M_p

Link Category	Compactness Ratio	Current AISC Limits	Limits Derived in Berman and Bruneau (2005a)	Limits Based on Part 1 FE Results
Shear Links	b'/t_f	$0.64\sqrt{E_s/F_{yf}}$	$1.02\sqrt{E_s/F_{yf}}$	$0.64\sqrt{E_s/F_{yf}}$
	Stiffened d'/t_w	a	b	$1.67\sqrt{E_s/F_{yw}}$ c
	Unstiffened d'/t_w	$0.64\sqrt{E_s/F_{yw}}$	b	$0.64\sqrt{E_s/F_{yw}}$
Intermediate Links	b'/t_f	$0.64\sqrt{E_s/F_{yf}}$	$1.02\sqrt{E_s/F_{yf}}$	$0.64\sqrt{E_s/F_{yf}}$
	Stiffened d'/t_w	a	b	d
	Unstiffened d'/t_w	$0.64\sqrt{E_s/F_{yw}}$	b	$0.64\sqrt{E_s/F_{yw}}$
Flexural Links	b'/t_f	$0.64\sqrt{E_s/F_{yf}}$	$1.00\sqrt{E_s/F_{yf}}$	$0.64\sqrt{E_s/F_{yf}}$
	Stiffened d'/t_w	a	b	d
	Unstiffened d'/t_w	$0.64\sqrt{E_s/F_{yw}}$	b	$0.64\sqrt{E_s/F_{yw}}$

a AISC does not consider stiffened HSS Walls.

b Stiffener spacing equations rather than compactness ratio limits for webs were derived in Berman and Bruneau (2005a).

c The stiffened web compactness limit was found by limiting the stiffener spacing to the practical lower bound of approximately $0.4d'$.

d Finite element results indicate that stiffeners do not enhance the performance of intermediate or flexural links because flange buckling typically occurs prior web buckling.

It was also observed in Part 1 of the study that all flexural links with flange compactness ratios less than or equal to 24.0, for any of the four web compactness ratios considered, achieved their target rotation. As a result the limit flange compactness ratio for flexural links could be increased to $1.00\sqrt{E_s/F_{yf}}$. However, for simplicity, and because they are not commonly used, the compactness ratio requirements for flexural links are recommended to be the same as those for shear and intermediate links, namely, $0.64\sqrt{E_s/F_{yf}}$. Finally, as mentioned above, it may be possible to allow larger flange compactness ratios for shear and intermediate links if the limit plastic rotation was made a function of both the link length and flange compactness. The corresponding recommended rotation limits if one considered using such a more complex approach are presented in Appendix B and are not included in the proposed design requirements here for simplicity and to keep the requirements for rectangular links similar to the current requirements for WF links.

3.6 Parameter Selection - Part 2

Since rectangular links may be fabricated with four plates welded together, hybrid cross-sections where the yield stresses of the webs and flanges are different could be used advantageously. Since this option is a practical possibility, it is investigated in this section. Furthermore, the increased use of low yield point and high performance steels indicates a practical need for verifying the revised design requirements for a range of possible yield stresses. Part 2 of the finite element parametric study will therefore investigate links with cross-sectional properties near the revised limits of Section 3.5.4 while also incorporating different yield stresses for both the webs and flanges.

Three yield stresses are considered for this part of the study, namely, 250 MPa (36 ksi), 345 MPa (50 ksi), and 450 MPa (65 ksi) as these are representative of some of the steels currently available. The same normalized link lengths used in Part 1 of the study will be used in Part 2 (i.e., ρ values of 1.2, 1.6, 2.1, and 3.0). Table 3-11 shows the limits for web and flange compactness as calculated using the revised design requirements and those used in Part 2 of the study (selected to be as close as possible and never less than the design limits). Table 3-12 gives the link dimensions, number of elements per web or flange, and

element edge length-to-thickness ratios for the Part 2 models corresponding to the compactnesses of table 3-11. A web thickness of 9.5 mm (0.375 in) and flange thickness of 12.7 mm (0.5 in) were used in the models of Part 2. Table 3-13 shows the resulting cross-section aspect ratios for the Part 2 models. Models with web compactness near $1.67\sqrt{E_s/F_{yw}}$ were modeled with stiffeners satisfying or slightly exceeding the spacing dictated by (3-1) while those with web compactness near $0.64\sqrt{E_s/F_{yw}}$ did not have stiffeners.

TABLE 3-11 Limit Compactness and Used Compactness Ratios for Part 2 Links

F_y (MPa)	250	345	450
$0.64\sqrt{E_s/F_y}$	18.2	15.4	13.5
$1.67\sqrt{E_s/F_y}$	47.4	40.2	35.3
b'/t_f Used	18.2	15.5	13.6
d'/t_w Used (Unstiffened)	18.2	15.5	13.6
d'/t_w Used (Stiffened)	47.5	40.3	35.4

Although the revised design requirements do not allow intermediate or flexural links with web compactnesses greater than $0.64\sqrt{E_s/F_{yw}}$, in compliance with the objectives of a complete block factorial experimental design which would require investigating all parameter combinations listed in table 3-11, stiffened links with the larger d'/t_w values given in table 3-11 will be modeled and analyzed at all four link lengths considered (i.e. ρ = 1.2, 1.6, 2.1, 3.0). Therefore, as in Part 1 of the study, Part 2 examines every combination of every parameter, making it a complete block design in the context factorial experimental design (as described in Section 3.2.1). Each of the three considered web yield stresses is considered with two web compactnesses (a stiffened and unstiffened compactness), with each of the three flange yield stresses (a single flange compactness), and for all four link lengths considered. This results in 72 models for Part 2 of the finite element parametric study.

TABLE 3-12 Cross-Section Dimensions for Part 2 Links

Flange Dimensions			
b'/t_f	18.2	15.5	13.6
b' (mm)	231.1	196.9	172.7
b (mm)	250.2	215.9	191.8
No. Elements	9	8	7
El. Edge-to-Thickness [a]	2.1	1.8	2.0
Unstiffened Web Dimensions			
d'/t_w	18.2	15.5	13.6
d' (mm)	173.4	147.6	129.5
d (mm)	198.8	173.0	154.9
No. Elements	7	6	6
El. Edge-to-Thickness [a]	2.8	2.8	2.5
Stiffened Web Dimensions			
d'/t_w	47.5	40.3	35.4
d' (mm)	452.4	383.9	337.2
d (mm)	477.8	409.3	362.6
No. Elements	18	16	14
El. Edge-to-Thickness [a]	2.7	2.6	2.6

[a] The mesh refinement study of Section 2 indicated values between 1.6 and 3.2 gave acceptable results.

TABLE 3-13 *b*/*d* Ratios for Part 2 Links

d'/t_w \ b'/t_f	18.2	15.5	13.6
18.2	1.16 	0.99 	0.87 
15.5	1.34 	1.14 	1.00 
13.6	1.49 	1.27 	1.12 
47.5	0.48 	0.41 	0.36 
40.3	0.57 	0.48 	0.42 
35.4	0.64 	0.54 	0.48 

Table 3-13 gives the plastic moment, M_p, reduced plastic moment for the presence of full plastic shear (Berman and Bruneau, 2005a), M_{pr}, plastic shear, V_p, and balanced link length, e^*, for the links in Part 2 of the parametric study. Actual link lengths, selected as exact multiples of 25.4 mm (1.0" being the element edge length in the longitudinal link direction), for the different values of normalized link length are given in table 3-14. The maximum stiffener spacings for the models with the larger d'/t_w ratios calculated using both the theoretical equation (3-2) and the proposed design equation (3-1) are given in table 3-15, while the actual stiffener spacings used in the models are given in table 3-16. Note that the actual stiffener spacings used in the models exceed the maximums calculated from the proposed design equation so that somewhat conservative results are obtained (i.e., if a link reaches its target rotation with a slightly larger stiffener spacing than the maximum allowed in the revised design requirements, it should also reach that target rotation when the stiffener

spacing requirements are met). Recall that the proposed stiffener spacing equation for design is more restrictive than the theoretical one, for reasons explained in Berman and Bruneau (2005a).

Material properties for Part 2 models were scaled versions of the data for Steel C from Kaufmann et al. (2001). The stabilized half cycle curves were input using the method described in Section 2. To scale the curves, the stresses were simply multiplied by the ratio of the yield stress of Steel C to the desired yield stress. Since input to ABAQUS requires the use of true plastic strain, no change in Young's Modulus, E, resulted from the scaling procedure. The material curves are shown in figure 3-2.

Loading was again consistent with the AISC seismic provision loading protocol for link-to-column connections and comprised of three cycles at each total link plastic rotation level of 0.0025, 0.005, and 0.01 radians, followed by two cycles at 0.01 radian increments up to 0.2 rads. Some models that exhibited large amplitude buckling did not converge prior to reaching 0.2 rads, but in all cases the limit plastic rotation could be identified and was not effected by numerical difficulties. The boundary conditions were the same as those used in Part 1 of the parametric study and the same method employed in Part 1 to determine the limit plastic rotation for each link was followed. For links in Part 2 of the parametric study, the naming convention is S-F_{yf}-F_{yw}-ρ, where S denotes a stiffened link and N denotes an unstiffened one, and the F_y values are in ksi. For example, link N-36-50-1.6 is an unstiffened link with F_{yf} = 36 ksi (250 MPa), F_{yw} = 50 ksi (345 MPa), and normalized link length of 1.6. This link has b'/t_f = 18.2 and d'/t_w = 40.3 (since it is stiffened it has the larger of the web compactness ratios for F_{yw} = 345 MPa) as given in table 3-10.

TABLE 3-14 Resulting Link Properties for Part 2 Models

b'/t_f	d'/t_w	M_p (kN-m)	M_{pr} (kN-m)	V_p (kN)	e^* (mm)
18.2	18.2	182	127	473	770
18.2	15.5	166	110	560	593
18.2	13.6	155	98	639	485
18.2	47.5	609	347	1235	986
18.2	40.3	564	301	1455	775
18.2	35.4	536	272	1662	644
15.5	18.2	207	148	473	875
15.5	15.5	187	128	560	669
15.5	13.6	174	113	639	544
15.5	47.5	671	405	1235	1086
15.5	40.3	617	351	1455	848
15.5	35.4	582	315	1662	701
13.6	18.2	230	168	473	970
13.6	15.5	207	144	560	739
13.6	13.6	191	128	639	598
13.6	47.5	727	459	1235	1177
13.6	40.3	665	396	1455	914
13.6	35.4	625	354	1662	752

TABLE 3-15 Link Lengths Used - Part 2 Models, mm (in)

b'/t_f	d'/t_w	ρ = 1.2	ρ = 1.6	ρ = 2.1	ρ = 3.0
18.2	18.2	457.2 (18)	609.6 (24)	812.8 (32)	1143.0 (45)
18.2	15.5	355.6 (14)	482.6 (19)	635.0 (25)	889.0 (35)
18.2	13.6	279.4 (11)	381.0 (15)	508.0 (20)	736.6 (29)
18.2	47.5	584.2 (23)	812.8 (32)	1016.0 (40)[a]	1473.2 (58)[a]
18.2	40.3	457.2 (18)	609.6 (24)	812.8 (32)[a]	1168.4 (46)[a]
18.2	35.4	406.4 (16)	508.0 (20)	685.8 (27)[a]	965.2 (38)[a]
15.5	18.2	533.4 (21)	711.2 (28)	914.4 (36)	1320.8 (52)
15.5	15.5	406.4 (16)	533.4 (21)	711.2 (28)	1016.0 (40)
15.5	13.6	330.2 (13)	431.8 (17)	584.2 (23)	812.8 (32)
15.5	47.5	660.4 (26)	863.6 (34)	1143.0 (45)[a]	1625.6 (64)[a]
15.5	40.3	508.0 (20)	660.4 (26)	914.4 (36)[a]	1270.0 (50)[a]
15.5	35.4	457.2 (18)	558.8 (22)	736.6 (29)[a]	1041.4 (41)[a]
13.6	18.2	584.2 (23)	787.4 (31)	1016.0 (40)	1447.8 (57)
13.6	15.5	431.8(17)	584.2 (23)	787.4 (31)	1117.6 (44)
13.6	13.6	355.6 (14)	482.6 (19)	635.0 (25)	889.0 (35)
13.6	47.5	711.2 (28)	965.2 (38)	1244.6 (49)[a]	1778.0 (70)[a]
13.6	40.3	558.8 (22)	711.2 (28)	965.2 (38)[a]	1371.6 (54)[a]
13.6	35.4	457.2 (18)	609.6 (24)	787.4 (31)[a]	1117.6 (44)[a]

[a] Links that do not satisfy the design requirements but are included for comparison purposes.

TABLE 3-16 Required Stiffener Spacing, mm (in)

d'/t_w	ρ = 1.2	ρ = 1.6	ρ = 2.1	ρ = 3.0
Proposed Design Equation (3-1)				
47.5	130.8 (5.15)	130.8 (5.15)	211.8 (8.34)	N.A.
40.3	139.4 (5.49)	139.4 (5.49)	220.2 (8.67)	N.A.
35.4	145.3 (5.72)	145.3 (5.72)	226.1 (8.90)	N.A.
Theoretical Equation (3-2)				
47.5	170.7 (6.72)	170.7 (6.72)	223.3 (8.79)	N.A.
40.3	174.5 (6.87)	174.5 (6.87)	231.6 (9.12)	N.A.
35.4	178.6 (7.03)	178.6 (7.03)	241.6 (9.51)	N.A.

TABLE 3-17 Stiffener Layout Used for Part 2 Stiffened Links (in)

b'/t_f	d'/t_w	ρ = 1.2	ρ = 1.6	ρ = 2.1	ρ = 3.0
18.2	47.5	8-7-8	7-6-6-6-7	10-10-10-10 [a]	14-30-14 [ab]
18.2	40.3	6-6-6	6-6-6-6	11-10-11 [a]	14-18-14 [ab]
18.2	35.4	8-8	7-6-7	9-9-9 [a]	14-10-14 [ab]
15.5	47.5	7-6-6-6-7	7-7-6-7-7	9-9-9-9-9 [a]	12-40-12 [ab]
15.5	40.3	7-6-7	7-6-6-7	9-9-9-9 [a]	12-26-12 [ab]
15.5	35.4	6-6-6	7-8-7	10-9-10 [a]	12-17-12 [ab]
13.6	47.5	7-7-7-7	6-6-7-7-6-6	10-10-9-10-10 [a]	11-48-11 [ab]
13.6	40.3	7-8-7	7-7-7-7	10-9-9-10 [a]	11-32-11 [ab]
13.6	35.4	6-6-6	6-6-6-6	10-11-10 [a]	11-22-11 [ab]

[a] Links that do not satisfy the design requirements but are included for comparison purposes.

[b] Flexural links have stiffeners only at 1.5*b* from each end.

3.7 Results of Parametric Study - Part 2

Link shear vs. plastic rotation hystereses for all links in Part 2 of the parametric study are given in Appendix A. Limit plastic link rotations (found using the same procedure as used for Part 1 of the parametric study described in Section 3.4), maximum link shear force normalized by V_p, and maximum link end moment normalized by M_p, are summarized in tables 3-17, 3-18, and 3-19, respectively. From table 3-17 it can be observed that all Part 2 links that met the revised design requirements reach their target rotation prior to 20% strength degradation (see Section 3.4). Figures 3-13 through 3-16 respectively show limit plastic rotation versus link length for: (i) unstiffened links (those with web compactness near $0.64\sqrt{E_s/F_{yw}}$) grouped by web yield stress; (ii) stiffened links (those with web compactness near $1.67\sqrt{E_s/F_{yw}}$) grouped by web yield stress; (iii) unstiffened links grouped by flange yield stress and; (iv) stiffened links grouped by flange yield stress, respectively. Tables 3-18 and 3-19 give insight into link overstrength and will be discussed further in following sections.

As shown in figures 3-13 and 3-14, all unstiffened links (i.e., those with web compactness near $0.64\sqrt{E_s/F_{yw}}$) reached their target rotations, and all stiffened links, except some at the intermediate length of 2.1, reached their target rotations. The links that did not reach their target rotation in figure 3-14 are intermediate links that do not satisfy the revised design requirements. These links were included for comparison purposes, and have the stiffened webs with a compactness ratio near $1.67\sqrt{E_s/F_{yw}}$, which is only allowed for shear links.

Figure 3-13 also shows that the maximum plastic rotation achieved was generally larger for links with the larger web yield stresses, especially at longer link lengths. This can be attributed to the fact that the webs with lower yield stress have a larger d'/t_w value, making them more prone to web buckling even though the ratio is near $0.64\sqrt{E_s/F_{yw}}$ (i.e., near 18.2 for F_{yw} = 250 MPa, 15.4 for F_{yw} = 345 MPa, and 13.5 for F_{yw} = 450 MPa). This trend is less significant in figure 3-14, indicating that for stiffened links there is not a significant relationship between limit plastic rotation and web yield stress. Furthermore, figures 3-15

and 3-16 indicate that there is no significant trend between limit plastic rotation and flange yield stress.

TABLE 3-18 Limit Plastic Rotations for Part 2 Links (rads)

b'/t_f	d'/t_w	$\rho = 1.2$ $\gamma_t = 0.08$	$\rho = 1.6$ $\gamma_t = 0.08$	$\rho = 2.1$ $\gamma_t = 0.05$	$\rho = 3.0$ $\gamma_t = 0.02$
18.2	18.2	0.137	0.128	0.066	0.046
18.2	15.5	0.196	0.155	0.095	0.062
18.2	13.6	0.194	0.194	0.177	0.079
18.2	47.5	0.200	0.087	0.047 [a]	0.027 [a]
18.2	40.3	0.196	0.156	0.046 [a]	0.036 [a]
18.2	35.4	0.195	0.165	0.062 [a]	0.036 [a]
15.5	18.2	0.137	0.113	0.065	0.044
15.5	15.5	0.195	0.155	0.086	0.053
15.5	13.6	0.194	0.174	0.103	0.076
15.5	47.5	0.197	0.085	0.042 [a]	0.026 [a]
15.5	40.3	0.196	0.121	0.046 [a]	0.036 [a]
15.5	35.4	0.185	0.115	0.055 [a]	0.035 [a]
13.6	18.2	0.195	0.113	0.064	0.049
13.6	15.5	0.195	0.174	0.077	0.060
13.6	13.6	0.194	0.183	0.101	0.075
13.6	47.5	0.197	0.087	0.040 [a]	0.033 [a]
13.6	40.3	0.166	0.096	0.046 [a]	0.045 [a]
13.6	35.4	0.195	0.125	0.056 [a]	0.034 [a]

[a] Links that do not satisfy the design requirements but are included for comparison purposes.

TABLE 3-19 Maximum Link Shear Normalized by V_p for Part 2 Links

b'/t_f	d'/t_w	ρ = 1.2	ρ = 1.6	ρ = 2.1	ρ = 3.0
18.2	18.2	1.56	1.51	1.33	0.97
18.2	15.5	1.58	1.51	1.31	0.97
18.2	13.6	1.61	1.51	1.34	0.96
18.2	47.5	1.48	1.37	1.21 [a]	0.92 [a]
18.2	40.3	1.51	1.39	1.21 [a]	0.92 [a]
18.2	35.4	1.44	1.38	1.19 [a]	0.93 [a]
15.5	18.2	1.57	1.51	1.35	0.97
15.5	15.5	1.59	1.53	1.34	0.97
15.5	13.6	1.60	1.54	1.33	0.99
15.5	47.5	1.52	1.41	1.24 [a]	0.94 [a]
15.5	40.3	1.50	1.41	1.21 [a]	0.94 [a]
15.5	35.4	1.47	1.39	1.23 [a]	0.95 [a]
13.6	18.2	1.57	1.52	1.36	0.98
13.6	15.5	1.60	1.54	1.35	0.98
13.6	13.6	1.61	1.54	1.36	0.99
13.6	47.5	1.52	1.42	1.25 [a]	0.94 [a]
13.6	40.3	1.48	1.43	1.24 [a]	0.95 [a]
13.6	35.4	1.51	1.41	1.24 [a]	0.96 [a]

[a] Links that do not satisfy the design requirements but are included for comparison purposes.

TABLE 3-20 Maximum Link End Moment Normalized by M_p for Part 2 Links

b'/t_f	d'/t_w	ρ = 1.2	ρ = 1.6	ρ = 2.1	ρ = 3.0
18.2	18.2	0.93	1.19	1.40	1.44
18.2	15.5	0.95	1.23	1.40	1.45
18.2	13.6	0.92	1.19	1.40	1.45
18.2	47.5	0.88	1.13	1.27 [a]	1.37 [a]
18.2	40.3	0.89	1.10	1.27 [a]	1.39 [a]
18.2	35.4	0.91	1.09	1.27 [a]	1.39 [a]
15.5	18.2	0.95	1.23	1.41	1.47
15.5	15.5	0.96	1.22	1.42	1.47
15.5	13.6	0.97	1.22	1.43	1.47
15.5	47.5	0.93	1.12	1.30 [a]	1.40 [a]
15.5	40.3	0.90	1.10	1.31 [a]	1.41 [a]
15.5	35.4	0.96	1.11	1.29 [a]	1.40 [a]
13.6	18.2	0.94	1.23	1.42	1.47
13.6	15.5	0.93	1.22	1.44	1.47
13.6	13.6	0.96	1.24	1.44	1.48
13.6	47.5	0.92	1.17	1.32 [a]	1.42 [a]
13.6	40.3	0.91	1.11	1.31 [a]	1.42 [a]
13.6	35.4	0.92	1.14	1.30 [a]	1.43 [a]

[a] Links that do not satisfy the design requirements but are included for comparison purposes.

Since all Part 2 links that satisfied the revised design requirements met their target rotations, these requirements appear to be satisfactory. However, the revised requirements above have been written in a format similar to the requirements for WF links in the AISC Seismic Provisions. It may be possible, as mentioned in the preceding sections, to allow a wider a range of link compactnesses, especially for intermediate links, if the target rotation can be

expresses as a function of both flange compactness and link length. This is the subject of Appendix B.

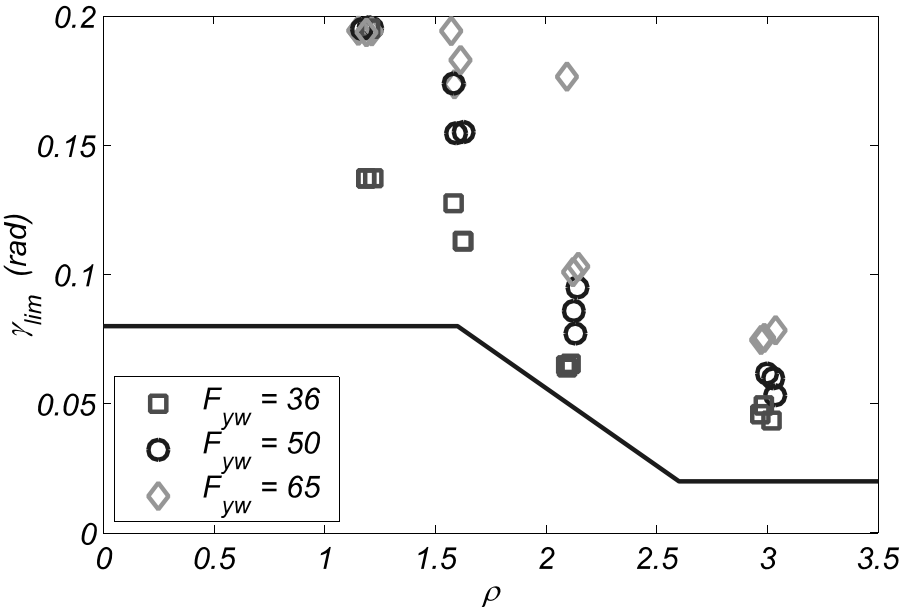

FIGURE 3-13 Limit Plastic Rotation vs. Normalized Link Length for Unstiffened Part 2 Links - Sorted by Web Yield Stress

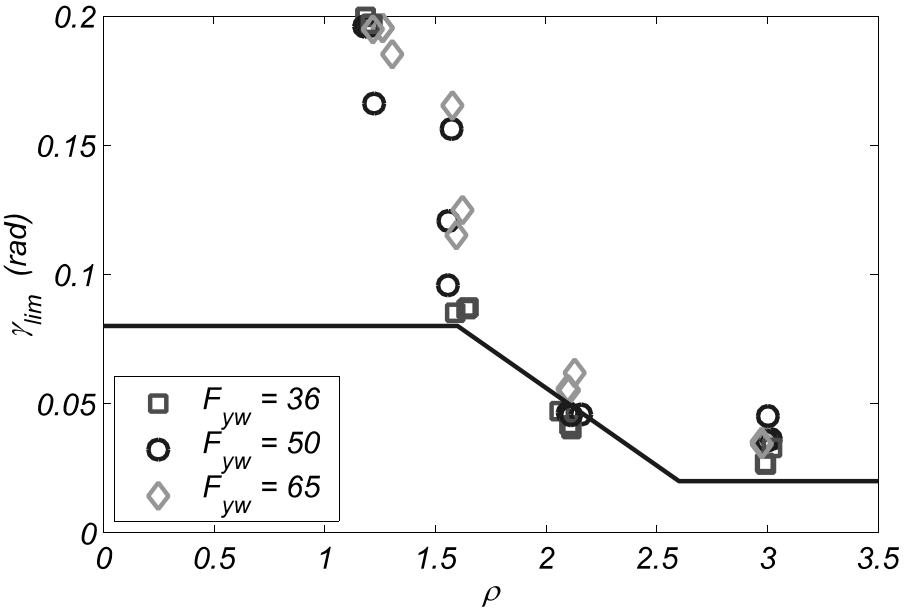

FIGURE 3-14 Limit Plastic Rotation vs. Normalized Link Length for Stiffened Part 2 Links - Sorted by Web Yield Stress

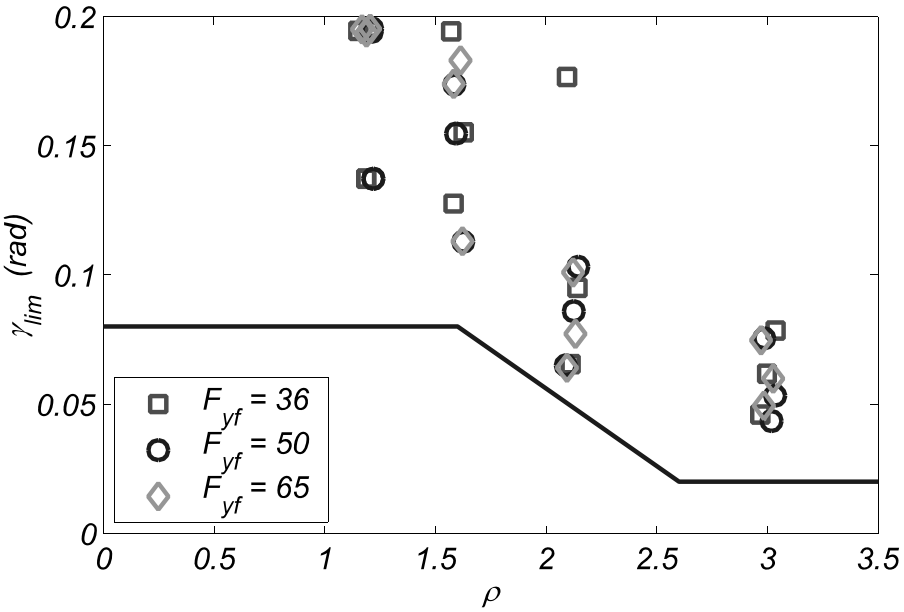

FIGURE 3-15 Limit Plastic Rotation vs. Normalized Link Length for Unstiffened Part 2 Links - Sorted by Flange Yield Stress

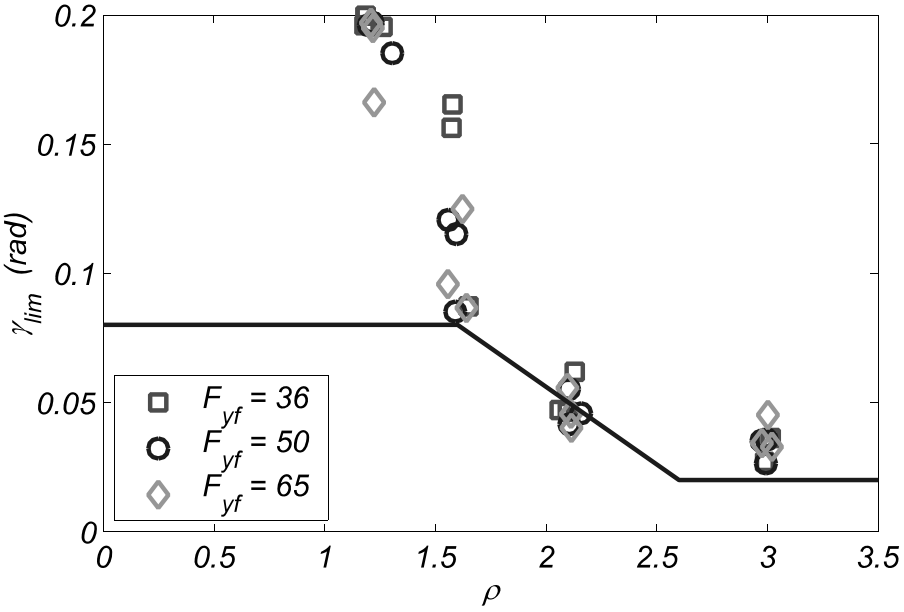

FIGURE 3-16 Limit Plastic Rotation vs. Normalized Link Length for Stiffened Part 2 Links - Sorted by Flange Yield Stress

3.8 Energy Dissipation of Links

Links in eccentrically braced frames are expected to dissipate earthquake energy through plastic deformations while the rest of structure remains essentially elastic. The energy

dissipated in a cycle is equal to the integration of the link shear force over the link plastic shear deformations. Cumulative energy dissipation is the sum of the energy dissipation for each cycle, *i*, up to the maximum number of cycles being considered, *N*, or:

$$E_H = \sum_{i=1}^{N} \left(\int V e d\gamma \right)_i \tag{3-4}$$

where V is the link shear force and $ed\gamma$ is the link end plastic shear deformation written as the product of the incremental link rotation, $d\gamma$, times the link length, e. For the purposes of comparing the energy dissipation for links of various cross-sections, the cumulative energy dissipation may be normalized by the product of the yield link shear force, V_y, and the yield end displacement, $e\gamma_y$:

$$E_{HN} = \frac{E_H}{V_y e \gamma_y} \tag{3-5}$$

The yield link shear is defined as the minimum of V_p or $2M_p/e$ where V_p and M_p are calculated using the nominal yield stresses of the webs and flanges (345 MPa for Part 1 links and either 250, 345, or 450 MPa for Part 2 links). Furthermore, the yield rotation is defined as V_y/K_e, where K_e is the elastic stiffness of the link in terms of link shear and link rotation. Substituting these definitions along with (3-4) into (3-5) gives the normalized cumulative energy dissipation definition used in this section:

$$E_{HN} = \frac{\sum_{i=1}^{N} \left(\int V d\gamma \right)_i}{\min\left(\frac{V_p^2}{K_e}, \frac{4M_p^2}{e^2 K_e} \right)} \tag{3-6}$$

Figure 3-17 shows the cumulative energy dissipation, E_H, for Part 1 links up to the point where the limit plastic rotation for each link is reached. The figure groups the links by length, stiffener condition (stiffened or unstiffened), web compactness and flange compactness ratios. As expected, stiffened shear links with large web and flange compactness ratios dissipate the most energy, since they have the most material undergoing plastic deformations and also have stiffeners to preclude web buckling and allow larger limit plastic rotations to be achieved.

Figure 3-18 shows the normalized cumulative energy dissipation, E_{HN}, for Part 1 links when the limit plastic rotation for each link is attained, grouped by properties in the same manner as for figure 3-17. Note that normalizing the energy dissipation of the links resulted in similar values for this quantity for all the stiffened shear links with $b'/t_f = 8.0$, regardless of the d'/t_w values. Since these links had different plastic shear forces and similar limit rotations, the fact that their normalized energy dissipation values are similar serves to validate the normalization procedure.

3.8.1 Normalized Energy Observations - Part 1 Shear Links

Comparing the E_{HN} for unstiffened versus stiffened links with a normalized length of 1.2 shows that, for large web compactness ratios, stiffeners significantly increase the energy dissipation capacity of the link, while they have no effect on energy dissipation for links with small web compactness ratios. Additionally, links of length 1.2 with larger flange compactness ratios had less normalized cumulative energy dissipation than links with smaller flange compactness ratios and length of 1.2 for both the stiffened and unstiffened cases.

Examining figure 3-18 also indicates that there are large differences in E_{HN} between links S-8-36-1.2 and S-40-36-1.2 even though it was previously reported that all links with a normalized length of 1.2 achieved their target rotation prior to strength degradation. This stems from the difference in limit plastic rotations for these links. The limit plastic rotation for S-8-36-1.2 was 0.196 rads while the limit plastic rotation for S-40-36-1.2 was 0.118 rads. Therefore, S-8-36-1.2 had many more high deformation cycles counted in the E_{HN} calculation, even though both links achieved their target rotation. Stiffened links with ρ = 1.6 show decreasing E_{HN} as the flange compactness ratio increases, highlighting the importance of preventing flange buckling at this transition link length.

When comparing the energy dissipation of shear links to that of intermediate and flexural links, it is observed that regardless of cross-section, the shear links have greater energy dissipation. Recall that no attempt to model fracture was made in the FE analyses and that some shear links would likely suffer fracture of the webs or flanges prior to reaching the

limit plastic rotations reported here, however, they should all be able to reach the target rotation of 0.08 rads prior to fracture.

3.8.2 Normalized Energy Observations - Part 1 Intermediate and Flexural Links

For intermediate or flexural links (ρ = 2.1 or 3.0), stiffeners did little to increase the energy dissipation, which was the same conclusion drawn regarding limit plastic rotations for links of these lengths. Additionally, it is observed from figure 3-18 that flange compactness is significantly more important than web compactness in terms of energy dissipation because the deformation capacity of longer links is, for the most part, limited by flange buckling. This trend is also visible in figure 3-17 for E_H.

3.8.3 Energy Observations - Part 2 Links

Figure 3-19 shows cumulative energy dissipation for Part 2 links, grouped by web and flange yield stress, normalized link length, and whether they were unstiffened with a web compactness ratio near $0.64\sqrt{E_s/F_{yw}}$ or stiffened with a web compactness ratio near $1.67\sqrt{E_s/F_{yw}}$. The normalized cumulative energy dissipation for Part 2 links is shown in figure 3-20. All Part 2 links met the revised design criteria of Section 3.5.4 except the intermediate and flexural links with the larger web compactness ratios and stiffeners, as only shear links are allowed to have webs with compactness ratios exceeding $0.64\sqrt{E_s/F_{yw}}$ in the revised requirements.

The most significant trend observed for the Part 2 links is that the normalized cumulative energy dissipation decreases substantially with increasing normalized link length, which was also observed for Part 1 links. Furthermore, for all Part 2 links, it is observed that there is little difference in normalized cumulative energy dissipation between stiffened links with the larger web compactness ratios and unstiffened links with the smaller web compactness ratios, assuming the normalized length is the same.

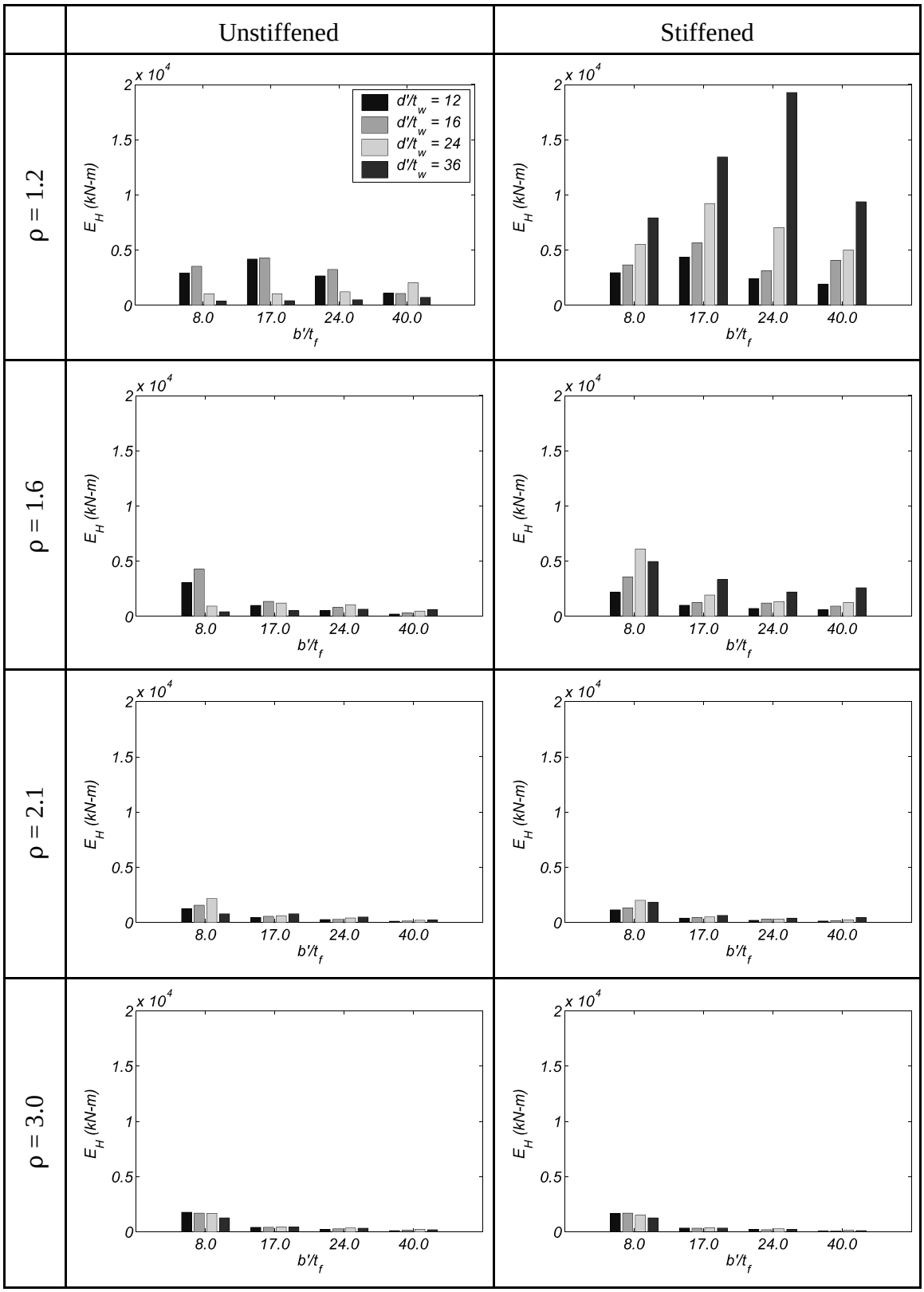

FIGURE 3-17 Cumulative Energy Dissipation for Part 1 Links - Summed to the Limit Plastic Rotation for Each Link

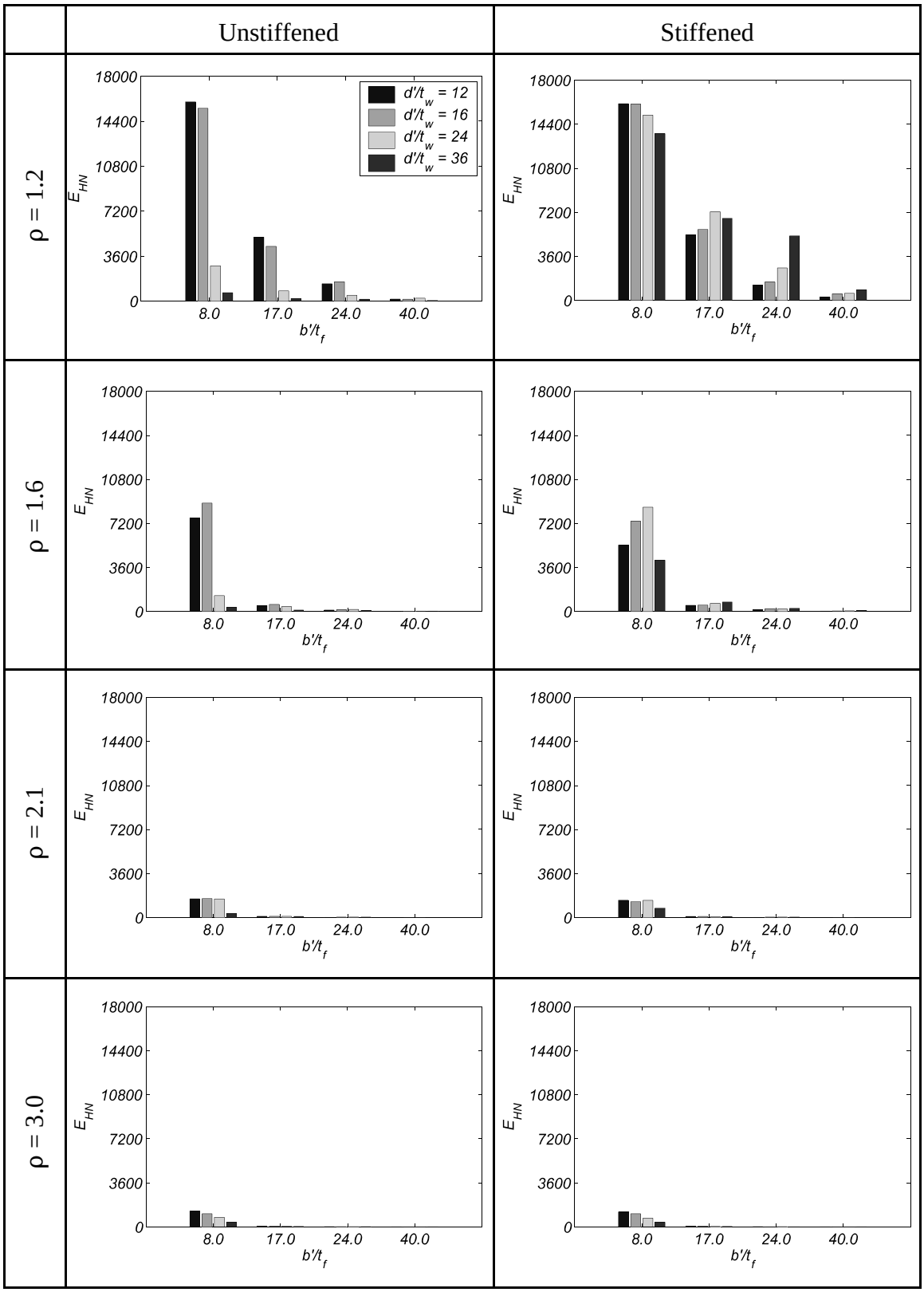

FIGURE 3-18 Normalized Cumulative Energy Dissipation for Part 1 Links - Summed to the Limit Plastic Rotation for Each Link

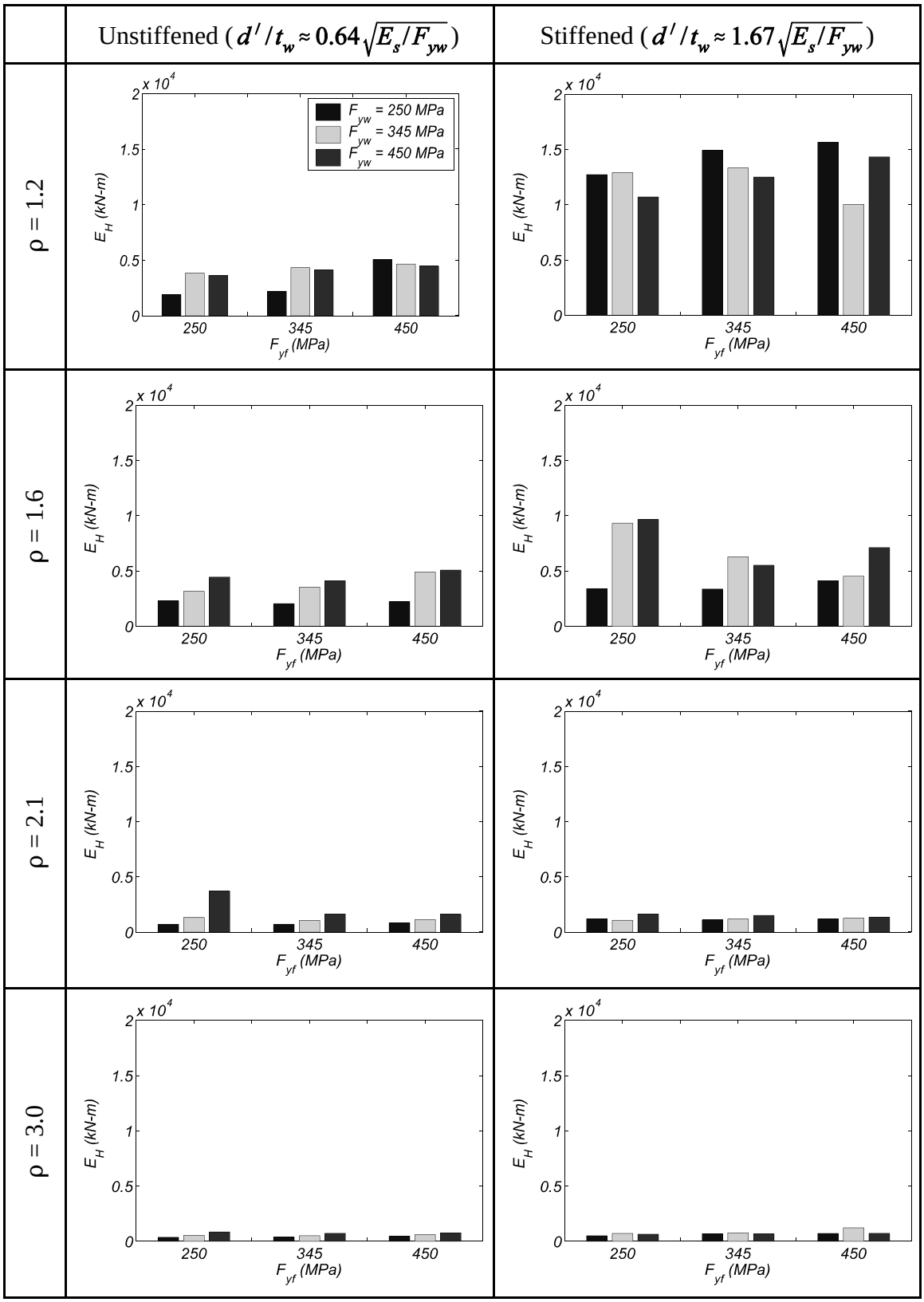

FIGURE 3-19 Cumulative Energy Dissipation for Part 2 Links - Summed to the Limit Plastic Rotation for Each Link

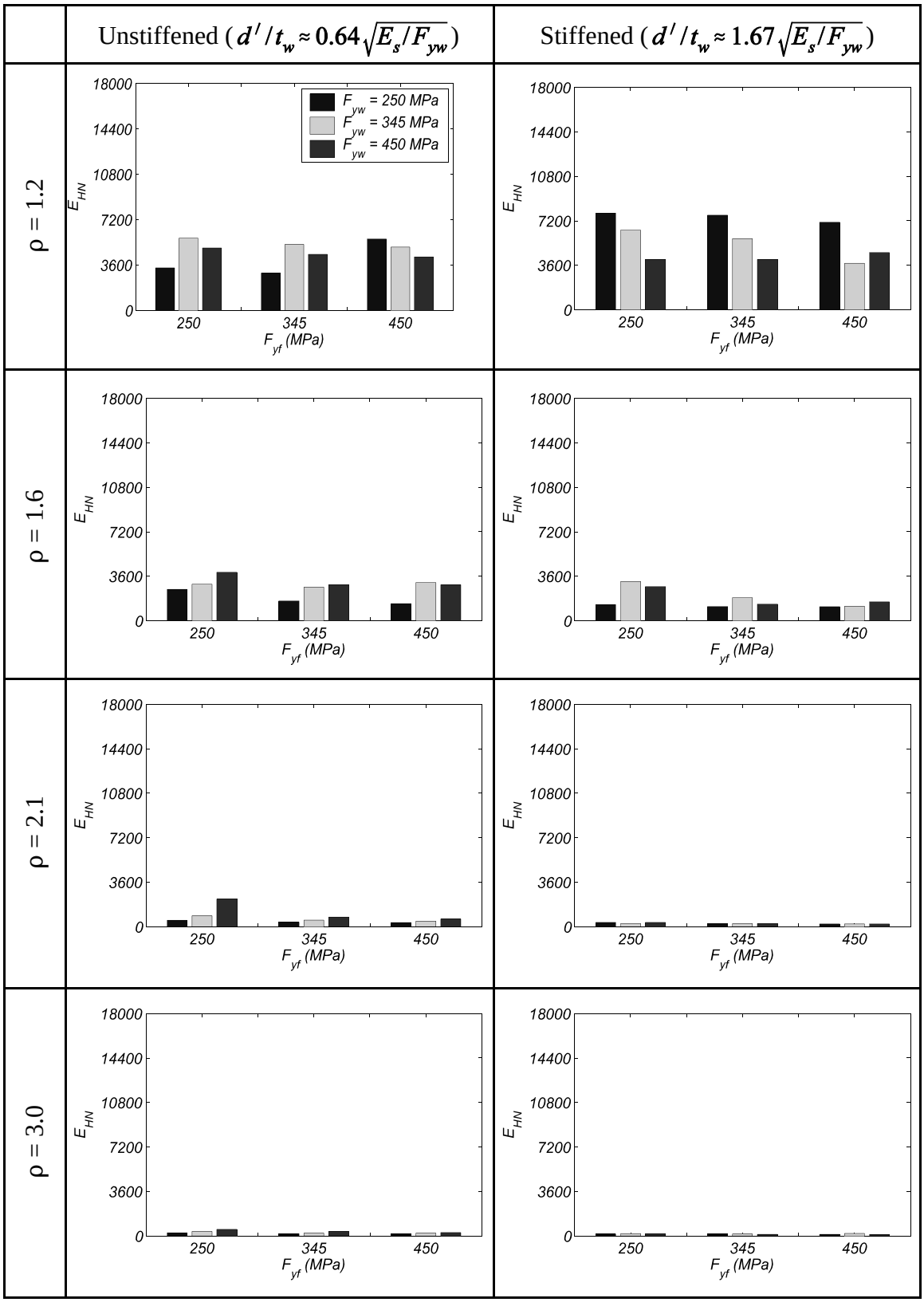

FIGURE 3-20 Normalized Cumulative Energy Dissipation for Part 2 Links - Summed to the Limit Plastic Rotation for Each Link

3.8.4 Energy Observations - Energy Dissipated per Cycle

Another way to investigate the energy dissipation of the links in this parametric study is to use the normalized energy dissipation per cycle. Figure 3-21 shows energy dissipated per cycle versus the maximum plastic link rotation achieved during that cycle for two Part 1 links, namely N-17-24-1.2 and S-17-24-1.2, to illustrate the effect of stiffeners on a given cross-section. Note that only data for the final cycle at each rotation level is shown and that the limit plastic rotations are indicated. The noticeable changes in slope indicate the onset of buckling; web buckling in the case of N-17-24-1.2 and flange buckling in S-17-24-1.2, although in both cases the buckling of either the webs of flanges is closely followed by buckling of the other. For N-17-24-1.2 web buckling occurs during the cycles at 0.04 rads and the strength of the link drops below 80% of the maximum strength obtained at 0.065 rads. After the onset of buckling, the rate of increase of energy dissipated per cycle drops significantly as shown in the figure. Comparing this behavior with that of S-17-24-1.2, for which some flange buckling and change in the rate of increase of energy dissipated per cycle occurs at approximately 0.11 rads of plastic rotation, but strength degradation does not reach 20% until 0.194 rads, indicates the effectiveness of stiffeners to stabilize energy dissipation.

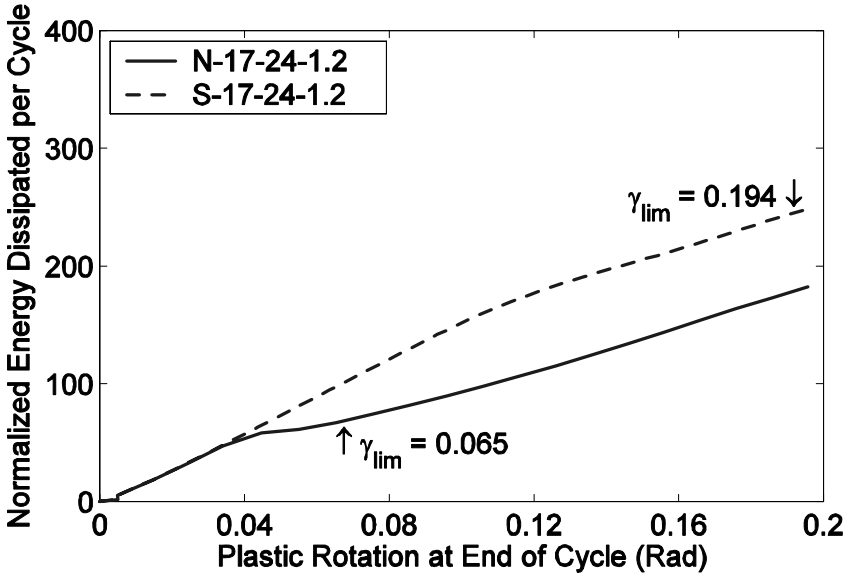

FIGURE 3-21 Energy Dissipated per Cycle for a Unstiffened and Stiffened Link of the Same Cross-Section

Figure 3-22 shows normalized energy dissipated per cycle versus the maximum plastic rotation achieved during that cycle for two links with differing flange compactness; N-8-12-1.2 with a flange compactness of 8 and N-24-12-1.2 with a flange compactness of 24. The figure shows that while the limit plastic rotations for both links exceed the target rotation of 0.08 rads, the normalized energy dissipation per cycle is greater and more stable for the link with the lower flange compactness ratio, N-8-12-1.2 which achieves a limit plastic rotation of 0.193 rads. N-24-12-1.2 suffers flange buckling at a approximately 0.1 rads (where the slope of the energy dissipated per cycle versus plastic rotation curve changes) and the strength degrades to 80% of the maximum link shear obtained at the limit plastic rotation of 0.122 rads.

Figure 3-23 compares normalized energy dissipated per cycle for links of the same cross-section but of different length; S-8-36-1.2 and S-8-36-3.0, which have normalized lengths of 1.2 and 3.0 respectively. As shown the shear link, S-8-36-1.2, has significantly larger energy dissipation per cycle at low plastic rotations and although buckling does occur at a plastic rotation of approximately 0.11 rads, the stiffeners prevent that link from suffering 20% strength degradation and a limit plastic rotation of 0.196 rads is achieved. The stiffeners also work to minimize the decrease in slope of the energy dissipation per cycle curve following buckling, which can be seen by comparing the slope of the curve in figure 3-23 before and after 0.11 rads for S-8-36-1.2. Contrasting this behavior with that of S-8-36-3.0, which is a flexural link and shows web and flange buckling at a plastic rotation of 0.045 rads and significant strength degradation by 0.055 rads. The difference in energy dissipation per cycle after 0.045 rads between S-8-36-1.2 and S-8-36-3.0 is significant.

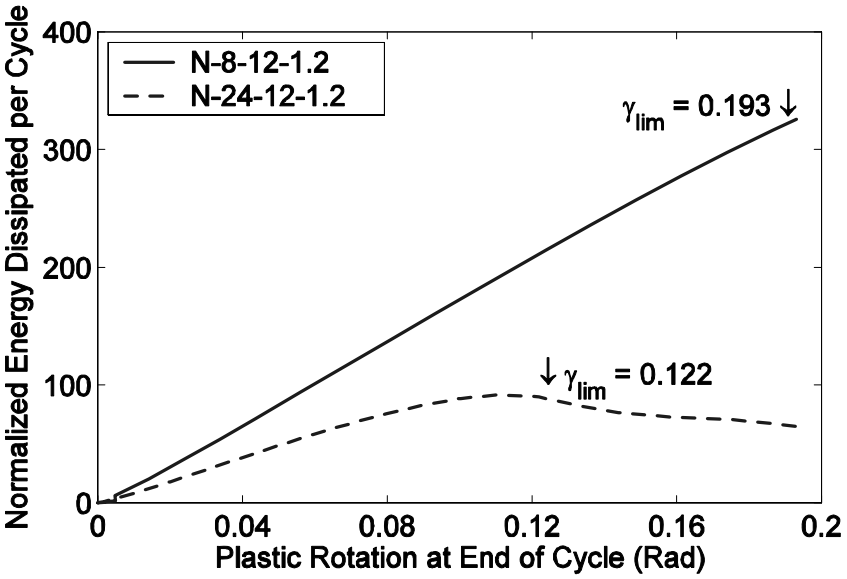

FIGURE 3-22 Energy Dissipated per Cycle for Two Links with Differing Flange Compactnesses

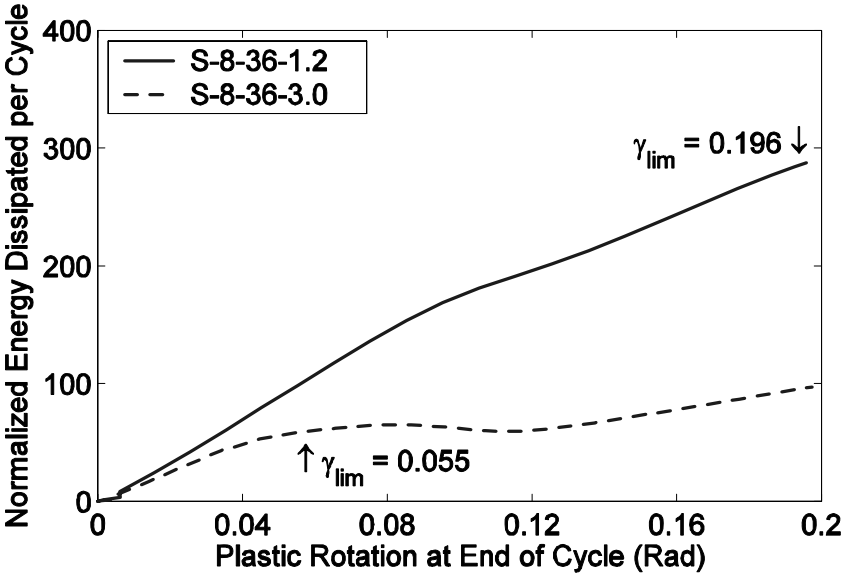

FIGURE 3-23 Energy Dissipated per Cycle for a Shear and a Flexural Link

3.9 Link Overstrength

Overstrength is defined here as the ratio of the maximum link shear divided by the plastic shear for shear links, or the maximum end-moment divided by the plastic moment for flexural and intermediate links. For the results reported for Part 1 links in tables 3-8 and 3-9, the overstrength obtained varies from 1.9 to 1.1 considering the maximum of shear and flexural overstrength for each link. To examine the trends in link overstrength, consider figure 3-24 which, for the unstiffened Part 1 links, shows maximum link shear obtained, V_{max}, normalized by V_p, versus normalized link length, ρ, for various link web compactness ratios. Also, figure 3-26 shows for unstiffened Part 1 links the maximum link end-moment obtained, M_{max}, normalized by M_p, versus normalized link length, ρ for various link flange compactness ratios. Note that values of overstrength in these figures that are less than 1.0 occur when examining the shear force overstrength for a flexural link which never develops a shear force equal to V_p. The opposite also occurs when examining flexural overstrength in shear links.

These figures show two trends, first, the maximum overstrength is generally larger for shear links (ρ = 1.2, 1.6), with values between 1.3 and 1.9 (figure 3-24), than it is for longer links (ρ = 2.1, 3.0), with values between 1.1 and 1.6. Second, the overstrength varies as a function of web compactness for shear links (it is larger for more compact webs, see figure 3-24) and as a function of flange compactness for longer links (it is larger for more compact flanges, see figure 3-26). These same observations appear to be true for the stiffened links considered in the same parametric study, as shown in figures 3-25 and 3-27.

Some of the overstrengths reported in figures 3-24 to 3-27 are large, especially for the short shear links. However, since fracture was not considered in the finite element analyses, it is possible that, in some cases, the overstrength that would be obtained experimentally could be less then the values reported here.

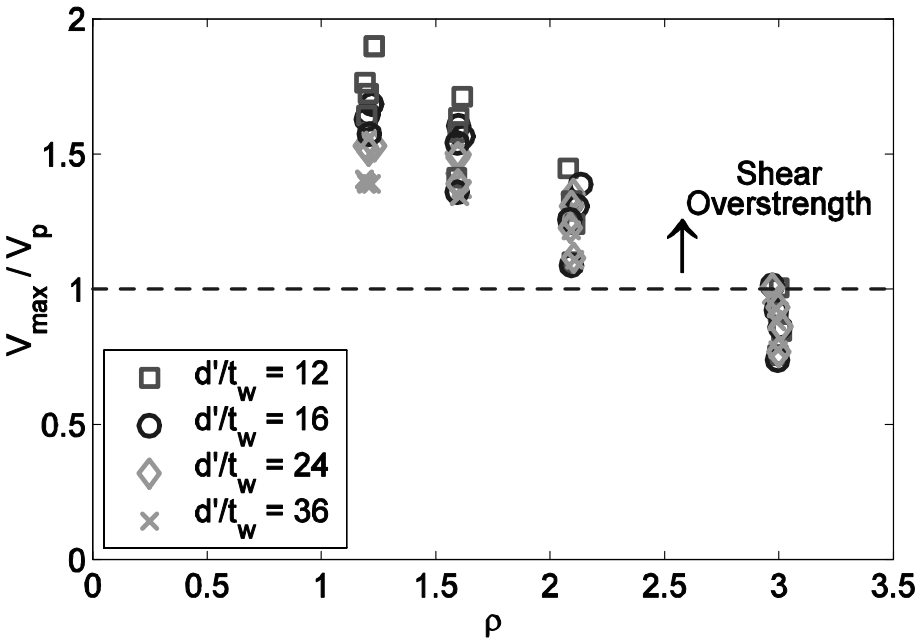

FIGURE 3-24 V_{max}/V_p for Unstiffened Part 1 Links

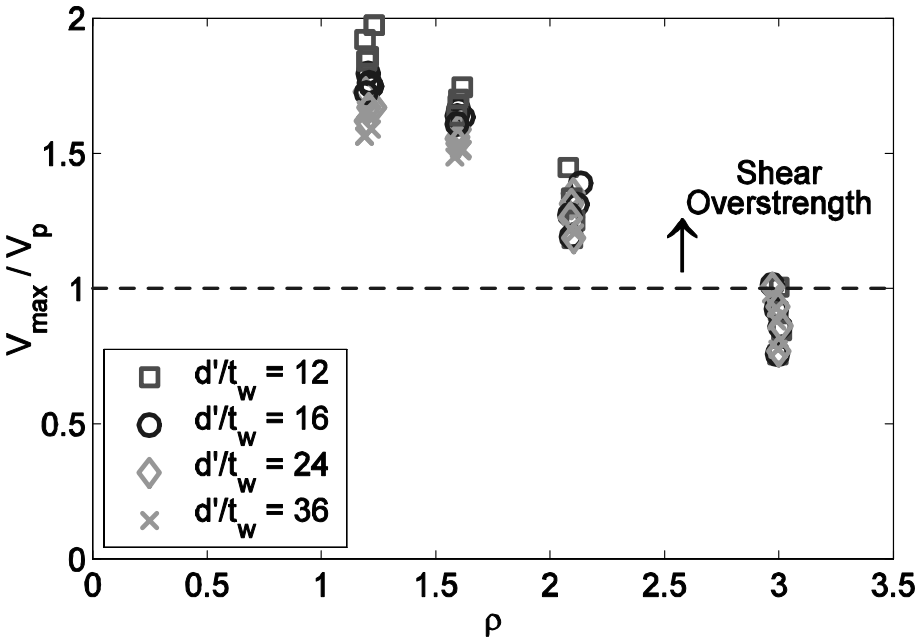

FIGURE 3-25 V_{max}/V_p for Stiffened Part 1 Links

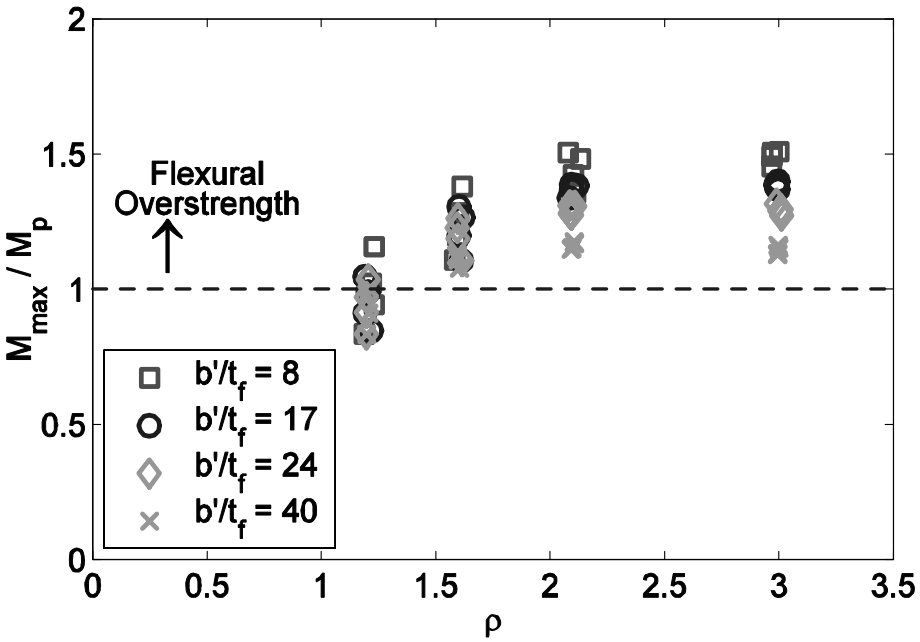

FIGURE 3-26 M_{max}/M_p for Unstiffened Part 1 Links

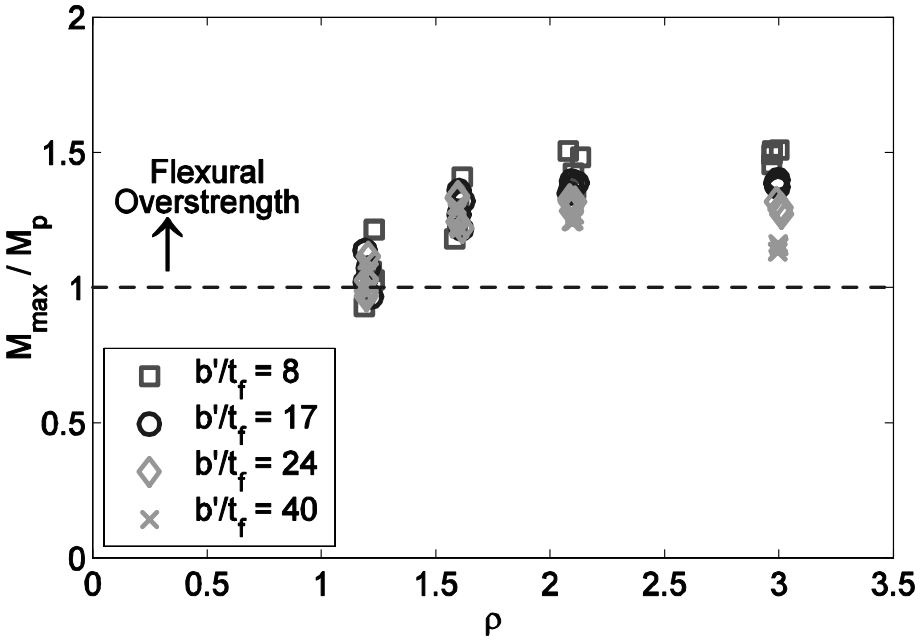

FIGURE 3-27 M_{max}/M_p for Stiffened Part 1 Links

It is informative to compare these calculated overstrength with values considered by design specifications. The 2002 AISC Seismic Provisions (AISC, 2002) require that beams outside the link region and braces to be designed for $1.1R_y$ and $1.25R_y$ times the lesser of V_p or $2M_p/e$, respectively (some inelastic behavior is allowed in the beam outside the link, explaining the lower 1.1 factor as opposed to the 1.25 factor for the brace). R_y is given as 1.1 for the A572 Gr. 50 steel considered in the finite element analyses reported here. The brace or beam strength under consideration is then factored using a resistance factor of 0.9 for flexure or 0.85 for compression. Defining the cyclic hardening factor, Ω, as the $1.1R_y$ or $1.25R_y$ factor divided by the resistance factor for the type of member strength being considered, the framing outside the link is being designed for overstrength in the range of:

$$\frac{1.1R_y}{0.9} = \Omega R_y = 1.34 \quad (\Omega = 1.22) \qquad to \qquad \frac{1.25R_y}{0.85} = \Omega R_y = 1.62 \quad (\Omega = 1.47) \tag{3-7}$$

If the AISC seismic provisions were used for the specific case of tubular links, based on the results of the finite element analyses presented here, the range above would adequately encompass observed overstrengths for intermediate or flexural links, but could be unconservative for shear links, particularly for short shear links with flanges having low compactness ratios together with either stiffened webs or webs with low compactness ratios. Using the overstrength formulations by Richards and Uang (2002) and modified in Berman and Bruneau (2005a), it may be possible to determine an overstrength factor that more closely matches the observed results from the finite element studies and also accounts for the different overstrength values observed between shear and flexural links . The following investigates that possibility.

In Berman and Bruneau (2005a), three different methods for estimating the maximum shear force strength of a link were presented. The first was based on simply using the full web depth of the section (i.e., using dt_w rather $(d\text{-}2t_f)t_w$ as the shear area). The second used the method derived in Richards and Uang (2002) that accounts for the flange contribution to the link shear and includes this contribution for links with $\rho \leq 1.6$. The third adapted the panel zone shear strength equation for beam-to-column connections to links. Regarding the second approach, it is noteworthy that Richards and Uang (2002) observed similar overstrength trends in their finite element analyses of WF links in that overstrength was observed to vary

with link length and flange compactness. Considering the similarities between the observation made by Richard and Uang regarding overstrength of WF links and the observations made here regarding overstrength of tubular links, their approach is slightly modified and it's applicability to tubular links is investigated below.

Recall that in Berman and Bruneau (2005a), the expression given by Richards and Uang to account for the additional shear force carried by the flanges had been modified to account for links of rectangular cross-sections, resulting in:

$$V_f = \frac{F_y b t_f^2}{2e} - \frac{F_y t_w^2 e}{8b} \tag{3-8}$$

Then the maximum link shear expected to develop in the link, V_{ult}, can be taken as the product of the plastic shear force, V_p, the cyclic hardening factor, Ω, and the ratio of mean to nominal material yield stress, R_y:

$$V_{ult} = \Omega R_y V_p \tag{3-9}$$

where $V_p = 0.6F_y(d-2t_f)t_w + 2V_f$ if $\rho \leq 1.6$ and is $0.6F_y(d-2t_f)t_w$ for links with $\rho > 1.6$. Richards and Uang then suggest that the cyclic hardening parameter defined above should vary with link length as:

$$\begin{aligned} \Omega &= 1.44 && \rho \leq 1.6 \\ \Omega &= 1.44 - 0.4(\rho - 1.6) && 1.6 < \rho \leq 2.6 \\ \Omega &= 2.7/\rho && \rho \geq 2.6 \end{aligned} \tag{3-10}$$

where the 2.7 value in the last expression in (3-10) is found by assuming that the maximum moment that can develop is $1.35M_p$ (less than the 1.44 used for shear links due to flange buckling limiting the strength of flexural links and the fact that stiffeners do not prevent this failure mode) and employing the link shear-moment relationship for flexural links ($V = 2M_p/e$).

Consider figures 3-28 and 3-29 which show the maximum link shear obtained in the finite element analyses of Part 1 links normalized by V_{ult} as defined above, versus normalized link length for unstiffened and stiffened links respectively. The solid line in the figures indicates

the curve for the cyclic hardening factor as given by (3-10) multiplied by an R_y value of 1.1 (appropriate for the A572 Gr. 50 steel considered here). It appears that the overstrength equations proposed by Richards and Uang for WF links and modified here for rectangular links adequately estimates the maximum link shear force (from which the maximum link end moment may be found). This procedure seems to provide a more uniform level of safety relative to a single valued overstrength factor, in terms of capacity protection of structural members outside the link, for all link lengths and yielding types. The points at small normalized link lengths that are above this proposed overstrength may suffer flange fracture prior to reaching the large overstrengths obtained from the finite element analyses, but further investigation of this is necessary before further changes are considered to address these extremes. Overstrength will be experimentally investigated in the following sections to assess whether results predicted here for the cyclic hardening factors applicable to rectangular links are appropriate.

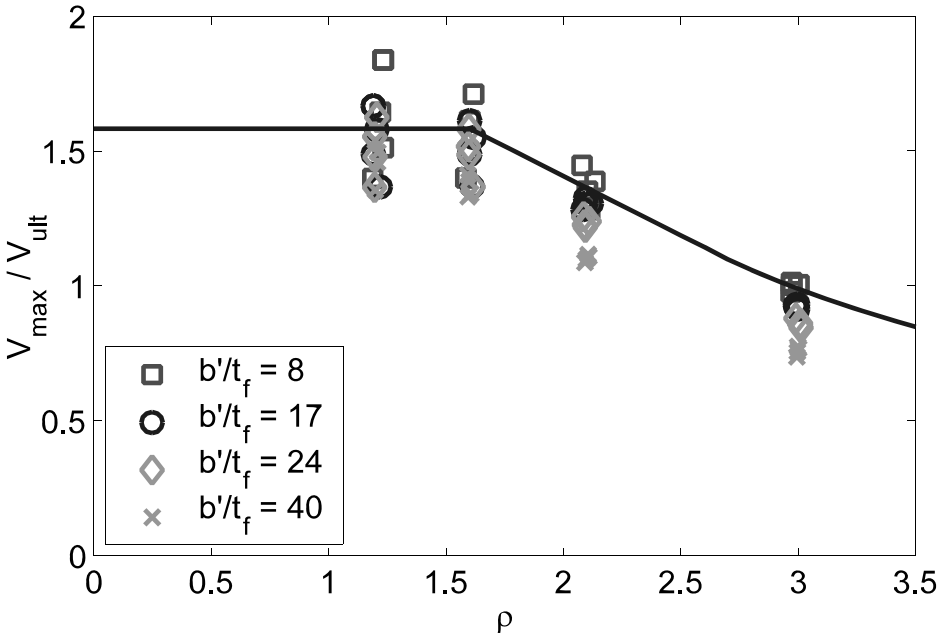

FIGURE 3-28 V_{max}/V_{ult} for Unstiffened Part 1 Links

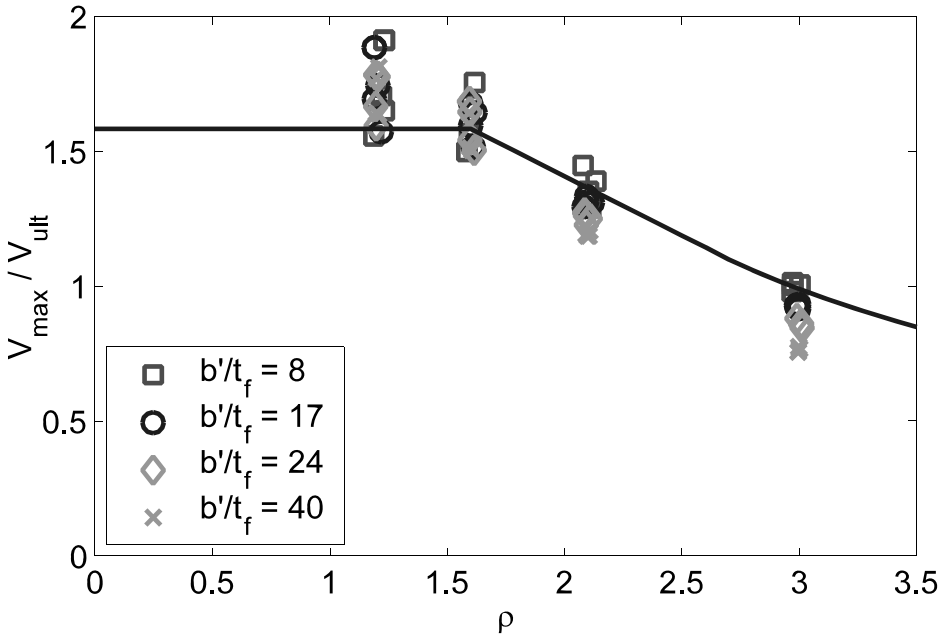

FIGURE 3-29 V_{max}/V_{ult} for Stiffened Part 1 Links

3.10 Summary

A finite element parametric study of rectangular links for eccentrically braced frames has been conducted. Details of the study and results have been presented in this section. The study consisted of two parts. Part 1 considered a wide range of link geometries both satisfying and not satisfying the design recommendations proposed in Berman and Bruneau (2005a). Results of Part 1 were then used to revise those proposed recommendations. Part 2 considered links that had geometries near the revised compactness limits and investigated the use of webs and flanges with differing yield stresses, i.e., hybrid rectangular link sections. Part 2 showed that the revised design recommendations of Section 3.5.4 were applicable for hybrid rectangular links in the context of finite element analyses. Results from both parts of the study were then used to investigate link energy dissipation and overstrength. Throughout the review of results from the finite element analyses, particular attention was paid to the effects of stiffeners, web compactness, flange compactness, and link length. The results presented in this section were used to select the link cross-sections to be tested to validate the concepts developed as part of this research as described in the next section.

SECTION 4

DESIGN AND SETUP OF LINK TESTING

4.1 General

This section describes the design and detailing of links for quasi-static cyclic testing, the design of a setup to carry out the testing, and the instrumentation used to capture results. The compactness values, lengths, and stiffeners of the links to be tested are selected using the results of the finite element parametric study and the revised design recommendations described in Section 3. Monotonic and cyclic coupon test results for the material used to fabricate the links are reported. The setup for quasi-static link testing is shown in figure 4-1 and is modular to allow for different link lengths (the figure shows the configuration for links with normalized length, ρ, of 3.0). Design of the setup is based on an actuator force of 1110 kN (250 kip) along with appropriate safety factors for the various components and failure modes as described in this section. Instrumentation for the testing is described, including; strain gages, string displacement potentiometers, the Krypton dynamic measurement device, and video recording. Finally, two of the links are redesigned with different end connections that more closely resemble those of the proof-of-concept test. The experimental data, as well as the analytical data already presented, will then be used in following sections to assess the adequacy of the design recommendations, examine link overstrength and energy dissipation, and provide insight into the general behavior of links with hollow rectangular cross-sections.

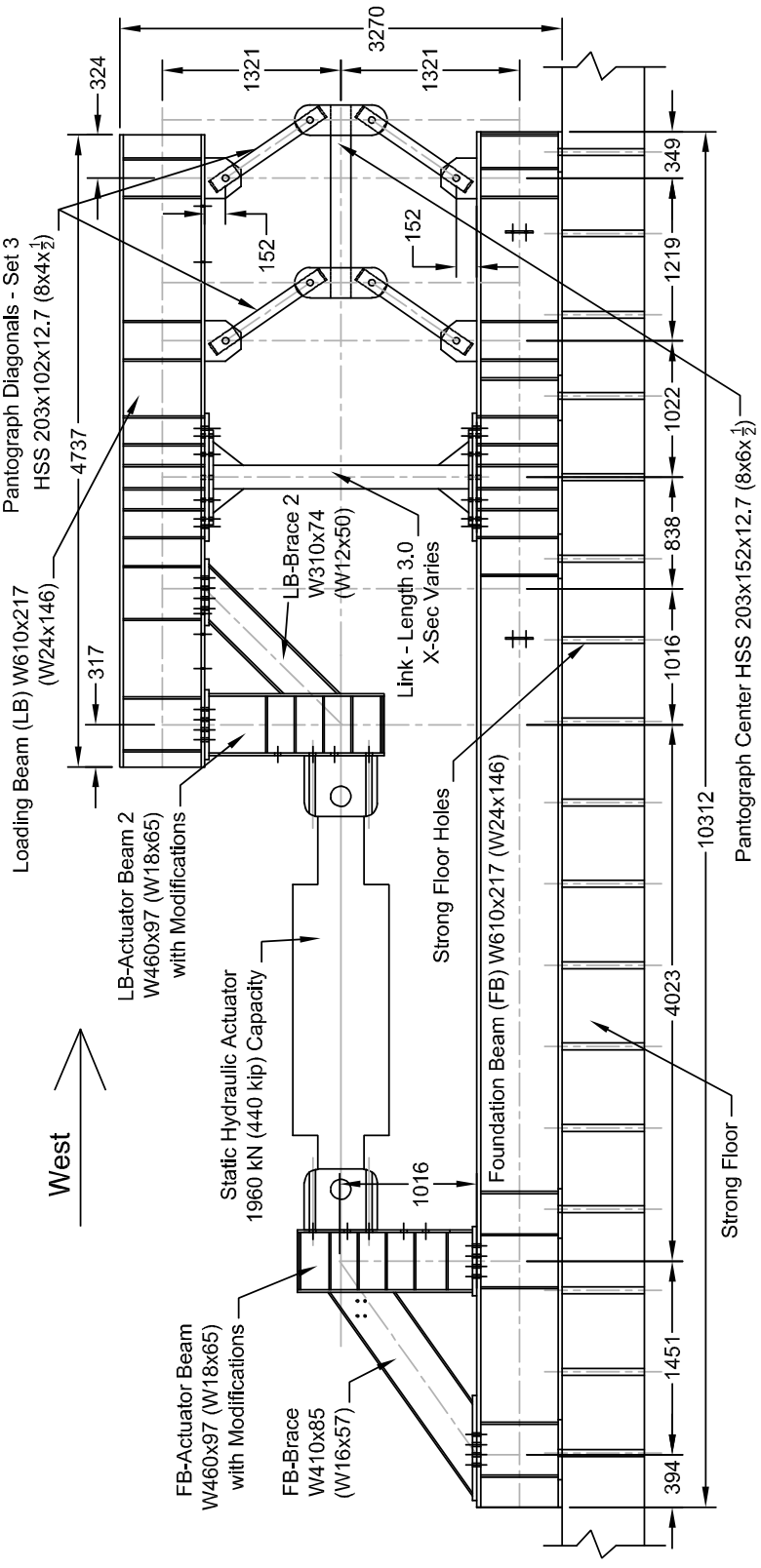

FIGURE 4-1 Test Setup for Specimens with a Normalized Link Length of 3.0

4.2 Link Selection

Twelve specimens, consisting of three link cross-sections and four link lengths, were selected for quasi-static cyclic testing. Two of the cross-section geometries were selected to be near the revised limits for web and flange compactness for the cases of stiffened and unstiffened webs as described in Section 3.5.4. The third cross-section was designed to have compactness values well below the proposed limits to investigate link overstrength in such situations. During the design procedure, A572 Gr. 50 plate material with a nominal yield stress, F_y, of 345 MPA (50 ksi) was assumed for both the webs and flanges of all three cross-sections.

In addition to having cross-sections and lengths meeting the above descriptions, several practical issues associated with the test setup were also considered while selecting link specimen geometries. First, the capacity of the actuator and setup had to be sufficient to test the specimens to failure. Second, the cross-sections were constrained to be similar in overall size so that, at most, two different connections to the setup were necessary. Finally, the number of setup configurations were limited to insure that testing was completed in a reasonable time period. Therefore, actual link lengths and expected maximum shear forces were selected to be as similar as possible for links having different cross-sections and the same normalized link length.

Link specimens are denoted by cross-section number and normalized length, i.e., Specimen X1L1.2 has cross-section 1 and a normalized length of 1.2. Table 4-1 gives cross-section geometry details for the links in this experimental study as well as their plastic shear forces, moments, and balanced link lengths calculated using the nominal yield stress of 345 MPa. Figure 4-2 shows the corresponding three cross-section details and table 4-2 has the target and provided normalized link lengths, as well as the specified link lengths, which correspond to normalized lengths that may differ slightly from the target normalized link lengths (specified in this case meaning as they appear on design drawings used for fabrication). As shown in table 4-2, for a given normalized link length, all link cross-sections have specified link lengths that are similar to satisfy the design considerations above. Note that the dimensions in the tables have been rounded to the nearest tenth of a millimeter (mm) and

that US customary units were used during the design process because of requirements from the fabricator. Furthermore, note that the design link plastic shear forces in table 4-1 are approximately three times that required for the two story pier in Pollino and Bruneau (2004) and approximately 1/4 and 2/5 of the design link shear forces for the links of the San Francisco-Oakland Bay Bridge piers and Richmond-San Rafael Bridge piers, respectively (Dusicka et al., 2002, and Itani, 1997).

TABLE 4-1 Link Specimen Cross-Section Geometries and Properties

Cross-Section ID	b (mm)	t_f (mm)	d (mm)	t_w (mm)	b'/t_f	d'/t_w	b/d	V_p (kN)	M_p (kN-m)	e^* (mm)
X1	260.4	15.9	177.8	9.5	15.2	15.3	1.46	554	266	960
X2	209.6	12.7	266.7	6.4	15.5	38	0.79	610	297	973
X3	238.1	22.2	158.8	12.7	9.6	9	1.50	578	278	961

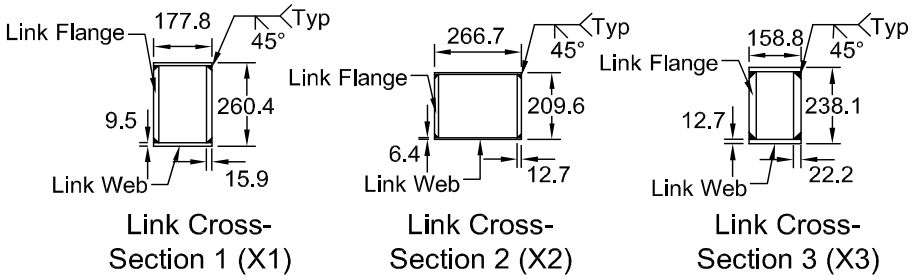

FIGURE 4-2 Link Specimen Cross-Section Details

4.2.1 Cross-Section 1 (X1)

Link cross-section 1, X1, was designed to have compactness values near the proposed limits for unstiffened links in Section 3.5.4. The flange compactness value of 15.2 is near the proposed limit of 15.4 from $b'/t_f \le 0.64\sqrt{E_s/F_{yf}}$, with F_{yf} = 345 MPa and E_s = 2 x 10^6 MPa. To achieve this compactness value, a flange thickness of 15.6 mm (5/8") and width of 260.4 mm (10.25") were selected. A web depth of 177.8 mm (7") and thickness of 9.5 mm (3/8") were selected as they correspond to a web compactness value of 15.3, which is near the proposed limit for unstiffened webs of 15.4 from $d'/t_w \le 0.64\sqrt{E_s/F_{yw}}$ with F_{yw} = 345 MPa

and E_s = 2 x 10^6 MPa. Full penetration groove welds, similar to those used for the link in the proof-of-concept testing described in Berman and Bruneau (2005a), were specified to assemble the hollow rectangular cross-section.

TABLE 4-2 Link Lengths for Specimen

Length ID	Link Lengths	Cross-Section ID		
		X1	X2	X3
L1.2	ρ_{target}	1.2	1.2	1.2
	e Specified (mm)	578	610	578
	ρ_{actual}	1.20	1.25	1.20
L1.6	ρ_{target}	1.6	1.6	1.6
	e Specified (mm)	768	787	768
	ρ_{actual}	1.60	1.62	1.59
L2.1	ρ_{target}	2.1	2.1	2.1
	e Specified (mm)	1010	1067	1010
	ρ_{actual}	2.10	2.19	2.10
L3.0	ρ_{target}	3.0	3.0	3.0
	e Specified (mm)	1442	1461	1442
	ρ_{actual}	3.00	3.00	3.00

As shown in table 4-2, the selected lengths for the X1 links resulted in actual normalized lengths equal to the target normalized lengths. Furthermore, the selected lengths cover the range of link behavior that was investigated in the finite element parametric study, namely, short shear links (ρ = 1.2), shear links at the transition length to intermediate links (ρ = 1.6), intermediate links (ρ = 2.1), and flexural links (ρ = 3.0). Elevation views of the four X1 links, X1L1.2, X1L1.6, X1L2.1, and X1L3.0 are shown in figure 4-3. As shown, each link has a haunch at each end and an end-plate. The haunch serves three purposes: it provides a weld across the flange at the link end, which is similar to the gusset stiffener weld near the flange fracture in the proof-of-concept test; it increases the constraint against plastic flow

in the flange, again similar to the gusset stiffener in the proof-of-concept test; and it reduces flexural and shear stresses at the intersection with the end-plate to prevent fracture of the weld connecting the link to the end-plate as has occurred in many WF link tests (Kasai and Popov, 1986a, and Arce, 2002, among many). The active link length is then the distance between the haunches at each end. Design of the haunches and end-plates are discussed further in Sections 4.2.4 and 4.2.5 respectively.

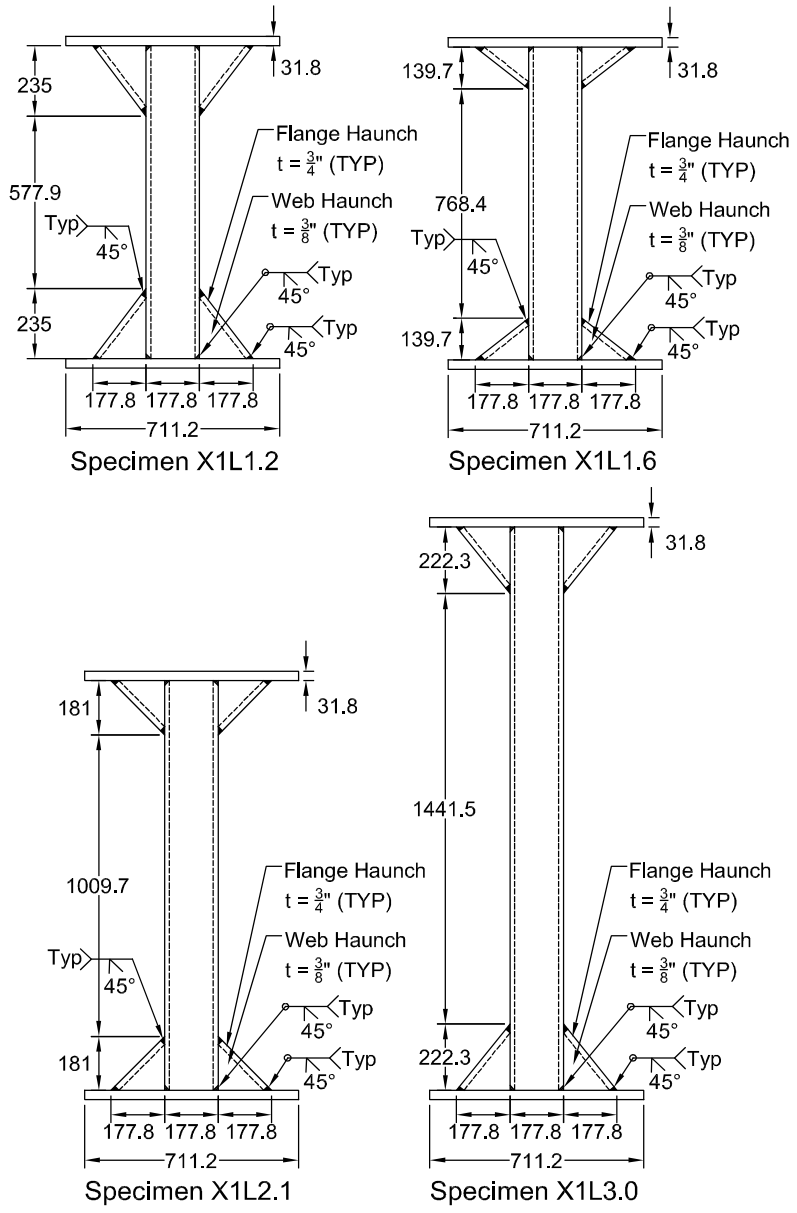

FIGURE 4-3 X1 Link Specimen

4.2.2 Cross-Section 2 (X2)

The second link cross-section, X2, was selected to have a web compactness value of 38, which is near the proposed upper limit for shear links with stiffened webs of 40.2 from $d'/t_w \le 1.67\sqrt{E_s/F_{yw}}$, with F_{yw} = 345 MPa and E_s = 2 x 10^6 MPa. For completeness, and to investigate the finite element results indicating that intermediate links with this web compactness value and stiffeners meeting the revised requirements do not consistently achieve their target rotation, specimens at all four lengths were designed even though the revised design requirements limit the use of this larger web compactness limit to stiffened shear links. A web depth and thickness of 266.7 mm (10.5") and 6.4 mm (0.25") were used to achieve this compactness value while also providing a plastic shear force near that of the X1 specimens. Stiffener spacings for X2 specimens were designed according to the proposed stiffener spacing equation (3-1), with the exception of X2L3.0 which has stiffeners only at 1.5*b* from the ends. The stiffeners were designed to meet the proposed strength requirements in Berman and Bruneau (2005a). Two different stiffener types were required, one for Specimens X2L1.2 and X2L1.6, and one for Specimens X2L2.1 and X2L3.0, the latter type having slightly larger plan dimensions. These stiffener details are shown in figure 4-4 and elevations of the four X2 specimens are shown in figure 4-5. As noted in figure 4-4, the stiffeners at the ends of links X2L1.2, X2L1.6, and X2L2.1 are welded only to the web to prevent adding to the already significant amount of weld (residual stresses and constraints) at the flange haunch plate to link flange location. These web stiffener welds are then terminated 19.1 mm (3/4") from the flange. The link length is taken as the distance between the inside edges of the end stiffeners.

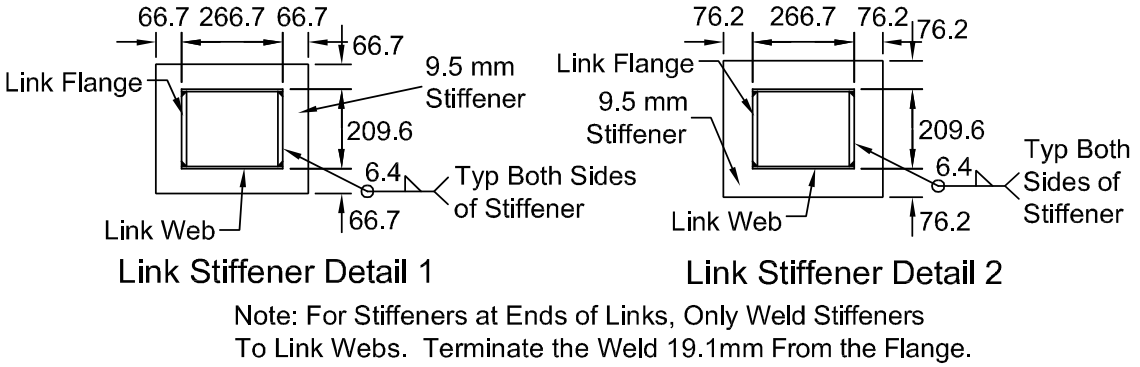

FIGURE 4-4 Stiffener Details for X2 Links

The flanges of the X2 specimens were designed to have a compactness value near the limit of 15.4, from $b'/t_f \leq 0.64\sqrt{E_s/F_{yf}}$ for the nominal flange yield stress of 345 MPa (50 ksi). A width of 209.6 mm (8.25") and thickness of 12.7 mm (0.5") were selected, which resulted in a flange compactness value of 15.5 while also having a balanced link length similar to that for specimens with cross-section X1.

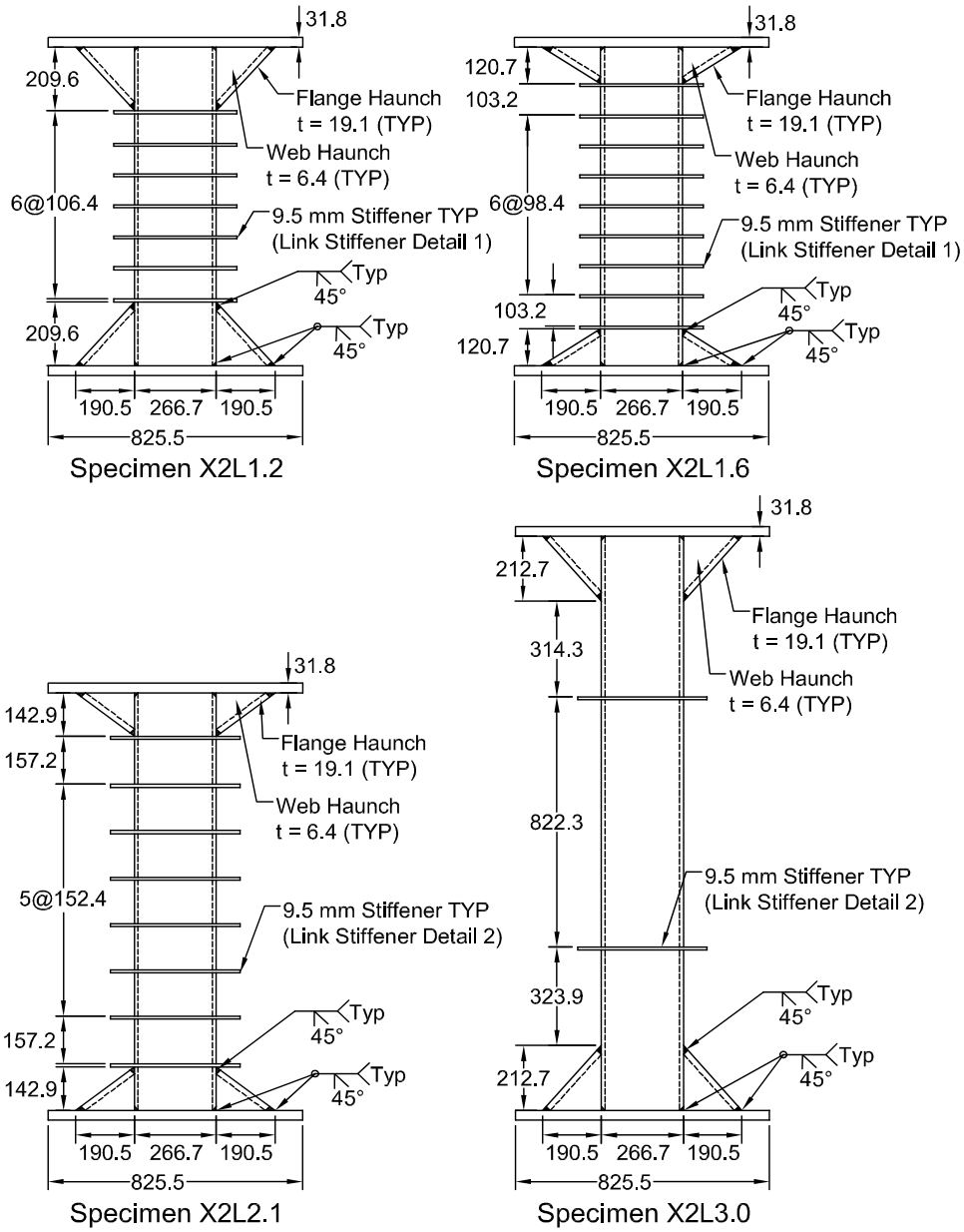

FIGURE 4-5 X2 Link Specimens

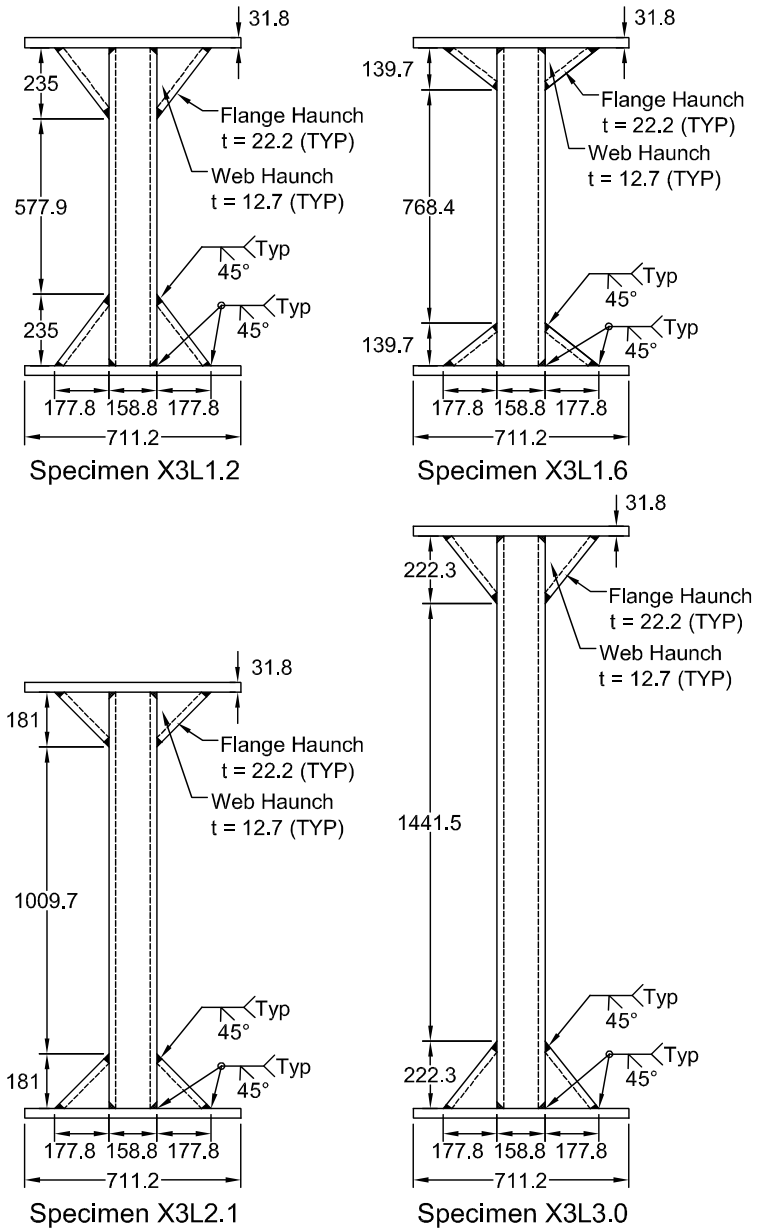

FIGURE 4-6 X3 Link Specimens

4.2.3 Cross-Section 3 (X3)

The third cross-section, X3, to be investigated experimentally was designed to have compactness values well below the revised limits for flanges and unstiffened webs to investigate the overstrength that may be expected when such cross-sections are used. This cross-section is shown in figure 4-2 and elevations of the four X3 links are shown in figure 4-6. The webs were designed to have depths of 158.8 mm (6.25") and thicknesses of 12.7 mm (0.5") corresponding to web a compactness value of 9, which is 42% below the limit of

15.4 for unstiffened webs with F_{yw} = 345 MPa (50 ksi). Flanges were designed to have widths of 238.1 mm (9.375") and thicknesses of 22.2 mm (0.875") corresponding to a flange compactness value of 9.6, which is 38% below the 15.4 limit for flanges with F_{yf} = 345 MPa (50 ksi). These dimensions were selected because they meet the requirements for low compactness ratio and also provide plastic shear strength and link lengths that are compatible with the setup and other link cross-sections. Lengths for the X3 specimens were selected to be as close as practicable to the desired normalized lengths and are given in table 4-2.

4.2.4 Link Material Testing

Monotonic tension and cyclic test were performed on coupons from the plate material used to fabricate the various link cross-sections described above. The monotonic tension coupons conformed to ASTM A370 and the results are shown in figures 4-7 and 4-8 for the web and flange materials respectively. Note that the same plate material was used to fabricate the web of the X3 specimens and the flange of the X2 specimens. During testing, force was recorded by an internally mounted load cell in a Tinius Olsen material testing machine and strain was monitored using a MTS extensometer with a 50.8 mm (2 in) gage length. Observed yield and ultimate stresses for each material are given in table 4-3. Note that the thinner materials used for the webs and for the flange of the X2 specimens do not have a distinct yield plateau and that the 0.2% offset method was used to determine their yield stress. The thicker materials used for the flanges of the X1 and X3 specimens have a typical mild steel stress-strain curve with a yield plateau. All coupons showed good ductility reaching strains on the order of 20% before fracture except the material used for the flanges of the X2 specimens and webs of the X3 specimens. The maximum strain reached for that material was approximately 15%, however, necking in this specimen occurred outside the gage length of the extensometer and was not captured by that instrument. Therefore, the actual strain at failure for that coupon was likely larger than that shown in figure 4-8.

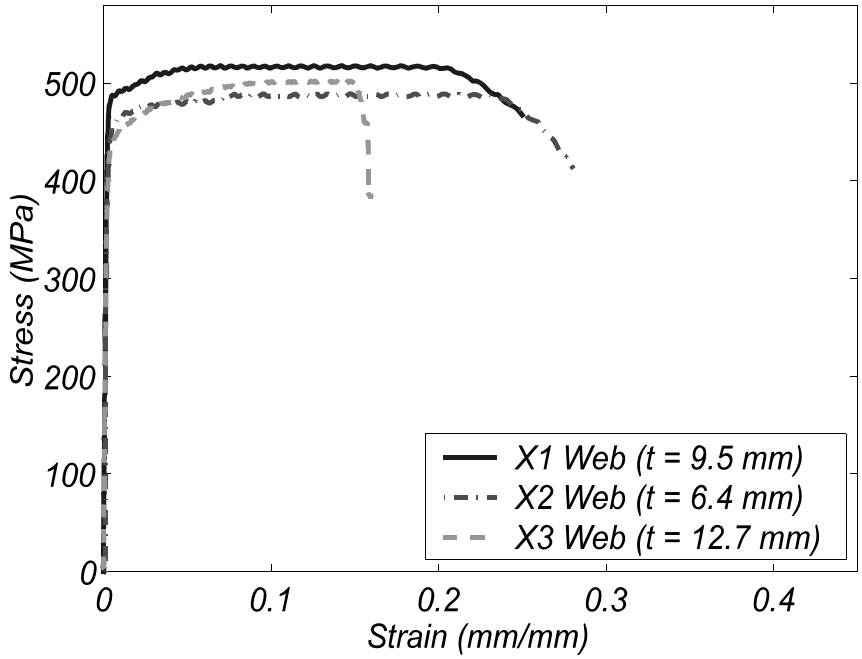

FIGURE 4-7 Tension Coupon Test Results for Web Materials

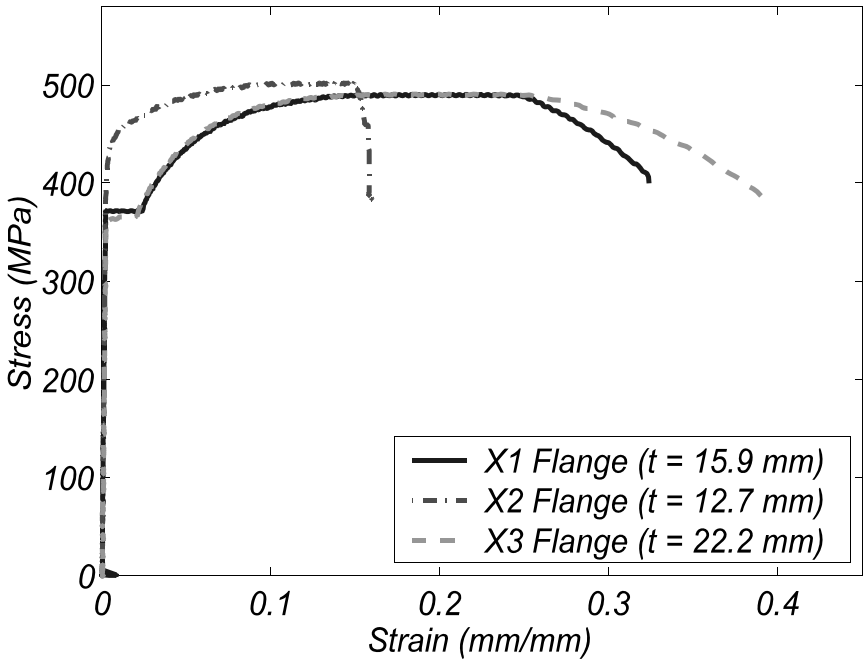

FIGURE 4-8 Tension Coupon Test Results for Flange Materials

TABLE 4-3 Material Test Results

Cross-Section ID	Element	F_y (MPa)	F_u (MPa)	Cyclic Strain (mm/mm)	Cycles to Failure
X1	Web	480	516	0.024 [a]	29 [a]
	Flange	371	489	0.013	101
X2	Web	475	496	0.022	17
	Flange	430	501	0.0215	90
X3	Web	430	501	0.0215	90
	Flange	365	490	0.020	43

[a] The cyclic coupon for the web material of X1 specimens was subjected to 6 cycles at a strain 0.0126 and one cycle at a strain of 0.019 rads prior to 22 additional cycles at a strain of 0.024.

Cyclic coupon test results are shown in figure 4-9, and cyclic strain values and number of cycles to failure at that strain level are given in table 4-3. These coupons complied with ASTM E 606-92 for strain controlled fatigue testing. Force was recorded with an internally mounted load cell in the MTS cyclic testing machine and the deformation was recorded with a 25 mm (1 in) gage length MTS extensometer with a deformation capacity of 6.4 mm (0.25 in). The target strain range for the cyclic material testing was ±0.02 mm/mm, as this is near the values expected during testing of the link specimens. This cyclic data will also be useful for input in ABAQUS for finite element models of the specimens presented in Section 6. The control for testing was the displacement of the loading head of the machine, therefore, deformation of the coupons outside the gage length and small slippage of the coupons in the grips caused some differences between the target and recorded strain range. However, the purpose of the cyclic tests was not to calibrate a low cycle fatigue curve for these materials as only one coupon was tested for each material (a minimum of three coupons at three different strain ranges is typically used for that purpose), but rather to determine the general shape of the cyclic stress-strain curve for input in ABAQUS (recall that no attempt to model fracture in ABAQUS was made as part this work). The difference between the target and recorded strain values in this context is of little importance.

The large difference in number of cycles to failure between coupons for the webs of X1 and X2 specimens as compared with the other coupons is due to small notches in those coupons resulting from machining. These two coupons were designed differently because of their small thickness and were considerably more sensitive to machining defects. Figure 4-10 schematically shows the difference between these coupons and the other coupons. Regardless of these issues, the data obtained from the cyclic coupon testing is adequate for its intended purpose of application in ABAQUS models.

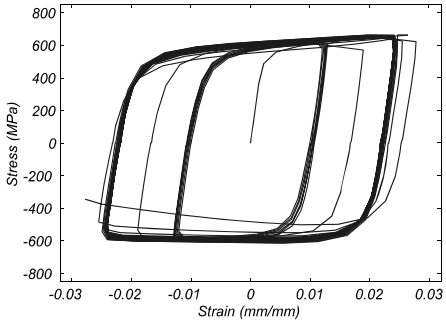

(a) X1 Web

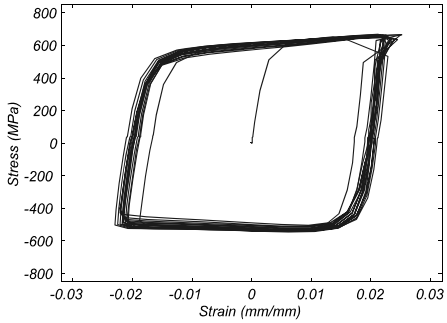

(b) X2 Web

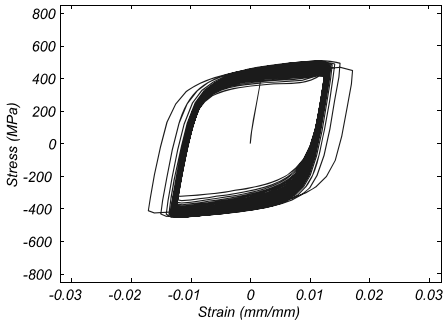

(c) X1 Flange

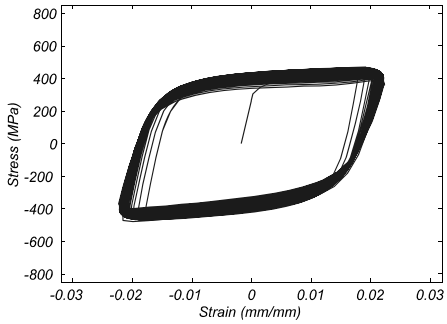

(d) X2 Flange and X3 Web

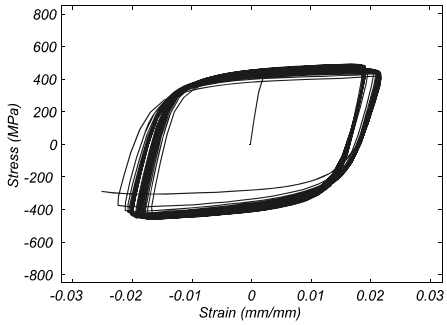

(e) X1 Web

FIGURE 4-9 Cyclic Stress-Strain Curves for Link Materials

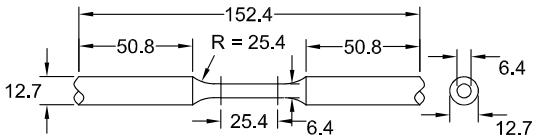

Notes:
Coupon is Cylindrical Over Entire Length.
Blend Radius Into Straight Section - Do Not Undercut.
19.1 mm Minimum 25.4 mm Maximum Dimension for Straight Section (Maximum is Shown).
Tol. on 6.4 mm Reduced Diameter = ± 0.2.
Tol. on 12.7 mm Dia. End Sections = +0.05, -0.000

Cyclic Coupon for X1 Flange, X2 Flange, and X3 Flange Materials

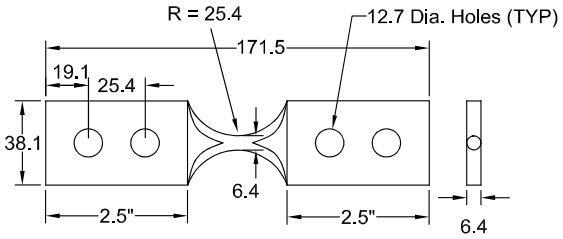

Notes:
Coupon is Cylindrical at Center.
Blend Radius Into Center Section - Do Not Undercut - There is No Straight Section on This Coupon.
Tol. on 6.4 mm Reduced Diameter = ± 0.2.
Tol. on 12.7 mm Dia. Holes: +1.3, -0.000.

Cyclic Coupon for X1 Web, and X2 Web Materials

FIGURE 4-10 Cyclic Coupon Schematics

As mention above, the cyclic coupons for the web materials of X1 and X2 were more sensitive machining defects and failed at a lower number cycles than the other cyclic coupons. However, the stress-strain relationship found for these coupons is unaffected by these machining defects, which only affect the fracture life of the coupons. Therefore, the stabilized half cycle data found from these coupon results and used for the material model in ABAQUS is still valid despite their reduced fracture life from machining defects.

4.2.5 Haunch Design

As shown in the elevation views of the specimens, each has a haunch at each end prior to the connection to the end-plate. The primary reason for the haunch is to replicate the end condition of the link in the proof-of-concept testing where the flanges are continuous through the end of the link and into the brace-to-link connection. That link had a gusset connection for the braces which was stiffened with a plate perpendicular to the flange, referred to as the

gusset stiffener, which was connected to the flange with a fillet weld. Fracture of the link flange occurred at the toe of this weld, in the heat affected zone, as described in Berman and Bruneau (2005a). The flange haunch, shown in cross-section at about mid height of the haunch in figure 4-11, has a similar weld to the link flange that is perpendicular to the longitudinal axis of the link and direction of primary stress in the flange.

A secondary benefit of this haunch is to prevent fracture of the weld connecting the link to the end-plate, which other researchers have reported in WF link testing, and to simulate the transverse weld across the flange that was used in the proof-of-concept test. By increasing the depth and inertia of the cross-section, the haunch reduces the stresses at the end-plate connection. A general schematic cross-section through the haunch is shown in and all haunch plates were specified to be A572 Gr. 50. The flanges of the haunch for each cross-section were designed such that the combined plastic moment capacity of the haunch and link flanges at the intersection with the end-plate was at least twice the maximum anticipated end moment using nominal yield stresses. The webs of the haunches were selected to be of the same thickness as the link webs for each cross-section. Since the link shear force is constant for the entire specimen length, including the haunches, the web haunches reduce the shear stress near the end-plate. In all cases the active link length is taken to be the distance between the haunches at each end. Note that this configuration, or a similar one, could be used in practice to provide for easily removable links. This would present a cost tradeoff between the ease of link replacement following a seismic event and up-front fabrication costs.

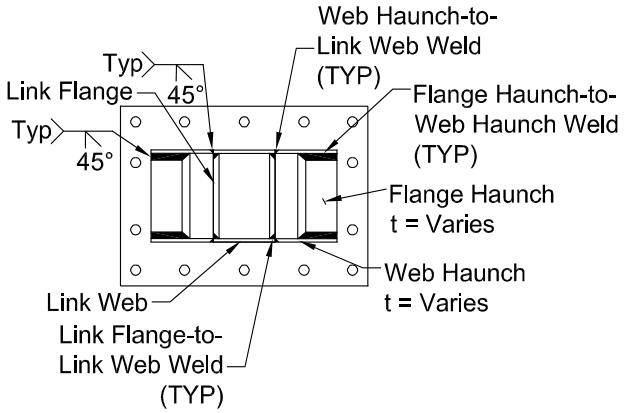

FIGURE 4-11 General Haunch Cross-Section

4.2.6 Link End-Plates

End-plate thicknesses for the links were selected to resist prying action forces determined from twice the actuator load necessary to obtain a link shear force of V_p or $2M_p/e$ for nominal link yield stresses. Two different end-plates were designed, the first type is used for X1 and X3 specimens, and the second type used for X2 specimens, both types were specified to be 31.8 mm (1.25") thick A572 Gr. 50 plate. The end-plate details are shown in figure 4-12 where end-plate 1 is for X1 specimens, end-plate 2 is for X2 specimens and end-plate 3 is for X3 specimens but is actually the same plate size and hole pattern as end-plate 1. Hole layouts and bolt sizes were selected such that the connection would be slip critical up to a load of at least 1.6 times the actuator load necessary to obtain a link shear force of V_p or $2M_p/e$ for nominal link yield stresses. For other limit states such as bearing at bolt holes, and bolt fracture the connection and end-plate was designed to provide a resistance of at least 2.5 that actuator load.

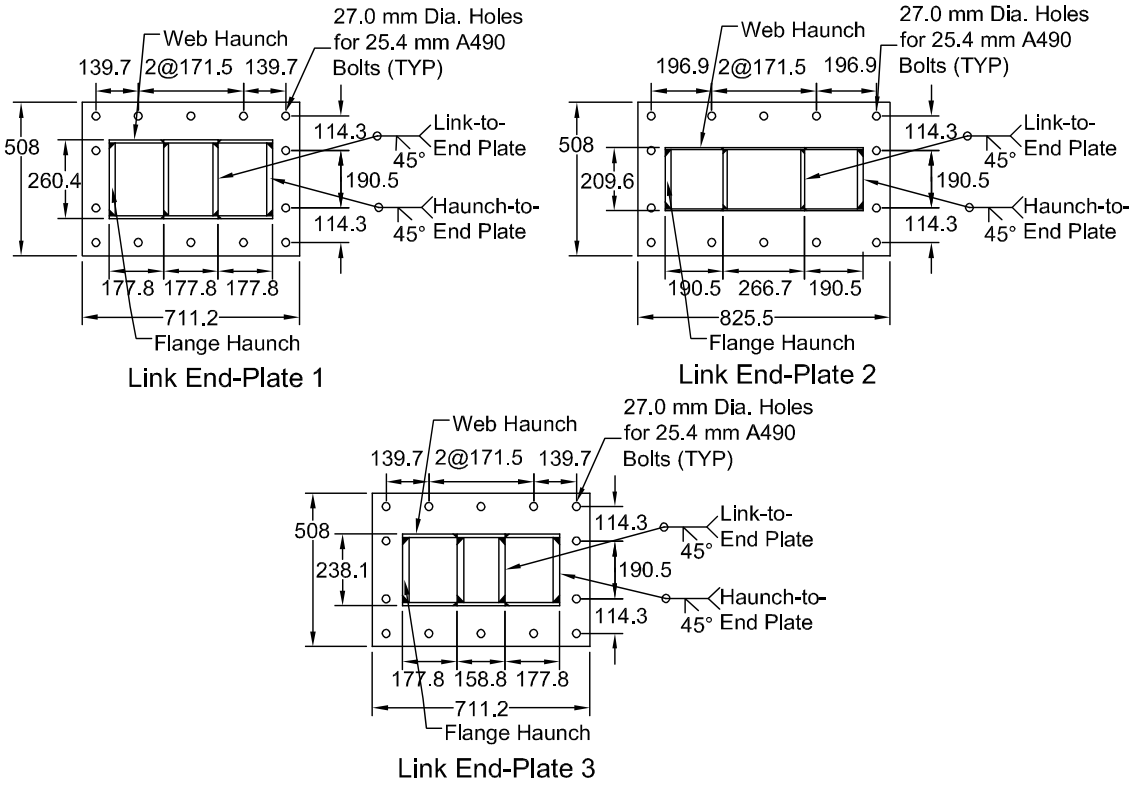

FIGURE 4-12 Link End-Plates

4.3 Test Setup Design

The setup shown in figure 4-1 was designed to be reconfigurable to accommodate three different overall specimen lengths (including the link, haunches and end-plates). The tallest setup is shown in that figure while the other two are shown in figures 4-13 and 4-14. All specimens with normalized link lengths of 1.2 and 1.6 have the same overall length of 1111.3 mm (43.75"), the specimens with normalized link lengths of 2.1 have overall lengths 1435.1 mm (56.5"), and the specimens with normalized link lengths of 3.0 have overall lengths of 1949.5 mm (76.75"). As the actuator extends or contracts load is transferred on the west end of the actuator to the loading beam (LB) through the LB actuator beam and LB actuator brace. The results is constant axial load and moment in the loading beam that is transferred as shear and end moment to the link and then to the foundation beam (FB) again as axial load and moment. Note that the actuator force coincides with the link midpoint, resulting in equal and opposite link end moments and zero moment at the link midpoint, assuming rigid loading and foundation beams. At the east end of the actuator, the load is transferred to the FB through the FB actuator beam and FB brace. The results is that the setup is a self-restrained reaction frame, meaning that the actuator force is resisted by axial load in the foundation beam, not by friction between the strong floor and foundation beam. Attachment to the strong floor was therefore designed only to resist uplift forces as described further below.

As mentioned above, for all three setup configurations the centerline of the actuator coincides with the link midpoint. Therefore, assuming rigid foundation and loading beams, the actuator load is equal to the link shear force and there is no load in the pantograph members (the pin-ended members at the west end of the test setup). As described below, the pantograph functions to prevent rotation of the loading beam while allowing the link to deform unrestrained in the axial and horizontal directions, preventing the introduction of axial load in the link when deformed in shear and flexure. Design loads for the pantograph members were found by considering the condition where the flanges at one end of the link suffer fracture, resulting in zero moment capacity at that end and flexure in the loading beam which is resisted by the pantograph members.

A Sap2000 model of the setup was developed and analyzed for loads corresponding to the maximum of 1112 kN (250 kip) or 2.0 times the anticipated link shear $2M_p/e$ for the flexural and intermediate links, found using the nominal yield stress of 345 MPa (50 ksi) for all link material. The 2.0 factor was applied to account for strain hardening and differences in nominal versus supplied yield stresses and is not considered a safety factor. For most components and connections the governing load case was X2 at a length of 2.1, where the maximum anticipated actuator load was 1112 kN (250 kip). Safety factors were assigned based on the failure modes being considered. Non-ductile modes of failure were generally given a larger factor of safety than ductile failure modes with the minimum value for all failure modes being 1.5. Therefore, the minimum design strengths for all setup components and connections was slightly less than 3.0 times those required considering the specified link material properties.

4.3.1 Foundation Beam (FB)

The foundation beam (FB) was designed as a beam-column for a compressive load of 1112 kN in combination with a 611 kN-m moment, both demands resulting from the configuration for specimen X2L2.1. A maximum foundation beam shear force demand of 676 kN was also considered. Safety factors of at least 2.0 were also incorporated, making the total strength almost 4 times what would be required to resist the nominal link shear forces. A W610x217 (W24x146) was selected for the FB and is shown schematically in figure 4-15. The FB was fastened to the floor in five locations along its length, with one 35 mm (1.375") dia. Gr. 150 diwidag bar on each side of the web at each location. The bars were checked for the maximum uplift forces of 778 kN (175 kip) obtained from analysis, and had a safety factor of approximately 2.5 with respect to bar yielding.

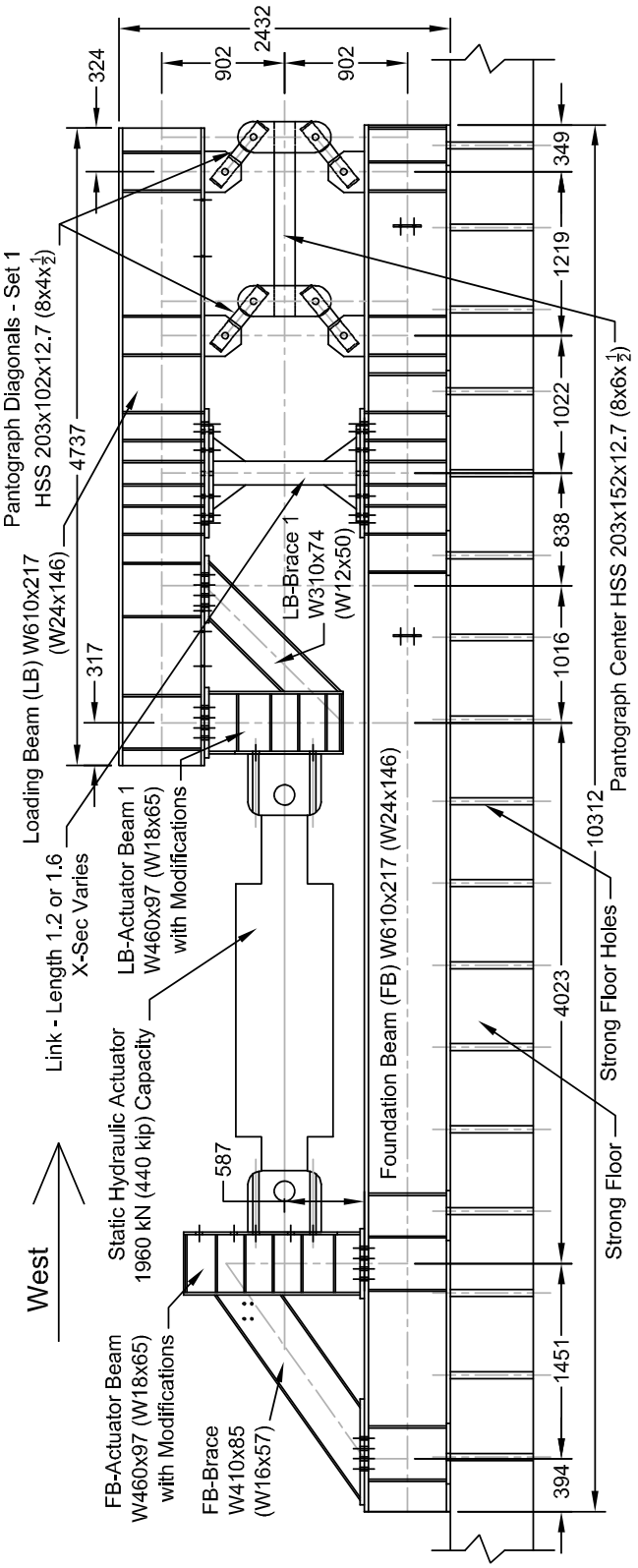

FIGURE 4-13 Test Setup for Specimens with a Normalized Link Length of 1.2 and 1.6

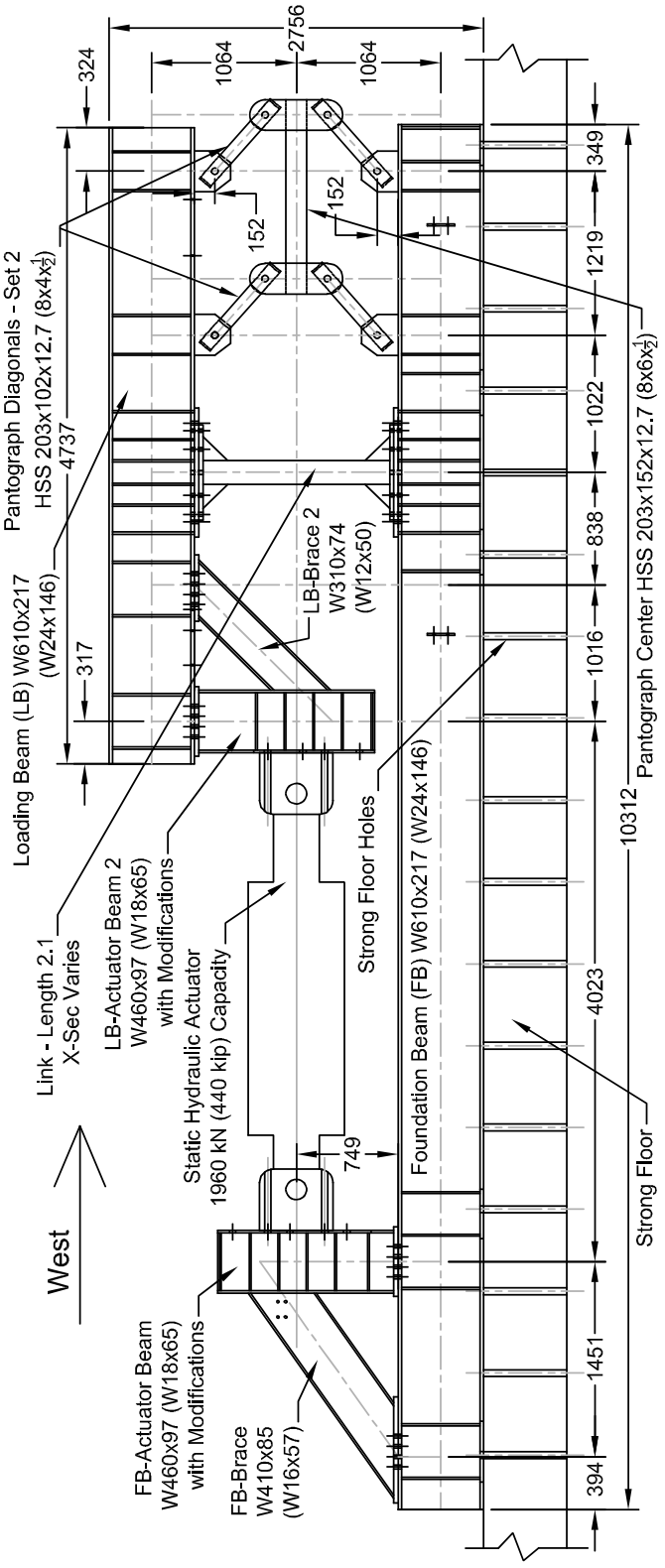

FIGURE 4-14 Test Setup for Specimens with a Normalized Link Length of 2.1

Holes in the strong floor of the SEESL are located in a grid at 609.6 mm (24") spacing in the north-south and east-west directions. Since the flange of the selected FB is less than the hole spacing, bottom flange extensions (also called foot plates) were necessary for attachment to the floor as shown in figure 4-15. As shown in figure 4-16, there were four different stiffener details necessary due to different geometries and functions, although all are dual sided stiffeners welded to both the flanges and the web. FB stiffener type A is a standard stiffener as shown in figure 4-16 and serves to limit prying action deformations and strengthen the web around connections. FB type B is used to limit prying action deformations at both the member connections to the top flange of the FB and the strong floor connections on the bottom flange. FB type C is used for the same purpose as type B except that is designed for the different geometry under the link mounting plate, as shown in figure 4-17. Finally, FB type D, also shown in figure 4-17, is used to limit prying action deformations of the link mounting plate and FB top flange at locations where there is no strong floor attachments.

The FB brace and FB actuator beam shown in figure 4-1 were designed for the same loading scenario as the FB. W450x97 (W18x65) and W410x85 (W16x57) were selected for the FB actuator beam and FB brace respectively. Their connection to the FB was designed to be slip-critical under loads resulting from 2.0 times the anticipated 1112 kN (250 kip) maximum link shear force and is shown in figure 4-18. Also shown is a cross-section of the stiffeners for the FB actuator beam, which serve to prevent prying action deformations at the actuator attachment points.

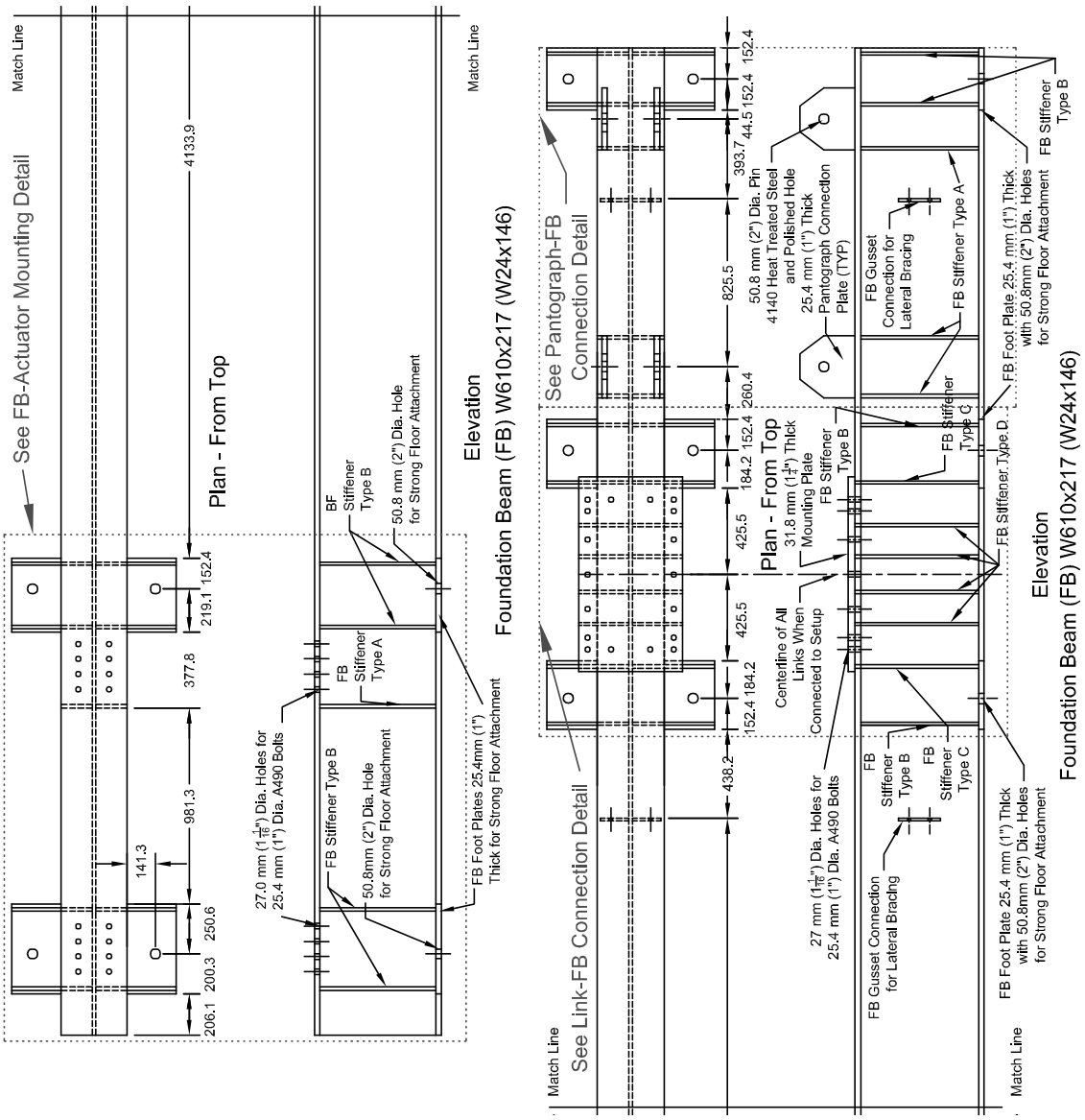

FIGURE 4-15 Foundation Beam (FB) Schematic

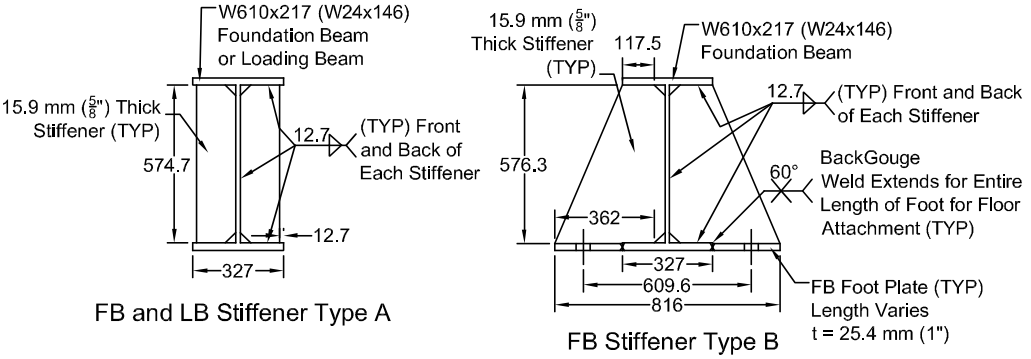

FIGURE 4-16 Foundation Beam Stiffeners A and B

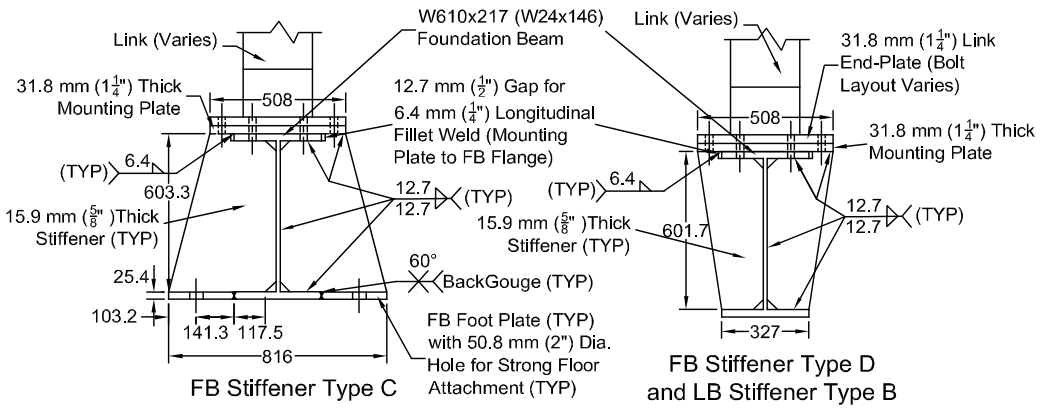

FIGURE 4-17 Foundation Beam Stiffeners C and D

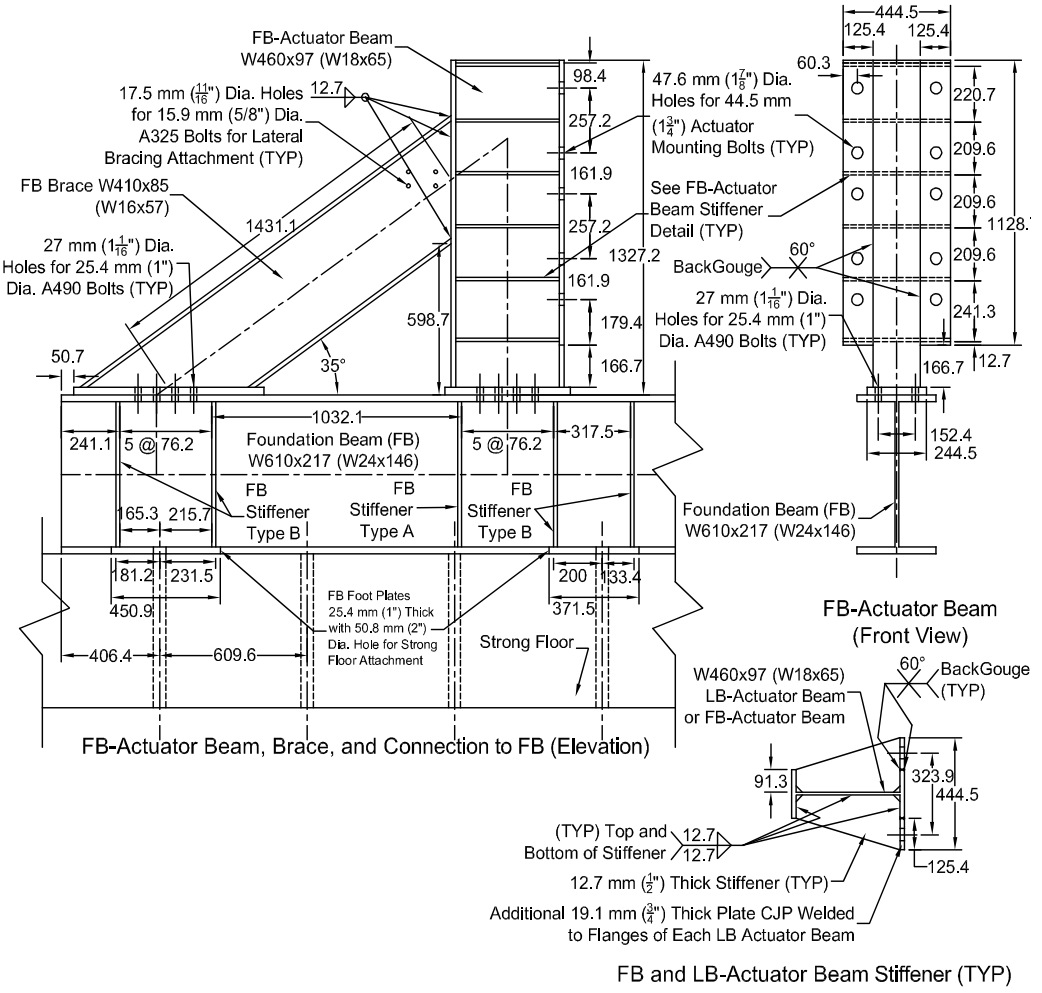

FIGURE 4-18 FB Actuator Beam and Brace and Connection to Foundation Beam

The link connection to the FB was designed to be slip critical for 1.6 times the demands from the model for Specimen X2L2.1 (actuator load of 1112 kN). The connection was also designed to resist 2.0 times those demands considering other limit states, such as bearing at bolt holes, prying action, and bolt rupture. The resulting connection involves a 31.75 mm (1.25") mounting plate fillet welded all around to the FB flange with holes to accept the bolts from the link end-plate. The mounting plate and connection to the FB flange is also reinforced by the presence of Type C and Type D FB stiffeners. Plan and elevation schematics of the link-to-FB connection are shown in figure 4-19.

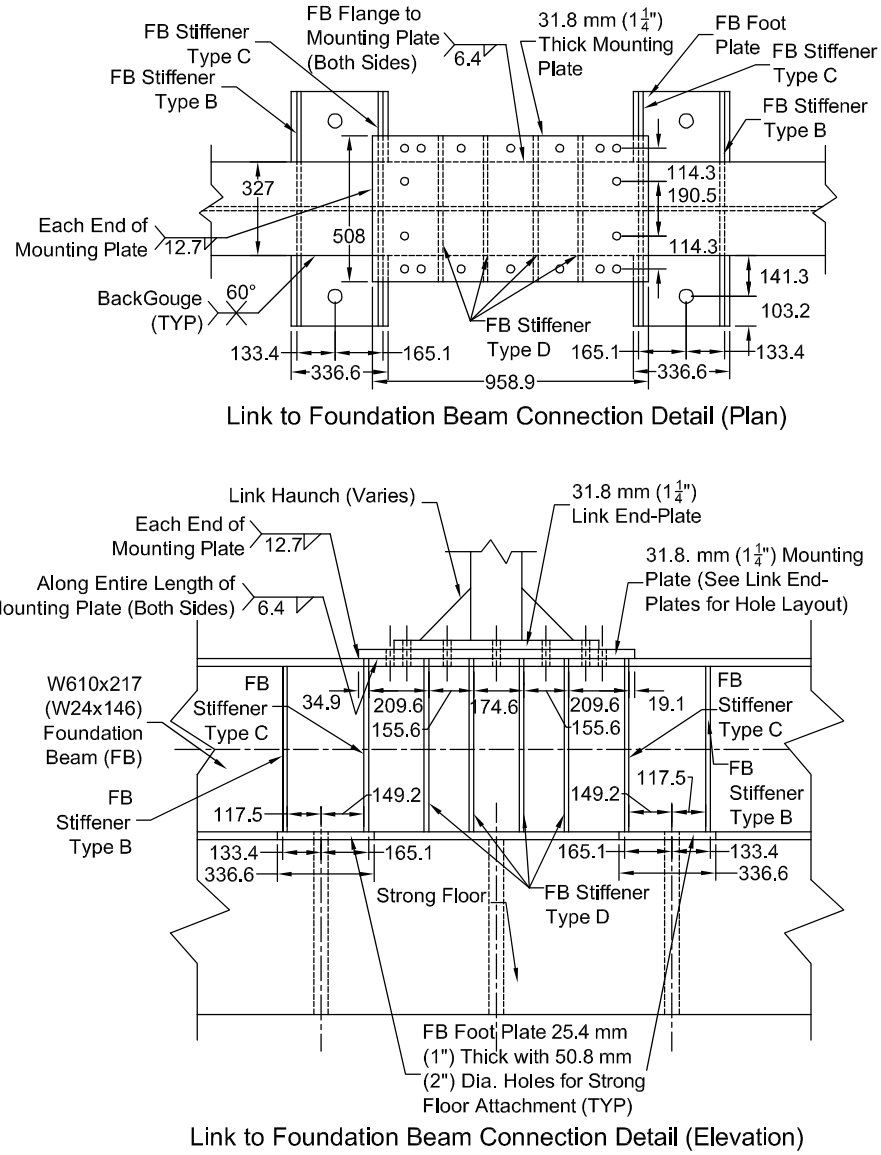

FIGURE 4-19 Foundation Beam-to-Link Connection

4.3.2 Loading Beam (LB)

The loading beam (LB) was also designed as a beam-column for the combined loading of 1110 kN (250 kip) of compression and a 1176 kN-m (867 kip-ft) moment, both occurring between the link and LB actuator brace. This loading combination also resulted from the setup configuration for Specimen X2L2.1. Considering the combined loading, the loading beam has a resulting factor of safety of approximately 1.5 on the above loads, and a capacity of 3.0 times the load considering the nominal link plastic shear force of 610 kN for X2. For convenience in fabrication, the same W610x217 (W24x146) section selected for the FB was also specified for the LB and is shown in figure 4-20. To resist prying action deformations, two different types of stiffeners were added to the LB at the connection regions, as shown in figures 4-12 and 4-13.

The LB actuator beam and LB brace shown in figures 4-1, 4-9, and 4-10 were designed for the same loading scenario as the LB itself, 2.0 times the actions from the setup model for Specimen X2L2.1 with a normalized length of 2.1. Two sets were necessary to accommodate the different heights of the specimens. Set one, for links with normalized lengths of 1.2 and 1.6, is shown in figure 4-21. Set two was designed with a taller LB actuator beam for links with normalized lengths of 2.1 and 3.0. In both cases a W460x97 (W18x65) was selected for the LB actuator beam and a W310x74 (W12x50) was selected for the LB brace. The connection of these members to the LB was designed to be slip critical for 2.0 times the loads resulting from the analysis for Specimen X2L2.1. The same detail and stiffener used for the FB actuator beam and shown in figure 4-14 was used to extend the flange width of the LB actuator beam for connection with the actuator.

The link-to-LB connection was designed in a similar manner as the link-to-FB connection and utilizes similar mounting plate and stiffener reinforcement configurations, as shown in figure 4-22.

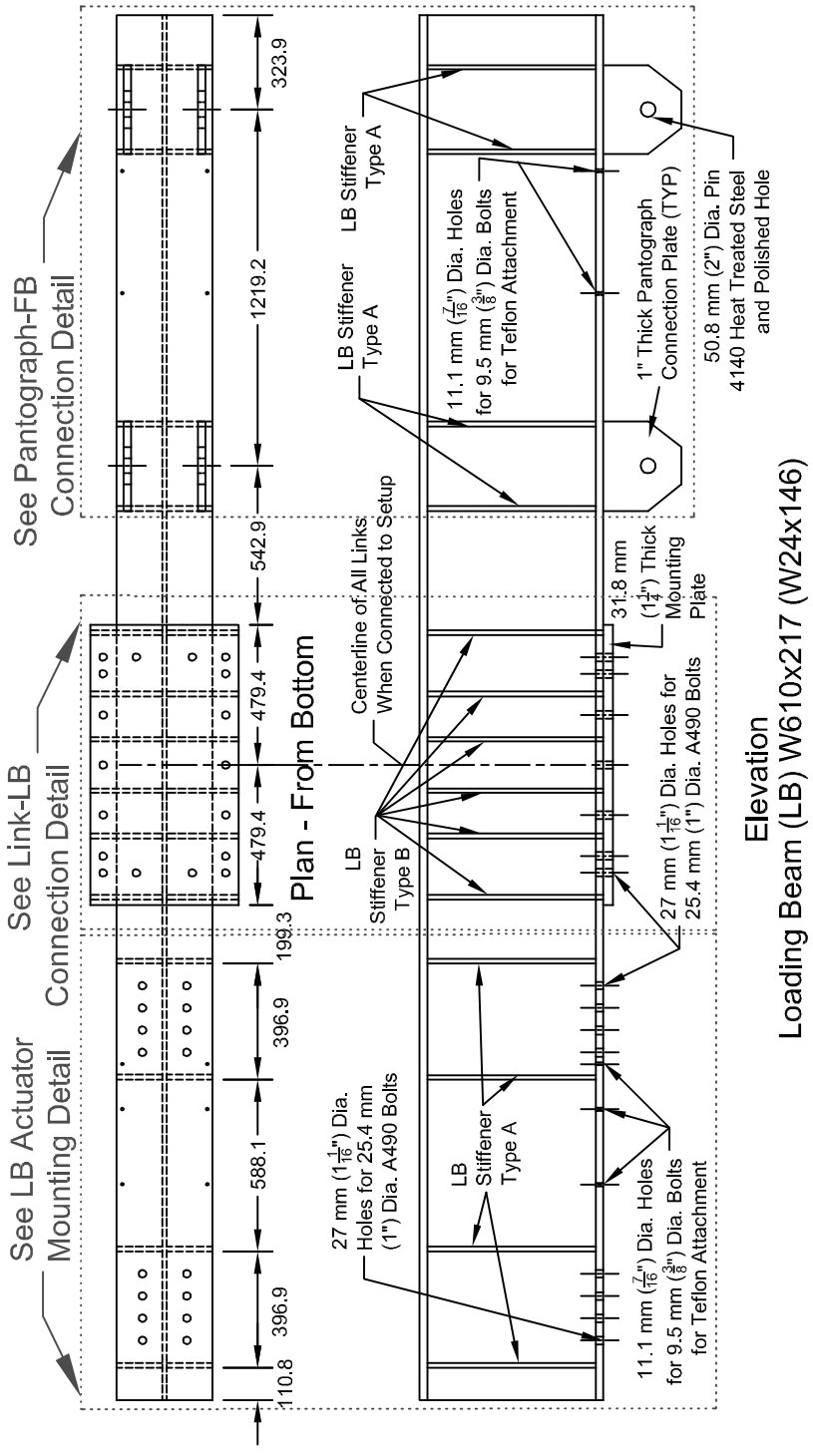

FIGURE 4-20 Loading Beam (LB) Schematic

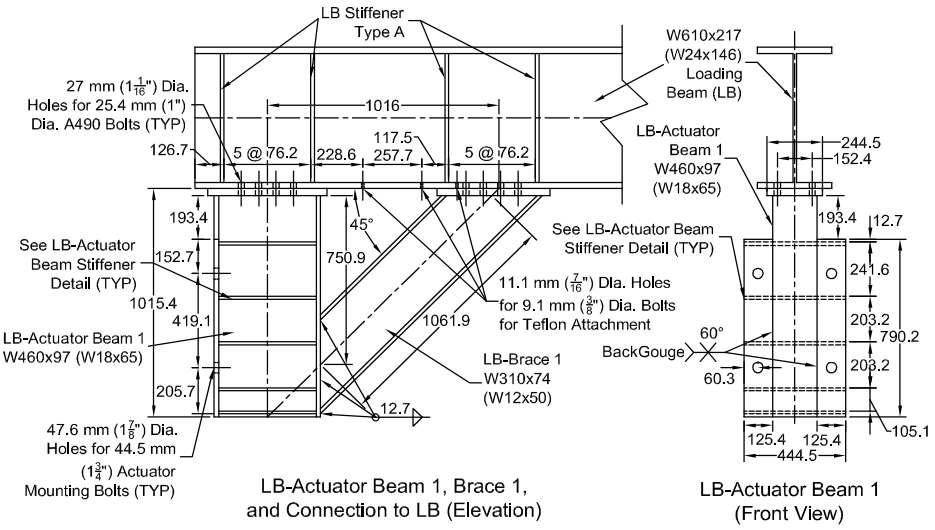

FIGURE 4-21 LB Actuator Beam and Brace and Connection to Loading Beam

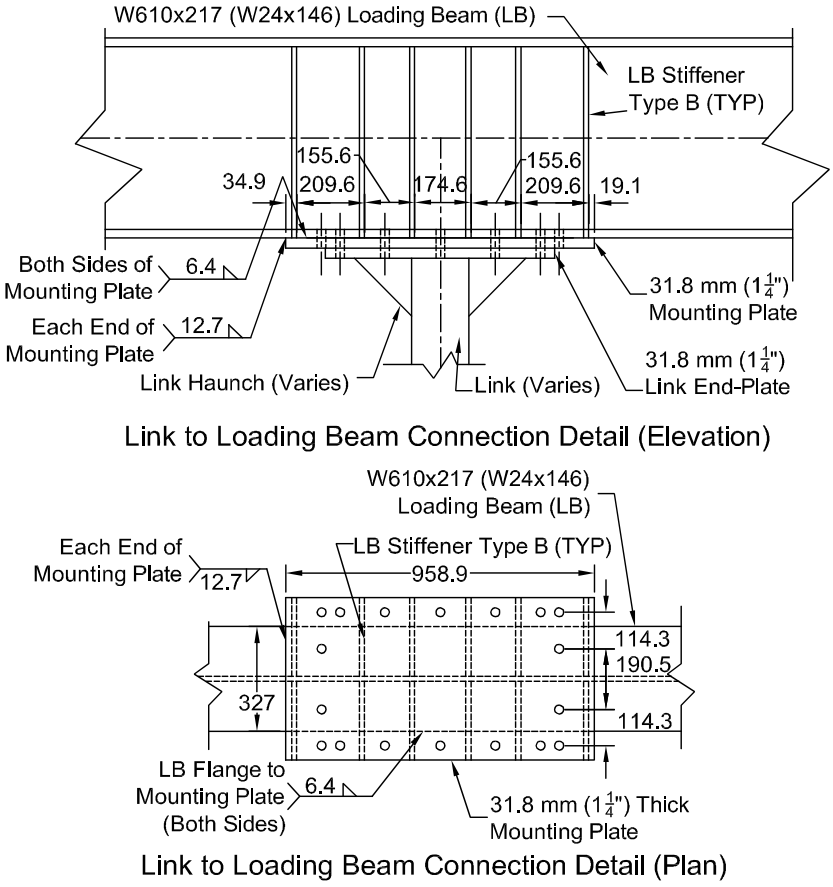

FIGURE 4-22 Loading Beam-to-Link Connection

4.3.3 Pantograph

The pantograph is configured using diagonal truss members oriented at a certain angle with the horizontal, that varies for the different link lengths, connected to a center member and the loading and foundation beams via large high strength pin connections. This configuration allows the loading beam to translate vertically and horizontally with no resistance but does not allow it to rotate, thereby preventing axial force in the link while also providing for approximately equal link end moments. The pantograph is similar to the one used in the test setup described in Nakashima et al. (1994).

The test setup is configured such that the actuator force, V_a, coincides with the midpoint of the links, for all link lengths, via the LB actuator beam and brace. Therefore, if the end moments of the link being tested are equal, there is no moment in the loading beam between the link and pantograph, and the pantograph members have zero axial force. However, if the link end moments are unequal, the axial force in the pantograph members can be related to the resulting moment at the link midpoint. Using figure 4-23, a free-body diagram of the loading beam and link (cut at the midpoint), the axial force in the diagonal pantograph members attached to the loading beam, P_{pt}, can be found in terms of the moment at the link midpoint, M_{CL}, as:

$$P_{pt} = \frac{M_{CL}}{L_{p2}\sin\alpha} \tag{4-1}$$

where α is the angle between the pantograph diagonal and horizontal. Unless some type of failure in moment capacity at one end of the link occurs, the link end moments are close to equal and opposite, the moment at the link centerline is near zero, and therefore, the axial forces in the pantograph members are zero. Therefore, to design the pantograph members for the worst case condition, it was assumed that the flexural strength at one end of the link drops to zero while the link is still able to carry a shear force equal to the minimum of 1112 kN (250 kip) or 2.0 times the maximum anticipated shear $2M_p/e$ (which is approximately 2.0 times the expected maximum link shear force considering the specified properties). The corresponding moment at the link centerline is then $V_u e/2$. Furthermore, from the free body diagram of figure 4-24, the axial force in the pantograph members attached to the foundation beam is:

$$P_{pb} = \frac{M_{CL}}{L_{p2} \sin\alpha} \tag{4-2}$$

and the axial force in the horizontal center member is:

$$P_{ph} = P_{pt} \cos\alpha + P_{pb} \cos\alpha \tag{4-3}$$

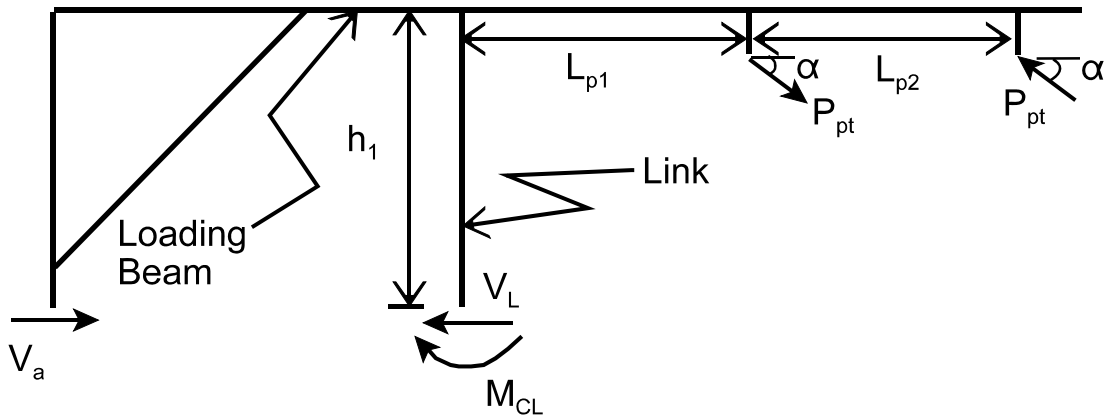

FIGURE 4-23 Free Body Diagram of Loading Beam and Link (Cut at Midpoint)

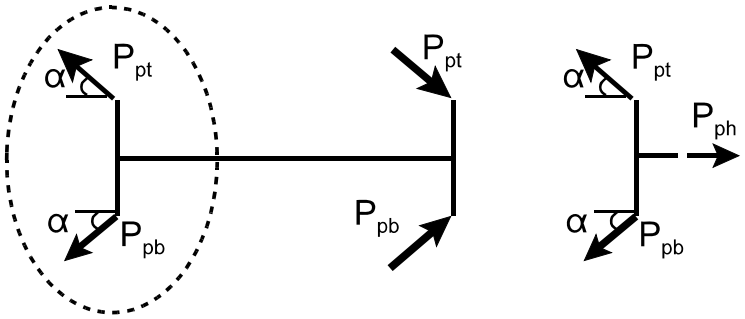

FIGURE 4-24 Pantograph Center Member Free Body Diagram

From (4-1), (4-2), and (4-3) it is clear that the deformation of the setup during testing, which may reduce or increase α, has an impact on the load carried by the pantograph members. If the relatively small vertical deflection of the loading beam is neglected (whish is a reasonable assumption given that they are relatively small), then the angle change for the top and bottom pantograph members is equal but opposite in sign, as shown in figure 4-25. Assuming the setup is rigid relative to the link, the angle change, δα, can be written in terms

of the displacement of the loading beam, Δ, the link length, *e*, and the link rotation angle, γ, as:

$$\delta\alpha = \sin^{-1}\left(\frac{\Delta}{2L_{pd}\sin\alpha}\right) = \sin^{-1}\left(\frac{\gamma e}{2L_{pd}\sin\alpha}\right) \tag{4-4}$$

where L_{pd} is the length of the diagonal pantograph members, from pin-to-pin. For the direction of motion shown in figure 4-25, δα is added to α for the upper pantograph diagonals and is subtracted from α for the lower members. This results in smaller upper member axial force, P_{pt}, larger lower member axial force, P_{pb}. The opposite is true for motion in the other direction.

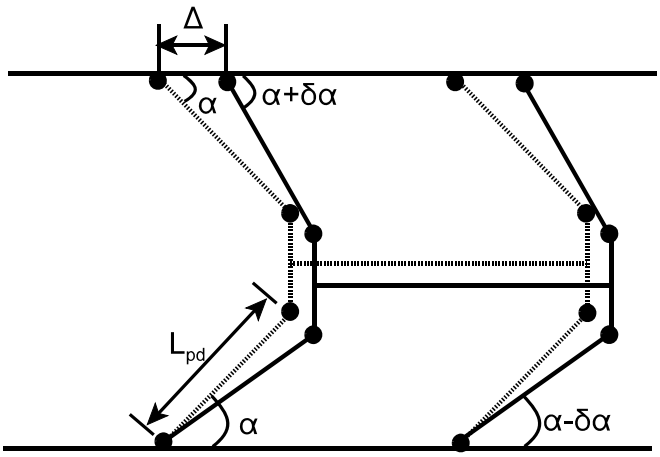

FIGURE 4-25 Pantograph Deformation Kinematics

Design loads for the pantograph members were calculated assuming loss of moment capacity of one end of the link as described above while accounting for deformation of the test setup. The angle change for pantograph members was found using the target rotations of the different link specimen. The controlling configuration was found to be for link X2L2.1 at a link rotation of 0.08 rads, link shear force of 1112 kN (250 kip), and complete loss of moment capacity at one end. The corresponding maximum axial force for the pantograph diagonals was 1059 kN (238 kip) and the maximum axial force for the pantograph center member was 1246 kN (280 kip). Factors of safety on these demands range from 1.4 to 3.0 for the various limit states considered in the design of the pantograph members and connections.

Pantograph diagonals and center member were selected to be HSS 203x102x12.7 (8x4x1/2) and HSS 203x152x12.7 (8x6x1/2) respectively. 50.8 mm (2") diameter 4140 heat-treated steel pins were specified for the pantograph connection and the pantograph diagonals were reinforced with a 12.7 mm (½") thick plate around the holes for every pin connection. 25.4 mm (1") plates and 22.2 mm (7/8") fillet welds were specified to connect the pantograph member to the loading and foundation beams. Details for the pantograph system are shown in figures 4-26 and 4-27.

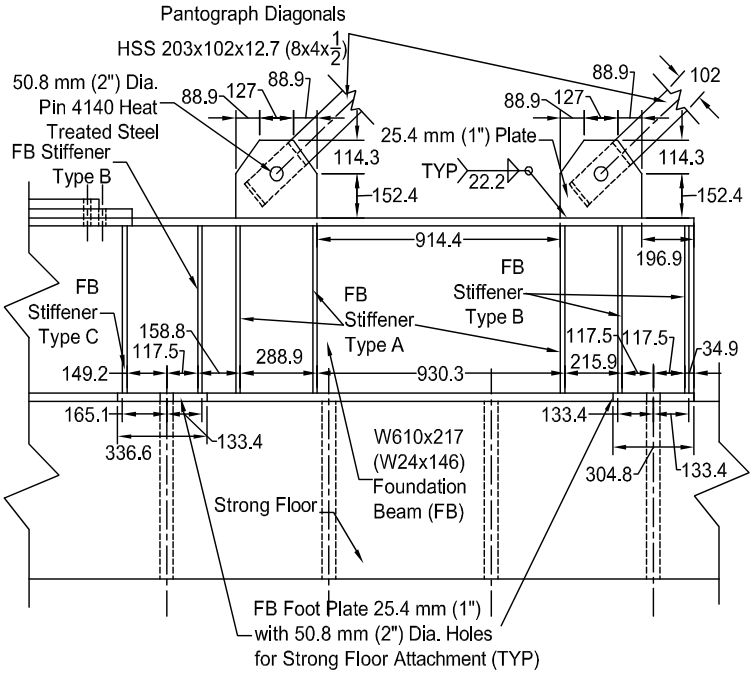

Pantograph-to-FB Connection Detail (Elevation)

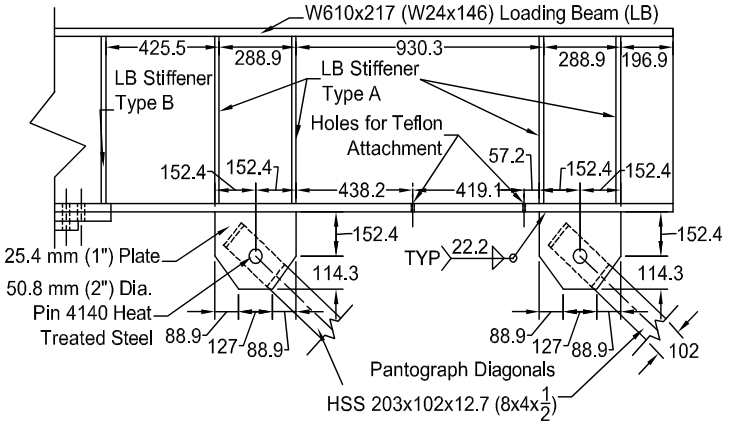

Pantograph-to-LB Connection Detail (Elevation)

FIGURE 4-26 Pantograph Connections to Foundation and Loading Beams

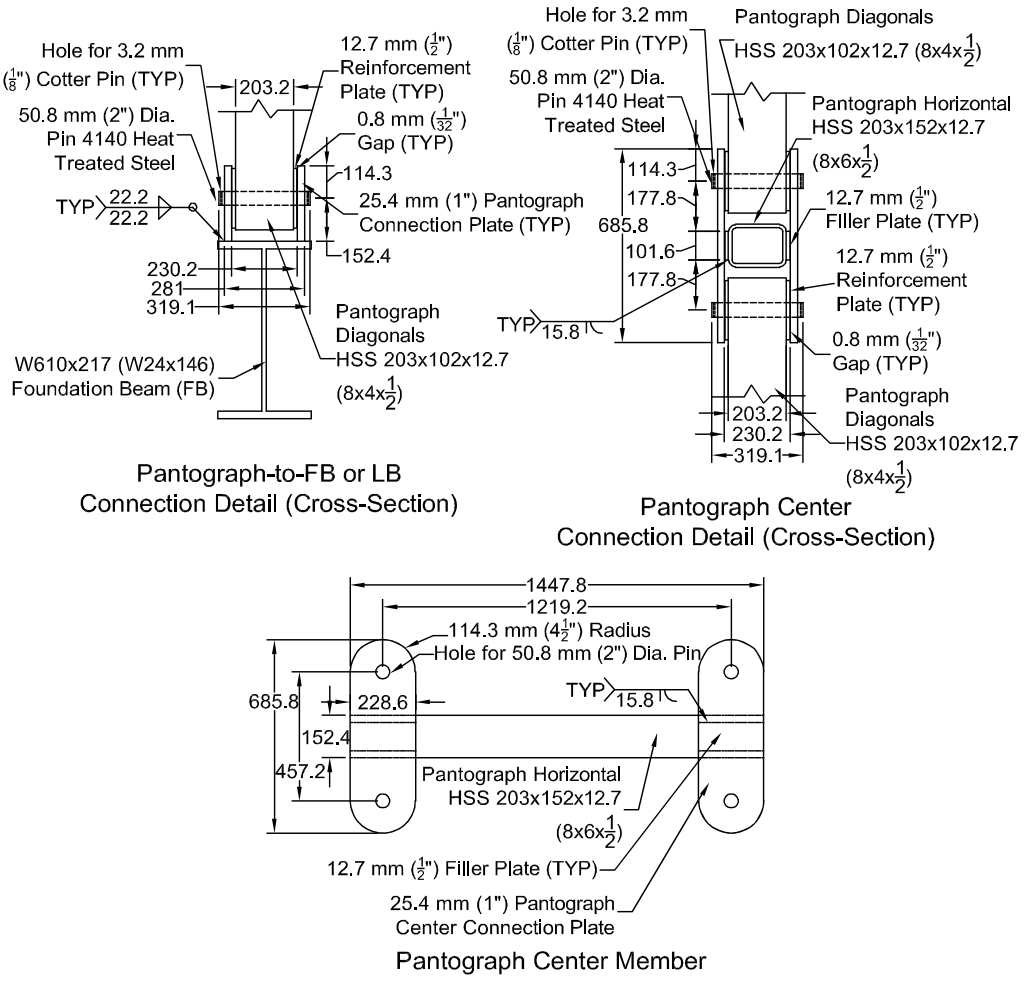

FIGURE 4-27 Pantograph Connection Details and Center Member

4.3.4 Lateral Bracing

Lateral bracing is provided to the test setup at three locations to prevent out-of-plane displacement of the actuator and loading beam, and lateral torsional buckling of the loading beam. No direct lateral bracing is provided to the links; only the out-plane stiffness of the setup restrains the link against out-of-plane deformations.

Lateral bracing attached to the FB brace, as shown in figure 4-28, was designed to meet the LRFD requirements for nodal bracing of columns (AISC, 2001), which provide a minimum required stiffness and strength, except that the required strength was increased from 1% of P_u to 5% of P_u, where P_u was taken as the maximum actuator for of 1112 kN (250 kip). Factors of safety were then based on 5% of P_u and varied from 2.0 to 5.5 for the various

components and connections shown in figure 4-28. As shown, the lateral bracing at that location consists of two HSS 50.8x50.8x6.4 (2x2x1/4) sections connected to the FB brace by bolts and then welded to channels that are fastened to the strong floor using a single 35 mm (1.375") diwidag bar at each location.

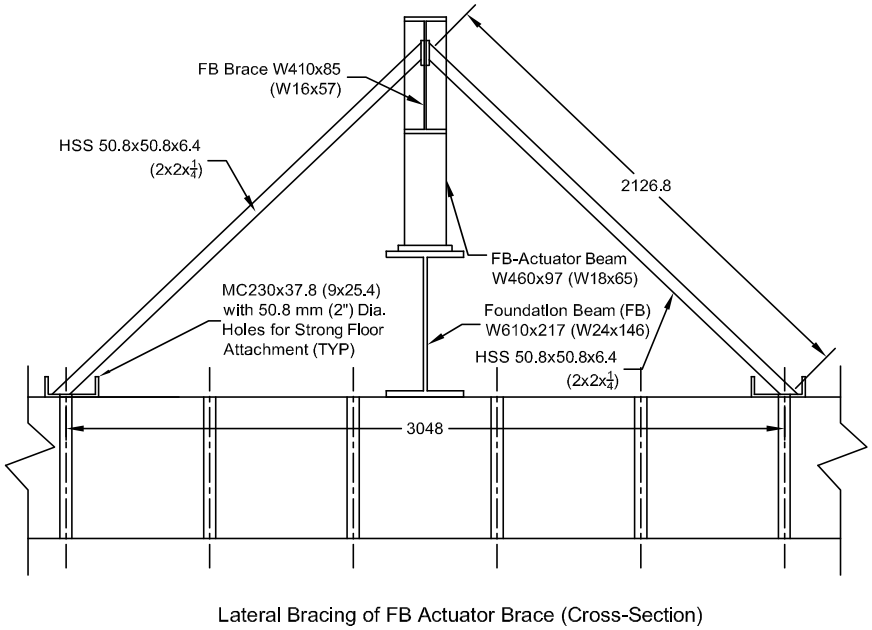

Lateral Bracing of FB Actuator Brace (Cross-Section)

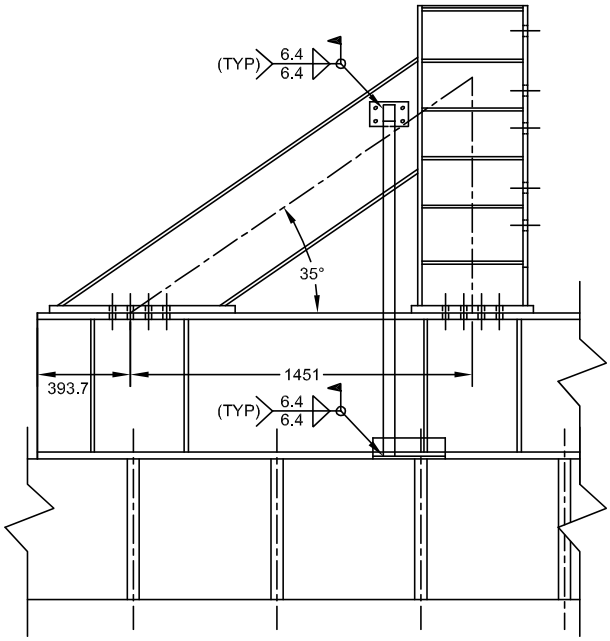

Lateral Bracing of FB Actuator Brace (Elevation)

FIGURE 4-28 Lateral Bracing of FB Brace

Lateral bracing for the loading beam utilized vertical W250x32.7 (W10x22) shapes to "sandwich" the beam at two locations as shown in figure 4-29 and 4-30. The vertical members are bolted to the foundation beam via gusset plates and were designed to bear against the loading beam. Teflon pads are provided on the vertical members to insure that the loading beam can move in plane with minimal friction resistance. Vertical members are then connected to each other using threaded rods which can be tightened to insure proper contact between the vertical members and the loading beam. At each of the two loading beam lateral bracing connections, one of the vertical members is then braced to the floor using a HSS 76.2x76.2x6.4 (3x3x1/4) connected to a channel which is fastened to the strong floor. The lateral bracing for the loading beam was designed to satisfy the AISC LRFD requirements for both nodal column bracing and lateral torsional bracing since the loading beam is subjected to both axial load and flexure. The design axial load and moment in the loading beam for use in calculating the design strength of the lateral bracing were 1112 kN (250 kip) and 1820 kN-m (10409 kip-in). Safety factors on the required stiffness of the lateral bracing for the loading beam ranged from 2.9 to 5.0, and from 4.3 to 11.0 for strength considering the various setup configurations.

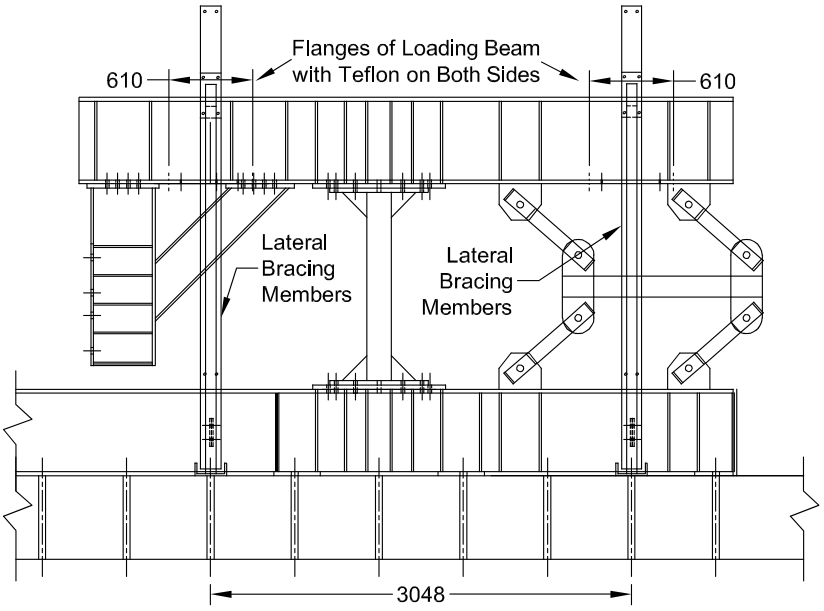

FIGURE 4-29 Elevation of Loading Beam Lateral Bracing

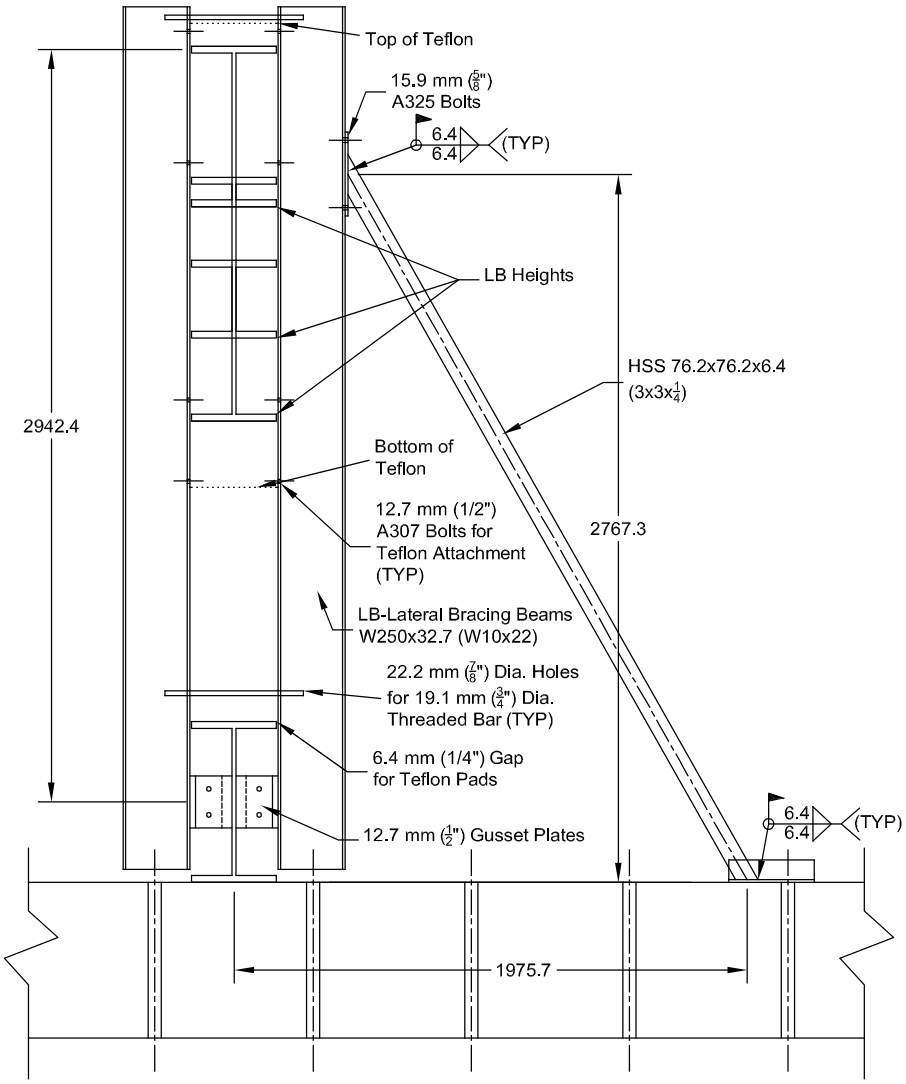

FIGURE 4-30 Cross-Section of Setup at Loading Beam Lateral Bracing

4.4 Instrumentation

Instrumentation for the link testing was designed such that key response parameters could be obtained from redundant data sources. The link rotation is the most important quantity and can be calculated from both the Krypton Dynamic Measurement Machine (Metris, 2005) and string displacement potentiometers. The layout of these instruments, as well as strain gages for the link specimens and video recording locations, are described below.

4.4.1 Strain Gages

Strain gage layouts for the various links were designed to indicate the yielding sequence during testing and possibly provide useful information for future low cycle fatigue calculations. All gages were high elongation EP-08-250-GB-120 gages from Vishay Micro-Measurements, Inc. The layout differs for shear and flexural links as shown in figures 4-31 and 4-32.

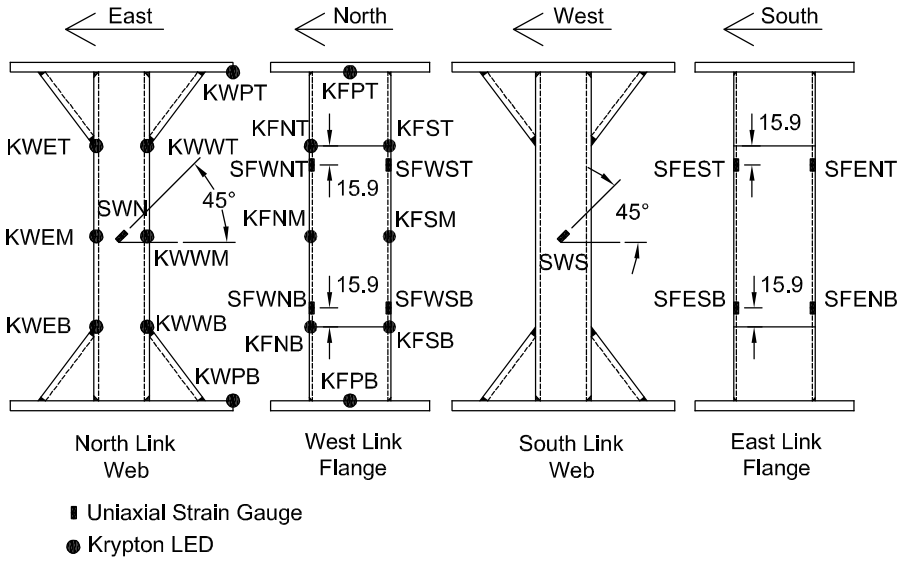

FIGURE 4-31 Instrumentation for Shear Links

Shear links have a single gage orientated at 45° in the middle of each web in order to give an estimate of the initiation and level of yielding in the webs in the anticipated direction of maximum principal strain. Shear links also have two gages in the longitudinal link direction at 25.4 mm (1") from each end (i.e. before the beginning of the haunches) and near the edges of each flange. These gages record strains that may be useful in calibrating the parameters of a low-cycle fatigue model for the failure mode of flange fracture similar to that observed in the proof-of-concept testing.

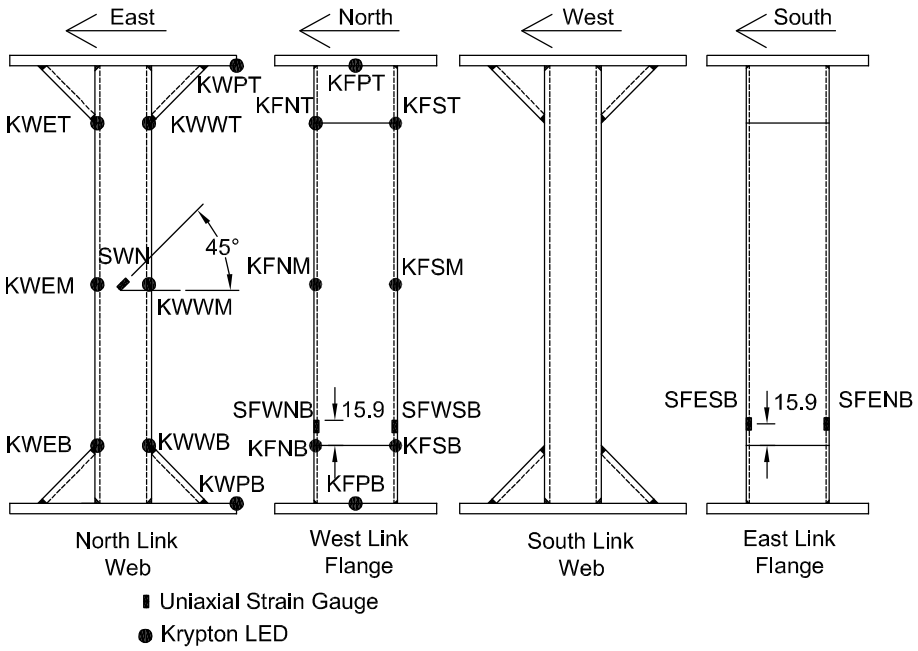

FIGURE 4-32 Instrumentation for Intermediate and Flexural Links

The strain gage layout for the intermediate and flexural links is similar to that used for the shear links except that it has gages on only one web and only on opposite sides of one of the link ends for the flanges. A simpler layout was used for practical reasons as these links were expected to suffer significant strength degradation due to flange buckling. Recorded strains may still be used in a low-cycle fatigue model if flange fracture does develop and flange buckling is not the controlling limit state.

4.4.2 String Displacement Potentiometers

Four string displacement potentiometers (string-pots) were used for each test and are shown in figure 4-33. The string pots were mounted on a vertical post (not shown) which was fastened to the strong floor. They were then connected to the specimen at the locations shown in the figure. Using the string-pot measurements the link rotation may be found from:

$$\gamma = \frac{\Delta_{p3} - \Delta_{p2}}{e} \tag{4-5}$$

where Δ_{p3} and Δ_{p2} are the displacements recorded by string pots P2 and P3 respectively.

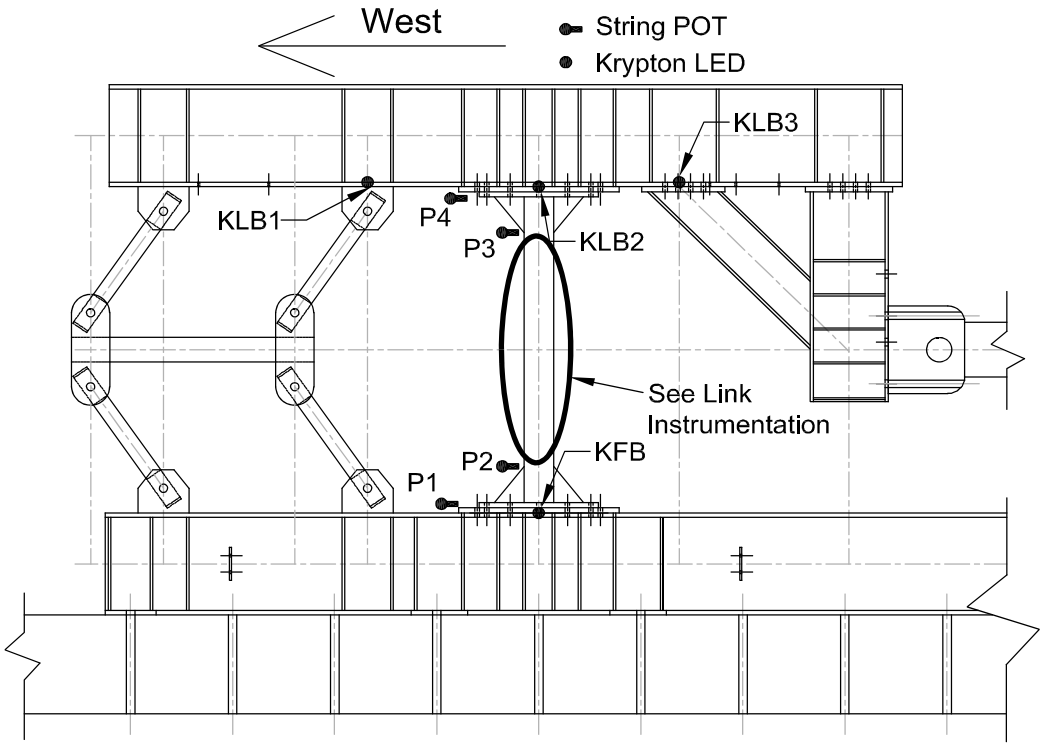

FIGURE 4-33 Instrumentation Outside the Links

4.4.3 Krypton Dynamic Measurement Machine

The Krypton Dynamic Measurement Machine is composed of three sensitive infrared cameras mounted on a moveable frame, numerous light-emitting diodes (LEDs), and an independent data acquisition system. LEDs are approximately 13 mm (½") in diameter and can be attached to the specimen or test setup at any location visible to the cameras via hot glue, magnets, or other approaches. The three cameras then triangulate the location, velocity, and acceleration of the LEDs relative to a user defined coordinate system. Accuracy of the Krypton is on the order of 0.1 mm (0.004") and can be as high as 0.05 mm (0.002"), depending on the distance from the camera to the LED's. Placement of the LED's is limited by the viewable window for the cameras, which increases as the distance between the LED's and cameras increases.

LED's were placed on the specimens and setup as shown in figures 4-27, 4-28, and 4-29. Numerous LED's were placed on the specimen for redundancy as attachment failure may occur under large strain conditions at the LED locations. Furthermore, the LED layout on

the specimen allows monitoring of possible twisting of the specimens during testing. Using the LED's at the top and bottom of the link at two locations on the north web and one location on the west flange, the link rotation can determined with triple redundancy from the Krypton system and a fourth redundant measure from the string-pots.

4.4.4 Video Recording

Digital videos of each test were recorded. Every test had at least one high definition digital video camera setup to view the specimen from the north. Additionally, several tests had a standard digital video recorder setup to view the specimen from an angle of approximately twenty degrees north of west. The first camera captures overall specimen deformation while the second captures flange buckling. Videos are available via http://nees.buffalo.edu.

4.5 Supplementary Link Specimens

After testing the twelve links described in this section, two supplementary link specimens were designed with an alternative connection to the link end-plates. As described in Sections 5 and 6, the constraint of plastic flow in the link flange at the intersection with the flange haunch plate and web haunch plate introduced high tri-axial stresses in the web-to-flange welds of the links. The tri-axial stresses in the web-to-flange welds in the haunch connection scenario were likely larger than those in the proof-of-concept test because of the presence of the web haunch plates in addition to the flange haunch plates. In the proof-of-concept test, the gusset for the link-to-brace connection was located in the middle of link flange, away from the web-to-flange weld of the link. However, in the link specimens described in this section, the web haunch plates are located at the outer edges of the flanges, directly over the web-to-flange weld of the links. This additional constraint likely caused flange fracture to occur earlier in the loading history than what would have been the case if the web haunch plates were not located directly over the web-to-flange weld. Furthermore, the flange haunch plates used here were thicker and oriented at a shallower angle with respect to the link's longitudinal direction than the gusset stiffener of the link-to-brace connection in the proof-of-concept test. These factors could have resulted in Specimens X1L1.6, X2L1.6, and X3L1.6, suffering flange fracture prior to achieving their target rotation as described in Sections 5 and 6. Additionally, the failure mode of all specimens

was flange fracture, and inspection of the fracture surfaces indicated that fracture likely initiated in the web-to-flange weld adjacent to the flange and web haunch intersection. This observation contradicts the observation made regarding the fracture of the proof-of-concept test, which indicated fracture initiated in the flange itself and not in the weld.

With these differences and results in mind, two supplementary links were designed. The links used cross-sections and lengths identical to Specimens X1L1.6 and X2L1.6 with the alternative end-plate connections shown in figure 4-34. The connections were designed to be similar to the link-to-brace connections used in the proof-of-concept test in that they have a single stiffened gusset at each link end that connects to the flange at the mid-width of the flange, away from the web-to-flange welds. Furthermore, the connection is not symmetric, in that the gusset is only located on one flange face, and the gusset stiffener is connected to the flange using fillet welds instead of full-penetration groove welds. Finally, the gusset stiffener is configured perpendicular to the longitudinal axis of the link, rather than at an angle as was the case for the previous link specimens described in this section. Results for these supplementary links, AX1L1.6, and AX2L1.6, will be reported with results for the other links in the following sections.

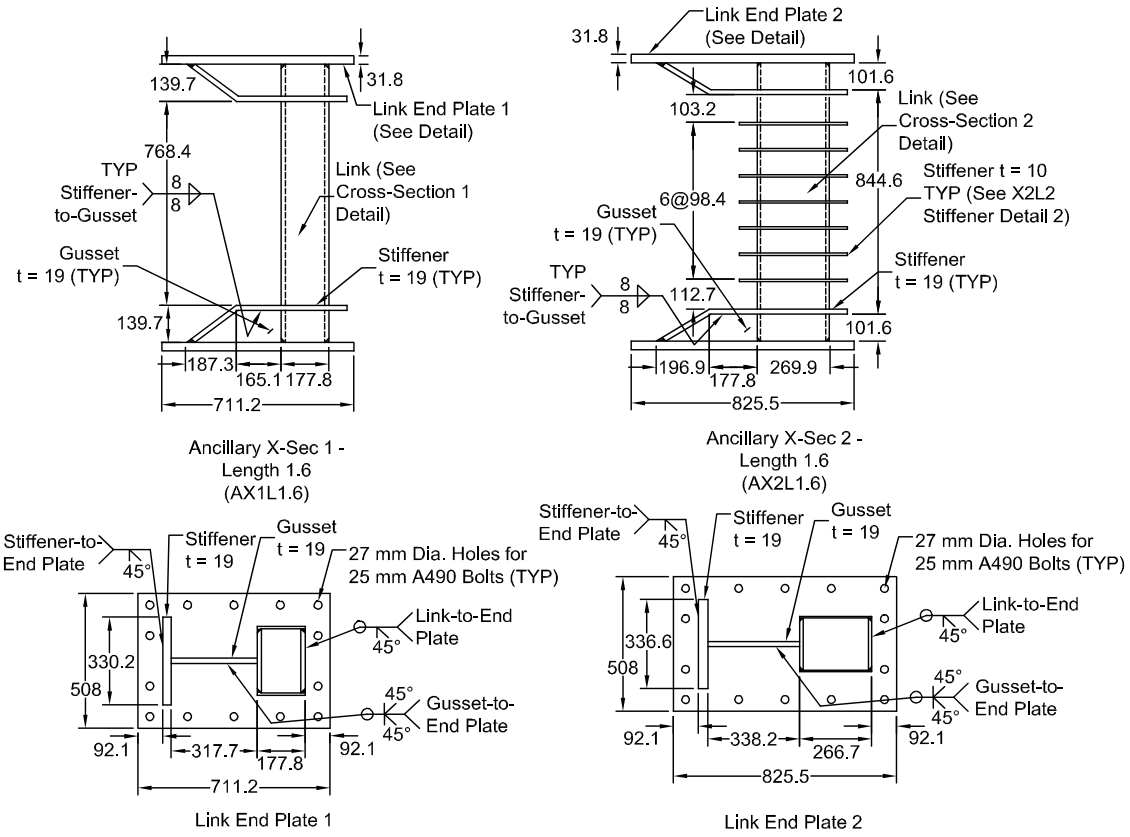

FIGURE 4-34 Supplementary Links and Details

SECTION 5
LINK TESTING OBSERVATIONS

5.1 General

This section describes the loading protocol used and observations made during the quasi-static testing of the twelve hybrid rectangular link specimens described in Section 4. The target loading protocol is described first. Then for each link the recorded values of peak rotation are tabulated. Finally, specimen link shear versus total rotation hysteresis curves are plotted (note that these differ slightly from the target rotations considered for the loading protocol due to flexibility in the test setup). Photographs and a brief description of observations made during the cyclic history are also provided for each link, along with a description of the failure modes. Throughout this section, positive link rotation refers to loading to the west, negative rotation indicates loading to the east (see figure 4-1), and all are rotations referred to are total rotations, i.e., combined elastic and plastic rotations.

5.2 Loading Protocol

The loading protocol used for testing the thirteen of the fourteen hybrid rectangular link specimens is the one specified by the 2002 AISC Seismic Provisions. It is the same protocol, based on total link rotation, that was used for the links in the finite element parametric study described in Section 3. This loading protocol specifies three cycles at each of the total link rotation levels of 0.0025, 0.005, and 0.01 radians, followed by two cycles at each 0.01 radian increment, up to the maximum code specified rotation. However, for this testing program the loading was continued with two cycles at each 0.01 rad increment until failure. Displacement of the actuator was used as the control parameter during testing, which required that the specified rotation levels be converted into displacements using the link and setup geometries. For this purpose the haunch ends and setup were considered to

be rigid and the actuator displacement was taken as the rotation times the link length. As described below, the flexibility of the setup caused the measured rotations to be less than the specified rotations in the protocol for all cases. Therefore, for some specimens the protocol was modified slightly during testing to keep the measured rotations as near the desired rotations as practicable. Target total rotations are given in the seismic provisions based on link length. For links with a normalized length of 1.2 or 1.6, 2.1, and 3.0 the target is to achieve one complete cycle at 0.08 rads, 0.05 rads, and 0.03 rads of total rotation respectively.

The ancillary link with cross-section 2, AX2L1.6, was tested using the loading protocol specified in the recent 2005 AISC Seismic Provisions (AISC, 2005). This protocol was derived on the basis of tabulated cumulative plastic rotation and cumulative energy dissipation demand from various eccentrically braced frames subjected to many ground motions. The protocol requires more cycles at lower rotation levels and fewer cycles at larger rotations relative to the protocol of the 2002 Seismic Provisions. Specifically it requires 6 cycles at 0.00375 rads, 0.005 rads, 0.0075 rads, and 0.01 rads, 4 cycles at 0.015 rads, and 0.02 rads, 2 cycles at 0.03 rads, one cycle at 0.04 rads and 0.05 rads, and then a single cycle at 0.02 rad increments from there. Similar assumptions to those described above were made for the calculation of actuator displacement for this protocol. The protocol was switched because, as described in section below, the links at the transition length did not reach their target rotation. However, they may have reached their target had this new protocol been used, therefore, one link is tested with the 2005 protocol to observe the effects of loading protocol on link rotation capacity.

5.3 Experimental Observations

Below is a description of the performance of each of the twelve links tested. Accompanying these descriptions are the link shear force versus total rotation hysteresis curves, where the rotation is calculated from data measured by the Krypton LED's, along with photographs of the deformed specimens and failure modes. In the observations below, the term sequence refers to all the cycles at a given rotation level and loading for each cycle begins with a positive rotation excursion.

5.3.1 Specimen X1L1.2

The link shear force versus rotation hysteresis for Specimen X1L1.2 is shown in figure 5-1. Table 5-1 gives the recorded peak rotations and link shear forces for each load sequence. As shown, this link, which had web and flange compactness ratios near the proposed limits for unstiffened cross-sections, sustained two cycles of rotation at 0.103 rads prior to failure during the second cycle at 0.11 rads. The target rotation for this link was 0.08 rads. Strain gage readings indicate that the specimen remained mostly elastic through the first three sequences of loading. During Sequence 3 some slight yielding at the outer fibers of the flanges was recorded by the strain gages. During Sequence 5 the strain gage data indicated that the webs were yielding and by Sequence 6 peak shear strains on the order of 3 times the shear yield strain of 0.00259 were recorded on the web. Also during Sequence 5 the flange strain gages indicated strains on the order 1.5 times the yield strain of 0.00172 and twice those values by Sequence 6. Flange yielding at the rotation level of 0.19 rads during Sequence 6 was also observed by flaking of the whitewash as shown in figure 5-2. The severity of yielding increased throughout the subsequent sequences. During Sequence 11 some small magnitude flange buckling was observed, however, no drop in link shear force was associated with this buckling.

During the cycles in Sequence 14, a small crack was noticed in the upper east flange of the specimen as shown in figure 5-3a. However, no significant loss of strength was observed at that point. During the second half of the first cycle of Sequence 15, the previously mentioned crack propagated quickly across the flange causing a rapid strength loss. This was closely followed by fracture of the lower west flange. Upon load reversal, during the second cycle of Sequence 15, the other two remaining flanges fractured in a similar manner. An example of the fractured flange is shown in figure 5-3b. The fracture in the upper east flange appears to have initiated in the weld used to connect the flange to the adjacent web at the toe of the weld that connects the flange haunch plate to the flange. In this area, plastic flow in the flange in severely restrained creating large triaxial stresses similar to the flange in pre-northridge moment resisting connections (Bruneau et al. 1998). This is also similar to what was observed in the proof-of-concept test, except that the restraint against plastic flow is likely larger here. The causes for larger restraint in this case are the presence of the

web haunch plate and corresponding weld, thicker flange haunch plate (19 mm thickness) relative to the gusset stiffener in the proof-of-concept test (12.7 mm thickness). This increase in restraint against plastic flow in the flange likely accounts for some difference in rotation capacity relative to the proof-of-concept link. Despite this fact, Specimen X1L1.2 exceeded its target rotation.

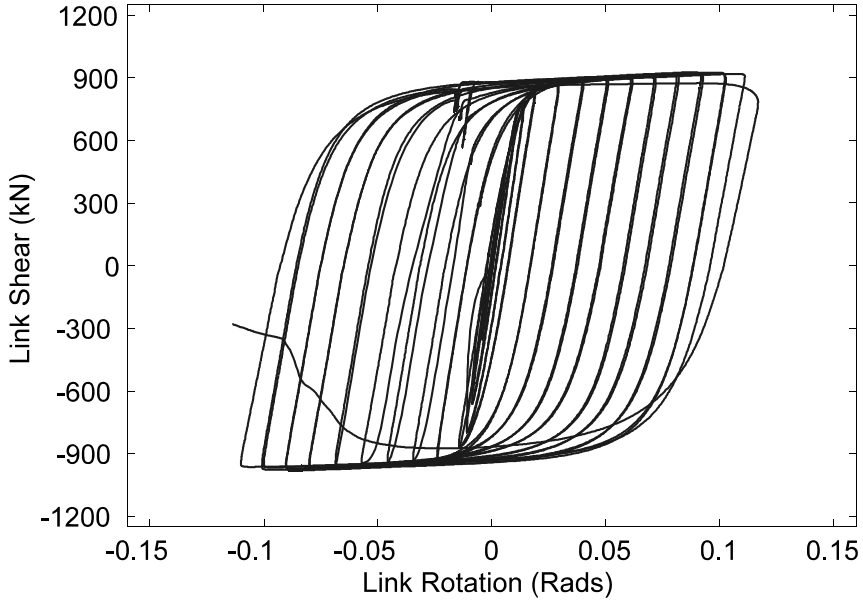

FIGURE 5-1 Link Shear vs. Rotation Hysteresis for Specimen X1L1.2

TABLE 5-1 Loading History for Specimen X1L1.2

Sequence Number	Cycles	γ (rads)	Link Shear (kN)	Sequence Number	Cycles	γ (rads)	Link Shear (kN)
1	3	0.0009	81	9	2	0.051	877
2	3	0.0022	170	10	2	0.062	882
3	3	0.050	356	11	2	0.072	891
4	2	0.010	666	12	2	0.082	895
5	2	0.014	786	13	2	0.093	901
6	2	0.019	828	14	2	0.103	908
7	2	0.029	858	15	1	0.117	905
8	2	0.040	877				

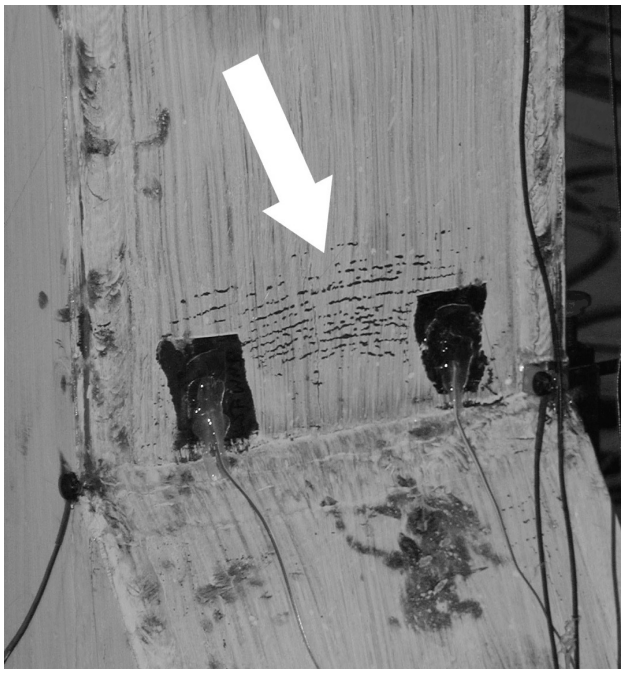

FIGURE 5-2 Whitewash Flaking from Flange of Specimen X1L1.2 During Sequence 6

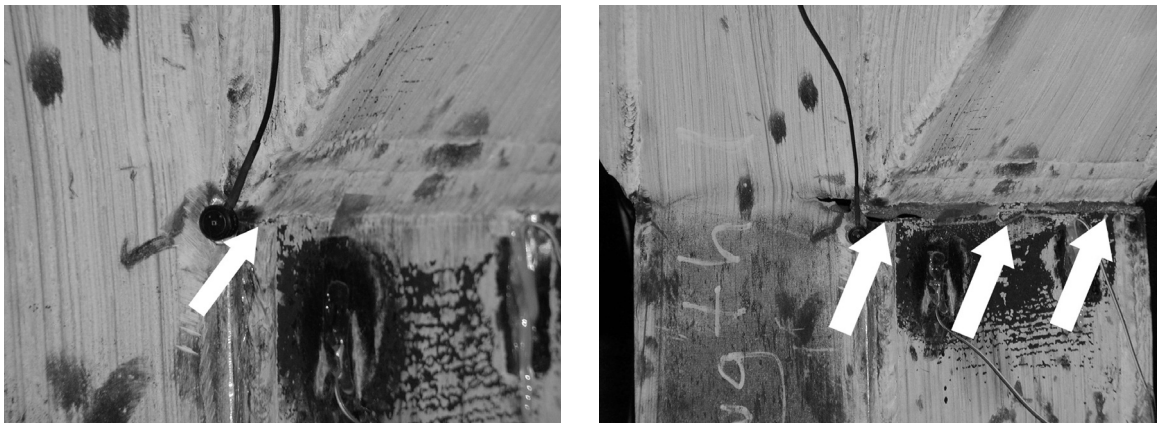

(a) **(b)**

FIGURE 5-3 Flange Fracture of Specimen X1L1.2 During: (a) Sequence 14; and (b) Sequence 15

5.3.2 Specimen X2L1.2

The link shear force versus rotation hysteresis for Specimen X2L1.2 is shown in figure 5-4 and recorded peak shear forces and rotations for each sequence of loading are given in table 5-2. Note that the hysteresis curve shows unloading spikes in the positive shear and negative rotation quadrant of the graph. These are due to relaxation of the specimen while the test is paused for inspection between sequences and did not effect the overall specimen behavior. These unloading spikes are visible in the hysteresis curves for most specimens. Specimen X2L1.2, which had web and flange compactness ratios near the proposed limits for stiffened cross-sections for shear links, reached a rotation of 0.098 rads prior to strength degradation, which exceeds the target rotation of 0.08 rads. Strain gage recordings indicate that both shear yielding of the web and outer fiber yielding of the flange occurred during the first cycle of the third loading sequence, which had a rotation of 0.01 rads. By Sequence 5 the shear strain in the webs had reached 5.5 times the yield shear strain (0.00259) and the flange strain in the outer fibers had reached 2.5 times the yield normal strain (0.00172). The deformed shape of the link was similar to that observed for the proof-of-concept test in that significant "curl" of the stiffeners was observed. Figures 5-5a and 5-5b show Specimen X2L1.2 at the positive and negative rotations peaks of Cycle 2 of Sequence 11 where the peak rotation was 0.09 rads. During Sequences 10, 11, and 12, flange buckling of small

magnitude was observed, although there was no associated strength reduction. No evidence of web buckling was observed for the duration of the test.

Fracture was first noticed during the final cycle of Sequence 12 but strength degradation did not occur until the first excursion of the next sequence at which point the rapid loss of shear capacity evident in the hysteresis curve occurred. Fracture initiated in the full-penetration welds joining the webs to the flanges adjacent to the transverse weld for the flange haunch. Figures 5-6a, 5-6b, 5-6c, and, 5-6d show the progress of a similar fracture which caused the large strength drop in the negative excursion of what would have been Cycle 1 of Sequence 13. As shown, the fracture propagated well into the web, below and above the end stiffeners. Figure 5-7 shows the low-cycle fatigue striations on the bottom west flange fracture surface, from which it may be surmised that the fracture initiated in the web-to-flange weld adjacent to the web haunch. The fracture was likely caused by the large restraint against plastic flow at that location due to the presence of the flange and web haunch plates as described for Specimen X1L1.2. The same type of fracture was evident at all four flanges at the end of testing.

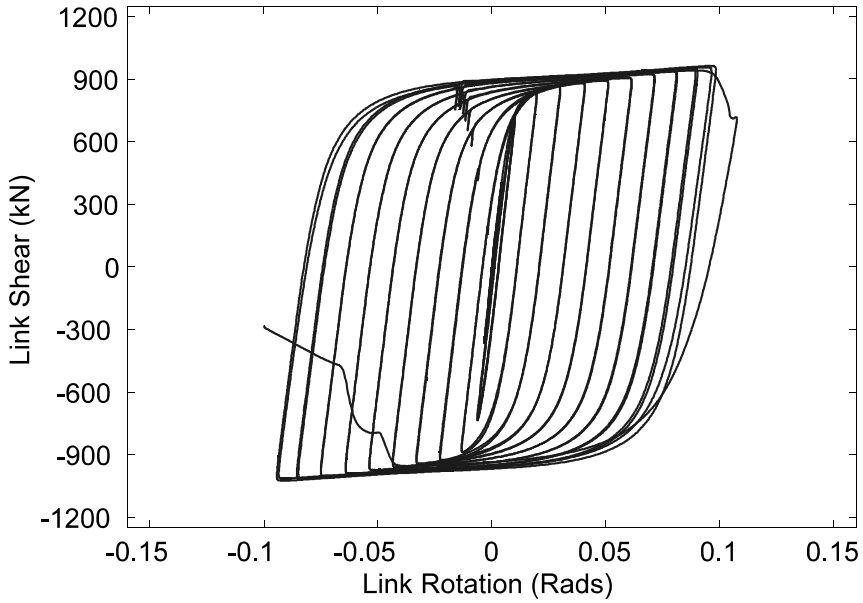

FIGURE 5-4 Link Shear vs. Rotation Hysteresis for Specimen X2L1.2

TABLE 5-2 Loading History for Specimen X2L1.2

Sequence Number	Cycles	γ (rads)	Link Shear (kN)	Sequence Number	Cycles	γ (rads)	Link Shear (kN)
1	3	0.0027	167	7	2	0.051	881
2	3	0.0043	396	8	2	0.062	888
3	3	0.010	725	9	2	0.072	902
4	2	0.020	828	10	2	0.081	928
5	2	0.030	855	11	2	0.090	941
6	2	0.041	873	12	2	0.098	948

(a) **(b)**

FIGURE 5-5 Deformed Specimen X2L1.2 During: (a) the Negative Peak of Cycle 1 of Sequence 11; and (b) the Positive Peak of Cycle 2 of Sequence 11

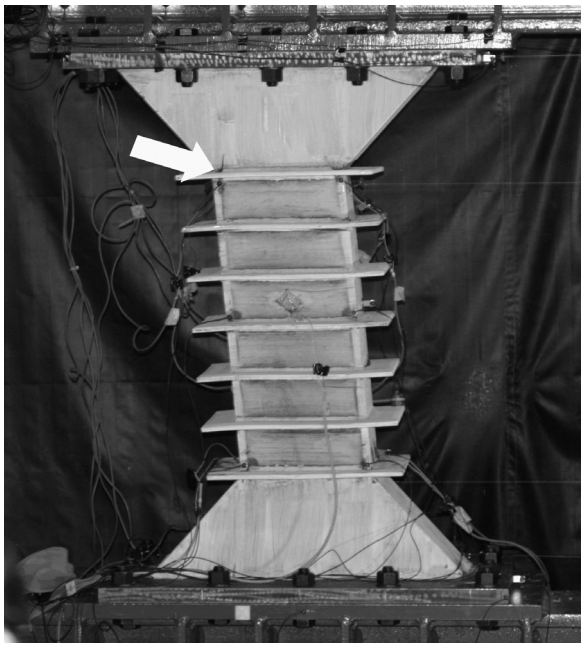

(a)

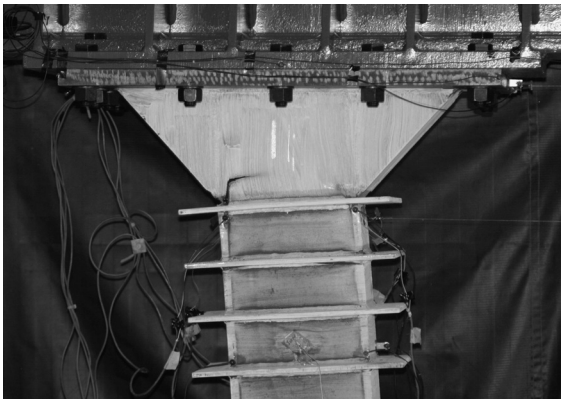

(b)

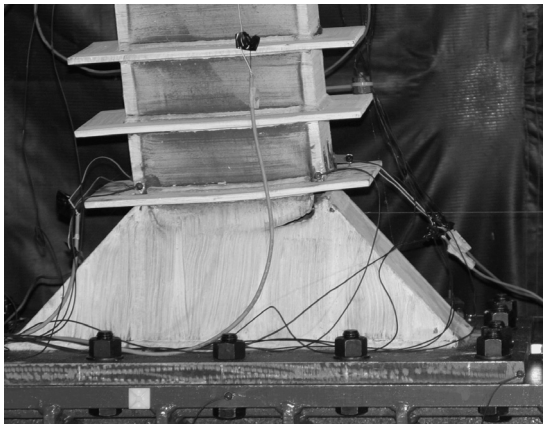

(c)

(d)

FIGURE 5-6 Fracture Propagation From: (a) Near the Midpoint of the Negative Excursion of Cycle 1 of Sequence 13; (b) and (c) the End of the Negative Excursion of the First Cycle of Sequence 13 and; (d) the Subsequent Positive Excursion of the First Cycle of Sequence 13

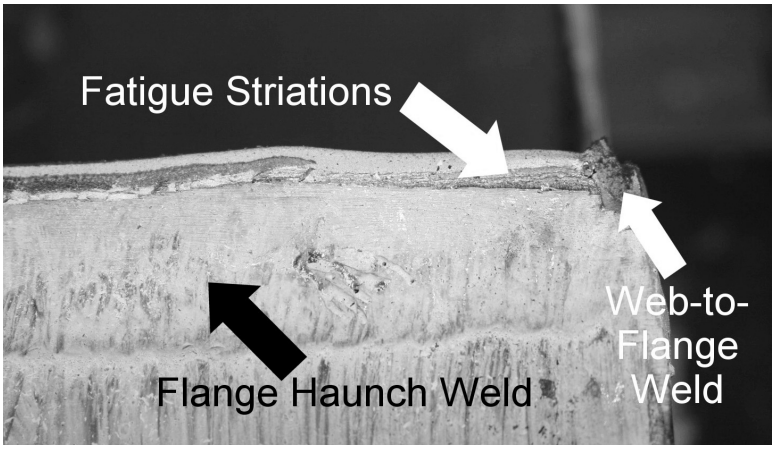

FIGURE 5-7 Bottom West Flange Fracture Surface and Fatigue Striations

5.3.3 Specimen X3L1.2

The link shear force versus rotation hysteresis for Specimen X3L1.2 is shown in figure 5-8 and recorded peak shear forces and rotations for each sequence of loading are given in table 5-3. This link, which had web and flange compactness ratios well below the proposed limits for unstiffened link cross-sections, reached a rotation of 0.11 rads prior to strength degradation, which exceeds the target rotation of 0.08 rads. Yielding of the outer flange fibers as well as shear yielding of the webs was first recorded by strain gages during Sequence 5 which had cycles at 0.017 rads of link rotation. Figure 5-9 shows Specimen X3L1.2 deformed at 0.10 rads during the Cycle 1 of Sequence 13. Again fracture occurred at the toe of the flange haunch weld and seems to have initiated in the web-to-flange weld material where there is high restraint against plastic flow due to the presence of the stiff flange and web haunches. Figure 5-10a shows the fracture as it extends around to the upper north web during the negative excursion in Cycle 1 of Sequence 14. Figure 5-10b shows the fracture in a similar location on the west flange during the positive excursion of what would have been Cycle 2 of Sequence 14. The fracture surface of the top east flange is shown in Figure 5-11 and again fatigue striations are visible along with markings that indicate fracture initiated in the web-to-flange weld where restraint against plastic flow is high.

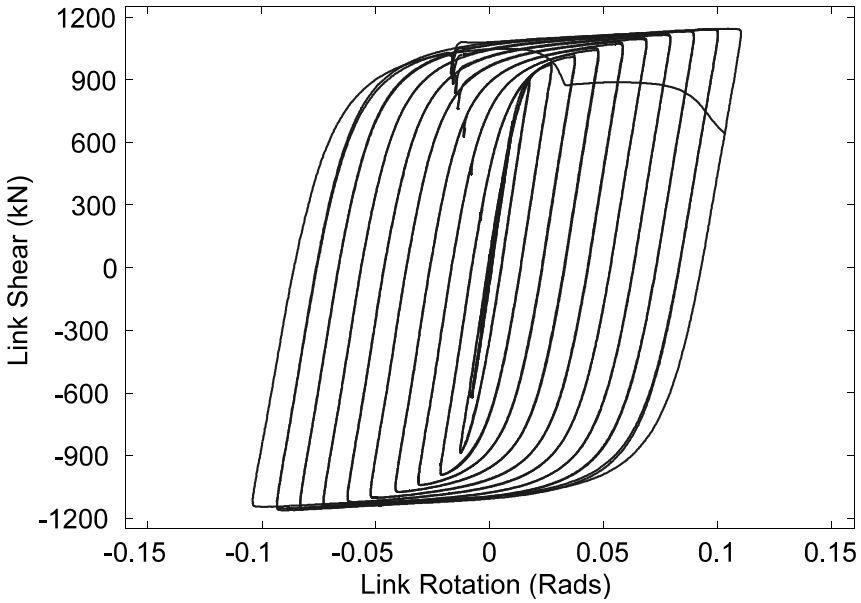

FIGURE 5-8 Link Shear vs. Rotation Hysteresis for Specimen X3L1.2

TABLE 5-3 Loading History for Specimen X3L1.2

Sequence Number	Cycles	γ (rads)	Link Shear (kN)	Sequence Number	Cycles	γ (rads)	Link Shear (kN)
1	3	0.001	85	8	2	0.048	1042
2	3	0.002	189	9	2	0.059	1065
3	3	0.005	374	10	2	0.069	1082
4	3	0.010	696	11	2	0.079	1108
5	2	0.018	901	12	2	0.090	1120
6	2	0.027	973	13	2	0.100	1125
7	2	0.037	1015	14	1	0.110	1129

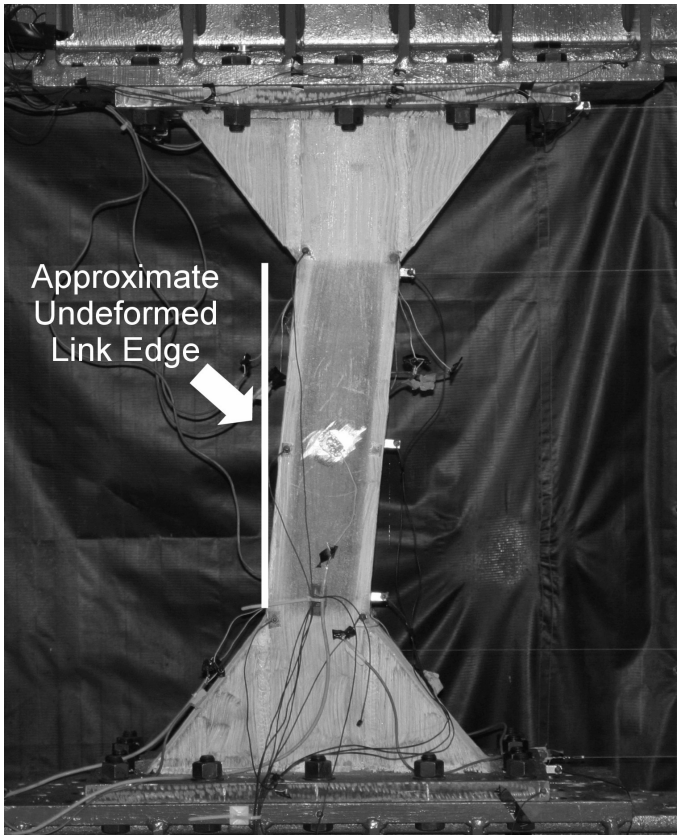

FIGURE 5-9 Specimen X3L1.2 at 0.10 rads of Cycle 1 of Sequence 13

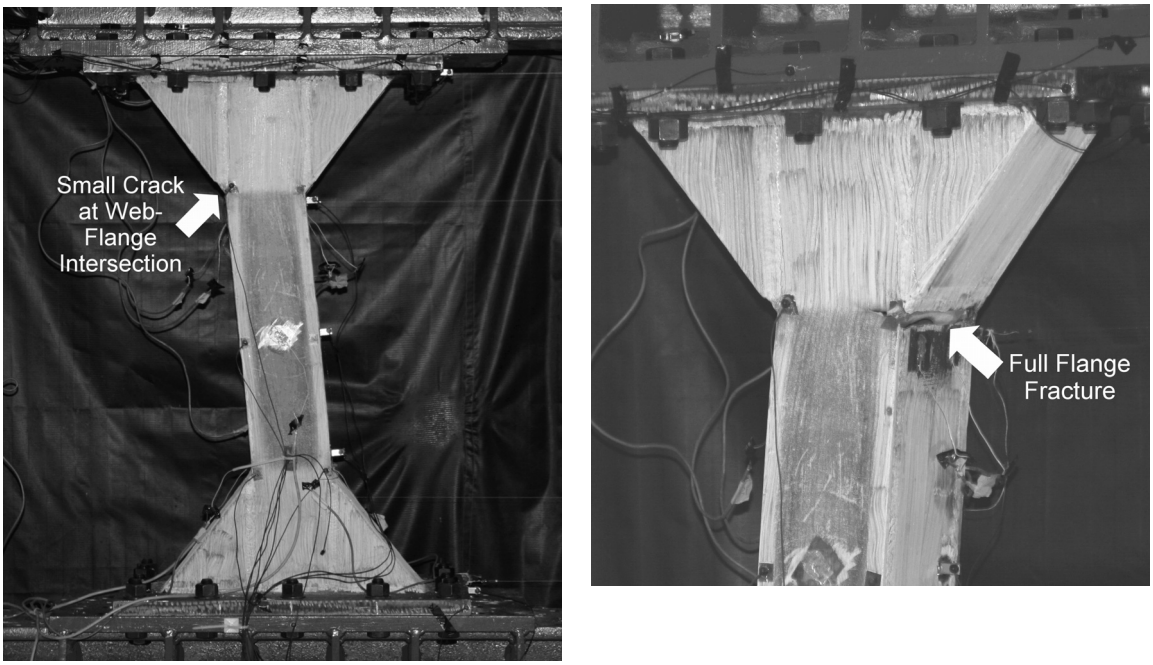

(a) **(b)**

FIGURE 5-10 Fractures Developing in Specimen X3L1.2 During: (a) the Negative Excursion of Cycle 1 of Sequence 14 and; (b) the Positive Excursion of Cycle 2 of Sequence 14

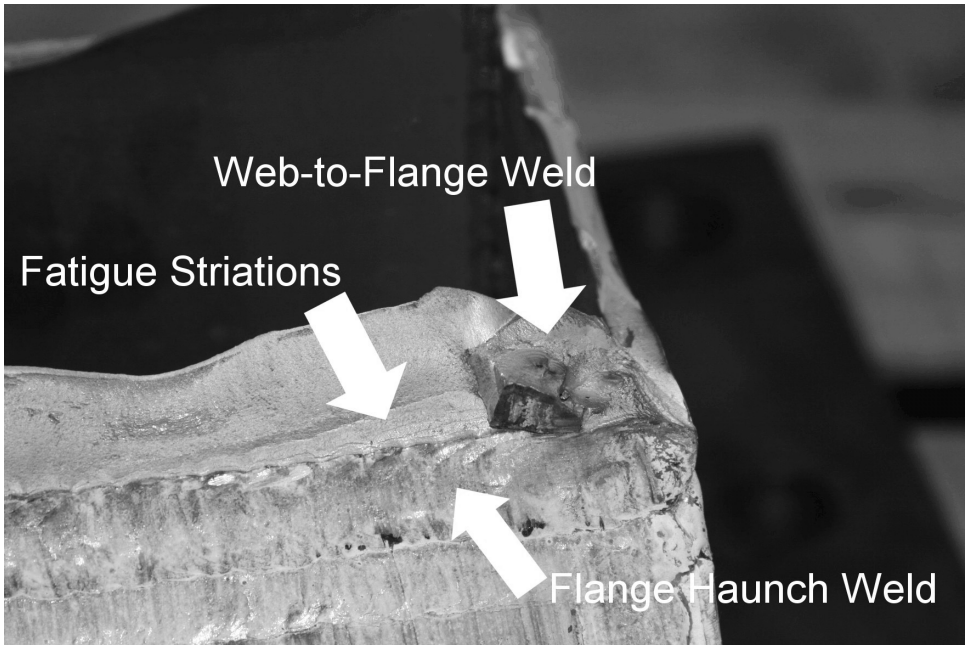

FIGURE 5-11 Fracture Surface of Top East Flange of Specimen X3L1.2

5.3.4 Specimen X1L1.6

The link shear force versus rotation hysteresis for Specimen X1L1.6 is shown in figure 5-12 and recorded peak shear forces and rotations for each sequence of loading are given in table 5-4. This link, which had web and flange compactness ratios near the proposed limits for unstiffened cross-sections and a normalized length corresponding to the transition point between shear and intermediate links, completed two cycles at a rotation of 0.066 rads prior to strength degradation from flange fracture on the first half of the first cycle to 0.083 rads. Yielding on the outer fibers of the flanges was recorded by the strain gages during Sequence 4 and yielding of the webs was indicated during Sequence 5. By Sequence 8 both the outer flange fiber strains and web strains were at values corresponding to approximately 8 times their yield strains of 0.00172 and 0.00259, respectively.

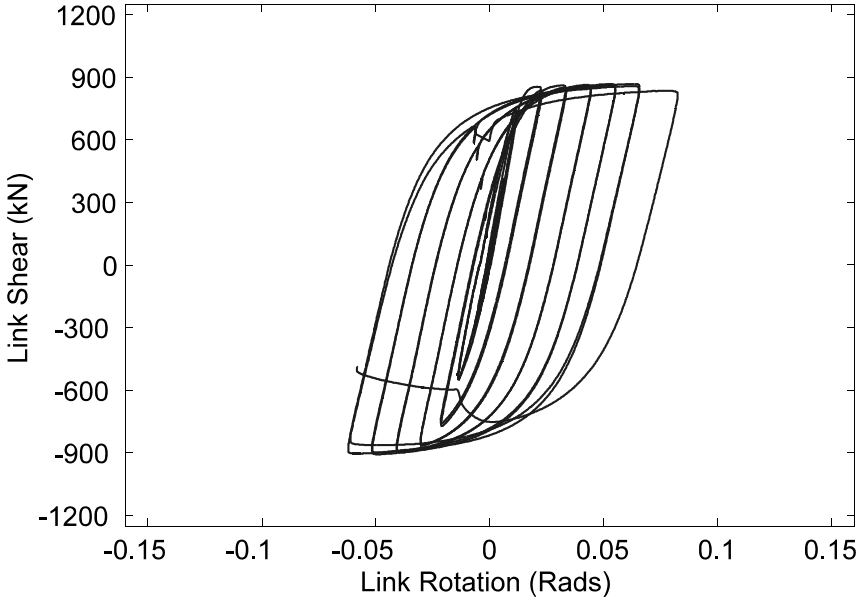

FIGURE 5-12 Link Shear vs. Rotation Hysteresis for Specimen X1L1.6

Figure 5-13 shows the link during the negative excursion of Cycle 1 of Sequence 8. Small magnitude web and flange buckling was observed at both link ends during Sequence 9, however, it did not seem to cause any strength degradation. Fracture of the top east flange occurred during loading in the negative (east) direction of the Cycle 1 of Sequence 10. Figures 5-14 and 5-15 show the flange fracture occurring and the fracture surface after testing respectively. This fracture surface differs from those discussed previously in that

there are no visible fatigue striations and instead visible chevron markings that point to the web-to-flange weld area, indicating that this location was where the fracture initiated.

TABLE 5-4 Loading History for Specimen X1L1.6

Sequence Number	Cycles	γ (rads)	Link Shear (kN)	Sequence Number	Cycles	γ (rads)	Link Shear (kN)
1	3	0.0017	85	6	2	0.034	846
2	3	0.003	193	7	2	0.045	850
3	3	0.006	403	8	2	0.055	854
4	3	0.012	751	9	2	0.066	851
5	2	0.023	825	10	0.5	0.083	811

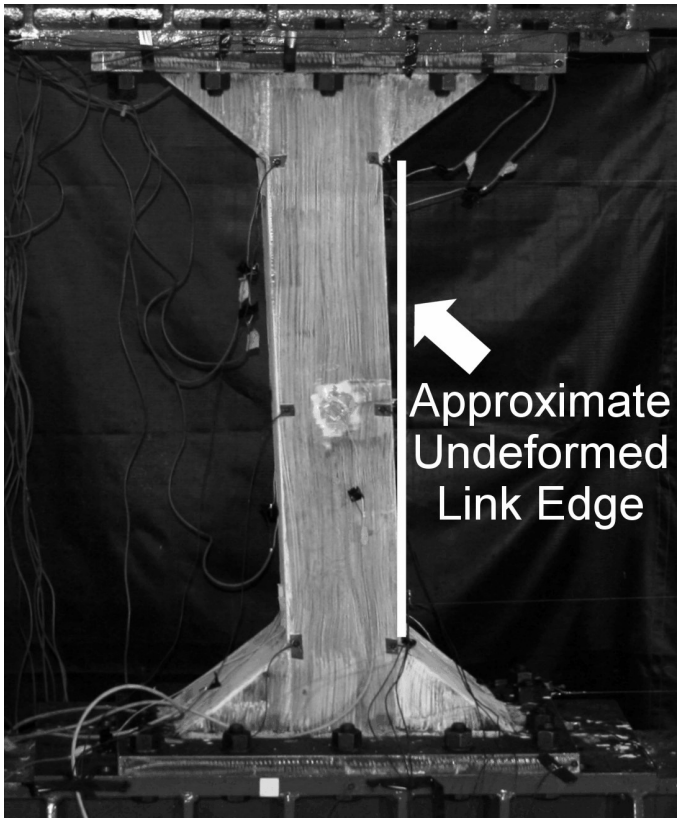

FIGURE 5-13 Specimen X1L1.6 at -0.055 rads During Cycle 1 of Sequence 8

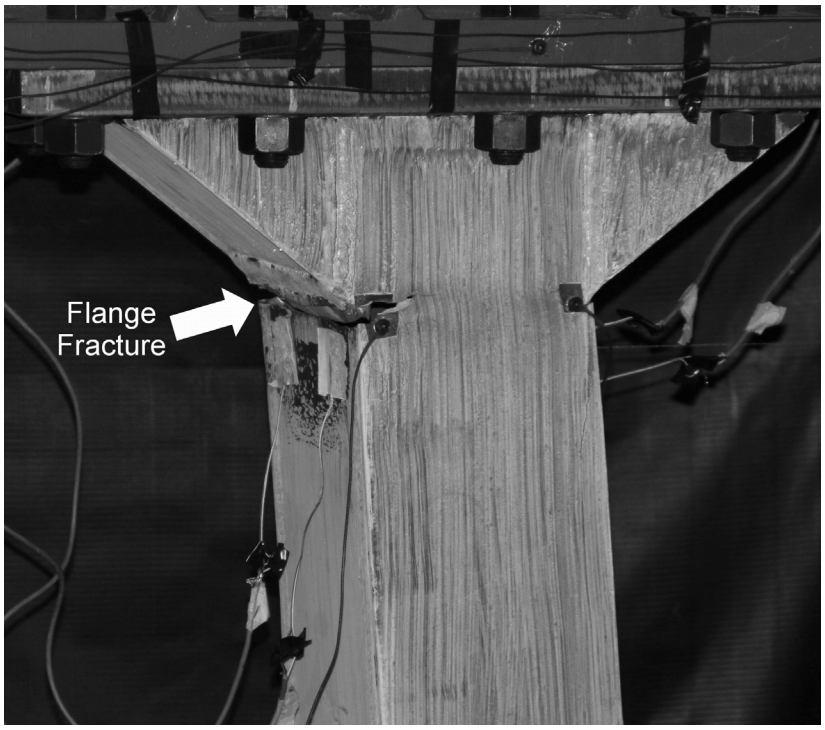

FIGURE 5-14 Flange Fracture of Specimen X1L1.6 During Cycle 1 of Sequence 10

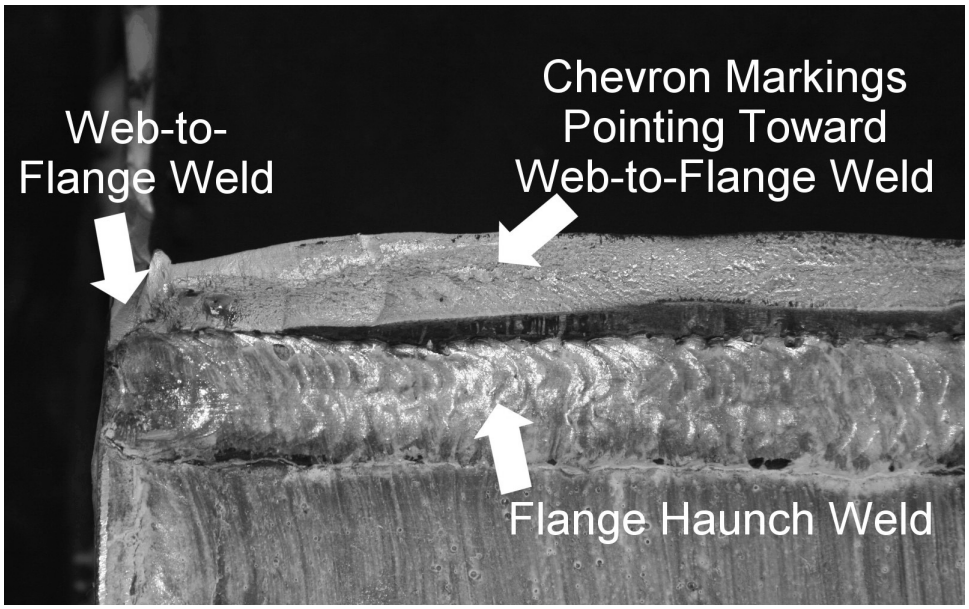

FIGURE 5-15 Fracture Surface of Top East Flange of Specimen X1L1.6

5.3.5 Specimen X2L1.6

Figure 5-16 shows the link shear force versus rotation hysteresis curve for Specimen X2L1.6 and recorded peak shear forces and rotations for each sequence of loading are given in table 5-5. This link had stiffeners along with web and flange compactness ratios close to the proposed limits for stiffened cross-sections and a normalized length at the transition point between shear and intermediate classification. The target rotation of 0.08 rads was not achieved as the link suffered flange fracture after Cycle 1 of Sequence 9, which had a peak rotation of 0.068 rads. Prior to flange fracture there was some small magnitude flange buckling. Strain gage recordings indicate that the outer flange fibers, as well as the webs began to yield during Sequence 4 and by Sequence 8 had reached strains of 10 and 8 times the yield strains respectively. Consistent with the proof-of-concept test and Specimen X2L1.2, stiffener "curl" was observed for Specimen X2L1.6. Figure 5-17 shows the deformed link at 0.058 rads during Cycle 2 of Sequence 8.

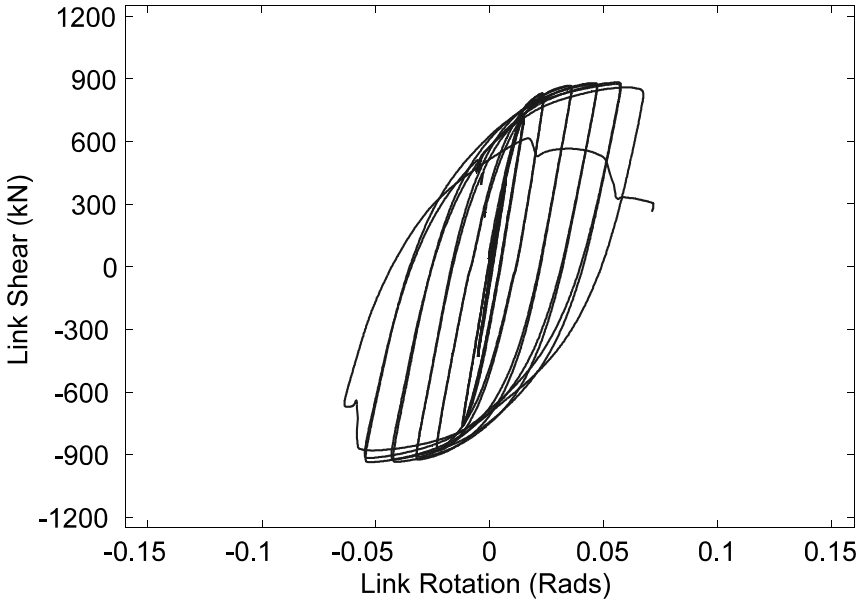

FIGURE 5-16 Link Shear vs. Rotation Hysteresis for Specimen X2L1.6

Fracture initiated at all four flange ends at approximately the same point in the loading history. The fractures began in the flanges in the flange-to-web welds and spread through the flanges and then the webs. Figure 5-18 shows an example of the fracture extending into the web while avoiding the stiffener. Figure 5-19 shows a close up of the flange and web fracture on the bottom east side of the specimen. Fatigue striations were visible in the

fracture surface at all fracture locations, an example of which is shown in figure 5-20. Similar to the previous links, the fracture surface markings indicate that fracture initiated in the web-to-flange weld adjacent to the weld for the web and flange haunches where there is high restraint against plastic flow.

TABLE 5-5 Loading History for Specimen X2L1.6

Sequence Number	Cycles	γ (rads)	Link Shear (kN)	Sequence Number	Cycles	γ (rads)	Link Shear (kN)
1	3	0.0027	96	6	2	0.036	857
2	3	0.004	212	7	2	0.047	867
3	3	0.007	426	8	2	0.058	870
4	2	0.015	727	9	1	0.067	833
5	2	0.023	822				

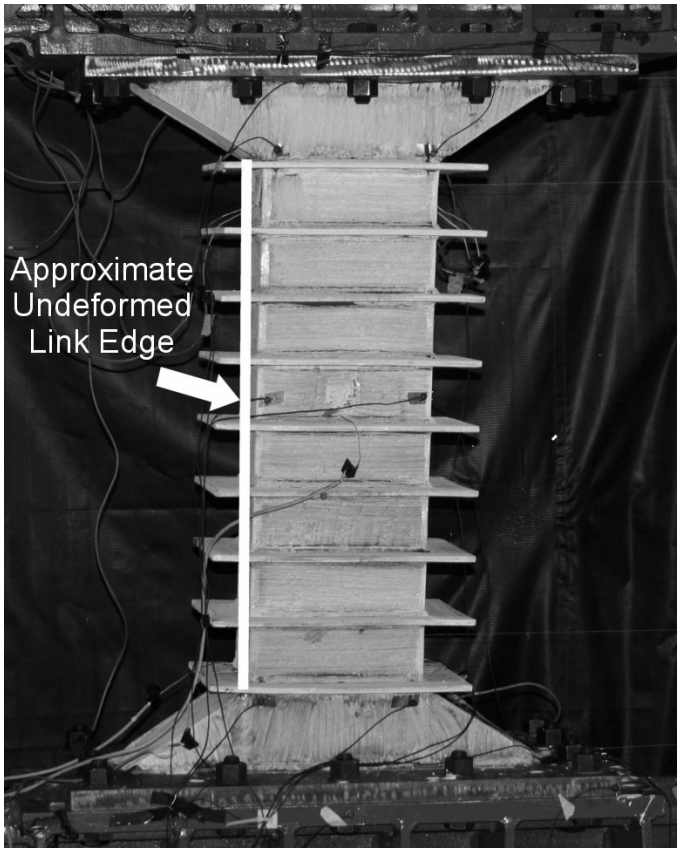

FIGURE 5-17 Specimen X2L1.6 at 0.058 rads During Cycle 2 of Sequence 8

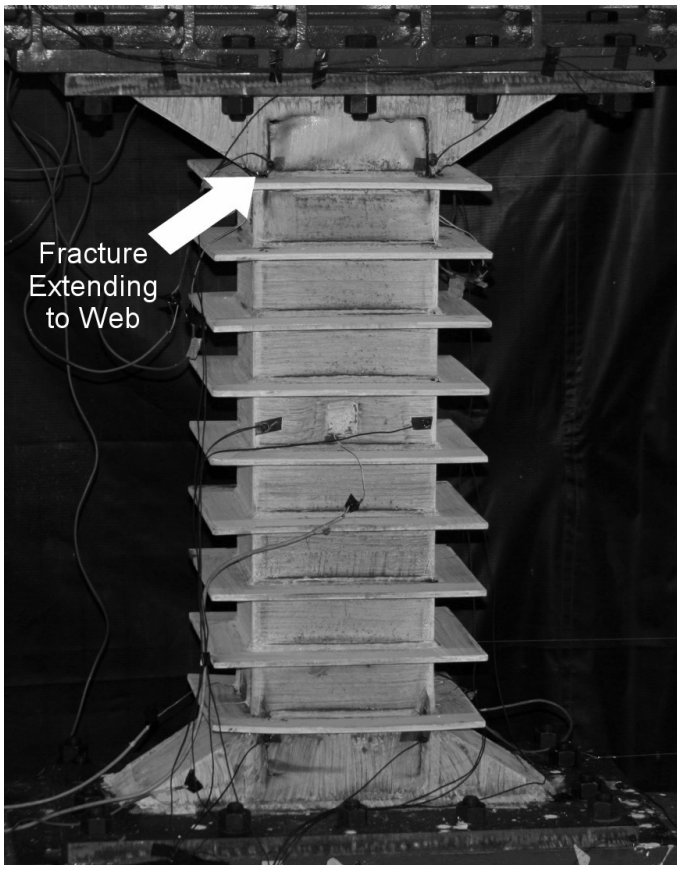

FIGURE 5-18 Fracture of Flange Extending to Web in Specimen X2L1.6

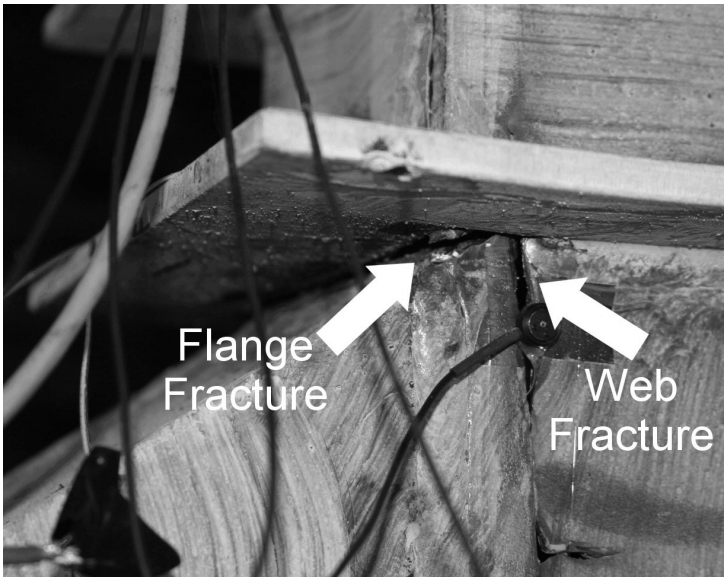

FIGURE 5-19 Close-up of Flange and Web Fracture of Specimen X2L1.6

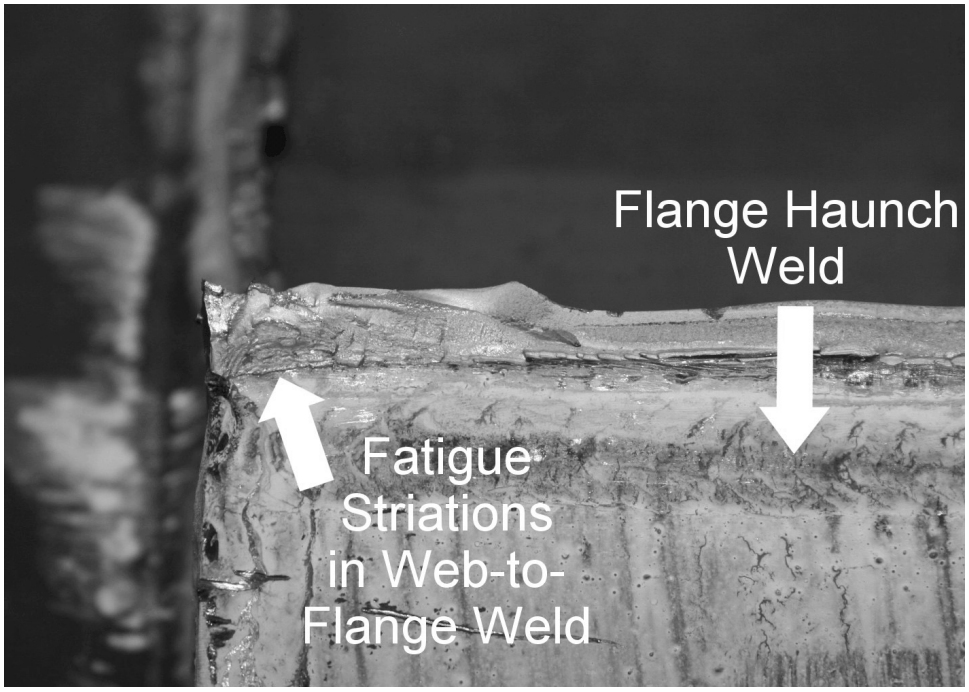

FIGURE 5-20 Fatigue Striations in Fracture Surface of Specimen X2L1.6

5.3.6 Specimen X3L1.6

Figure 5-21 shows the link shear force versus rotation hysteresis curve for Specimen X3L1.6 and recorded peak shear forces and rotations for each sequence of loading are given in table 5-6. This specimen had web and flange compactness values well below the proposed limit and a normalized length at the transition point between shear and intermediate links. The target rotation for this specimen was 0.08 rads, however the link suffered flange fracture during the negative excursion of the first cycle at 0.075 rads. No buckling of the flanges or webs was observed prior to fracture of this specimen. Strain gage data indicated yielding of the outer flange fibers during Sequence 4 and yielding of the webs during Sequence 5. Figure 5-22 shows the link deformed during Cycle 2 of Sequence 9 at a rotation of -0.064 rads. Fracture was similar to the fractures observed in other specimens and is shown in figure 5-23 during the negative excursion of Cycle 1 of Sequence 10. Figure 5-24 shows both chevron markings and fatigue striations on the bottom east flange and they indicate that the fracture again initiated in the web-to-flange weld adjacent to the web and flange haunch welds.

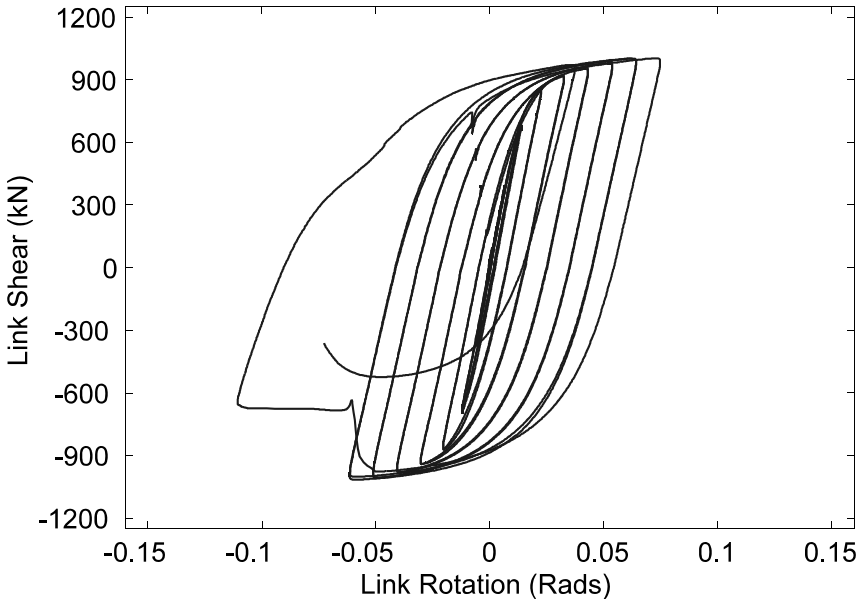

FIGURE 5-21 Link Shear vs. Rotation Hysteresis for Specimen X3L1.6

TABLE 5-6 Loading History for Specimen X3L1.6

Sequence Number	Cycles	γ (rads)	Link Shear (kN)	Sequence Number	Cycles	γ (rads)	Link Shear (kN)
1	3	0.0017	93	6	2	0.033	900
2	3	0.003	196	7	2	0.043	942
3	3	0.007	383	8	2	0.054	970
4	3	0.014	702	9	2	0.064	988
5	2	0.023	849	10	1	0.075	989

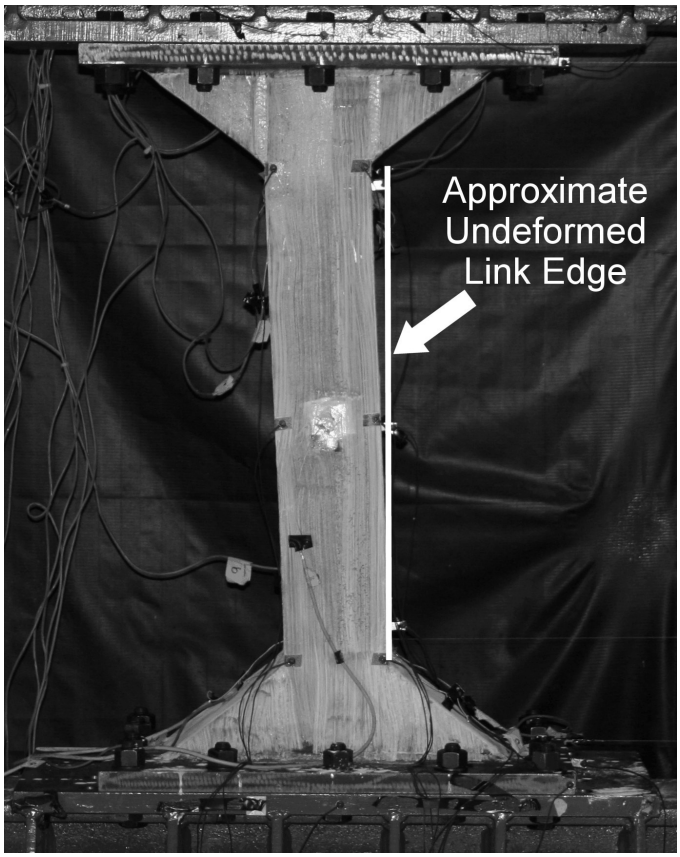

FIGURE 5-22 Specimen X3L1.6 at -0.064 rads During Cycle 2 of Sequence 9

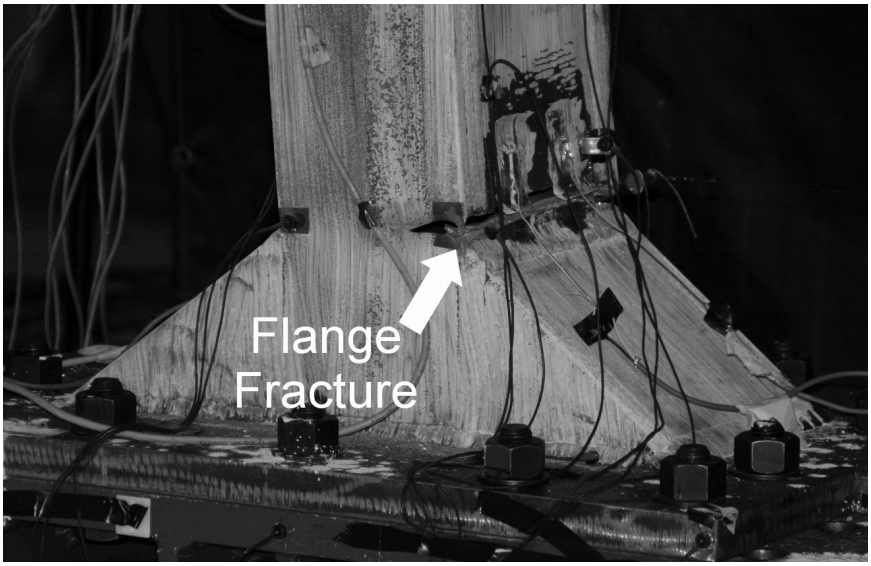

FIGURE 5-23 Flange Fracture in Specimen X3L1.6 During the Negative Excursion of Cycle of Sequence 10

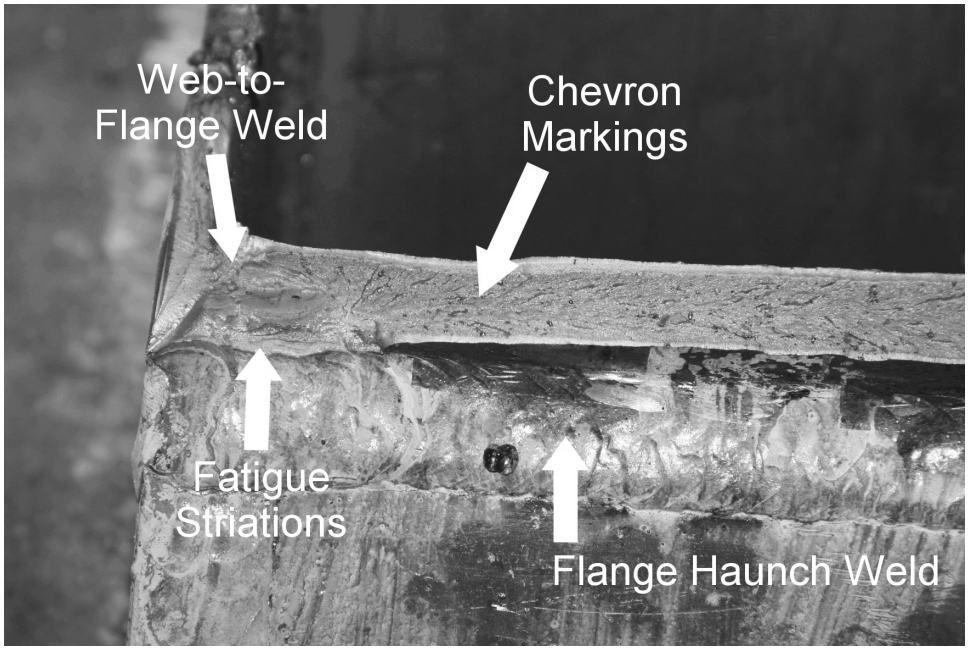

FIGURE 5-24 Fatigue Striations and Chevron Markings in Fracture Surface of Specimen X3L1.6

5.3.7 Specimen X1L2.1

Figure 5-25 shows the link shear force versus rotation hysteresis curve for Specimen X1L2.1 and recorded peak shear forces and rotations for each sequence of loading are given in table 5-7. This link had compactness ratios near the proposed limits for unstiffened cross-sections and a normalized length in the middle of the intermediate link range corresponding to a target rotation of 0.05 rads. The link sustained two full cycles at a rotation of 0.056 rads prior to suffering flange fracture during the negative excursion of Cycle 1 of Sequence 9 attempting to reach a rotation of -0.064 rads. The deformed link at 0.056 rads during Cycle 2 of Sequence 8 is shown in figure 5-26. Strain gage recordings indicate yielding of the outer fibers of the flanges during Sequence 3 while the webs remained elastic at the gage locations for the duration of testing. Significant flange buckling was observed during Sequence 8. Figure 5-27 shows the buckling at the end of testing. Flange fracture occurred at all four flange ends during Sequence 9 and an example of the fracture is shown in figure 5-28. As with the other specimens the fracture surface indicates that fracture initiation occurred in the web-to-flange welds adjacent to the weld of the flange haunch where plastic flow is highly restrained. An example of the fracture surface is shown in figure 5-29.

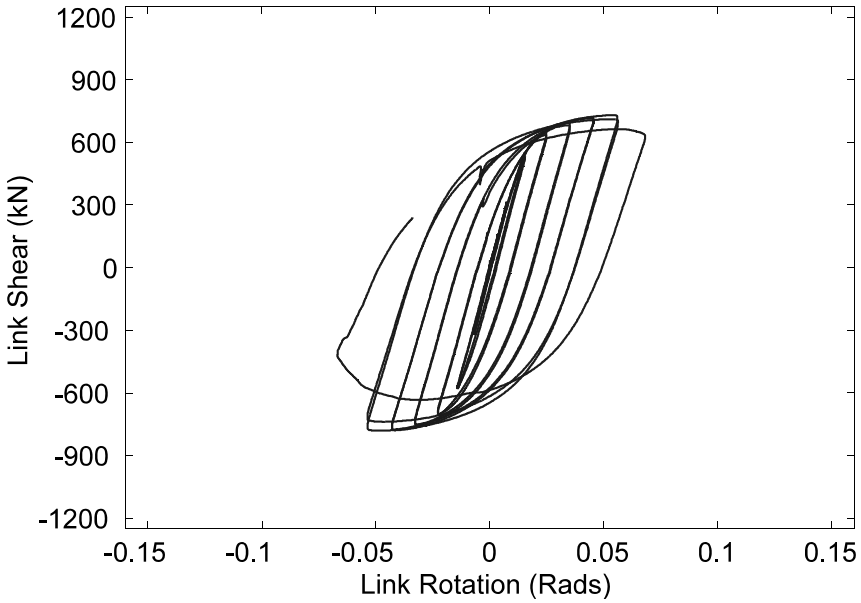

FIGURE 5-25 Link Shear vs. Rotation Hysteresis for Specimen X1L2.1

TABLE 5-7 Loading History for Specimen X1L2.1

Sequence Number	Cycles	γ (rads)	Link Shear (kN)	Sequence Number	Cycles	γ (rads)	Link Shear (kN)
1	3	0.002	74	6	2	0.035	688
2	3	0.004	156	7	2	0.046	715
3	3	0.008	312	8	2	0.056	721
4	2	0.016	551	9	1	0.064	631
5	2	0.025	646				

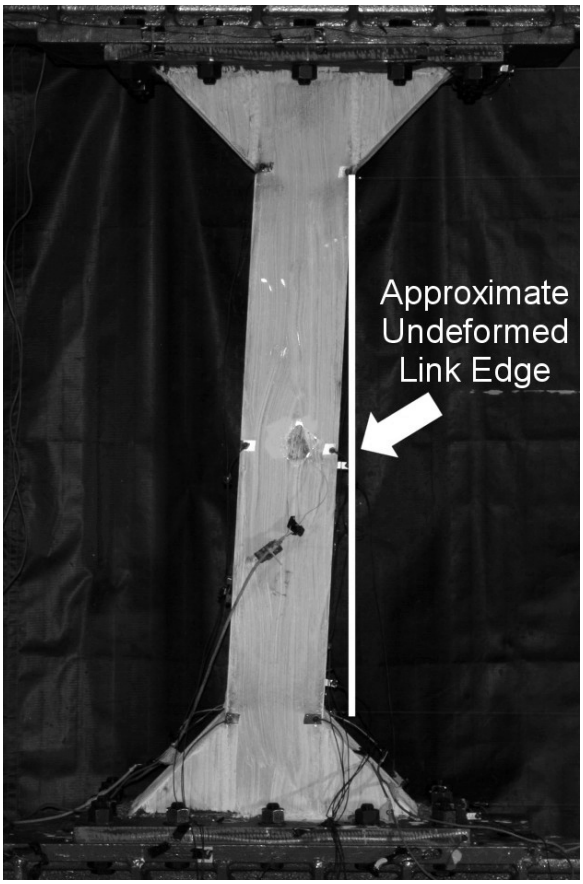

FIGURE 5-26 Specimen X1L2.1 at 0.056 rads During Cycle 2 of Sequence 8

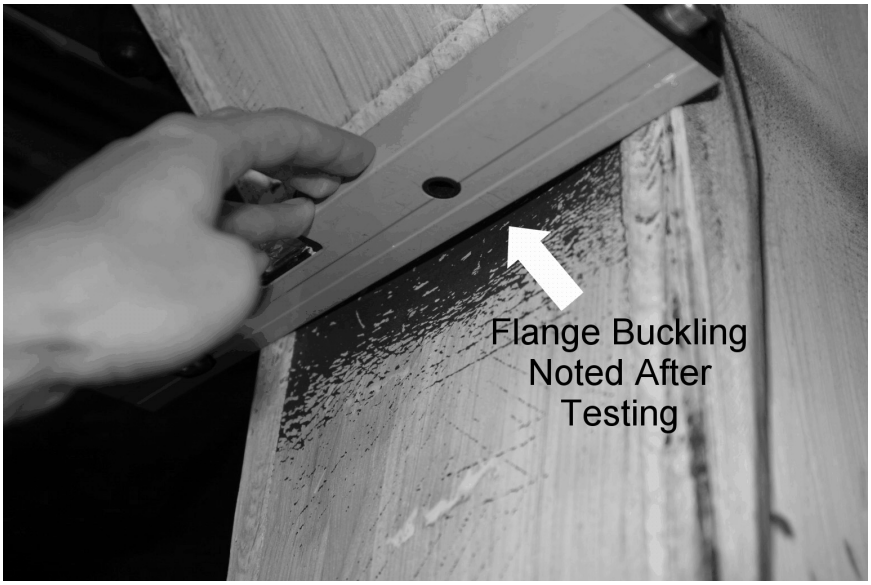

FIGURE 5-27 Magnitude of Flange Buckling After Testing of Specimen X1L2.1 Relative to a Straight Edge

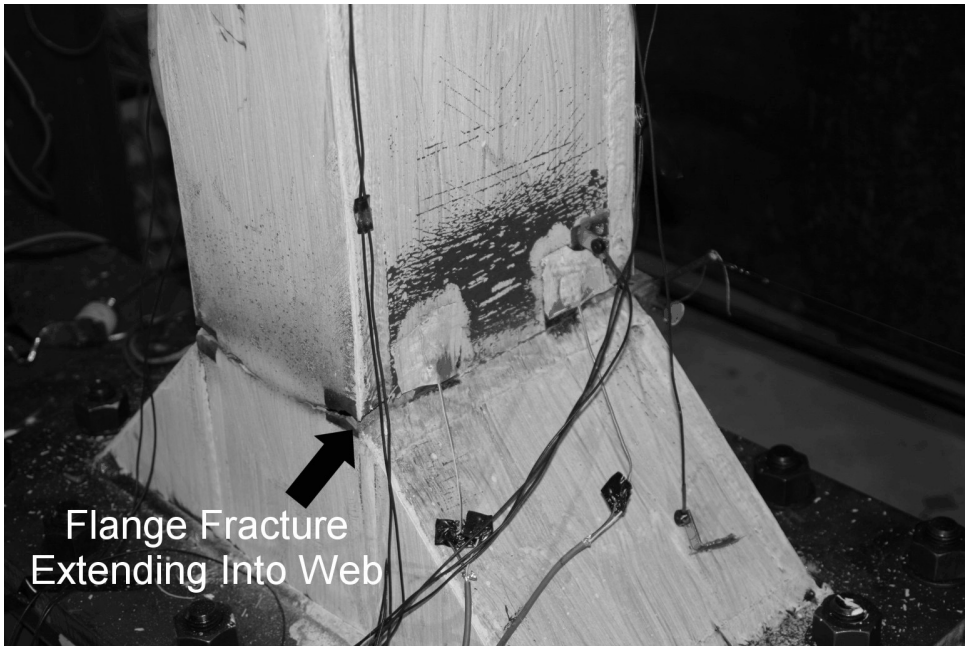

FIGURE 5-28 Fracture of Bottom West Flange Extending Into Web of Specimen X1L2.1

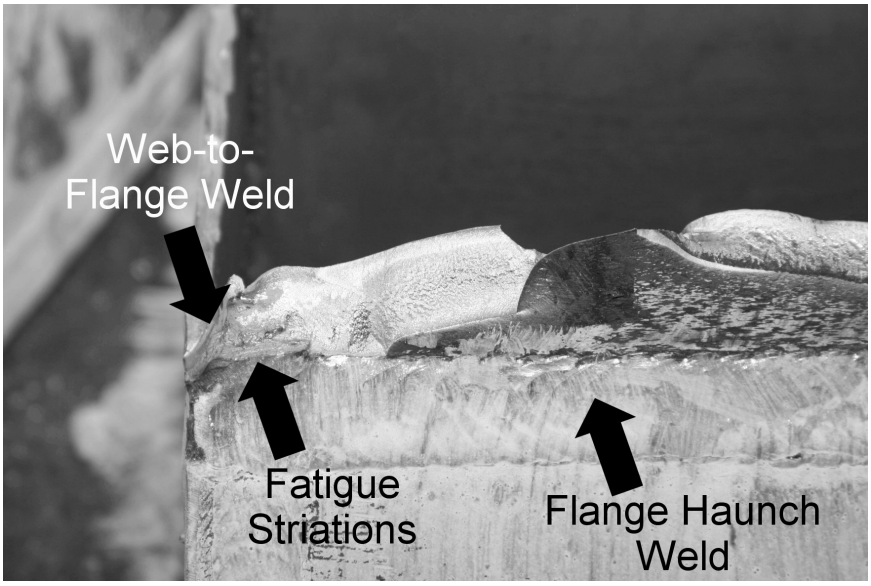

FIGURE 5-29 Fracture Surface of Bottom East Flange of Specimen X1L2.1

5.3.8 Specimen X2L2.1

Figure 5-30 shows the link shear force versus rotation hysteresis curve for Specimen X2L2.1 and recorded peak shear forces and rotations for each sequence of loading are given in table 5-8. This link did not satisfy the proposed design criteria because it had a larger web compactness than the proposed criteria allows for intermediate links. The link reached two cycles at a rotation of 0.042 rads but suffered flange fracture during the first cycle at 0.051 rads. The target rotation was two sustained cycles at 0.05 rads. Strain gage data indicates that the web, at the web gage location, remained elastic while the outer flange fibers yielded during Sequence 4 and reached strains of as much as 8 times the yield strain prior to failure. Web and flange buckling preceded flange fracture, and caused some strength degradation in Cycle 2 of Sequence 7. Figure 5-31 shows the link at 0.042 rads during Cycle 1 of Sequence 7 and figure 5-32 shows the magnitude of flange buckling after completion of the testing. Figure 5-33 shows the west flange fracture spreading into web below the last stiffener during the negative excursion of Cycle 1 of Sequence 8. Figure 5-34 shows the east flange fracture spreading into the web after testing where the end stiffener has been partially removed to permit visual inspection. The fracture surface was similar to the surfaces described for the previous links and evidence of fracture initiation from the web-to-flange weld was again visible.

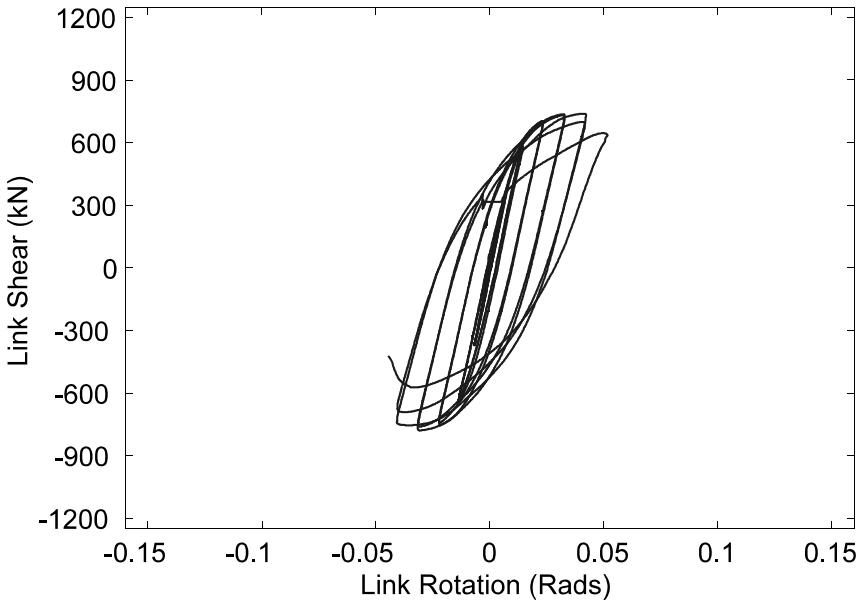

FIGURE 5-30 Link Shear vs. Rotation Hysteresis for Specimen X2L2.1

TABLE 5-8 Loading History for Specimen X2L2.1

Sequence Number	Cycles	γ (rads)	Link Shear (kN)	Sequence Number	Cycles	γ (rads)	Link Shear (kN)
1	3	0.0017	88	5	2	0.023	702
2	3	0.003	185	6	2	0.033	727
3	3	0.007	363	7	2	0.042	691
4	3	0.014	606	8	1	0.051	622

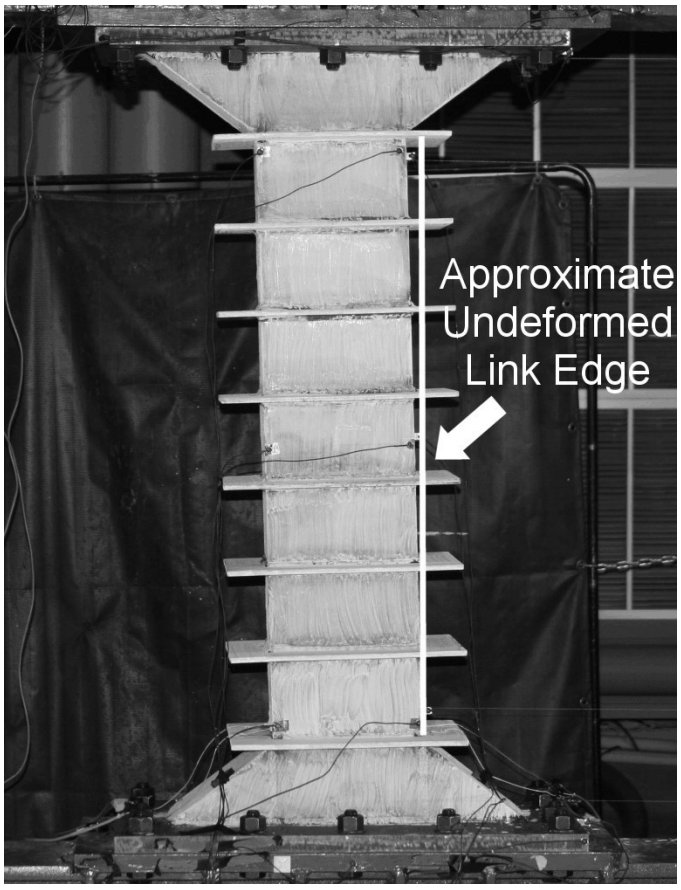

FIGURE 5-31 Specimen X2L2.1 at 0.042 rads During Cycle 1 of Sequence 7

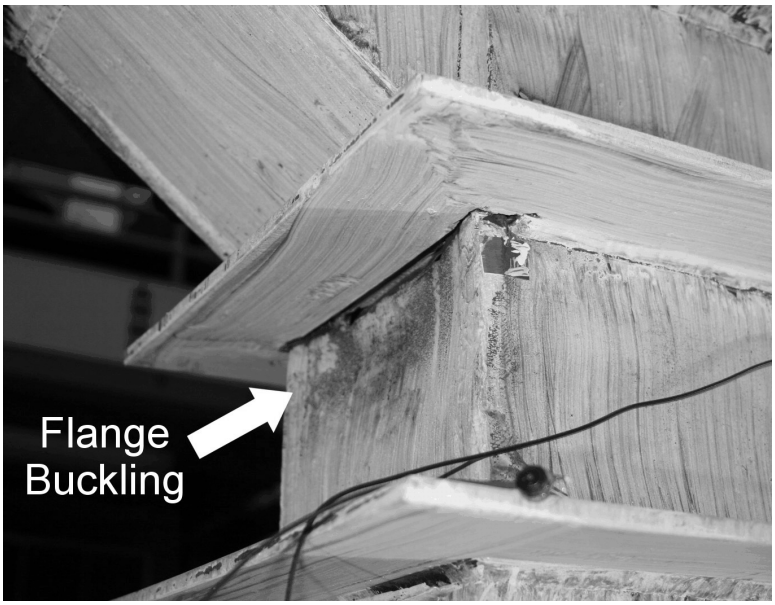

FIGURE 5-32 Flange Buckling of Specimen X2L2.1 After Testing

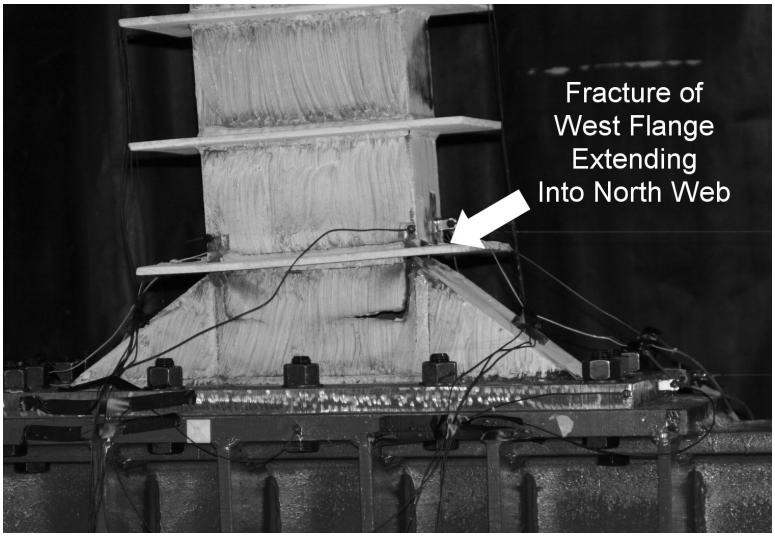

FIGURE 5-33 West Flange Fracture Extending into North Web of Specimen X2L2.1

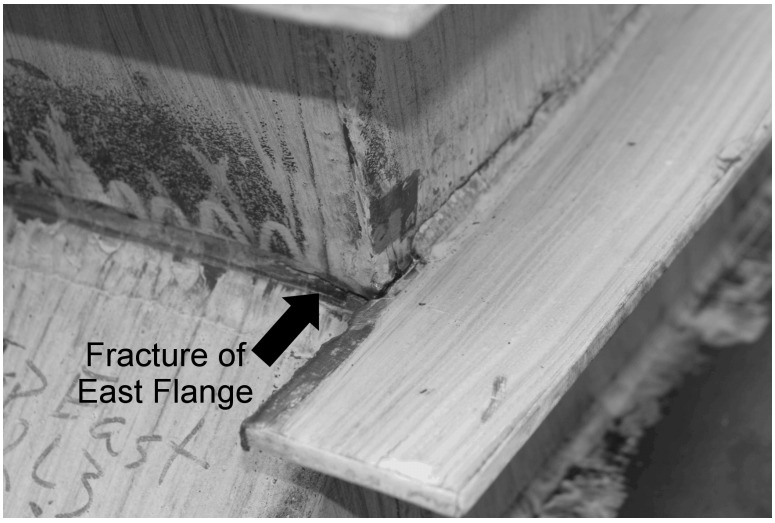

FIGURE 5-34 Fracture of Bottom East Flange of Specimen X2L2.1

5.3.9 Specimen X3L2.1

Figure 5-35 shows the link shear force versus rotation hysteresis curve for Specimen X3L2.1 and recorded peak shear forces and rotations for each sequence of loading are given in table 5-9. This specimen had web and flange compactness values well below the proposed limits for intermediate links and achieved two cycles at a rotation of 0.056 rads before suffering flange fracture in the subsequent cycle while attempting to achieve 0.066 rads. Data from the strain gages indicates outer fiber flange yielding during Sequence 4 and web yielding first occurring in Sequence 8. Figure 5-36 shows Specimen X3L2.1 at 0.056 rads during Cycle 2 of Sequence 8. The flange fracture resulting in the link failure occurred at all four flange ends and an example of the fracture after the testing was completed is shown in figure 5-37. The surface of that fracture is exposed in figure 5-38 where two fatigue striations are visible, indicating the fracture started two cycles before it propagated through the flange.

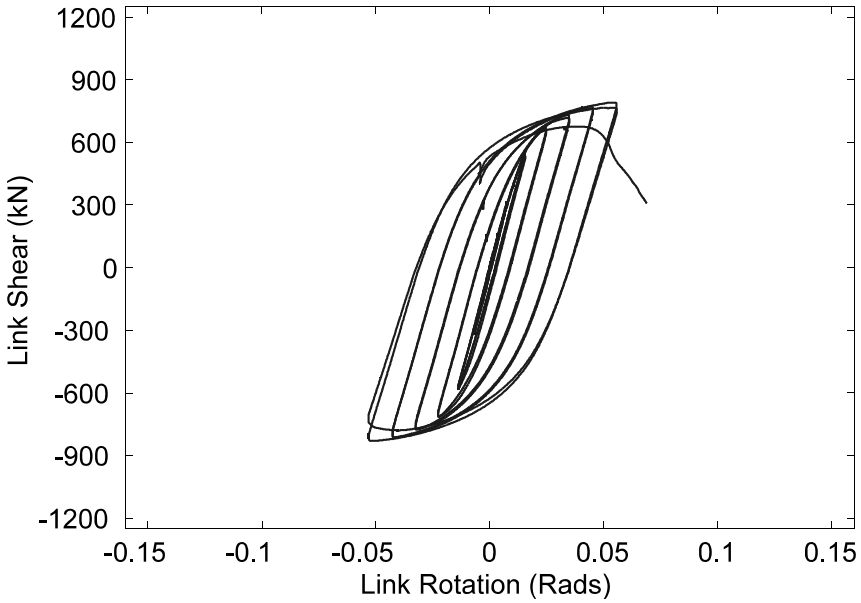

FIGURE 5-35 Link Shear vs. Rotation Hysteresis for Specimen X3L2.1

TABLE 5-9 Loading History for Specimen X3L2.1

Sequence Number	Cycles	γ (rads)	Link Shear (kN)	Sequence Number	Cycles	γ (rads)	Link Shear (kN)
1	3	0.0027	76	5	2	0.025	673
2	3	0.004	159	6	2	0.035	729
3	3	0.007	311	7	2	0.045	768
4	3	0.016	556	8	2	0.056	785

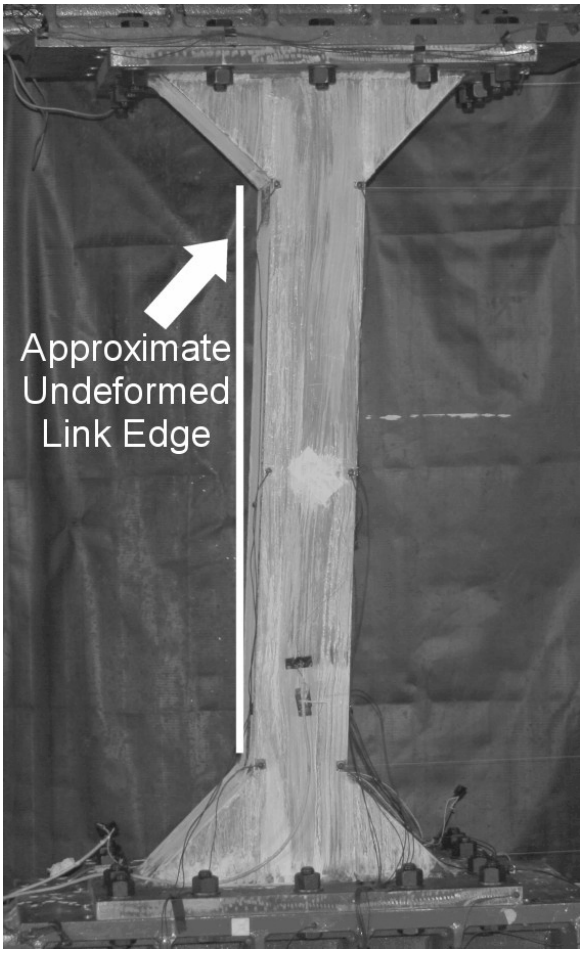

FIGURE 5-36 Specimen X3L2.1 at 0.056 rads During Cycle 2 of Sequence 8

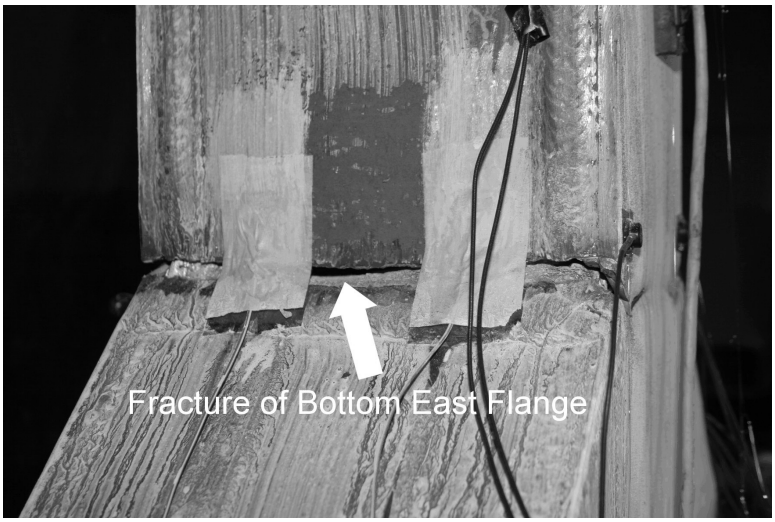

FIGURE 5-37 Fracture of the Bottom East Flange of Specimen X3L2.1 After Testing

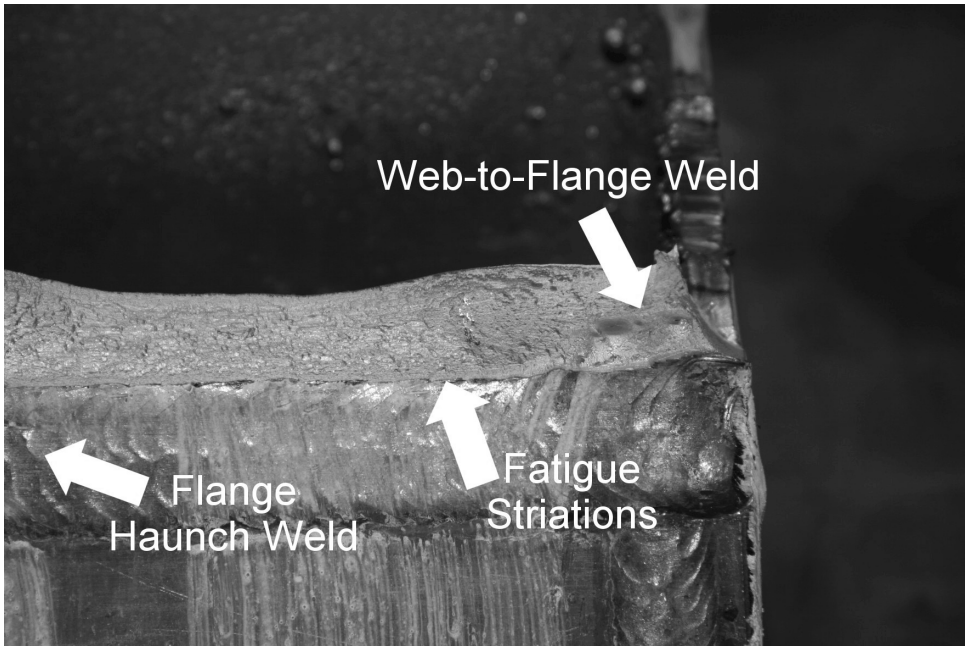

FIGURE 5-38 Fracture Surface of Bottom East Flange of Specimen X3L2.1

5.3.10 Specimen X1L3.0

Figure 5-39 shows the link shear force versus rotation hysteresis curve for Specimen X1L3.0 and recorded peak shear forces and rotations for each sequence of loading are given in table 5-10. This link had web and flange compactness values near the proposed limits for unstiffened cross-sections and had a normalized length in the flexural link range, corresponding to a target rotation of 0.02 rads. Specimen X1L3.0 sustained two cycles at a rotation of 0.058 rads prior to suffering flange fracture. The deformed link at -0.058 rads of Cycle 1 of Sequence 8 is shown in figure 5-40. Strain gage data indicates the webs remained elastic at the gage location for the duration of testing, while the flanges yielded during Sequence 3 and reached strains in excess of 10 times yield during Sequence 8. Flange buckling was noticed during Sequence 5 and caused modest strength reduction during Sequence 7. The magnitude of buckling of the bottom east flange after testing is shown in figure 5-41. Following buckling, fracture developed at all four flange ends. An example of a fracture in the web-to-flange weld on the top east flange is shown in figure 5-42 and that same fracture surface is shown in figure 5-43 where a single fatigue striation is visible.

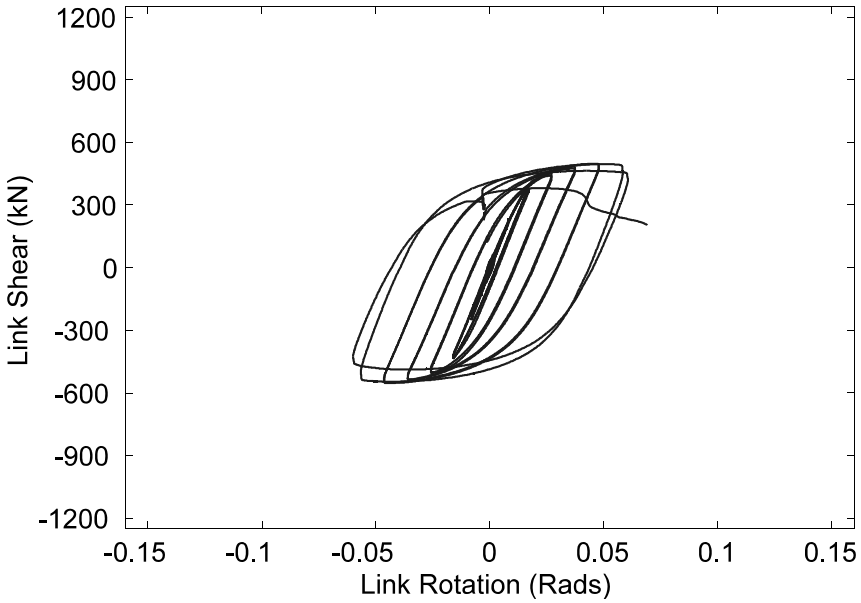

FIGURE 5-39 Link Shear vs. Rotation Hysteresis for Specimen X1L3.0

TABLE 5-10 Loading History for Specimen X1L3.0

Sequence Number	Cycles	γ (rads)	Link Shear (kN)	Sequence Number	Cycles	γ (rads)	Link Shear (kN)
1	3	0.0014	58	5	2	0.027	450
2	3	0.004	118	6	2	0.038	479
3	3	0.008	232	7	2	0.048	489
4	3	0.017	396	8	2	0.058	482

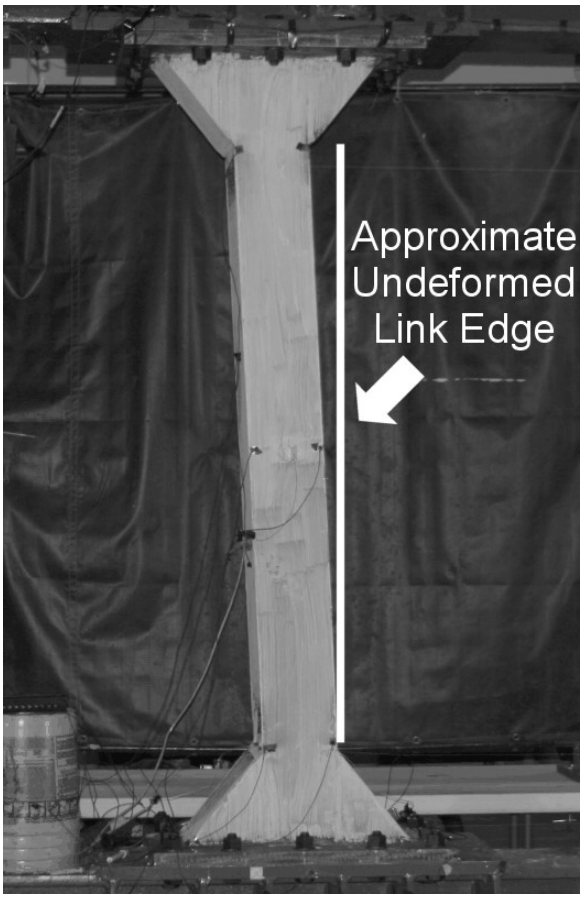

FIGURE 5-40 Specimen X1L3.0 at -0.058 rads During Cycle 1 of Sequence 8

FIGURE 5-41 Buckling Magnitude of Bottom East Flange of Specimen X1L3.9 Relative to a Straight Edge After Testing

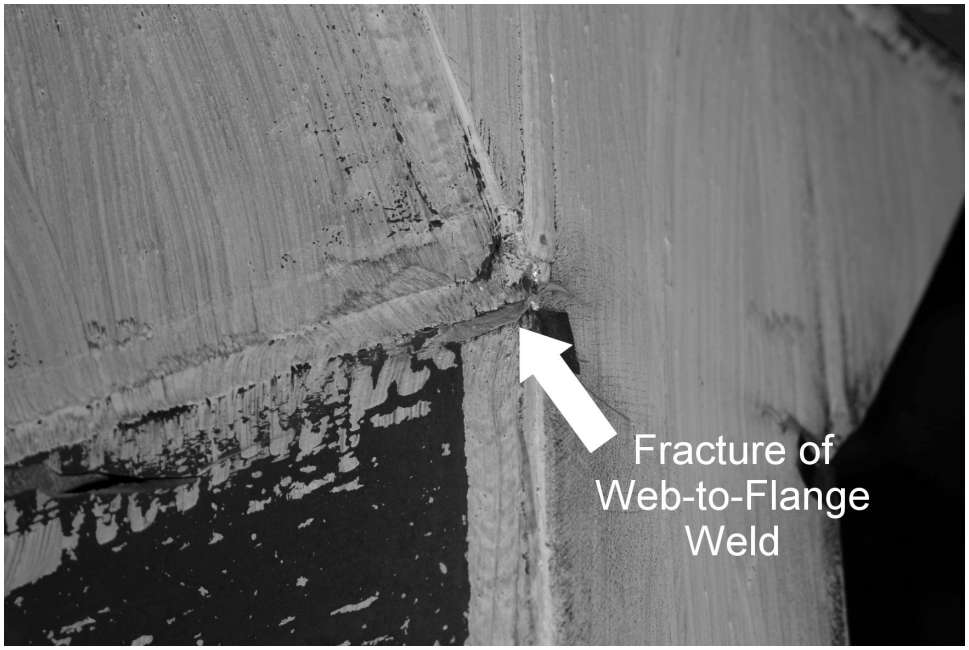

FIGURE 5-42 Fracture of Top East Flange Beginning in the Web-to-Flange Weld of Specimen X1L3.0

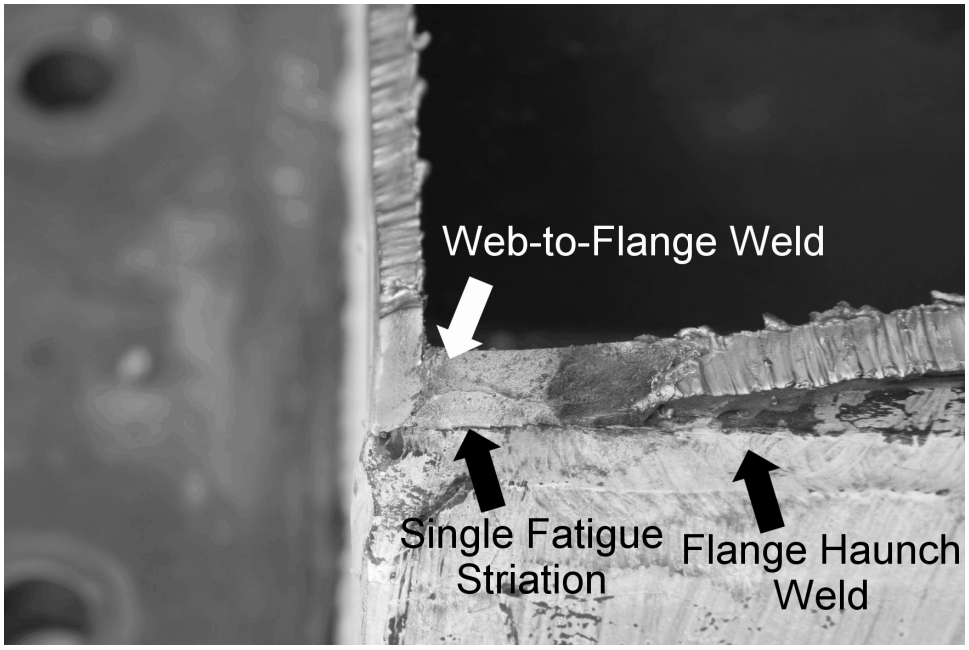

FIGURE 5-43 Fracture Surface of Top East Flange of Specimen X1L3.0

5.3.11 Specimen X2L3.0

Figure 5-44 shows the link shear force versus rotation hysteresis curve for Specimen X2L3.0 and recorded peak shear forces and rotations for each sequence of loading are given in table 5-11. This link had a web compactness value larger than the proposed maximum for flexural links, a flange compactness value near the proposed limit, and a normalized length well into the flexural link category. Specimen X2L3.0 achieved two cycles at a rotation of 0.044 rads, more than twice the target rotation for flexural links of 0.02 rads, before degrading severely during the following sequence. Figure 5-45 shows the link deformation at -0.044 rads during Cycle 2 of Sequence 7. Strain gage data indicates the outer fiber yielding of the flanges during Sequence 3. Visible web buckling preceded flange buckling but both became visible during Sequence 5 and had caused some strength degradation by Sequence 7. Figures 5-46 and 5-47 respectively, show the web and flange buckling after testing. The buckling, as well as the restraint at the web-to-flange weld near the flange haunch, caused fracture of the flange extending into the web during Sequence 8 at all four flange ends. An example of this fracture is shown in figure 5-48.

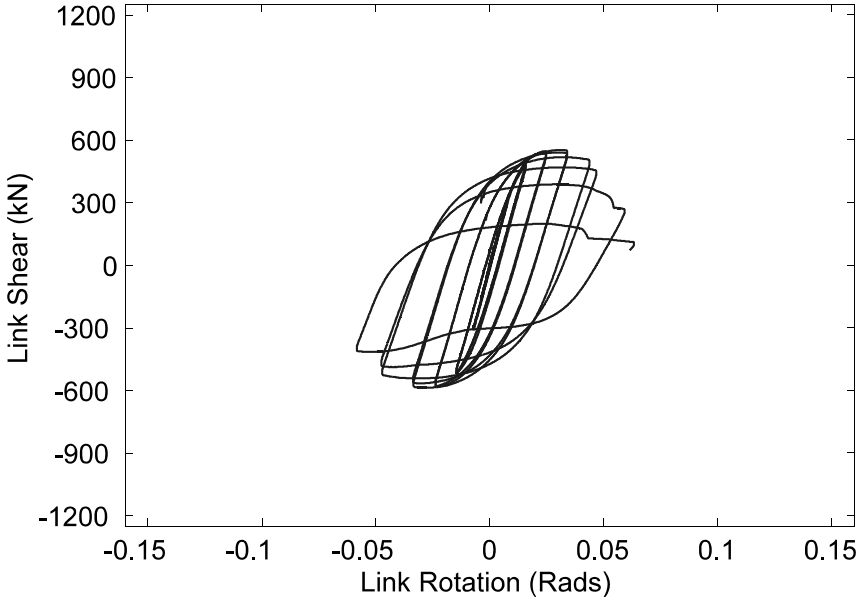

FIGURE 5-44 Link Shear vs. Rotation Hysteresis for Specimen X2L3.0

TABLE 5-11 Loading History for Specimen X2L3.0

Sequence Number	Cycles	γ (rads)	Link Shear (kN)	Sequence Number	Cycles	γ (rads)	Link Shear (kN)
1	3	0.0018	83	5	2	0.025	544
2	3	0.004	162	6	2	0.034	531
3	3	0.008	307	7	2	0.044	452
4	3	0.016	491	8	2	0.060	265

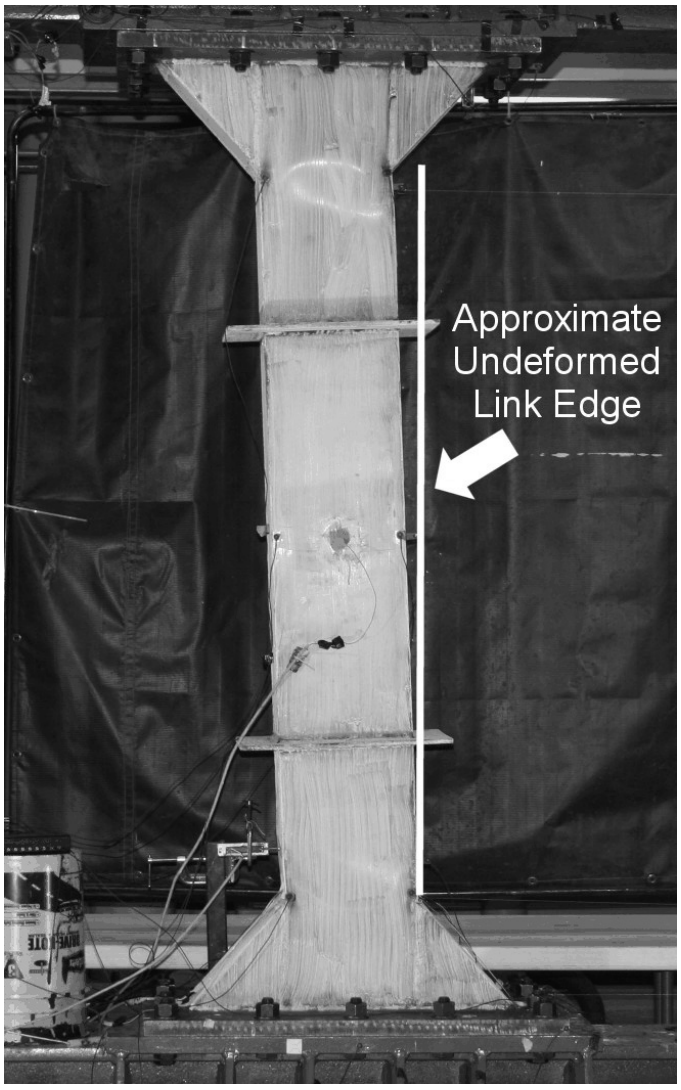

FIGURE 5-45 Specimen X2L3.0 at -0.044 rads During Cycle 2 of Sequence 7

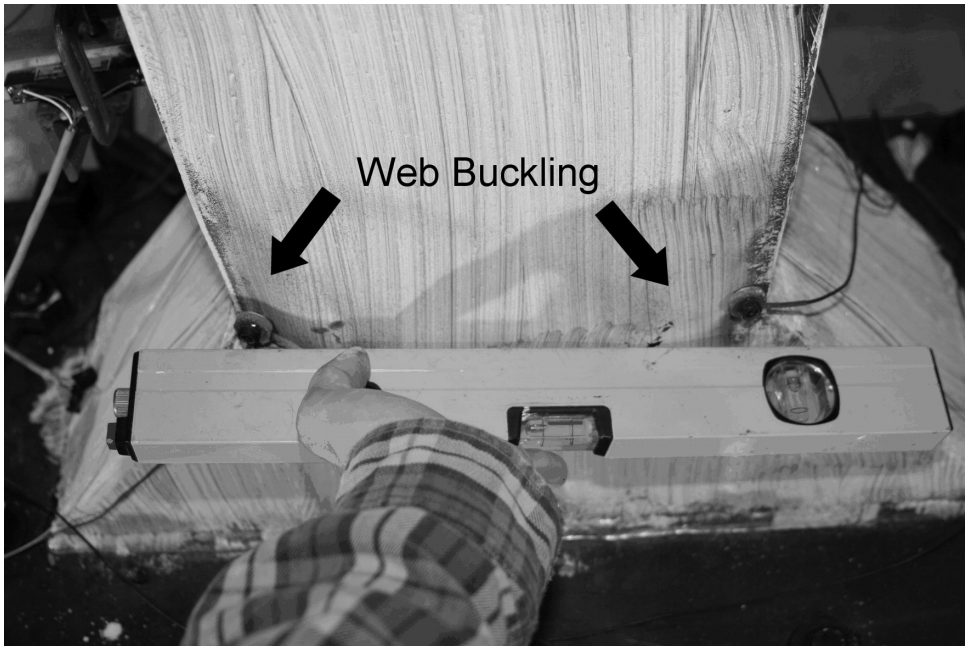

FIGURE 5-46 Buckling Magnitude of Lower North Web Relative to a Straight Edge After Testing of Specimen X2L3.0

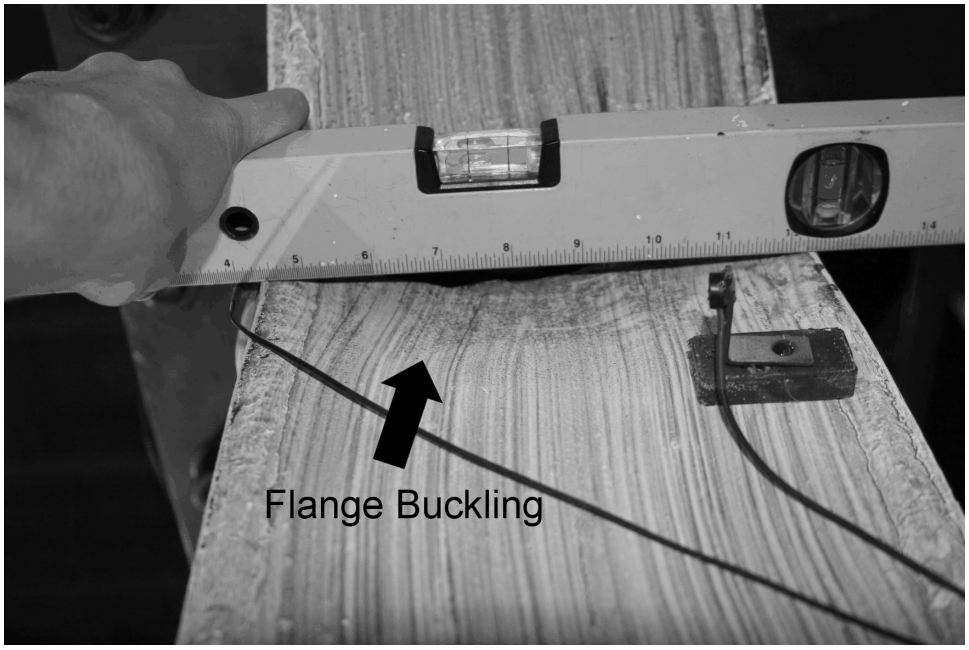

FIGURE 5-47 Buckling Magnitude of Top West Flange Relative to a Straight Edge After Testing of Specimen X2L3.0

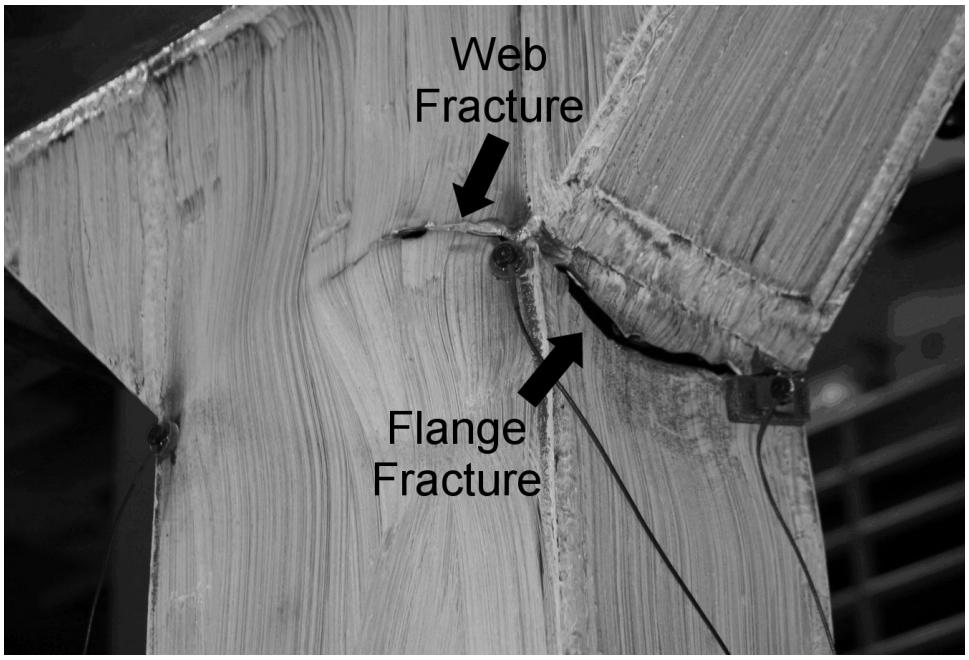

FIGURE 5-48 Web and Flange Fracture at Top of Specimen X2L3.0 During Cycle 2 of Sequence 8

5.3.12 Specimen X3L3.0

Figure 5-49 shows the link shear force versus rotation hysteresis curve for Specimen X3L3.0 and recorded peak shear forces and rotations for each sequence of loading are given in table 5-12. This link had web and flange compactness values well below the proposed limits and a normalized length well into the flexural category. The specimen suffered flange fractures during the first cycle of Sequence 9 at 0.07 rads after completing two full cycles at 0.059 rads during Sequence 8. Figure 5-50 shows Specimen X3L3.0 at -0.059 rads during Cycle 2 of Sequence 8. Strain gage data indicates that yielding of the outer flange fiber occurred during Sequence 4 with strains reaching 10 times the yield strain by Sequence 7. Fractures developed at all four flange ends and began in the web-to-flange weld adjacent to the flange haunch weld where the restraint against plastic flow is high and large triaxial stresses develop. An example of the fractures is shown in figures 5-51 and 5-52, the former is during Sequence 9 and the ladder is after testing was complete. No buckling of either the flanges or webs was observed during the testing of Specimen X3L3.0.

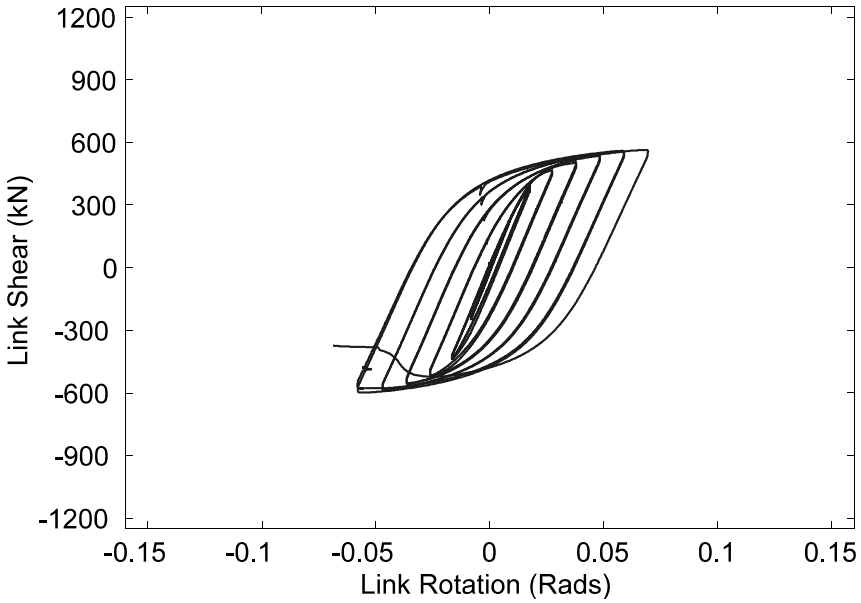

FIGURE 5-49 Link Shear vs. Rotation Hysteresis for Specimen X2L3.0

TABLE 5-12 Loading History for Specimen X3L3.0

Sequence Number	Cycles	γ (rads)	Link Shear (kN)	Sequence Number	Cycles	γ (rads)	Link Shear (kN)
1	3	0.0019	55	6	2	0.038	500
2	3	0.004	115	7	2	0.048	530
3	3	0.009	222	8	2	0.059	550
4	3	0.018	396	9	1	0.070	557
5	2	0.027	461				

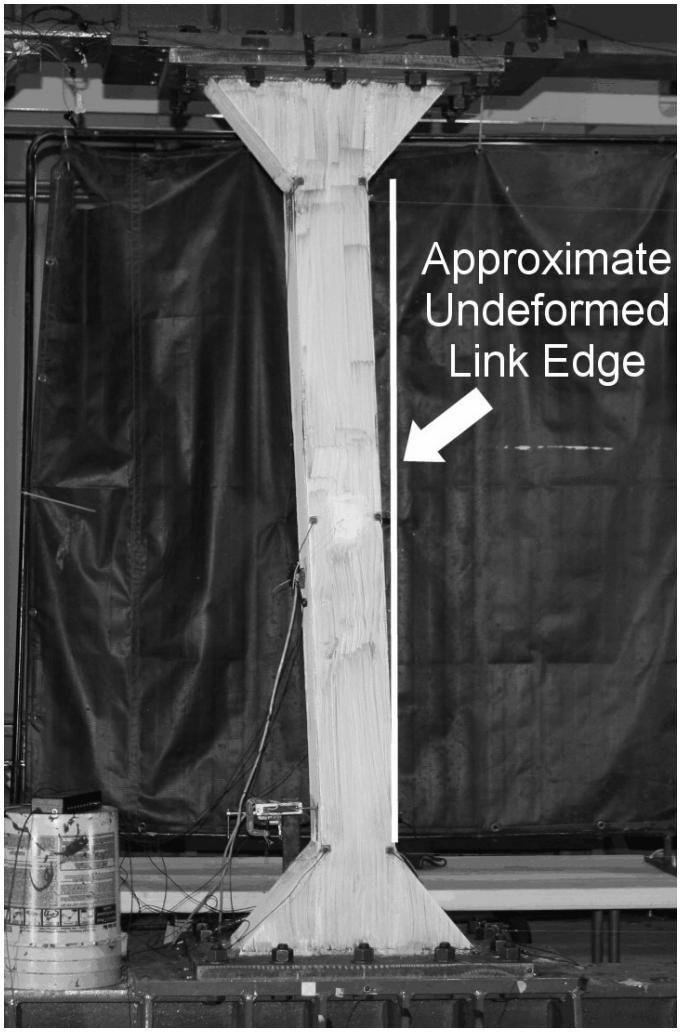

FIGURE 5-50 Specimen X3L3.0 at -0.059 rads During Cycle 2 of Sequence 8

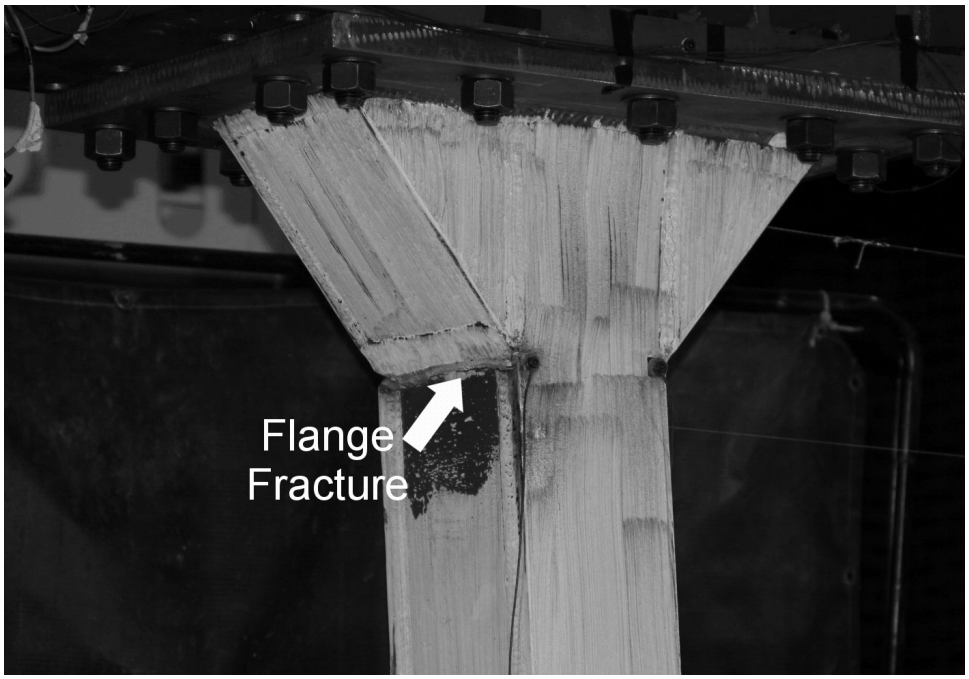

FIGURE 5-51 Fracture of Top East Flange of Specimen X3L3.0 During Cycle 1 of Sequence 9

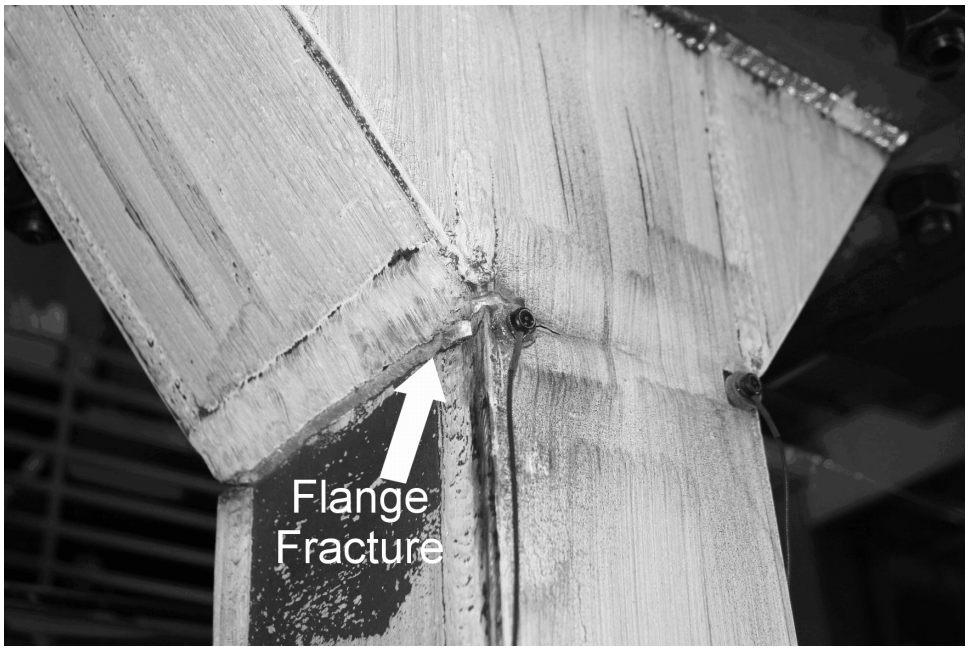

FIGURE 5-52 Top East Flange Fracture of Specimen X3L3.0 After Testing

5.3.13 Specimen AX1L1.6

Figure 5-53 shows the link shear force versus rotation hysteresis curve for Specimen AX1L1.6 and recorded peak shear forces and rotations for each sequence of loading are given in table 5-13. This link had web and flange compactness values near the proposed limits for unstiffened cross-sections and a normalized length at the transition point between shear and intermediate link classifications. While the cross-section and link length are identical to Specimen X1L1.6, Specimen AX1L1.6 utilized the alternate end connection described in Section 4.5 that was intended to delay the flange fracture mode observed in Specimen X1L1.6. This link sustained a single cycle at 0.068 rads of rotation prior to strength degradation from failure of the weld connection the gusset stiffeners to the flanges as described below. It should be noted that the link was subjected to five cycles at rotations between 0.06 and 0.07 rads as the end connections began to contribute more significantly to those rotations and effectively increased the link length as described below. As mentioned above, the actuator displacement was the control parameter and the Krypton LEDs at the active link ends (i.e. between the two end connections) were used to calculate the rotation achieved. Therefore, when the end connection began to participate in the rotation, the programmed actuator displacement was not large enough to create the desired rotation between the end connections, resulting in five cycles of similar rotation across the active link length, despite the increase in actuator displacement. Strain gage data indicates that outer flange yielding first occurred during Sequence 4 while web yielding first occurred during Sequence 5. By Sequence 8, the flange strain gages indicated strains on the order of 10 times yield and the web gages indicated strains of 4.5 times yield.

TABLE 5-13 Loading History for Specimen AX1L1.6

Sequence Number	Cycles	γ (rads)	Link Shear (kN)	Sequence Number	Cycles	γ (rads)	Link Shear (kN)
1	3	0.0017	83	7	2	0.042	720
2	3	0.003	172	8	2	0.051	752
3	3	0.006	337	9	2	0.060	777
4	3	0.013	566	10	2	0.062	719
5	2	0.023	637	11	1	0.068	684
6	2	0.034	675				

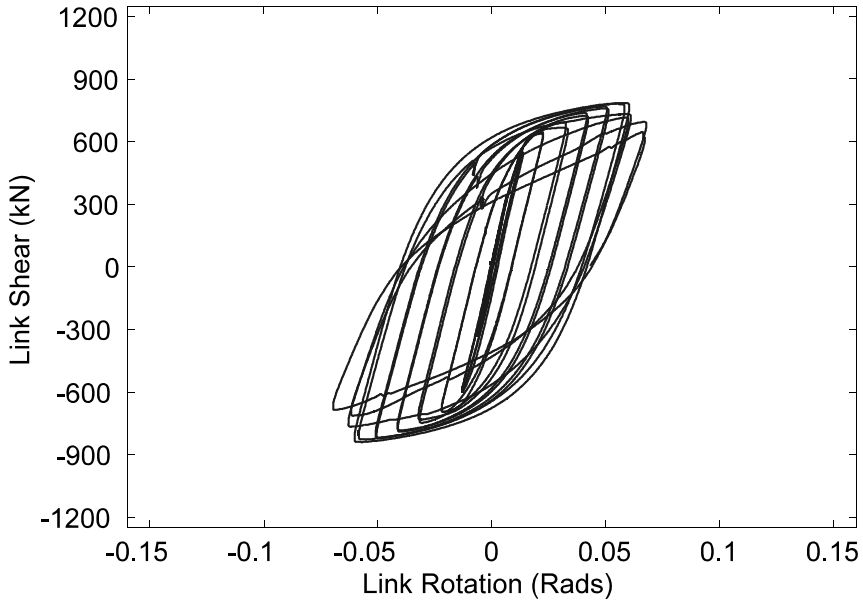

FIGURE 5-53 Link Shear vs. Rotation Hysteresis for Specimen AX1L1.6

As opposed to the links with haunch end connections, Specimen AX1L1.6 had some yielding of the end connection indicated by whitewash flaking off the gusset stiffener, occurring during Sequence 8 and shown in figure 5-54. Despite this, the behavior of the link between the end connections was similar to those previously tested. The deformed link at the negative peak of Cycle 1 of Sequence 9 is shown in figure 5-55. At the end of Sequence 9, small cracks in the bottom gusset stiffener were observed and are shown in figure 5-56.

During Sequence 10 these fractures began to open further as shown in figure 5-57. Similar fractures were observed in the gusset stiffener at the top. This did not immediately cause link failure however, but rather increased the effective link length as the flexural hinges moved toward the end-plates, as shown in figure 5-58. Severe strength degradation occurred when the welds connecting the end plate began to fracture during Sequence 11. Additionally, by the end of the loading history the gusset stiffener had completely separated from the link flange as shown in figure 5-59.

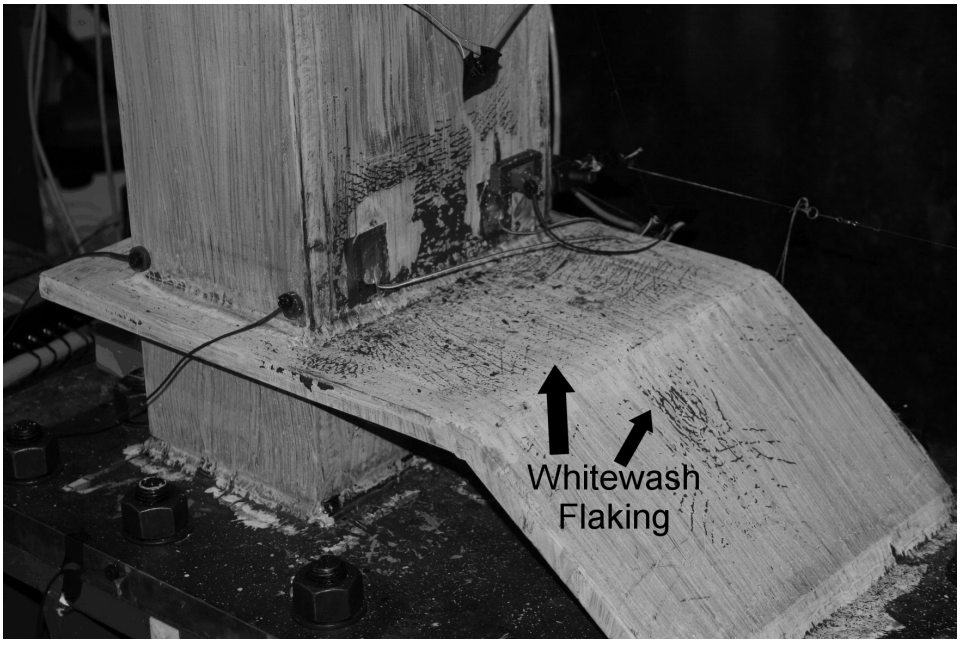

FIGURE 5-54 Whitewash Flaking off of Gusset Stiffener of AX1L1.6 After Sequence 8

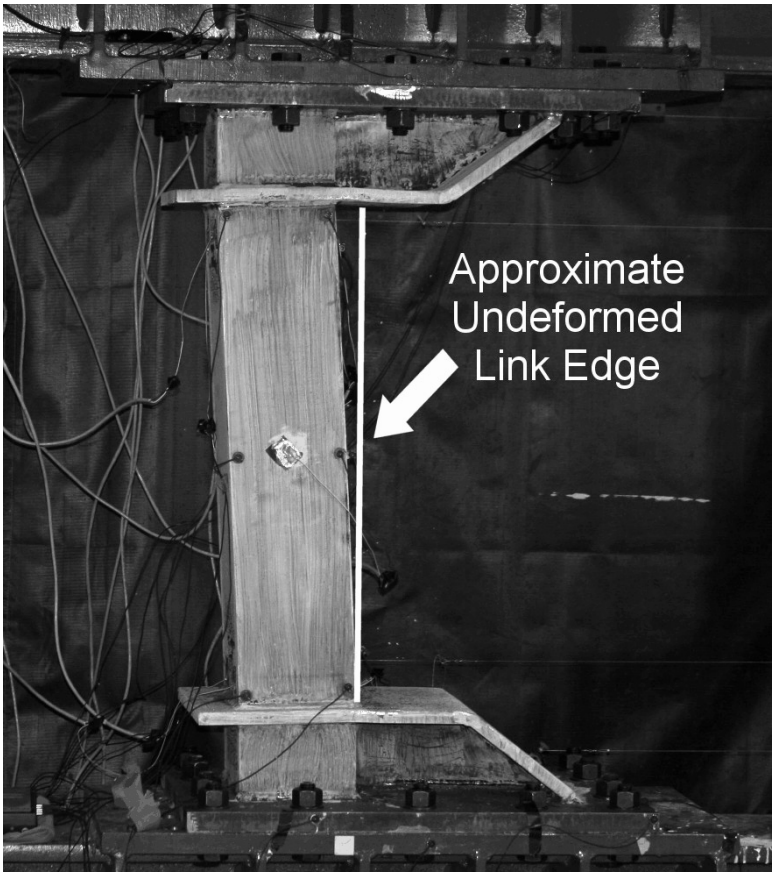

FIGURE 5-55 Specimen AX1L1.6 at -0.06 rads of Rotation During Cycle 1 of Sequence 9

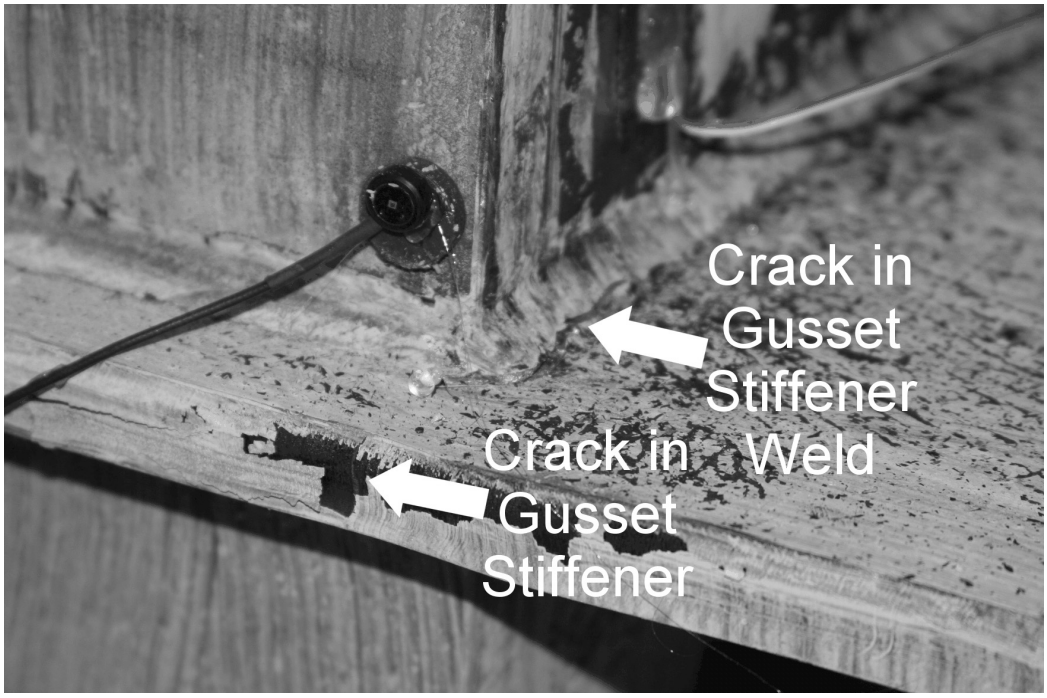

FIGURE 5-56 Initial Cracking of Bottom Gusset Stiffener and Weld on Specimen AX1L1.6 After Sequence 9

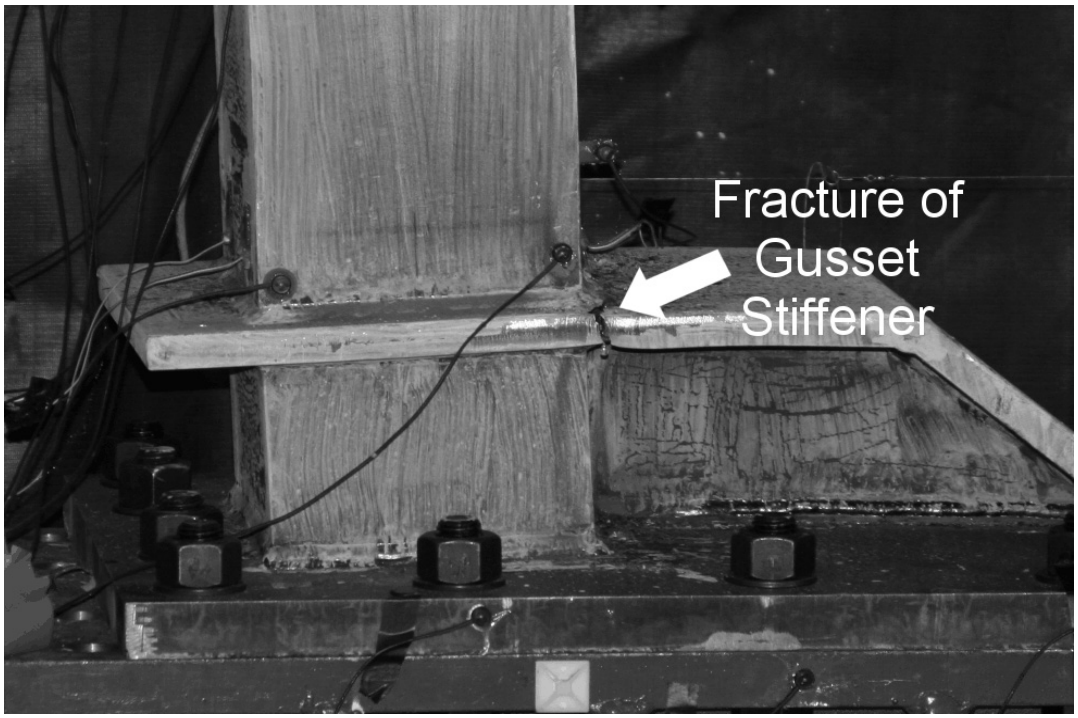

FIGURE 5-57 Fracture of Gusset Stiffener of AX1L1.6 During Cycle 1 of Sequence 10

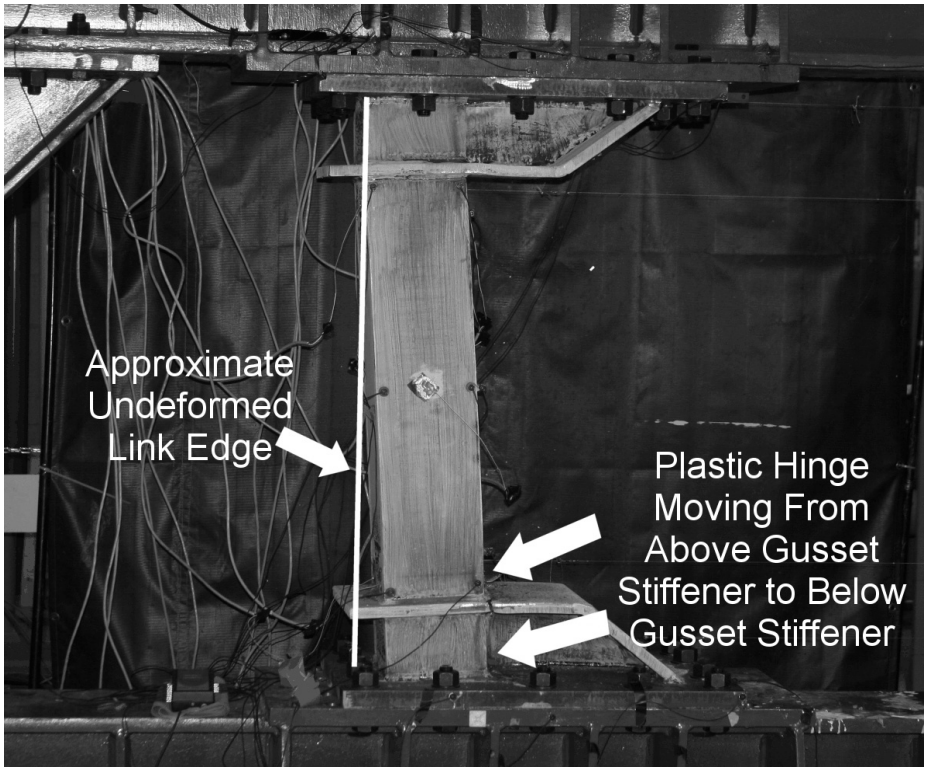

FIGURE 5-58 Gusset Stiffener Fracture and Plastic Hinge Movement During Cycle 1 of Sequence 10 for AX1L1.6

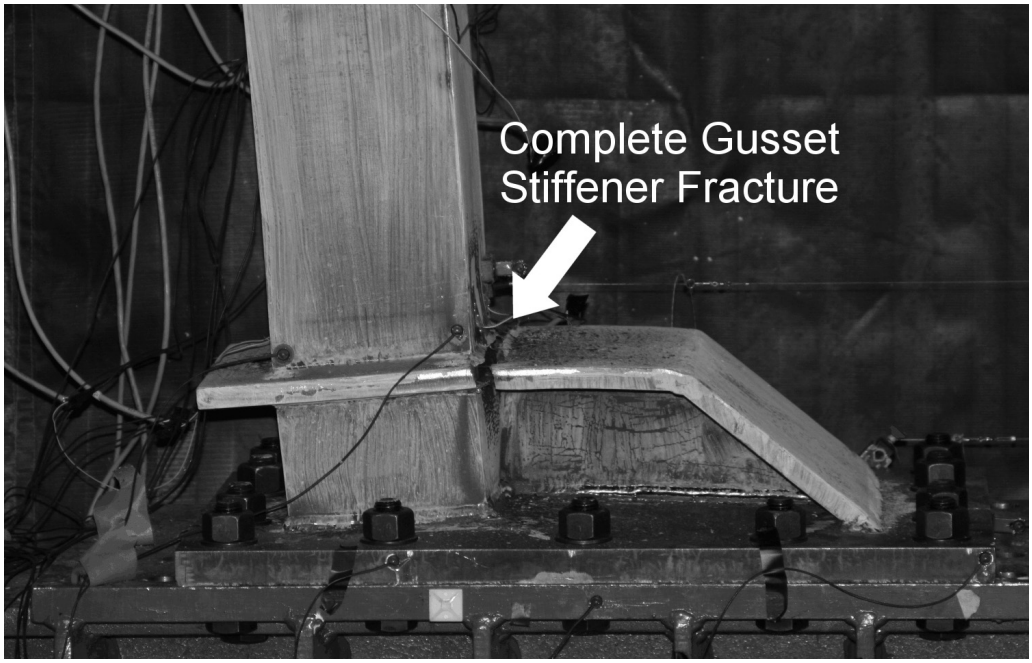

FIGURE 5-59 Complete Gusset Stiffener Fracture of AX1L1.6 During Cycle 1 of Sequence 11

5.3.14 Specimen AX2L1.6

Figure 5-60 shows the link shear force versus rotation hysteresis curve for Specimen AX2L1.6. Recorded peak shear forces and rotations for each sequence of loading are given in table 5-14. This link had web and flange compactness values near the proposed limits for unstiffened cross-sections and a normalized length at the transition point between shear and intermediate link classifications. While the cross-section and link length is identical to Specimen X2L1.6, Specimen AX2L1.6 utilized the alternate end connection described in Section 4.5 that was intended to delay the flange fracture mode observed in Specimen X2L1.6. Furthermore, recall from Section 5.2, the loading protocol used for this link was from the 2005 AISC Seismic Provisions and is somewhat less severe than the protocol from the 2002 AISC Seismic Provisions that was used for the other links described in this section. This specimen sustained a full cycle at 0.123 rads of rotation prior to suffering flange fracture during the negative excursion of the following cycle to 0.140 rads as described below. Strain gage data indicates outer fiber yielding of the flange first occurring during Sequence 4 and web yielding first occurring during Sequence 5. By Sequence 10, the flange strains had increased to approximately 12 times the yield value and the web strains had grown to approximately10 times the yield shear strain.

TABLE 5-14 Loading History for Specimen AX2L1.6

Sequence Number	Cycles	γ (rads)	Link Shear (kN)	Sequence Number	Cycles	γ (rads)	Link Shear (kN)
1	6	0.002	169	7	2	0.033	823
2	6	0.005	339	8	1	0.043	842
3	6	0.009	564	9	1	0.058	879
4	6	0.011	660	10	1	0.081	925
5	4	0.019	740	11	1	0.098	966
6	4	0.023	770	12	1	0.123	998

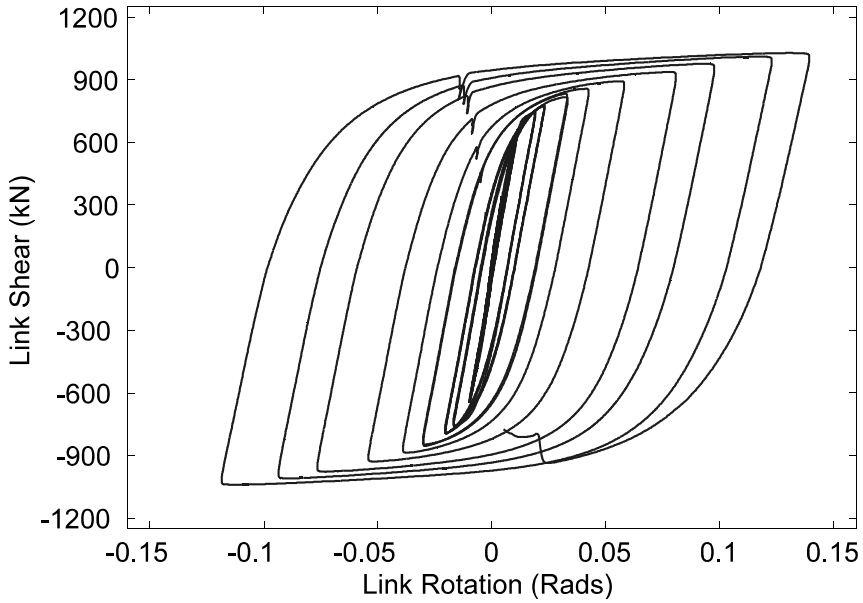

FIGURE 5-60 Link Shear vs. Rotation Hysteresis for Specimen AX2L1.6

As with Specimen AX1L1.6, the gusset stiffeners of Specimen AX2L1.6 also showed some whitewash flaking, indicating some nonlinear behavior of the end connection, as shown in figure 5-61. However, the behavior of the link between the end connections was similar to those previously tested. Figure 5-62 shows the link deformation at the 0.098 rad peak during Sequence 11. No fractures of the gusset stiffener, such as those noted for Specimen AX1L1.6, were observed for Specimen AX2L1.6. Instead the failure mode was very similar to that of the proof-of-concept test specimen described in Berman and Bruneau (2005a), that is fracture of the link flange adjacent to the toe of the weld that connects the gusset stiffener to the flange, as shown in figure 5-63. This fracture occurred after considerable flange buckling was noted in the same location. Flange buckling became visible during Sequence 10 and occurred at the same location in both the top and bottom connection regions. Flange buckling near the bottom end connection during Sequence 10 is shown in figure 5-64 and flange and gusset stiffener buckling near the top end connection after testing is shown in figure 5-65.

FIGURE 5-61 Whitewash Flaking on End Connection of AX2L1.6 After Sequence 5

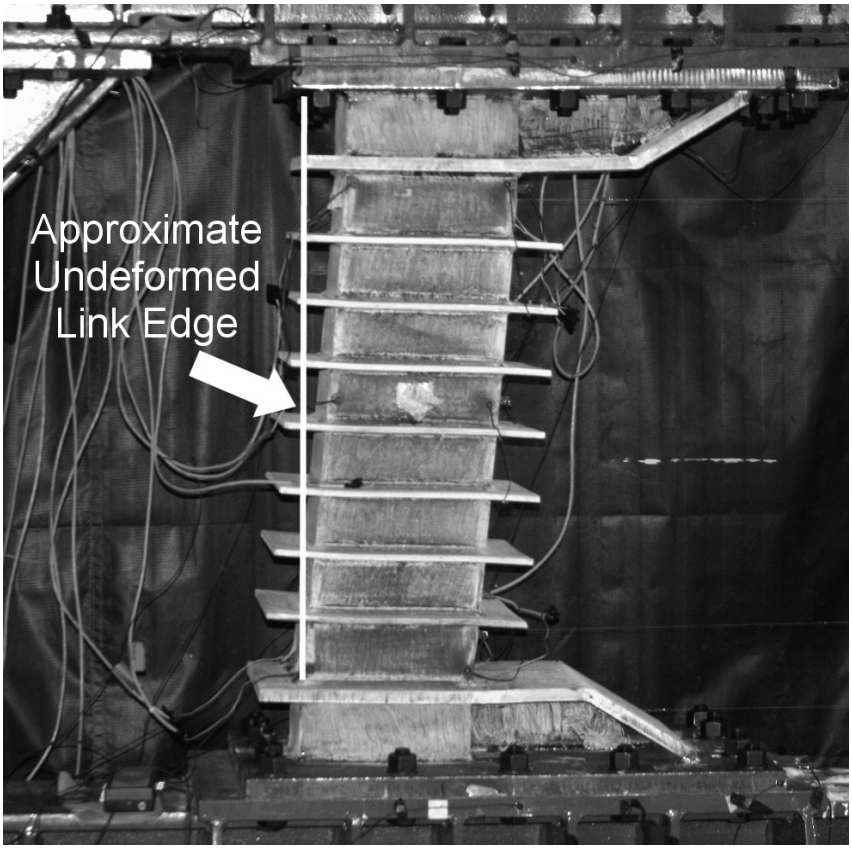

FIGURE 5-62 Specimen AX2L1.6 at 0.098 rads of Rotation During Cycle of Sequence 11

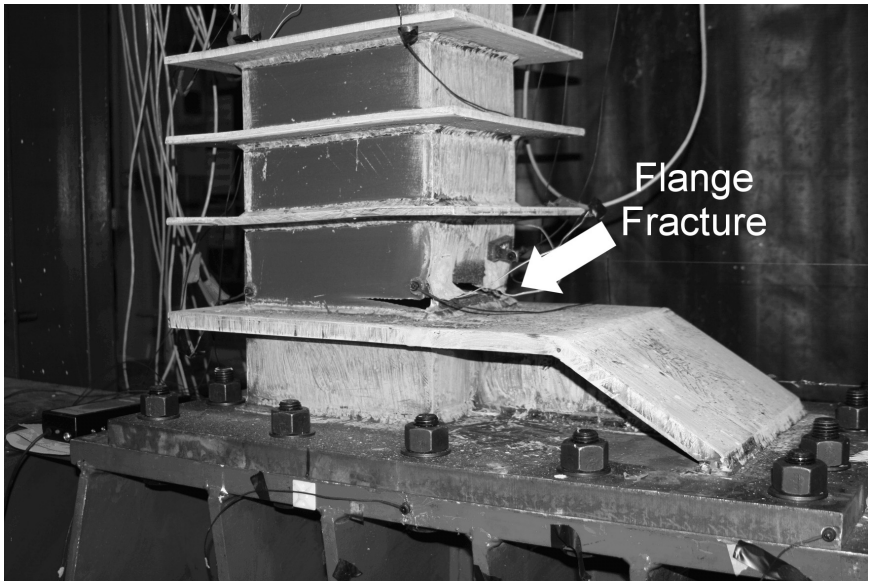

FIGURE 5-63 Flange Fracture of Specimen AX2L1.6 Near End Connection During Cycle 1 of Sequence 13

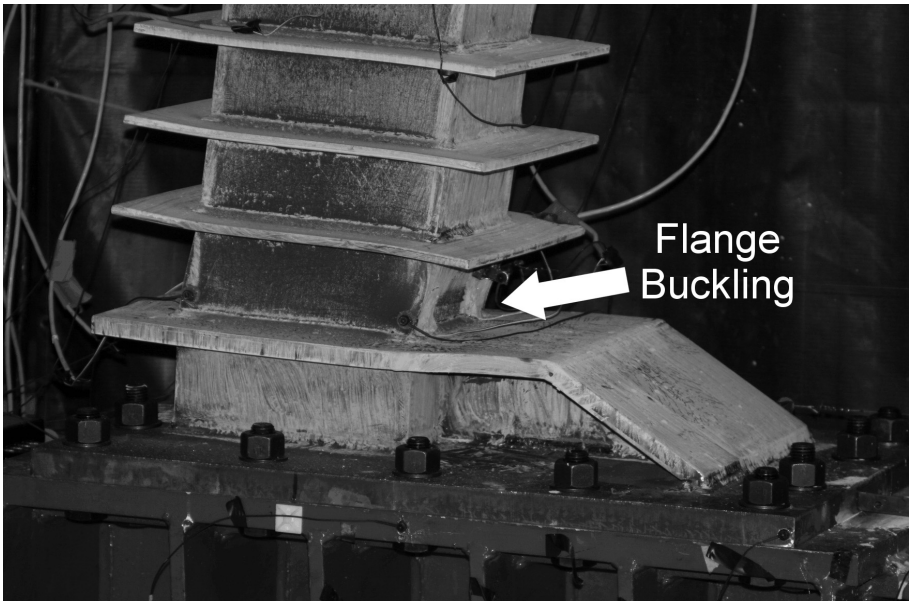

FIGURE 5-64 Flange Buckling of Specimen AX2L1.6 Near Bottom End Connection During Cycle 1 of Sequence 10

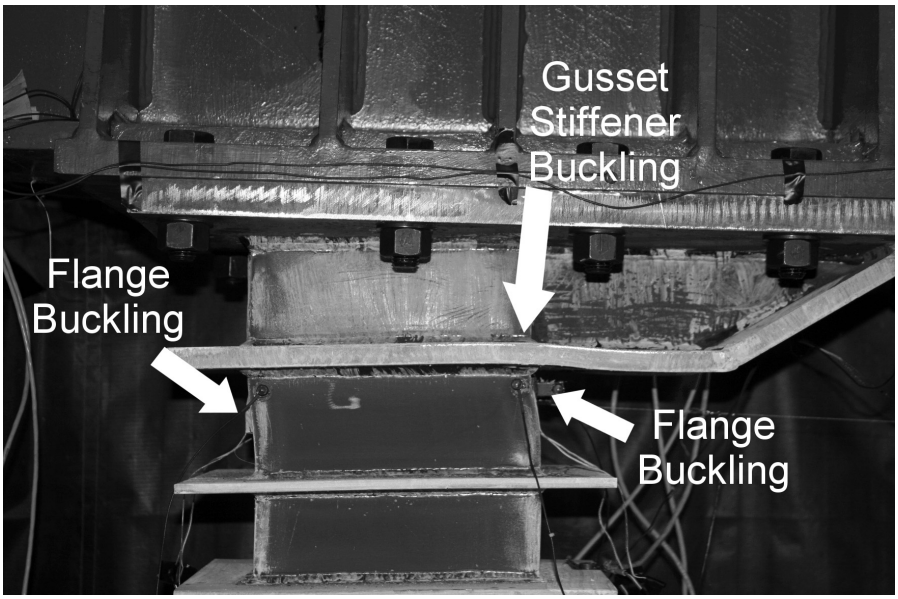

FIGURE 5-65 Flange and Stiffener Buckling of Specimen AX2L1.6 After Testing

5.4 Summary

Qualitative experimental observations have been given for each of the fourteen links tested as part of the experimental program to complement the finite element results used to develop proposed design rules for hybrid rectangular links for eccentrically braced frames. All links with the haunch end connections had generally the same failure mode: fracture of the link flanges near the weld connecting the flange haunch plate. Inspection of several of the fracture surfaces indicates that the fractures typically began in the web-to-flange connection, which was a full-penetration groove weld, adjacent to the flange haunch weld. The web haunch weld also terminates near this location. The intersection of these welds and plates causes high restraint against plastic flow in the flange and increases triaxial stresses, which are conditions that lead to eventual fracture.

The links with a normalized link length of 1.2 all achieved and exceeded their target rotation, which is the proposed rotation limit for shear links of 0.08 rads. None of the links with a normalized length of 1.6 and haunch end connections reached their target rotation as they all suffered flange fracture after completing sequences at rotations of approximately 0.065 rads. Of the specimens with a normalized length of 2.1 (intermediate links), the two links satisfying the proposed design rules, X1L2.1 and X3L2.1, met their target rotation of 0.05

rads, while the one not satisfying the proposed requirements, Specimen X2L2.1, did not reach its target rotation. All links tested that had normalized length of 3.0, i.e. flexural links, reached rotation levels exceeding their target rotations of 0.02 rads, despite the fact that one of them had compactness values exceeding the proposed limits (i.e., Specimen X2L3.0).

The two specimens with revised connections to the end-plates, AX1L1.6 and AX2L1.6, were tested to determine if this modification would increase the rotation capacity of the links with a normalized length of 1.6, since none of the specimens with the haunch end connections and this normalized length reached their target rotation. Conceptually, the revised end connections more closely resemble the gusset, stiffener, and brace configuration used at the link ends in the proof-of-concept testing. The goal of the connection was to delay the flange fracture initiated in the web-to-flange weld that occurred in Specimens X1L1.6, X2L1.6, and X3L1.6 by reducing the restraint against plastic flow and triaxial stresses in the flange at that location. To accomplish this, the web haunch plates were eliminated and replaced by a gusset located at the middle of the flange, away from the web-to-flange full penetration weld. Additionally, the flange haunch was eliminated in favor of a stiffener around the entire cross-section and attached to the gusset, similar to the configuration used in the proof-of-concept testing.

Specimen AX1L1.6 did not achieve its target rotation (0.08 rads) as it suffered fracture of the gusset stiffener of the end connection after one cycle at 0.068 rads. Specimen AX2L1.6 reached and exceeded its target rotation (0.08 rads) prior to suffering flange fracture near the end connection after completing a cycle at 0.123 rads. However, this final specimen was tested under the loading protocol in the 2005 AISC Seismic Provisions that is less severe for large rotations than the protocol of the 2002 AISC Seismic Provisions that was used for all other link specimens. By changing the link end connection and loading protocol the maximum link rotation increased from 0.067 rads for Specimen X2L1.6 to 0.123 rads for Specimen AX2L1.6. The results of the link testing discussed in this section are investigated further in Section 6.

SECTION 6
LINK TESTING RESULTS AND ANALYSIS

6.1 General

This section discusses, in quantitative detail, the results of the link testing program described in Sections 4 and 5. First, rotation capacity, and energy dissipation results are examined for the 12 primary links, which had three different cross-sections, four different normalized link lengths, and utilized the haunch end connection. The results for those specimens, which were tested using the loading protocol of the 2002 AISC Seismic Provisions, are then extrapolated to estimate the maximum rotations that would be achieved considering the new loading protocol in the 2005 AISC Seismic Provisions (AISC, 2005). Two different approaches are used for extrapolation. Next, the results of the two supplementary link tests are discussed in the perspective of improving the performance by delaying the flange fracture mode and improving the rotation capacity with the revised end connection. Following this, a discussion of the overstrength observed in tubular links for eccentrically braced frames is provided, as this is important for capacity design of surrounding framing. Cumulative plastic strain in the link flanges, near the end connections, is then presented and comparisons between specimens of different link lengths and end connection types are made. The experimental results are then compared with finite element analysis results considering models that utilize the geometry and material properties of the link specimens. Finally, recommendations regarding the proposed design requirements for hybrid rectangular (tubular) links are given in the context of the presented experimental results. Table 6-1 summarizes the results for the link specimens with haunch end connections and will be referenced throughout this section, where γ_{targ} is the target rotation (i.e., the maximum code specified rotation for that link length), γ_{lim} is the limit rotations obtained from the experimental results, γ_{plim} is the plastic rotation corresponding the limit rotation γ_{lim}, γ_{pcum}

is the cumulative plastic rotation, V_p and M_p are, respectively, the plastic link shear strength and plastic moment strength calculated using nominal material properties, V_{max} is the maximum link shear force obtained during the testing, and M_{max} is the maximum end moment obtained during the testing.

TABLE 6-1 Summary of Experimental Results for Link Specimens with Haunch End Connections

Specimen Name	γ_{targ} (rads)	γ_{lim} (rads)	γ_{plim} (rads)	γ_{pcum} (rads)	V_p (kN)	M_p (kN-m)	V_{max} (kN)	M_{max} (kN-m)
X1L1.2	0.080	0.103	0.090	2.09	554	266	981	283
X2L1.2	0.080	0.097	0.087	1.95	610	278	1024	312
X3L1.2	0.080	0.100	0.086	1.83	578	297	1164	336
X1L1.6	0.080	0.065	0.050	0.68	554	266	907	349
X2L1.6	0.080	0.055	0.040	0.60	610	278	936	360
X3L1.6	0.080	0.064	0.045	0.74	578	297	1017	391
X1L2.1	0.050	0.056	0.038	0.50	554	266	781	394
X2L2.1	0.050	0.042	0.027	0.29	610	278	779	401
X3L2.1	0.050	0.056	0.037	0.40	578	297	831	419
X1L3.0	0.020	0.060	0.043	0.46	554	266	555	400
X2L3.0	0.020	0.048	0.035	0.49	610	278	587	429
X3L3.0	0.020	0.059	0.037	0.47	578	297	599	432

6.2 Rotation Results

6.2.1 Limit Total Rotation and Limit Plastic Rotation

The rotation capacity of the link specimens is the primary factor considered in assessing the adequacy of the proposed design requirements that were revised in Section 3.5.4. Links with normalized lengths of 1.2 and 1.6 should sustain one complete cycle at a total rotation of 0.08 rads, while links with normalized lengths of 2.1 and 3.0 should sustain one complete cycle at total rotations of 0.05 rads and 0.02 rads, respectively. These requirements are

consistent with the 2002 AISC Seismic Design Provisions (AISC, 2002) and have been used in bridge applications (Itani, 1997, and Dusicka et al., 2002).

Table 6-1 contains the target rotations, γ_{targ}, and limit rotations (i.e., the maximum rotation for which the links sustained full cycle of loading before 20% strength degradation occurred as described in Section 3.4), γ_{lim}, and figure 6-1 shows the limit rotation for each link specimen versus normalized link length (not including the supplementary links). The solid line in the figure is the target rotation curve. As shown, there are four links that did not achieve their target rotation, namely, all three links with a normalized length of 1.6, and Specimen X2L2.1. Recall that Specimen X2L2.1 did not satisfy the proposed design requirements because it had a web compactness ratio near $d'/t_w \le 1.67\sqrt{E_s/F_{yw}}$, which exceeds the limit for intermediate links of $d'/t_w \le 0.64\sqrt{E_s/F_{yw}}$. This leaves the three links with a normalized length of 1.6 as the specimens that satisfied the proposed design requirements but did not achieve their target rotation due to flange fracture.

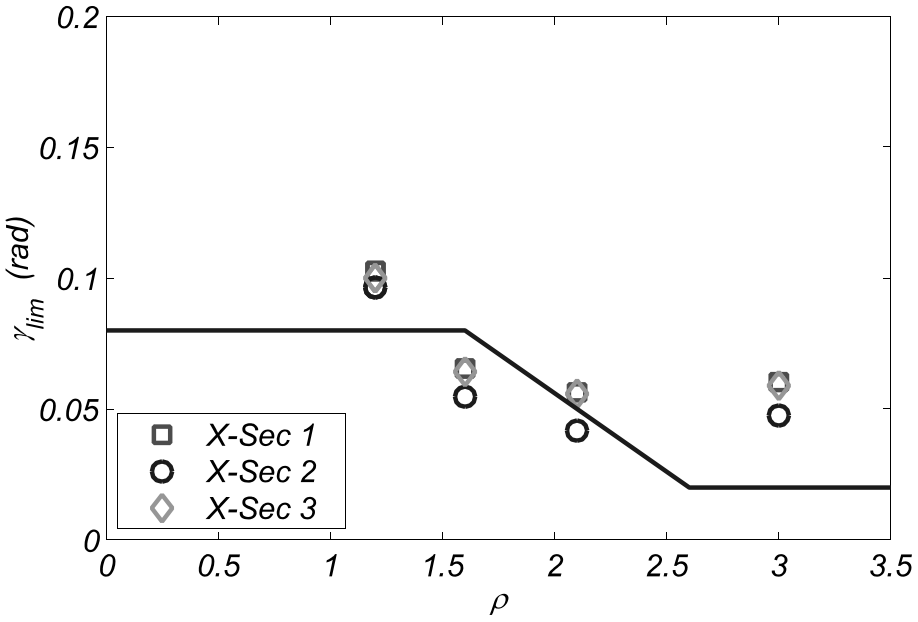

FIGURE 6-1 Total Rotation vs. Link Length for Link Test Specimens with Haunch End Connections

It is interesting to note that the rotation capacity of the links seems to increase with respect to normalized length when those lengths are above the transition point of intermediate to

flexural behavior. This is logical when one considers that the lower peak shear forces likely reduces the shear stresses that are carried by the flanges (see Section 3.9), thereby reducing the triaxial stresses at the location of flange fracture, relative to the links with normalized lengths of 2.1 and 1.6. Furthermore, the flexural links reached limit rotations of more than twice the current rotation limits. This is partly because the current limits for rotation of flexural links were established from links where lateral torsional buckling was commonly the controlling failure mode. Here the links are self-stabilizing with respect to lateral torsional buckling, owing to their rectangular cross-section and, therefore, are able reach rotations of more than twice the current 0.02 rad limit.

Although the seismic provisions use total rotation as an acceptance criteria for links, it is also interesting to examine the plastic rotation capacity of the links in this study, since energy dissipation and plastic strain are more closely related to this inelastic portion of total rotation. The same definition of plastic rotation used in Section 3.4 is used here, namely:

$$\gamma_p = \gamma_t - \frac{V_l}{k_{li}} \tag{6-1}$$

where γ_t is the total rotation, V_l is the link shear at the corresponding value of total rotation and k_{li} is the initial elastic stiffness of the link in terms of link shear per unit link rotation. Figure 6-2 shows the limit plastic rotations, γ_{plim}, also given in table 6-1, that correspond to the limit total rotation values shown in figure 6-1. As shown, if plastic rotation was used as the acceptance criteria for the link specimens none of the links at normalized lengths of 1.6 and 2.1 would be considered satisfactory. Again in this case, the flexural links ($\rho = 3.0$) have a larger plastic rotation capacity than the intermediate links ($\rho = 2.1$), similar to the observation made regarding total rotation.

Cumulative plastic rotation may also provide some insight into link behavior. It can be calculated by summing the absolute value of the plastic rotation range for each half cycle. The plastic rotation range is the difference between the plastic rotations at the beginning and end of a half cycle. Figure 6-3 shows the cumulative plastic rotations, γ_{pcum}, for all link specimens with haunch end connections, and this data is also given in table 6-1. As shown, there is a significant difference between the shear links with a normalized link length of 1.2

and the rest of the links. This difference is expected, because much of the cumulative plastic rotation occurs in the large rotation cycles, and the links with ρ = 1.2 were subjected to many more large rotation cycles than the other links. Figure 6-3 indicates that link length significantly effects the cumulative plastic rotation capacity, while cross-section type appears to have an insignificant effect. These observations are consistent with those made regarding limit rotation above. Cumulative plastic rotation will be revisited later to approximate peak rotations for a different loading protocol.

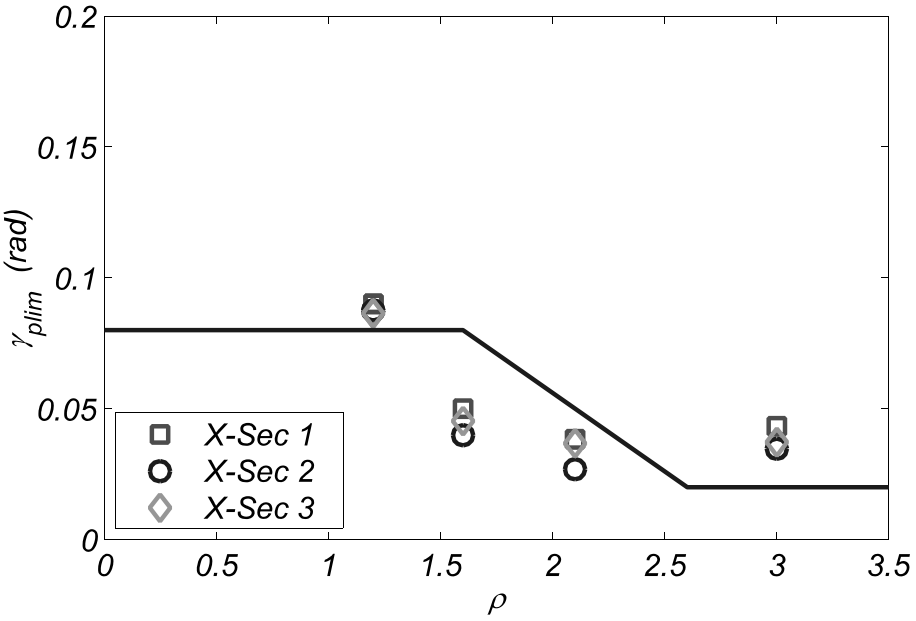

FIGURE 6-2 Plastic Rotation vs. Link Length for Link Test Specimens with Haunches

6.2.2 Discussion of Links with ρ = 1.6

As noted above, the links at a normalized length of 1.6 satisfied the proposed design recommendations but did not achieve their target rotation. Additionally they were found to have considerably lower maximum plastic rotation and cumulative plastic rotation than links at the normalized length of 1.2. There are two reasons for this that will be explored here and in later sections. Additionally, the two supplementary links were developed and tested to investigate these possible reasons for the links with ρ = 1.6 suffering flange fracture prior to reaching their target rotations as discussed in Section 6.5.

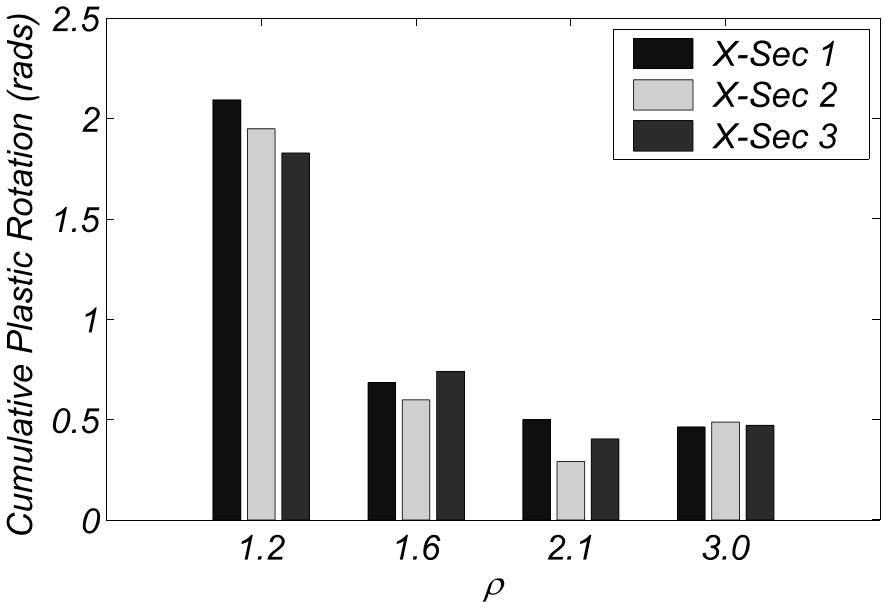

FIGURE 6-3 Cumulative Plastic Rotation vs. Link Length for Link Test Specimens with Haunches

The first reason considered here for links with ρ = 1.6 not achieving their target rotation is the effect of the loading protocol. The loading protocol used for testing, from the 2002 AISC Seismic Provisions, is considerably more rigorous than the new loading protocol in the 2005 AISC Seismic Provisions. This is discussed in detail in Section 6.4.

A second reason considered for the early fractures of the links with ρ = 1.6 is the combined effect of restraint of plastic flow in the flange caused by the rigid haunch end connection, and the large shear and flexural overstrength observed for links at this transition length. This is discussed briefly below and developed further in Sections 6.6 and 6.7.

The flanges of all the links tested here were subject to large triaxial stresses at the intersection with the haunch end connections, as the plastic flow in the flange was highly restrained at that location. However, the links at this transition length are also subjected to large shear forces, only slightly less than the similar links with normalized lengths of 1.2, and larger flexural demands associated with the longer link length, relative to the links with ρ = 1.2. Therefore, it is conceivable that this combination, triaxial stresses plus stresses from

large strength demands, could have caused flange fracture at lower rotation levels relative to the links with normalized lengths of 1.2.

6.3 Energy Dissipation Results

Cumulative energy dissipations for the link specimens with the haunch end connections are shown in figure 6-4 and have been calculated using the same definition given in Section 3, namely:

$$E_H = \sum_{i=1}^{N} \left(\int V e \, d\gamma \right)_i \tag{6-2}$$

where V is the link shear force and $ed\gamma$ is the link end displacement, written as the product of the incremental link rotation, $d\gamma$, times the link length, e. Normalized cumulative energy dissipation, defined as:

$$E_{HN} = \frac{\sum_{i=1}^{N} \left(\int V \, d\gamma \right)_i}{\min\left(\frac{V_p^2}{K_e}, \frac{4M_p^2}{e^2 K_e} \right)} \tag{6-3}$$

where K_e is the elastic stiffness of the link in terms of link shear and link rotation, is shown in figures 6-5 for link specimens with haunch end connections. Note that in figure 6-5, V_p and M_p are taken as the values used for design, assuming yield stresses of 345 MPa (50 ksi) for the webs and flanges.

The cumulative energy dissipation figures, similar to cumulative plastic rotation, indicate that link length plays a larger role in energy dissipation than cross-section. Links with a normalized length of 1.2 were subjected to more cycles at larger rotation levels, leading to substantially more energy dissipation than the longer links. Links with a normalized length of 1.6 dissipated only modestly more energy than the links at the intermediate and flexural lengths.

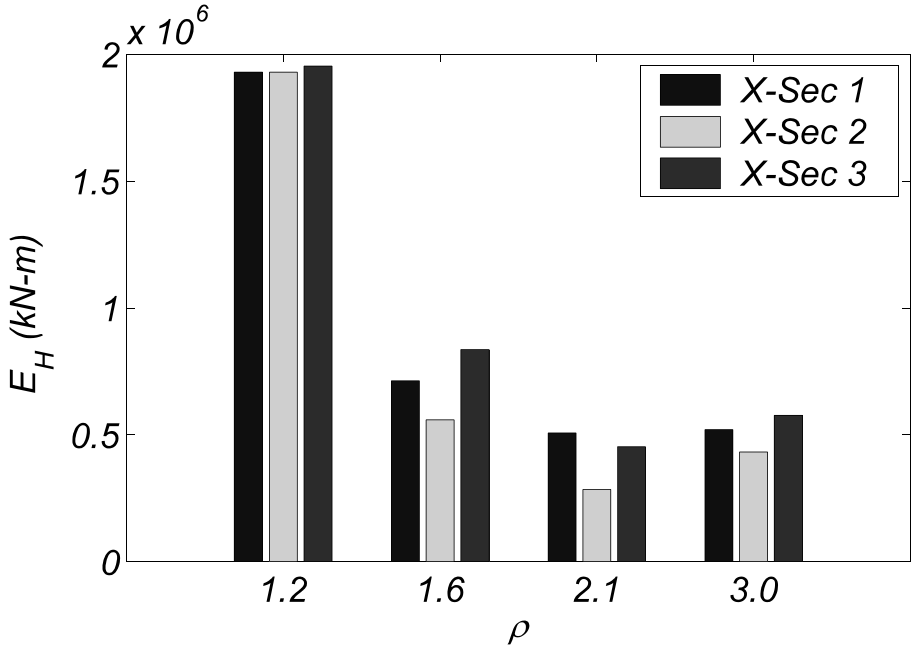

FIGURE 6-4 Energy Dissipation vs. Link Length for Link Test Specimens with Haunches

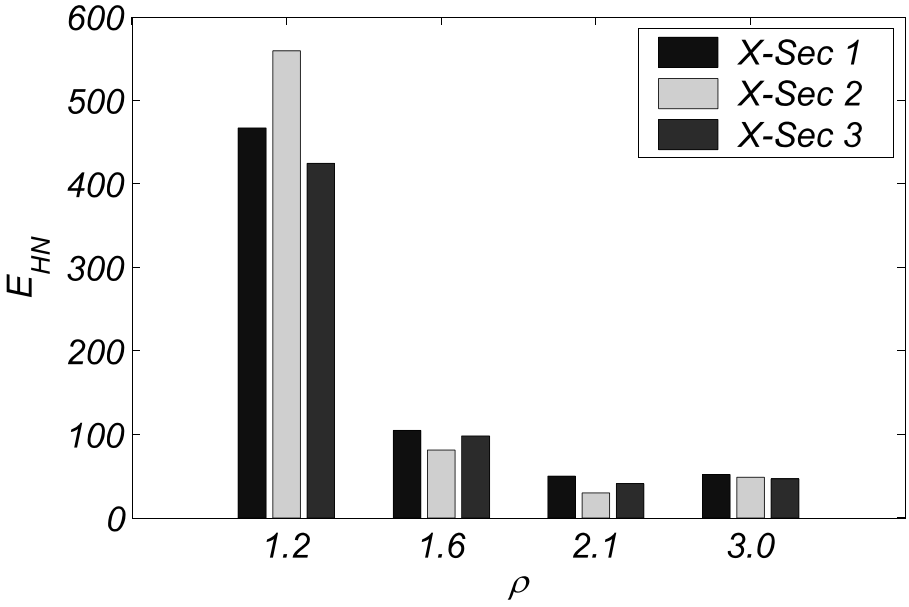

FIGURE 6-5 Normalized Energy Dissipation for Link Test Specimens with Haunches Using Design V_p and M_p Values

6.4 Extrapolation to Updated Loading Protocol

Research by Richards and Uang (2003) indicated that the loading protocol for EBF links in the 2002 AISC Seismic Provisions is overly demanding in terms of the number of high rotation cycles it requires. They based this observation on statistical analysis of analytical results for EBFs subjected to many ground motions. As such, they proposed a new loading protocol that has been adopted in the 2005 AISC Seismic Provisions that more realistically represents the maximum rotation demand EBF links must sustain. In light of this recent change, it is worthwhile to investigate what rotations might be achieved if the new loading protocol had been used for the testing of the hybrid rectangular links with haunch end connections. Furthermore, as mentioned above, the difference in rotation demand for the loading protocols could provide insight into why the links at a normalized length of 1.6 failed to reach their target rotation.

This section presents a procedure for projecting the rotations that would be achieved for the tested specimens under the new loading protocol. This procedure uses either cumulative energy dissipation or cumulative rotation as the central parameter to find the projected rotation for the 2005 loading protocol. These two parameters were chosen as they may be useful for fracture prediction using stress intensity factors or strain controlled low cycle fatigue , respectively.

Using cumulative energy dissipation and/or cumulative plastic rotation, it is possible to estimate the rotation that might have been achieved if the 2005 loading protocol had been used instead. The procedure followed to achieve this prediction consists of the following steps:

1. Fit a cyclic numerical model, such as a bounding surface model, to the test results for each specimen.
2. For the rotations from the 2005 loading protocol, determine the corresponding link shear forces using the cyclic model to develop the approximate hysteresis that would be obtained using the new protocol.

3. Find the cycle and corresponding rotation, using the 2005 loading protocol, for which the cumulative plastic rotation or cumulative energy dissipation equal the experimentally obtained maximum values.

The details and results of this procedure are discussed in the following sections. For reference, the 2005 loading protocol requires 6 cycles at 0.00375 rads, 0.005 rads, 0.0075 rads, and 0.01 rads, 4 cycles at 0.015 rads, and 0.02 rads, 2 cycles at 0.03 rads, one cycle at 0.04 rads and 0.05 rads, and then a single cycle at increasing 0.02 rad increments. The 2005 and 2002 loading protocols are shown in figure 6-6, where the approximate yield rotation for all links of 0.01 rads is also indicated. Note that a complete cycle without significant strength degradation must be achieved at the target rotation for the link to be acceptable according to the 2005 Seismic Provisions.

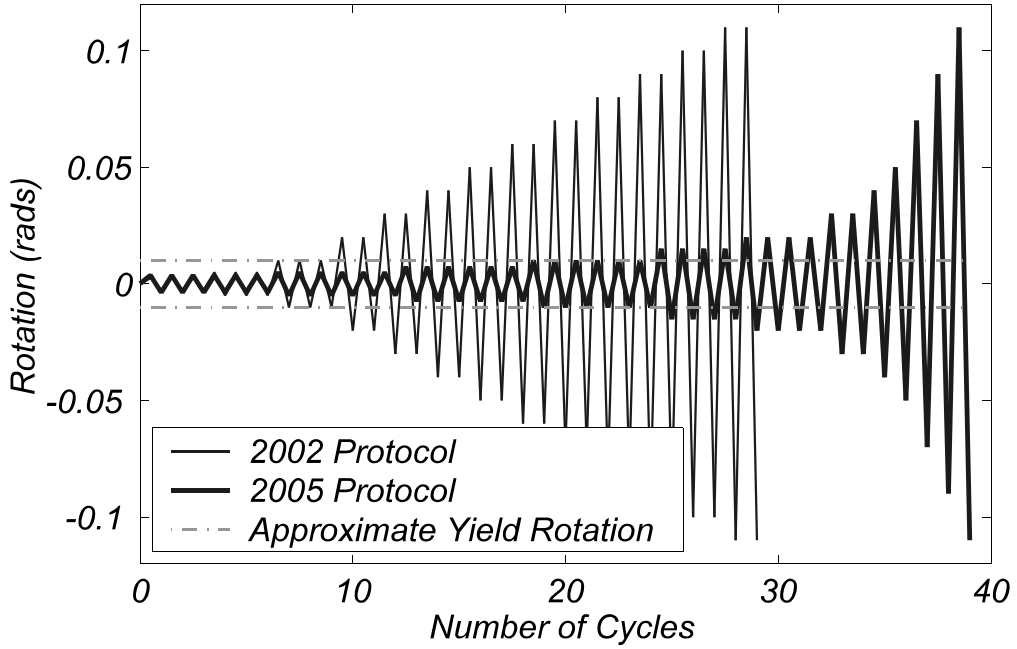

FIGURE 6-6 Comparison of the 2002 and 2005 AISC Loading Protocols for EBF Links

6.4.1 Bounding Surface Model

The first step in estimating the limit rotation that may have been achieved had the new loading protocol been used is to fit a cyclic model to the experimental data. For simplicity, because it can be easily programmed and quickly executed, the bounding surface model with

internal variables originally formulated by Dafalias and Popov (1976), and adapted by Cook (1983) and Goto et al. (1991), is selected for application here.

The bounding surface model with internal variables is defined here in incremental form as a link shear force-rotation relationship and is shown schematically in Figure 6-7. Since it is to be calibrated and used with hysteretic force-rotation curves it takes the form:

$$\Delta V = R_{kt}\,\Delta\gamma \tag{6-4}$$

where ΔV is the incremental base shear, R_{kt} is the tangent stiffness at the current displacement, and $\Delta\gamma$ is the incremental displacement. The tangent stiffness at the current displacement is expressed as:

$$R_{kt} = \frac{R_{ki}\,R_{kp}}{R_{ki} + R_{kp}} \tag{6-5}$$

where R_{ki} is the initial stiffness of the system and R_{kp} is the tangent plastic stiffness at a given displacement and is calculated as:

$$R_{kp} = R_b + h\left(\frac{d}{d_{in} - d}\right) \tag{6-6}$$

where R_b is the slope of the bounding lines with positive and negative force intercepts, R_{bf}^{+} and R_{bf}^{-}, and is calibrated to asymptotically match the largest rotation excursions in the experimental results, h is a hardening parameter (used to fit the model to the experimental data), d is the difference between the current force and the corresponding bound in the direction of current loading, and d_{in} is the value of d at the initiation of loading or at every load reversal. This model is designed to provide curves that asymptotically approach specified bounding lines.

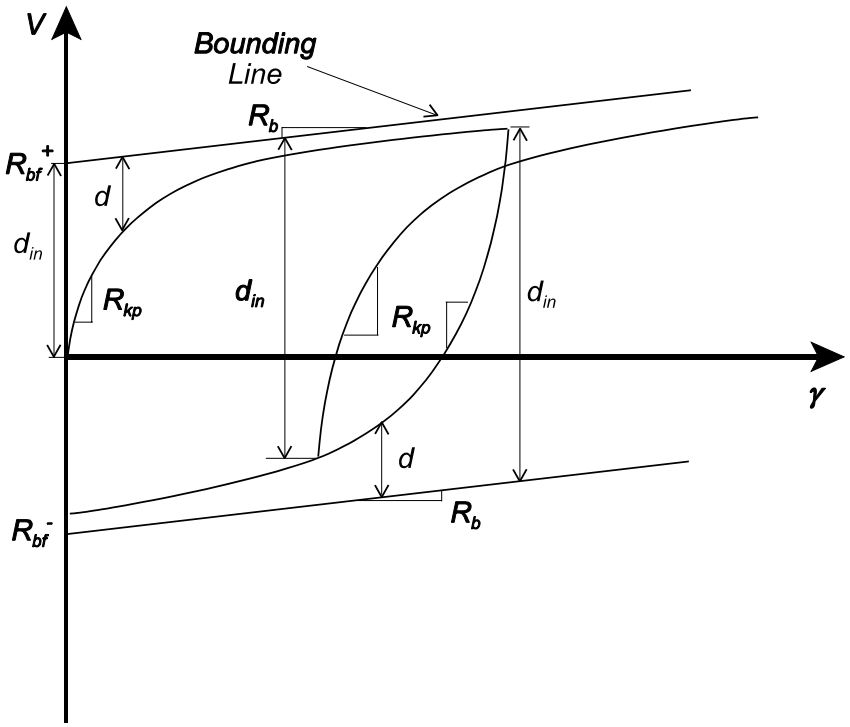

FIGURE 6-7 Bounding Surface Model
(Adapted from Chen et al. 1996)

Table 6-2 gives the parameter values used to implement the bounding surface model for each link and the resulting hysteresis curves, superimposed on the experimental curves for links with X1 cross-sections and haunch end connections, are shown in figure 6-8. From the figure it is observed that good agreement with the experimental results has been obtained from this simple numerical model. Similar agreement was obtained for the links with cross-sections X2 and X3. Note that most of the models slightly over predict the stiffness at large rotations, and will therefore slightly overestimate the energy dissipation. This will lead to conservative values for projected rotation, since the models will reach the cumulative energy dissipation values for the experimental specimens earlier in the loading history.

TABLE 6-2 Bounding Surface Model Parameters Used for Links with Haunch End Connections

Specimen Name	R_{ki} (kN/rad)	R_b (kN/rad)	R_{bf}^+ (kN)	R_{bf}^- (kN)	h
X1L1.2	71900	333	880	-950	170000
X2L1.2	103800	625	900	-975	200000
X3L1.2	83100	625	1080	-1120	180000
X1L1.6	54500	333	825	-875	160000
X2L1.6	60400	719	840	-910	150000
X3L1.6	52400	1330	940	-950	170000
X1L2.1	38700	857	675	-750	110000
X2L2.1	46500	917	710	-750	120000
X3L2.1	39800	2381	670	-730	160000
X1L3.0	26400	10	505	-560	115000
X2L3.0	37000	10	550	-575	110000
X3L3.0	25500	1950	475	-530	120000

6.4.2 Estimation of Limit Rotations for the 2005 Loading Protocol

After adequately calibrating the bounding surface model to each link's experimental results, the rotations from the 2005 loading protocol are applied to the bounding surface model and approximate hysteresis curves are obtained, which will be referred to as the projected results. From these projected curves, cumulative energy dissipation and cumulative plastic rotation are found using the procedures described above for the experimental results. Figures 6-9 and 6-10 show, respectively, both the experimental and projected cumulative energy dissipation and cumulative plastic rotation versus the number of half cycles in the respective loading protocol used. These figures are for Specimen X1L1.6. Similar figures for the other links with haunch end connections have also been developed.

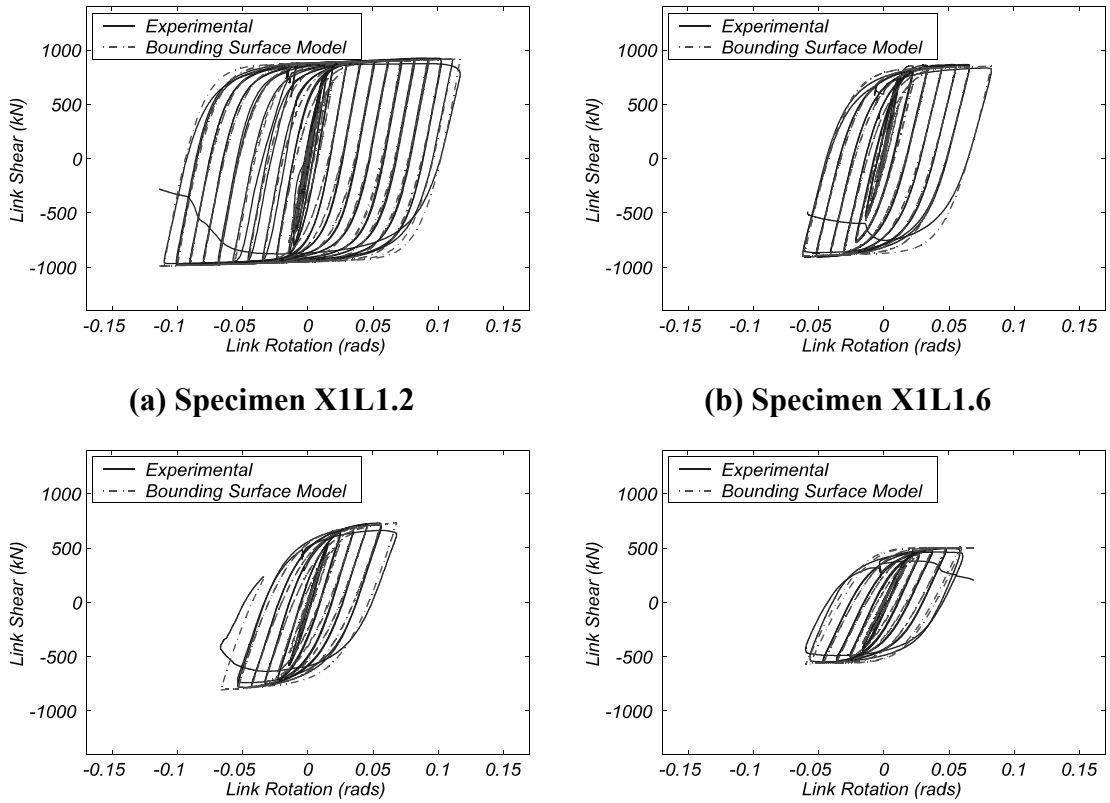

(a) Specimen X1L1.2 **(b) Specimen X1L1.6**

(c) Specimen X1L2.1 **(d) Specimen X1L3.0**

FIGURE 6-8 Comparison of Bounding Surface Model to Experimental Results for X1 Specimens

Also shown in figures 6-9 and 6-10 is the method used to estimate the half cycle number in the 2005 loading protocol that corresponds to the same cumulative energy dissipation or cumulative plastic rotation as the experimental results. The half cycle number is then rounded down to the nearest complete cycle to obtain the projected limit rotations considering the 2005 loading protocol. Table 6-3 gives the projected limit rotations found using both cumulative energy dissipation, γ_{limEH}, and cumulative plastic rotation, γ_{limRP}, the limit rotations from the experimental results, γ_{lim}, the target rotations, γ_{targ}, and the cumulative energy dissipation, E_H, and cumulative plastic rotation, γ_{cum}, values used to obtain the projected rotations for all links with haunch end connections. Figures 6-11 and 6-12 show the projected rotations versus the normalized link length considering cumulative energy dissipation and cumulative plastic rotation, respectively.

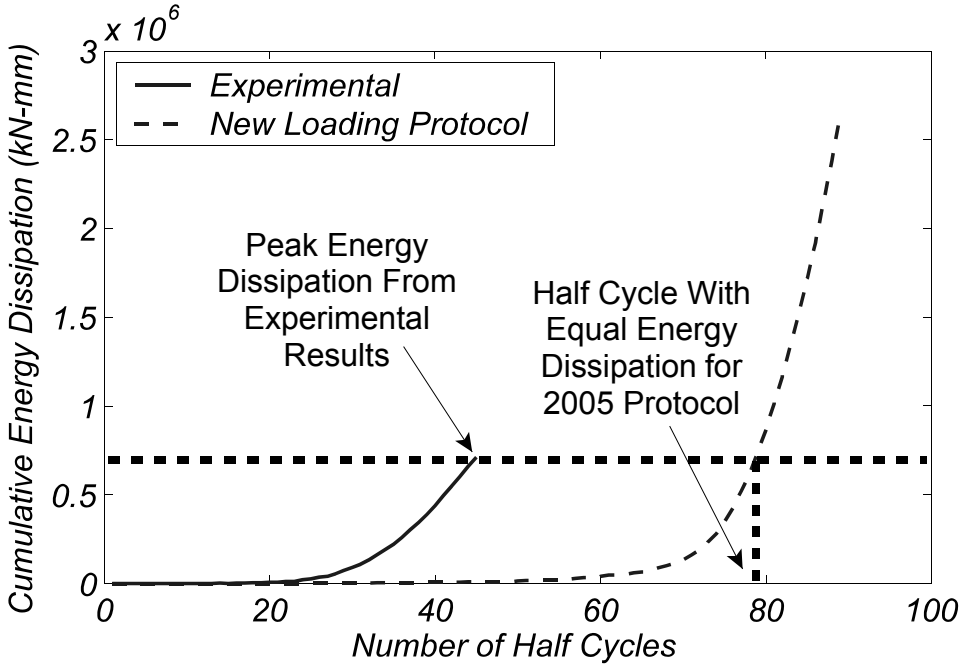

FIGURE 6-9 Cumulative Energy Dissipation for Both Experimental and Projected Results versus Half Cycle Number for Specimen X1L1.6

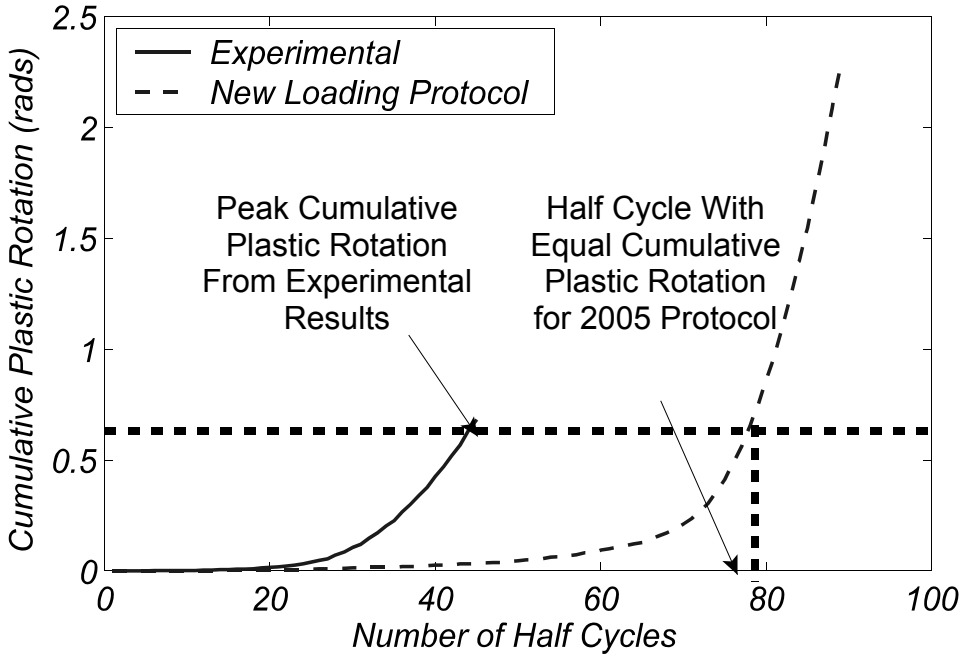

FIGURE 6-10 Cumulative Plastic Rotation for Both Experimental and Projected Results versus Half Cycle Number for Specimen X1L1.6

TABLE 6-3 Projected Limit Rotations Considering the 2005 Loading Protocol and Parameter Values Used to Approximate Them

Specimen Name	γ_{limEH} (rad)	γ_{limRP} (rad)	γ_{lim} (rad)	γ_{targ} (rad)	E_H (kN-mm)	γ_{cum} (rad)
X1L1.2	0.190	0.190	0.103	0.080	1930000	2.09
X2L1.2	0.170	0.170	0.097	0.080	1930000	1.95
X3L1.2	0.170	0.170	0.100	0.080	1950000	1.83
X1L1.6	0.090	0.090	0.065	0.080	710000	0.68
X2L1.6	0.070	0.090	0.055	0.080	560000	0.60
X3L1.6	0.090	0.090	0.064	0.080	840000	0.74
X1L2.1	0.070	0.090	0.056	0.050	510000	0.50
X2L2.1	0.040	0.040	0.042	0.050	280000	0.29
X3L2.1	0.070	0.070	0.056	0.050	450000	0.40
X1L3.0	0.070	0.070	0.060	0.020	520000	0.46
X2L3.0	0.050	0.070	0.048	0.020	430000	0.49
X3L3.0	0.090	0.090	0.059	0.020	580000	0.47

From figure 6-11 it is observed that all links are projected to reach their target rotations under the 2005 loading protocol when cumulative energy dissipation is considered, except Specimens X2L1.6 and X2L2.1. As mentioned above, Specimen X2L2.1 does not satisfy the proposed design requirements, leaving X2L1.6 as the only specimen satisfying the proposed design requirements that is not projected to meet the target rotation under the 2005 loading protocol considering cumulative energy dissipation.

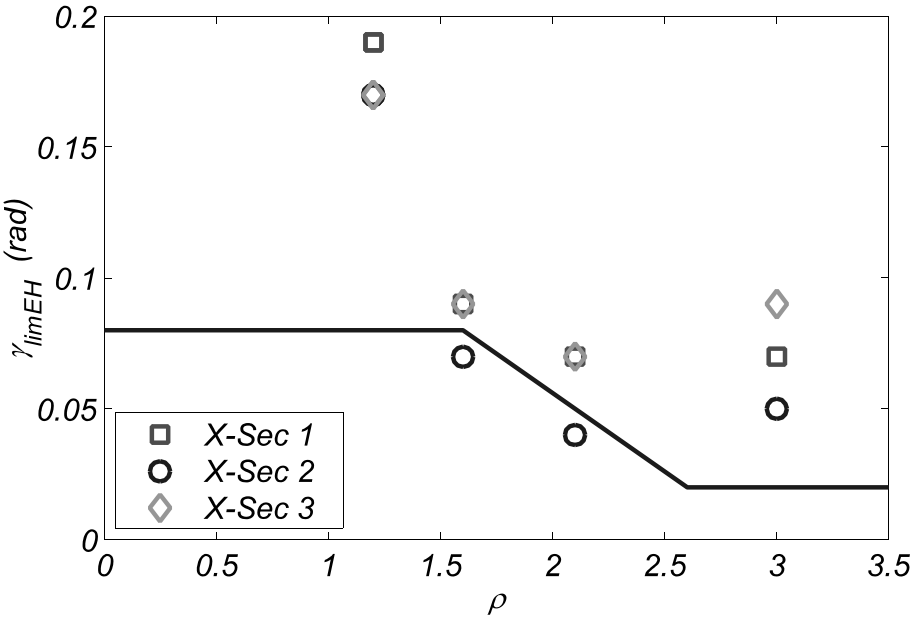

FIGURE 6-11 Projected Limit Rotation vs. Link Length for the 2005 Loading Protocol Considering Equal Cumulative Energy Dissipation - Links with Haunch End Connections

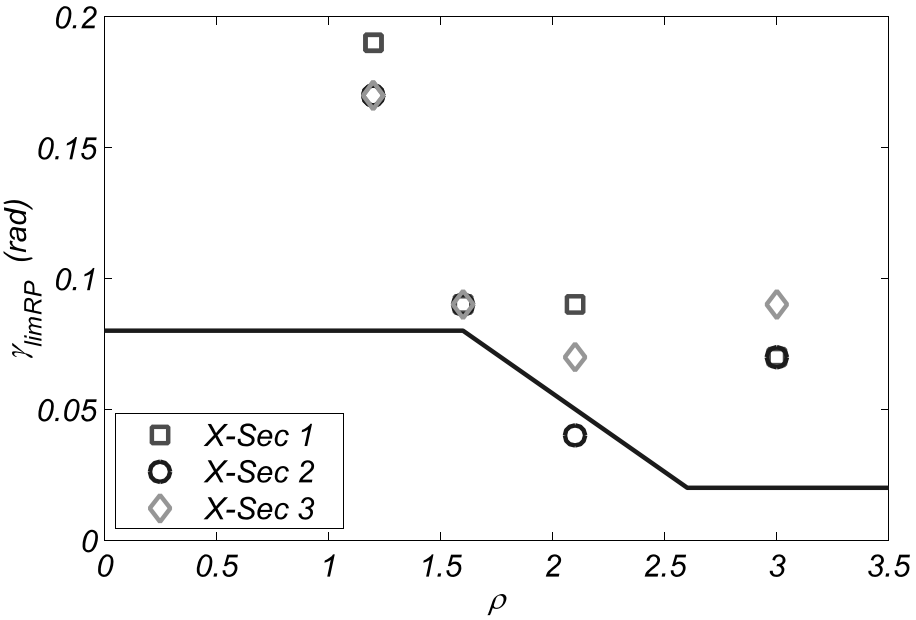

FIGURE 6-12 Projected Limit Rotation vs. Link Length for the 2005 Loading Protocol Considering Equal Cumulative Plastic Rotation - Links with Haunch End Connections

However, cumulative plastic rotation intuitively seems to be a more appropriate parameter to use for such projections, as it may be more closely related to plastic strain demands in the link flange, which is a factor in the triaxial stress condition that precipitated the observed flange fractures. Figure 6-12 shows that using cumulative plastic rotation to make the projections of limit rotations for the 2005 loading protocol results in a projected limit rotation of 0.09 rads for Specimen X2L1.6, which is above its target rotation of 0.08 rads. Furthermore, figure 6-12 shows that the only link not projected to reach its target rotation is Specimen X2L2.1, which does not satisfy the proposed design requirements. Based on the data presented above and in Section 6.2, it seems likely that tubular links satisfying the proposed design criteria and used in EBFs with link end conditions that do not restrain plastic flow to the degree of restraint present in the haunch end connections, will reach their target rotations considering the 2005 loading protocol. The supplementary link testing results presented below will provide more evidence for this conclusion.

6.5 Supplementary Link Test Results

The two supplementary link specimens, AX1L1.6 and AX2L1.6, utilized an alternate end connection that reduced the restraint against plastic flow in the link flanges. These end connections are similar to the gusset, gusset stiffener, and brace-to-link connection used in the proof-of-concept testing described in Berman and Bruneau (2005a). Specimens AX1L1.6 and AX2L1.6 were tested using the 2002 and 2005 loading protocol, respectively. Table 6-4 gives the same data obtained from the testing of these supplementary links, as was given in table 6-1 for the links with haunch end connections. For comparison purposes, the data for Specimens X1L1.6 and X2L1.6 are also given in table 6-4, as those specimens had identical cross-sections and link lengths as Specimens AX1L1.6 and AX2L1.6, respectively. Additionally, the data for the link from the proof-of-concept test has also been included, which was tested using the Applied Technology Council loading protocol (ATC, 1992) and had a normalized link length of 1.3 (Berman and Bruneau, 2005a). Application of that loading protocol to the proof-of-concept EBF resulted in a link rotation demand between the demands from the 2002 and 2005 AISC loading protocols. In table 6-4 and in the text the proof-of-concept link is referred to as POC1.3.

TABLE 6-4 Summary of Experimental Results for Supplementary Link Specimens and Similar Haunch Specimens

Specimen Name	γ_{targ} (rads)	γ_{lim} (rads)	γ_{plim} (rads)	γ_{pcum} (rads)	V_p (kN)	M_p (kN-m)	V_{max} (kN)	M_{max} (kN-m)
AX1L1.6	0.080	0.068	0.055	0.98	554	266	840	323
X1L1.6	0.080	0.065	0.050	0.68	554	266	907	349
AX2L1.6	0.080	0.123	0.109	1.06	610	278	1041	410
X2L1.6	0.080	0.055	0.040	0.60	610	278	936	360
POC1.3	0.080	0.123	0.105	1.42	495	158	750	172

Figure 6-13 shows the experimental results for limit rotation versus link length for all link specimens, including the supplementary specimens and proof-of-concept link. From this figure and table 6-4, it is observed that Specimen AX1L1.6 did not reach its target rotation despite having an end connection that reduced the restraint against plastic flow. However, the failure mode for that specimen was not flange fracture but fracture of the gusset stiffener followed by failure of the welds connecting the link to end plate. Additionally, the link was subjected to five cycles at rotation levels between 0.06 and 0.068 rads due to increasing deformations of the connection region, as explained in Section 5. Noting this, it is observed from table 6-4 that the cumulative plastic rotation of Specimen AX1L1.6 is almost 50% larger than the cumulative plastic rotation of Specimen X1L1.6, indicating that the different connection was somewhat effective in delaying the flange fracture mode. This increase in plastic rotation relative to Specimen X1L1.6 is shown in figure 6-14, which has cumulative plastic rotation for all links tested. However, there was no such increase in the normalized cumulative energy dissipation as shown in figure 6-15, which has normalized energy dissipation for all links tested. This is likely due to the smaller link shear forces obtained in the later cycles of the Specimen AX1L1.6 testing relative the link shear forces recorded during the testing of Specimen X1L1.6.

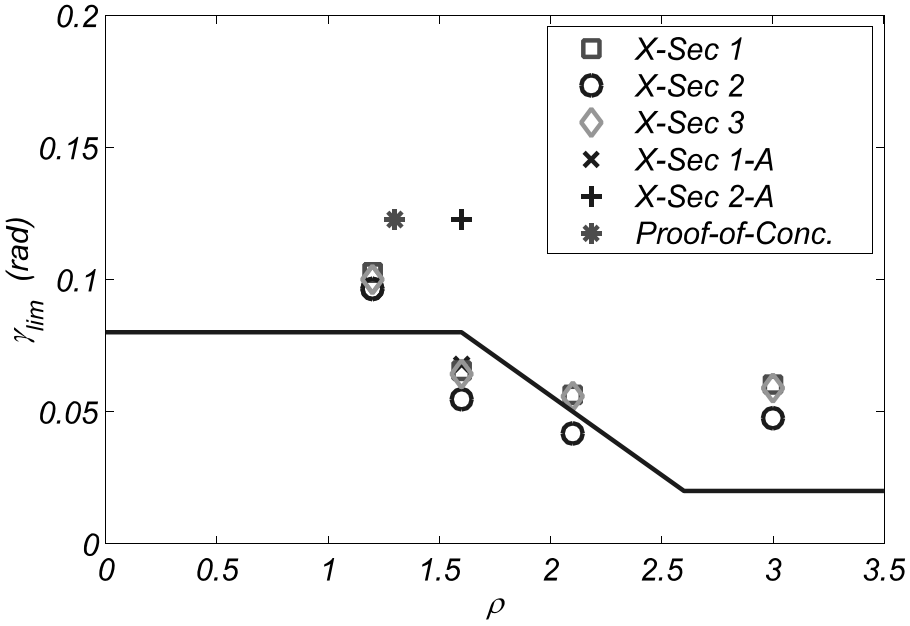

FIGURE 6-13 Limit Rotation vs. Link Length for All Link Specimens

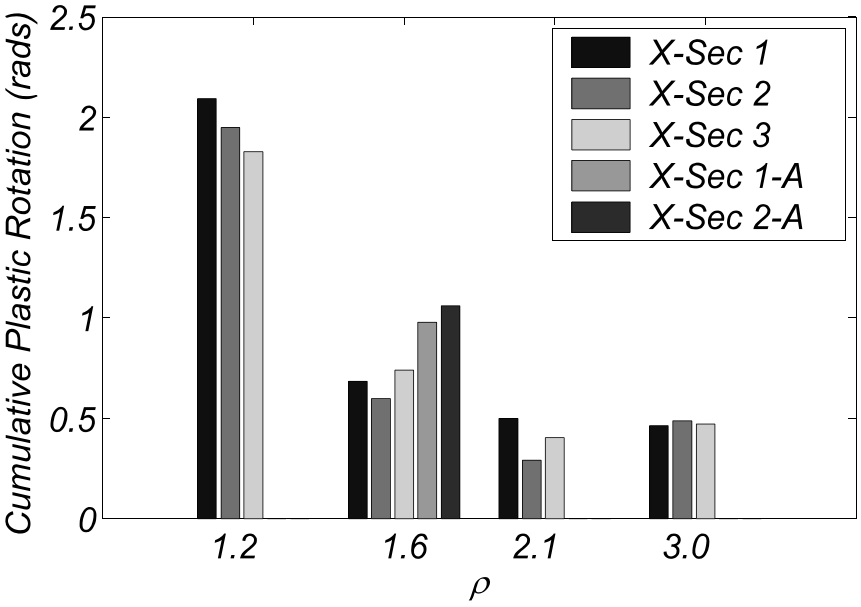

FIGURE 6-14 Cumulative Plastic Rotation vs. Link Length for All Link Specimens

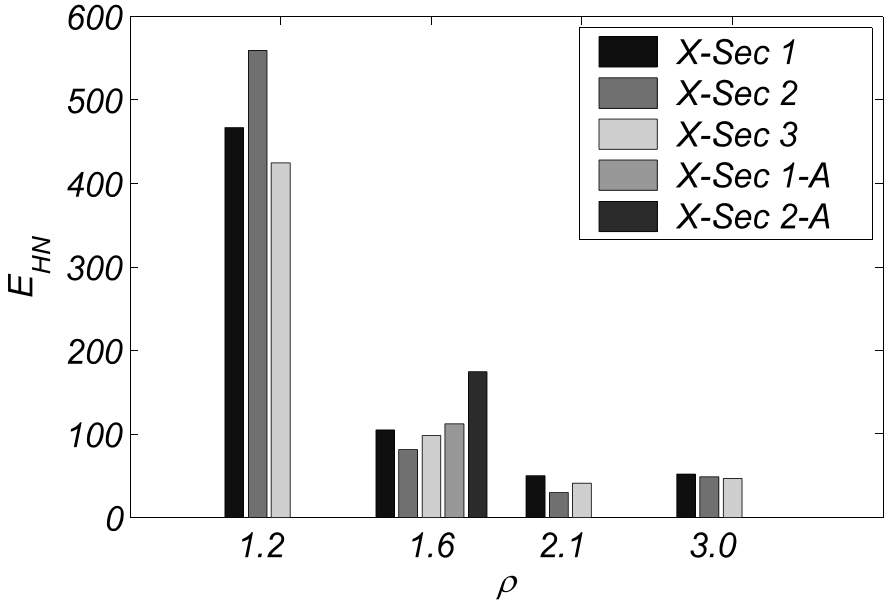

FIGURE 6-15 Normalized Energy Dissipation for All Link Specimens Using Design V_p and M_p Values

Figure 6-13 and table 6-4 indicate that both Specimen AX2L1.6 and POC1.3 reached limit rotations of 0.123 rads, exceeding their target rotation of 0.08 rads as well as the limit rotation of Specimen X2L1.6. Recall that AX2L1.6 was tested using the 2005 loading protocol and exceeded the rotation projected for Specimen X2L1.6 for that protocol, which was an intended result and the reason why different end connections were considered in the first place. Considering that this link had a cumulative plastic rotation similar to that of Specimen AX1L1.6, and that both were approximately 50% larger than those obtained for the corresponding specimens with haunch end connections, it is of interest to revisit the results for Specimen AX1L1.6 and project what it's limit rotation might have been had the 2005 loading protocol been used for testing. Also note that, as shown in table 6-4, Specimen POC1.3 achieved a cumulative plastic rotation of 1.42 rads, which is between the values obtained for links with a normalized length of 1.2 and the value obtained for Specimen AX2L1.6. The rotation for this link will also be projected for the 2005 loading protocol.

Table 6-5 gives the bounding surface model parameters used for approximating the hysteresis of Specimens AX1L1.6 and POC1.3 for the 2005 loading protocol. Table 6-6 gives the projected values of limit rotation for those specimens considering both cumulative

energy dissipation and cumulative plastic rotation. The projected values under the 2005 loading protocol for all links tested are then shown in figures 6-16 and 6-17 considering cumulative energy dissipation and cumulative plastic rotation, respectively. Note that the experimental data for Specimen X2L1.6 is shown in those figures as it was tested using the 2005 loading protocol.

TABLE 6-5 Parameter Values Used for the Bounding Surface Models for the Supplementary and Proof-of-Concept Specimens

Specimen Name	R_{ki} (kN/rad)	R_b (kN/rad)	R_{bf}^+ (kN)	R_{bf}^- (kN)	h
AX1L1.6	54600	1790	690	-760	100000
X1L1.6	54500	333	825	-875	160000
POC1.3	39300	476	675	-680	150000

TABLE 6-6 Projected Limit Rotations Considering the 2005 Loading Protocol for the Supplementary and Proof-of-Concept Specimens

Specimen Name	γ_{limEH} (rad)	γ_{limRP} (rad)	γ_{lim} (rad)	γ_{targ} (rad)	E_H (kN-mm)	γ_{cum} (rad)
AX1L1.6	0.110	0.110	0.068	0.080	690000	0.98
X1L1.6	0.090	0.090	0.065	0.080	710000	0.68
POC1.3	0.150	0.150	0.123	0.080	770000	1.42

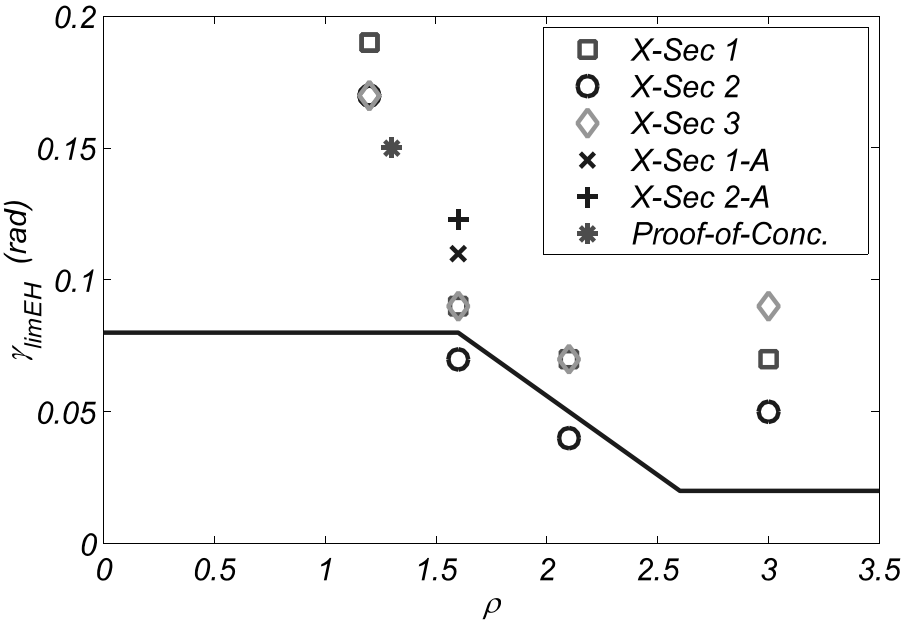

FIGURE 6-16 Projected Limit Rotation vs. Link Length for the 2005 Loading Protocol Considering Equal Cumulative Energy Dissipation - All Link Specimens

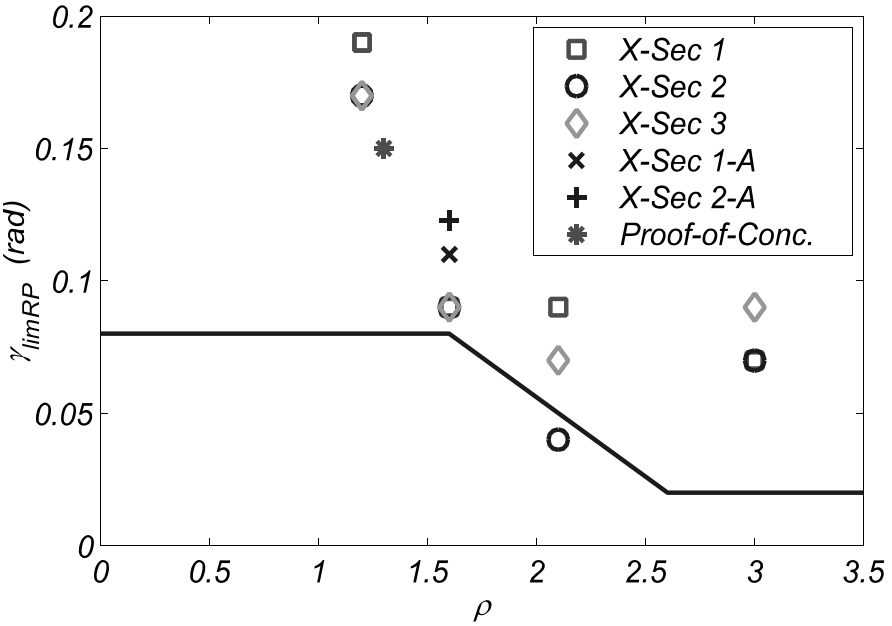

FIGURE 6-17 Projected Limit Rotation vs. Link Length for the 2005 Loading Protocol Considering Equal Cumulative Plastic Rotation - All Link Specimens

Considering the data presented, it appears that links satisfying the proposed design criteria will achieve their target rotation if connections similar to the proof-of-concept test are used (i.e., connections that do not overly restrain the plastic flow in the link flanges), and if they are tested using the loading protocol from the 2005 AISC Seismic Provisions rather than the protocol from the 2002 provisions.

The change in end connection from Specimen X1L1.6 to Specimen AX1L1.6 resulted in a slightly larger limit rotation but considerably more cumulative plastic rotation. This indicates that the end connection change resulted in modestly improved performance.

The change in loading protocol from the 2002 protocol for Specimen AX1L1.6 to the 2005 protocol for Specimen AX2L1.6 resulted in a significant increase in limit rotation. These specimens had the same cumulative plastic rotation and similar energy dissipation, yet Specimen AX2L1.6 reached a rotation of 0.123 rads using the 2005 loading protocol while Specimen AX1L1.6 only reached 0.068 rads under the 2002 loading protocol. Additionally, the proof-of-concept link, which had a shorter normalized length than the supplementary specimens, achieved a rotation of 0.123 rads using a loading protocol that is between the 2002 and 2005 loading protocols in terms of cumulative plastic rotation demand. Therefore, it seems that the difference in loading protocol intensity is largely responsible for the difference in obtained limit rotations.

This conclusion has significance in affirming that all the links with haunch end connections would achieve significantly larger limit rotations under the 2005 loading protocol relative to those achieved under the 2002 protocol, as projected in Section 6.4. Furthermore, considering both a connection that has less restraint against plastic flow in the flange and the updated loading protocol, i.e. comparing Specimens AX2L1.6 and X2L1.6, the increase in limit rotation was over 100%, from 0.055 rads for Specimen X2L1.6 to 0.123 rads for Specimen AX2L1.6.

6.6 Overstrength Results

Link overstrength is examined in this section using the experimental results for all link specimens. Table 6-1 has the maximum link shear forces, V_{max}, and maximum moments, M_{max}, for the links with haunch end connections and the same information is in table 6-4 for the supplementary link specimens. Also in those tables are the design values for plastic shear, V_p, and plastic moment, M_p, calculated assuming 345 MPa (50 ksi) yield stresses. Figures 6-18 and 6-19 show the link overstrength values for link shear and link moment respectively, where overstrength is defined as the maximum value from testing divided by the design value.

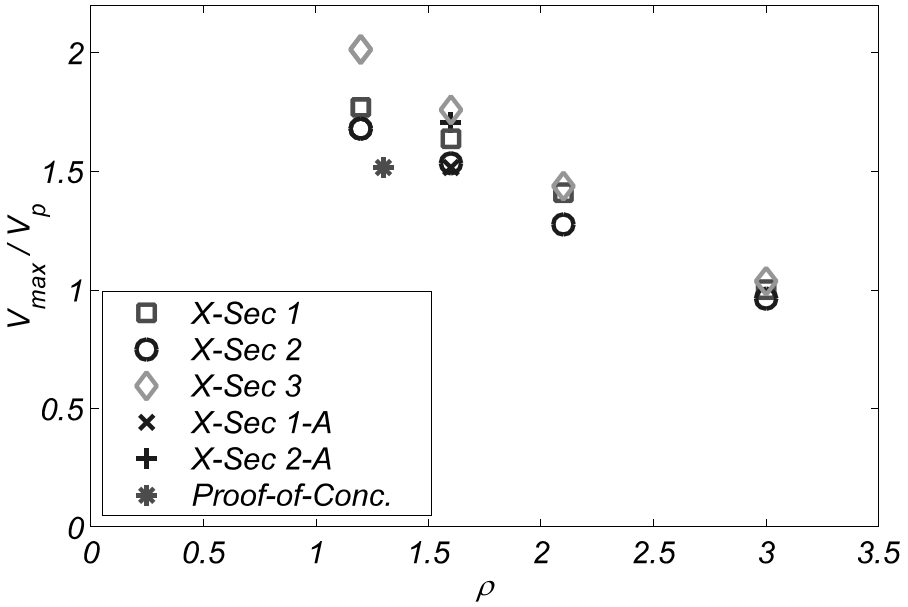

FIGURE 6-18 Link Shear Overstrength vs. Normalized Link Length for All Link Specimens

As expected, link shear force overstrength decreases with link length while flexural overstrength increases with link length. Figure 6-18 indicates that link shear overstrength has a nearly linear relationship with normalized link length, and since links with length less than 1.0 are rarely used as they have considerably large stiffness, the overstrength may be bounded by approximately 2.0. There is some dependence on cross-section evident as well, which becomes more significant with decreasing normalized link length. This is likely attributable to the flange shear force as described in Section 3.9. For the three cross-sections tested, X3 has flanges with the greatest thickness and compactness ratio followed by X1, and

then X2. As shown in figure 6-18, cross-section X3 had the largest overstrength at the shortest normalized length considered, 1.2, followed by X1 and then X2. Therefore, it is clear that links with thicker/more compact flanges, can be expected to have larger link shear overstrength values. Flexural overstrength, however, seems to be only dependent on link length and appears bounded by approximately 1.5.

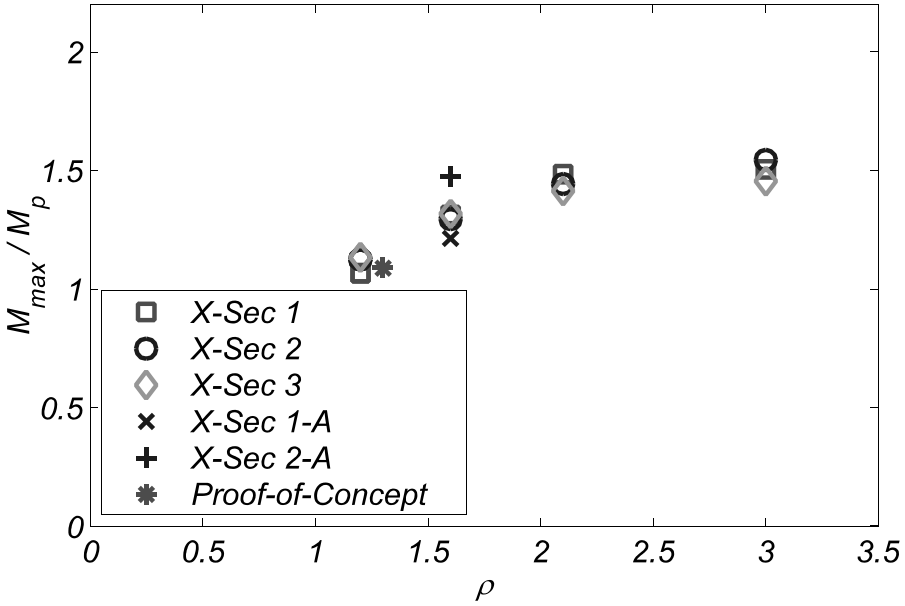

FIGURE 6-19 Link Flexural Overstrength vs. Normalized Link Length for All Link Specimens

The observations made above regarding link shear overstrength are consistent with those made the finite element results given in Section 3.9. Furthermore, they are similar to the observations made regarding wide-flange links by Richards and Uang (2002). As shown in Section 3.9, Richards and Uang developed a cyclic hardening factor that varies with the normalized link length, and an equation for link plastic shear that accounts for the contribution of the flanges. Generally, the maximum link shear force expected to develop is:

$$V_{ult} = \Omega R_y V_p \tag{6-7}$$

where Ω is the cyclic hardening factor as given by (3-10) and R_y is the ratio of mean to nominal material yield stress (1.1 for A572 Gr. 50 Steel). Note that the ratio of actual to nominal yield stresses for the webs of cross-sections X1, X2, and X3, were 1.39, 1.38, and 1.25, respectively, using the coupon test results reported in Section 4. Therefore, values

above the specified R_y value of 1.1 for A572 Gr. 50 steel will be absorbed into the cyclic hardening factor, Ω. Applying the formulation of Richards and Uang here results in the solid line in figure 6-20, where V_p for links with ρ ≤ 1.6 is now calculated by adding the flange contribution, $2V_f$, to the plastic shear considering only the web as explained in Section 3.9. The contribution of each flange to the plastic shear is given by:

$$V_f = \frac{F_{yf} b t_f^2}{2e} - \frac{F_y t_w^2 e}{8b} \tag{6-8}$$

where all variables are as previously defined. The figure shows that the Richards and Uang cyclic hardening factor, Ω, multiplied by R_y, and indicated by the solid line, does a reasonable job at predicting link overstrength for longer links but underestimates the overstrength for short links, particularly when ρ = 1.2.

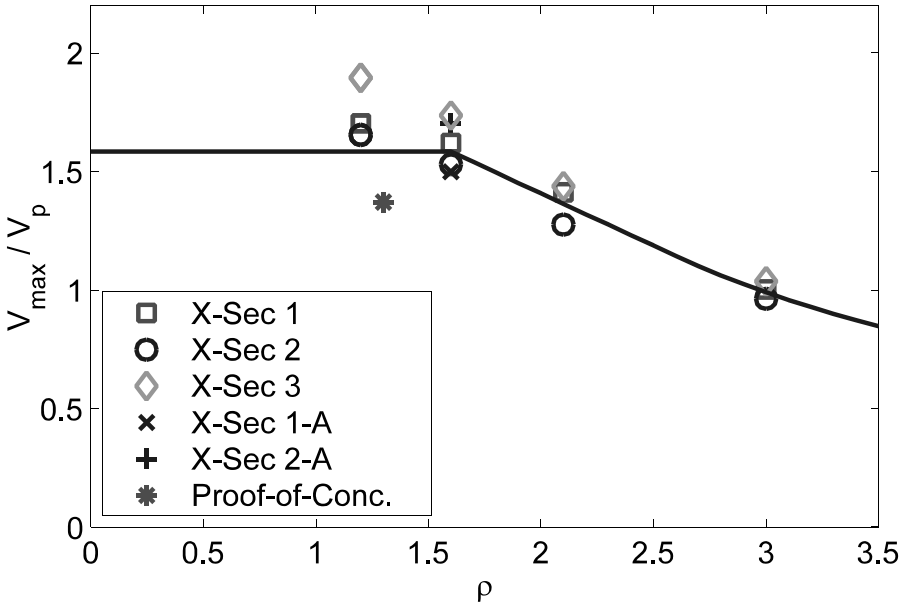

FIGURE 6-20 Link Shear Overstrength vs. Normalized Link Length for All Link Specimens - with Cyclic Hardening Factor

A more conservative formulation of the cyclic hardening factor can be achieved by changing the definition of the cyclic hardening factor (3-10), which was proposed for WF links, to:

$$\begin{aligned} \Omega &= 1.6 && \rho \le 1.6 \\ \Omega &= 1.6 - 0.56(\rho - 1.6) && 1.6 < \rho \le 2.6 \\ \Omega &= 2.7/\rho && \rho \ge 2.6 \end{aligned} \tag{6-9}$$

This slightly modified version of the cyclic hardening factor, results in a more conservative approximation of the overstrength observed for the rectangular links tested here, as shown in figure 6-21.

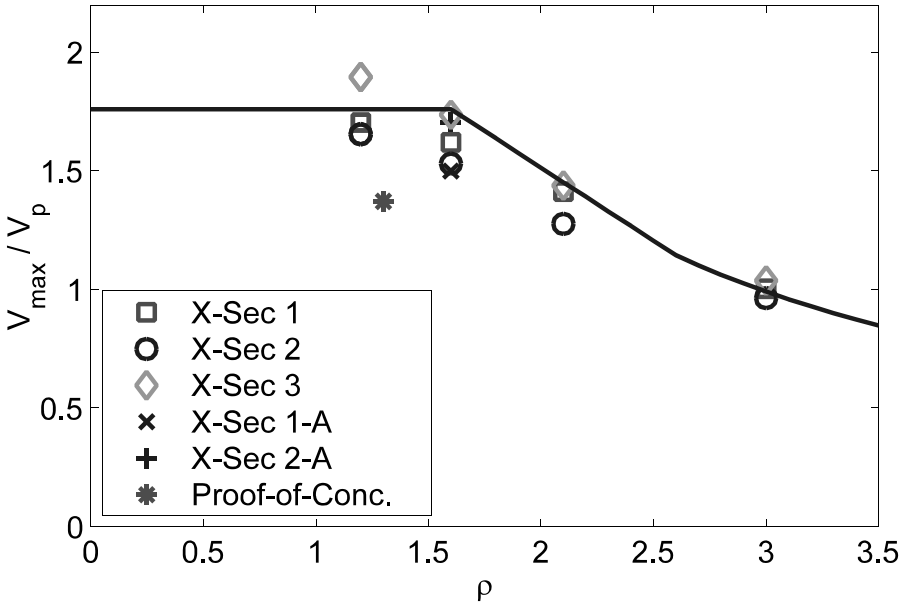

FIGURE 6-21 Link Shear Overstrength vs. Normalized Link Length for All Link Specimens - with Revised Cyclic Hardening Factor

6.7 Flange Strains

Considering that flange fracture occurred in the all specimens with haunch end connections and in one of the supplementary specimens as well, it is worthwhile to investigate the data from the flange strain gages (the proof-of-concept specimen did not have gages placed to record strains at a comparable location). As shown in figures 4-31 and 4-32, strain gages were placed 25.4 mm (1") away from the haunches (or gusset stiffeners for the supplementary specimens) and near the edges of the flanges of all links tested. Shear links had gages at each end of each flange while flexural links had gages at only one end of the link, but one both flanges at that end. Supplementary links had the same strain gage layout as the shear links with haunch end connections.

A convenient method for comparing strains between different specimens is to use cumulative plastic strain at the gage locations. However, since some gages peeled off from the flanges

at large rotations during the testing, data is not available at all gage locations. Furthermore, in order to provide comparisons with the supplementary specimens, which had an unsymmetric end connection, and where the maximum strains occurred on the west flange which was adjacent to the gusset (see figure 4-34), cumulative plastic strains will be calculated from the gages on bottom of the west flange of all links.

Cumulative plastic strain is calculated in a similar manner to cumulative plastic rotation. At the peaks of each cycle the plastic strain amplitude is calculated as the absolute value of total strain minus the yield strain, which is assumed to be constant and equal to 0.00172 (mm/mm), which corresponds to a yield stress of 345 MPa (50 ksi) and Young's Modulus of 200,000 MPa (29,000 ksi). The absolute values of these peak plastic strain amplitudes are then summed over all cycles of testing to obtain the cumulative plastic strain. Note that this differs slightly form the conventional plastic strain definition where the actual stress at the point in the loading history, divided by Young's Modulus, would be used as the updated yield strain as opposed to the constant 0.00172 (mm/mm) used here. However, for the purpose of comparing the cumulative strains in the flanges of the different links tested, the definition given above is adequate.

Figure 6-22 shows the cumulative plastic strain for each specimen. The plotted values are the averages of the cumulative plastic strains from gages at the bottom of the west flange (i.e., gages SFWNB and SFWSB in figures 4-31 and 4-32), or if one of those gages failed, the data is from just the gage that lasted for the duration of testing. Also note that because of the substantial flange buckling of Specimen X2L3.0 all gages on the flanges of that specimen peeled off. Therefore, for that specimen, the cumulative plastic strain is not calculated for the duration of loading but through the first cycle Sequence 6 (see table 5-11).

From this figure several observations can be made. First, it seems that the end connection used in supplementary link Specimens AX1L1.6 and AX2L1.6 was effective in increasing the strain that can develop in the flange prior to fracture, thus increasing the rotation capacity of those links relative to Specimens X1L1.6 and X2L1.6. Furthermore, considering that the cumulative plastic strain in the flange for Specimen AX1L1.6 is larger than that of Specimen

AX2L1.6, it seems likely that had Specimen AX1L1.6 been tested using the 2005 loading protocol, as Specimen AX2L1.6 was, it would have achieved its target rotation.

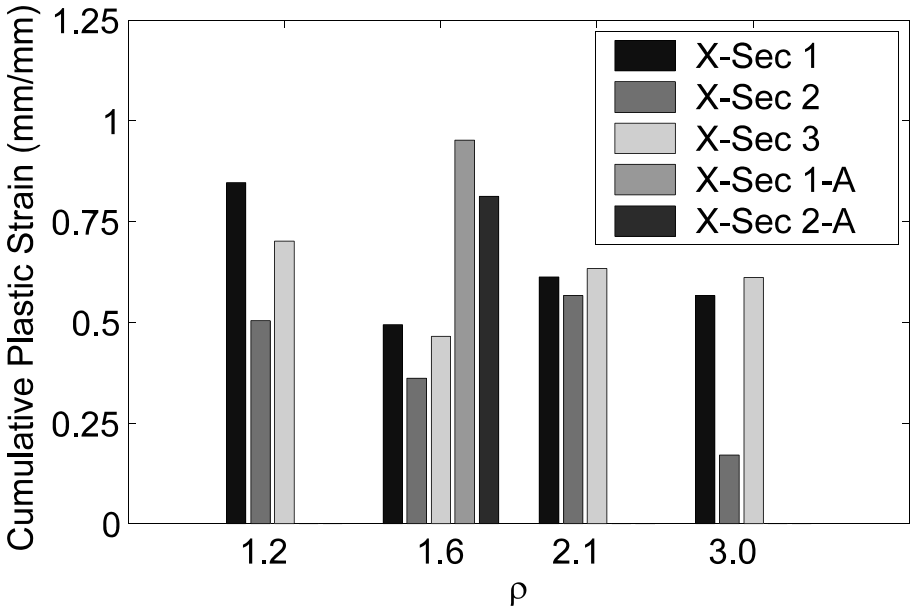

FIGURE 6-22 Approximate Cumulative Plastic Strain at Bottom of West Flange for All Link Specimens (Data Incomplete for Specimen X2L3.0 Due to Flange Buckling)

Figure 6-22 also shows that the smallest cumulative plastic flange strains, for which data was recorded for the entire test, were obtained on the specimens with normalized lengths of 1.6 and haunch end connections. This means that the flanges of these links fractured at lower cumulative plastic strain values than for the other links. Referring back to Section 6.2.2 where possible reasons for the links with $\rho = 1.6$ not achieving their target rotation were presented, recall that one of those possible reasons was the combined effect of overstrength and triaxial stresses.

Examining the link overstrength data presented in the previous section, and specifically, figures 6-17 and 6-18, it is observed that links at this transition length of 1.6 were subjected to both maximum shear forces near $1.65V_p$ and maximum moments above $1.3M_p$. For comparison, links with a normalized length of 1.2 were subjected to maximum shear forces near $2.0V_p$ in combination with moments of $1.1M_p$, and links with normalized lengths of 2.1 were subjected to maximum shear forces near $1.4V_p$ and maximum moments near $1.5M_p$.

Links at a normalized length of 1.6 had both large shear forces and large moments, not necessarily the largest values of each individually, but a severe combination of these values, which could, when combined with the triaxial stresses in the flanges of links with the haunch end connection configuration, result in fracture at lower cumulative plastic rotation values.

This can also be examined in the context of the flange shear forces as derived by Richard and Uang and modified in Section 3.7 for links with hollow rectangular cross-sections. According to that derivation, the shear force carried by the flange, V_f, can be approximated without accounting for strain hardening, by (6-9). For the links considered in this experimental study, the value of V_f is only positive for links with normalized lengths of 1.2 and 1.6, indicating that the shear force carried by the flanges of these links is considerably larger than that of links with normalized lengths of 2.1 or 3.0 (when strain hardening is considered, some flange shear in links with a normalized length of 2.1 is possible). Of the links with normalized lengths of 1.2 and 1.6, those at the latter length have already been shown to have maximum end moments that are considerably larger than those for links with normalized lengths of 1.2. Therefore, it appears likely that this combination of large flange shear, large flexural demand, and the restraint of the haunch end connections, made Specimens X1L1.6, X2L1.6, and X3L1.6 more susceptible to fracture at lower cumulative plastic strain values than links at the other lengths and with other end connections.

6.8 Comparison with Finite Element Results

Finite element models, similar to those described in Section 3, were developed using the exact dimensions and material properties of the link specimens with haunch end connections, to further verify the results of the finite element parametric study. The data from the cyclic coupon testing results given in Section 4.2.4 were used via the stabilized half cycle data function in ABAQUS as explained in Section 2. Boundary conditions were applied in the same way as presented in Section 3, and the S4R reduced integration shell elements and mesh density used in the parametric study were also employed in the specimen models.

Figures 6-23, 6-24, and 6-25 show the experimental and finite element hysteresis curves for links with cross-section X1, X2, and X3, respectively. Plastic rotation has been used for the

horizontal axis of these curves because it eliminates any flexibility differences in the boundary conditions. Fully restrained boundary conditions have been used in the ABAQUS models for the degrees of freedom shown in figure 2-1, while the experimental specimens had haunch end connections that were stiff, but still had a finite flexibility.

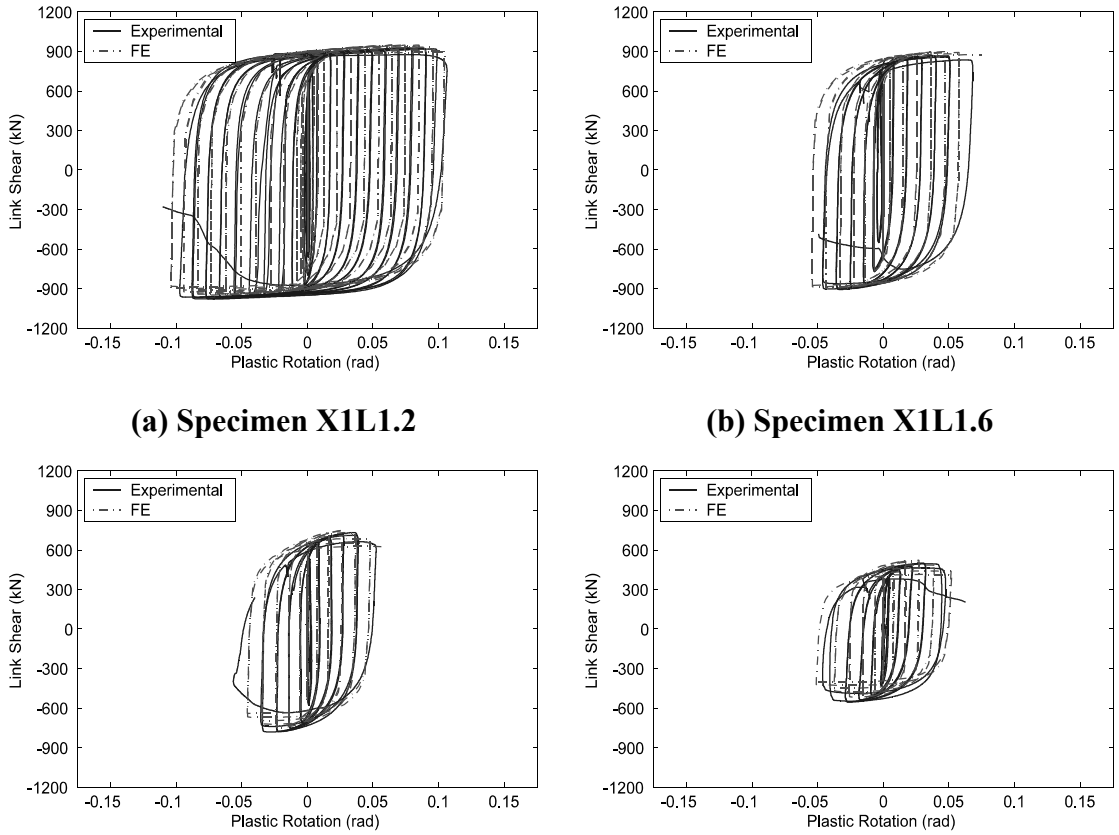

(a) Specimen X1L1.2

(b) Specimen X1L1.6

(c) Specimen X1L2.1

(d) Specimen X1L3.0

FIGURE 6-23 Comparison of Finite Element Models to Experimental Results for X1 Specimens

As shown in figures 6-23, 6-24, and 6-25, the finite element analyses agree well with the experimental results prior to strength degradation resulting from flange fracture. For example, consider the results for Specimen X2L1.6. As noted in Section 5, this specimen suffered flange fracture that began early in the loading history and caused the change in hysteretic behavior, i.e. the apparent decrease in yield strength at larger rotations, shown in the figure. Since the ABAQUS analyses do not account for fracture, the finite element results for Specimen X2L1.6 do not show this same decrease in apparent yield strength.

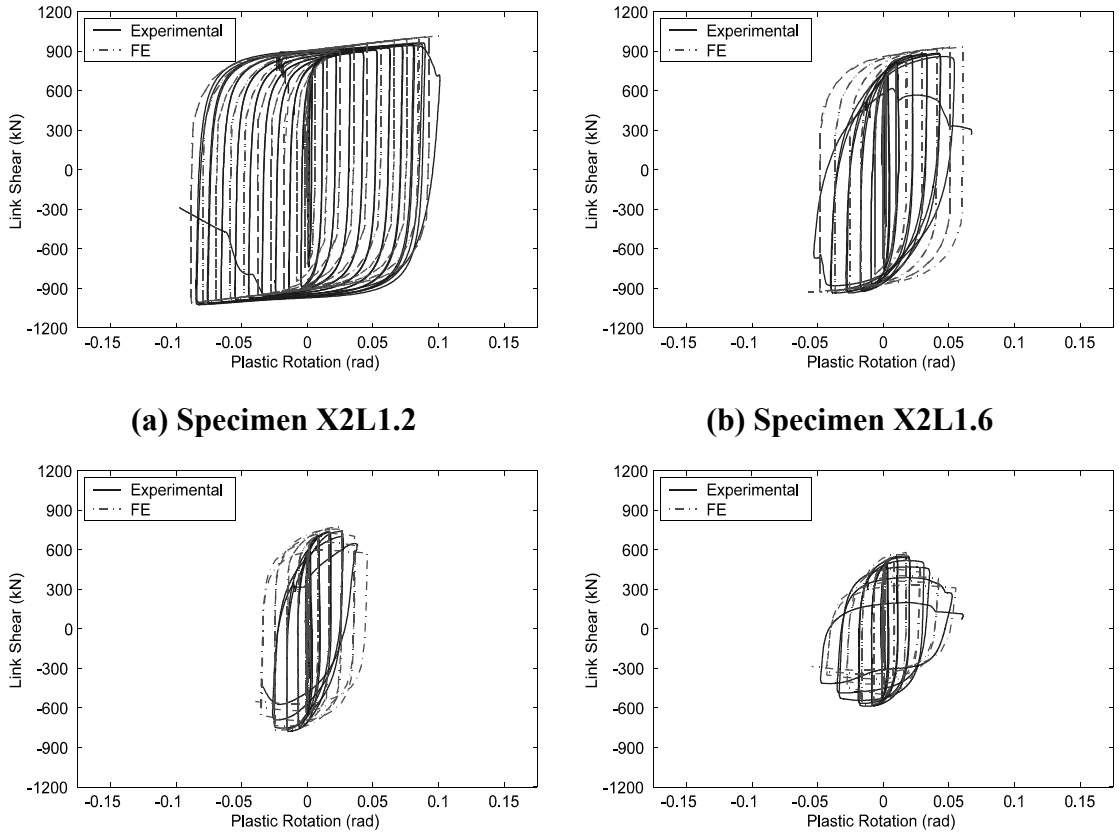

(a) Specimen X2L1.2 **(b) Specimen X2L1.6**

(c) Specimen X2L2.1 **(d) Specimen X2L3.0**

FIGURE 6-24 Comparison of Finite Element Models to Experimental Results for X2 Specimens

As opposed to the specimens that suffered only strength degradation from flange fracture, the results for links those that exhibited strength degradation due to web and/or flange buckling are more closely matched by the finite element analyses. Consider Specimen X2L3.0 in figure 6-24 which had degradation from both web and flange buckling as noted in Section 5. Here, the ABAQUS analysis is able to capture the strength loss resulting from that buckling and shows good agreement with the experimental results for the duration of the loading history. The finite element analyses for Specimens X1L2.1 and X1L3.0, which also had moderate strength degradation from flange buckling, show similar agreement with the experimental results.

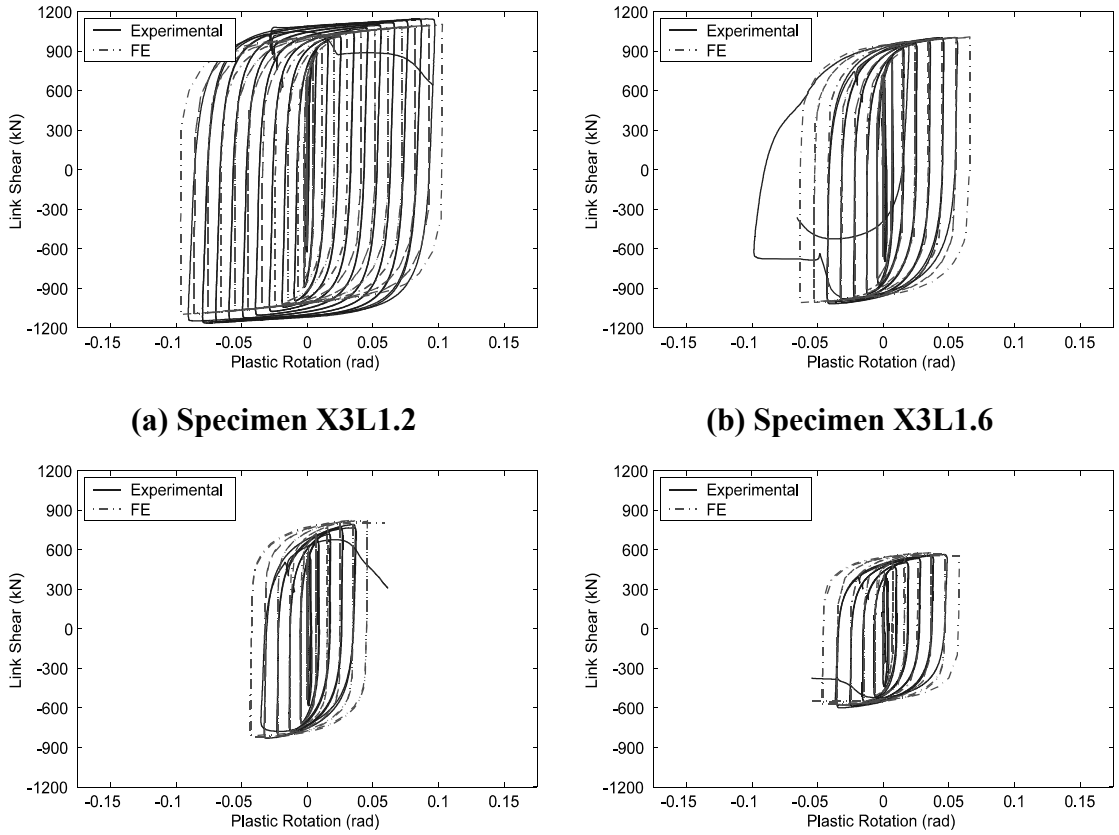

(a) Specimen X3L1.2 **(b) Specimen X3L1.6**

(c) Specimen X3L2.1 **(d) Specimen X3L3.0**

FIGURE 6-25 Comparison of Finite Element Models to Experimental Results for X3 Specimens

The specimens that suffered flange fracture quickly, that is, those that did not show significant strength degradation or a change in hysteresis shape prior to full flange fracture, are also simulated with reasonable agreement with the experimental results. Specimens X1L1.2, X1L1.6, X2L1.2, and all X3 specimens are examples of good agreement between the experimental hysteresis curves and finite element analysis hysteresis curves when no degradation prior to fracture is observed.

Based on the analyses and results presented above it is clear that the methods use to model rectangular links in this section and in Sections 2 and 3 adequately predict the hysteretic behavior of links that do not exhibit strength degradation prior to failure, or, exhibit degradation due only to buckling of the webs and/or flanges. However, these analyses do not capture strength degradation or failure from fracture, as they do not incorporate a

material fracture model. With this in mind, the proposed design rules, which focus on preventing web and flange buckling, and have been modified based on the results of the finite element parametric study in Section 3, seem reasonable for link design. However, proper link end connections that permit some plastic flow at the ends of the link flanges, similar to those used in the proof-of-concept test, must be used to avoid the detrimental flange fracture failure mode observed in many of the test specimens.

6.9 Impact on Proposed Design Requirements

As shown in this section, properly designed links with rectangular cross-sections can achieve their target rotations for the revised loading protocol in the 2005 AISC Seismic Provisions. The design requirements proposed in Section 3.5.4, which were developed to allow links to achieve their target rotations prior to web or flange buckling, seem adequate to prevent that buckling since no specimens suffered strength loss from buckling prior to reaching their target rotation. However, the problem of flange fracture has not been addressed in the proposed design requirements. Considering the differences reported in this section between specimens with haunch end connections and those with the gusset and stiffener connections (i.e., the supplementary specimens), it seems that the problem of flange fracture prior to the target rotations being achieved can be partly solved by using details that minimize the amount of welds and restraint of flange strain at the critical location.

The supplemental Specimen AX2L1.6, which had end connections similar to that of the proof of concept specimen, achieved its target rotation and also the largest rotation of any links tested in this phase of experiments. Extrapolation of the results for Specimen AX1L1.6 to the 2005 loading protocol indicates that it would also achieve its target rotation under that loading condition. Additionally, the proof-of-concept test specimen, which a similar end connection, achieved a rotation of almost twice its target. Therefore, it seems that end connections can be developed that allow the links to achieve their target rotation prior to flange fracture from restraint of plastic flow and development of large triaxial stresses. Gussets for brace connection to the link should be located at the center of the link flange and should be stiffened with as small a stiffener as necessary to avoid gusset buckling. Furthermore, the connections should use gussets that do not intersect the links at the web-

flange weld, as this is a critical location. In general, connections similar in configuration to those of the proof-of-concept test and supplementary links should be employed. These simple rules should guide engineers to end connections that do not overly restrain the flange and allow the link achieve its target rotation.

6.10 Summary

Results of the experimental program involving twelve links with haunch end connections, three different cross-sections, and four different normalized lengths, as well two supplementary links with end connections similar to that of the proof-of-concept test specimen, were reported. Results for total link rotation showed that most links that satisfy the proposed design recommendations of Section 3.5.4 can achieve their target rotation. Exceptions were the links with haunch end connections and a normalized length of 1.6, the transition length between shear and intermediate behavior, which suffered flange fracture prior to achieving their target rotations. A possible explanation for this is that these links appear to carry some of the link shear force through their flanges, while also being subject to relatively large moments. This may increase the triaxial stresses when plastic flow in the flange is highly restrained, as it is in the haunch end connections. One of the supplemental specimens, which utilized cross-section X2, had a normalized length of 1.6, and end connection similar to that of the proof-of-concept specimen, reached and exceeded its target rotation after being tested using the new loading protocol of the 2005 AISC Seismic Specifications. The other supplemental specimen, which utilized cross-section X1, had a normalized length of 1.6, and end connection similar to that of the proof-of-concept specimen, did not achieve its target rotation when tested using the older loading protocol of the 2002 AISC Seismic Specifications, but it did perform five complete cycles at rotations above 0.06 rads and showed cumulative energy dissipation, cumulative plastic rotation, and cumulative plastic strain values near those of the other supplemental specimen.

Results for all specimens tested were extrapolated to project the rotations that could be achieved if the 2005 loading protocol had been used in all cases. Cumulative plastic rotation and cumulative energy dissipation were both used to make these projections. It was found that only one of the links with a normalized length of 1.6 was not projected to achieve it's

target rotation, when cumulative energy dissipation was used, while all links at that length were projected to achieve their target rotations when cumulative plastic rotation was used.

Results for link overstrength were presented and the formulation developed by Richards and Uang, modified in Berman and Bruneau (2005a) for tubular links, and applied in Section 3 to examine it's predictions of overstrength in comparison to the finite element results, was again modified to ensure a more conservative prediction overstrength for use in capacity design. A larger value for the cyclic hardening factor for links with normalized lengths less 2.7 was proposed to achieve this more conservative prediction of overstrength for tubular links. The modified overstrength formulation seems to work well for links of different cross-section and link length and should help provide a more uniform safety factor considering the overstrength variation with respect to link length observed in both the experimental and finite element analysis data.

Comparison between finite element models of the specimens and the experimental results indicated that the models were adequate in predicting strength degradation from buckling. The models were also adequate in predicting the force-rotation hysteresis curves for specimens prior to strength degradation from fracture. However, as there was no fracture prediction model considered in the finite element analyses, they could not predict the flange fracture failures observed in many of the test specimens. With this in mind, the results of Section 3 seem valid as long as care is taken, via connection detailing, to minimize the restraint against plastic flow in the flange ends of tubular links.

The impact of this experimental program on the proposed design recommendations of Section 3.5.4 was to incorporate a requirement regarding minimizing flange restraint at the link end to delay flange fracture. However, even the specimens that had the heavily restrained haunch end connections were projected to reach their target rotation under the 2005 loading protocol as mentioned above. Since the web and flange compactness requirement and stiffener spacing formulation of Section 3.5.4 appear to be successful in preventing web and flange buckling prior to the link links achieving their target rotations, no other modifications to the proposed recommendations are made.

SECTION 7
SUMMARY, CONCLUSIONS, AND RECOMMENDATIONS FOR FURTHER RESEARCH

7.1 Summary

A previous report has identified, categorized, and qualitatively compared several options for the seismic retrofit of truss braced steel bridge piers (Berman and Bruneau. 2005a). Through these comparisons, strategies which were promising in terms of performance, but lacked fundamental research in areas necessary for their implementation, were identified as follows:

- Self-stabilizing links for eccentrically braced frames.
- Design of supplemental retrofit systems for protection of existing elements.

The objective of this report was then to develop design recommendations, based on analytical and experimental results, for self-stabilizing links for eccentrically braced frames.

Initial theoretical and experimental investigations regarding self-stabilizing links for EBFs were performed and reported in Berman and Bruneau (2005a). A link with a hybrid rectangular cross-section was selected to achieve the goal of self-stabilization, as these tubular cross-sections have high torsional rigidity and are not subject to lateral torsional buckling at the lengths that would be used in this application. Equations for plastic shear, plastic moment, link length, stiffener spacing, minimum flange compactness, and link overstrength were derived in manners consistent with the development of the existing codified design equations for WF links in EBFs. A proof-of-concept test specimen was designed and tested under cyclic, quasi-static conditions in the SEESL at UB. The proof-of-concept specimen met and exceeded performance objectives in terms of both link rotation and ductility. It reached a link rotation of 0.123 radians and a ductility of 6 in terms of frame

drift (and over 10 in terms of link rotation). No signs of lateral torsional buckling of the link and link beam were observed and comparison of the results of this single test specimen with the equations derived for design showed reasonable agreement in terms of strength calculations. The specimen eventually suffered fracture of the bottom link flange, adjacent to the connection with the north eccentric brace. From fractographic analysis with a light microscope, the failure was found to be due to a combination of large stresses and low cycle fatigue. This was all reported in Berman and Bruneau (2005a).

Using that previous work as a basis, a finite element model of the link from the proof-of-concept model was developed here using shell elements, nonlinear materials, and nonlinear geometry. After performing a mesh refinement study to determine the proper element size, the model was found to give results in reasonable agreement with the experimental results. No fracture model was considered in this analysis.

Using the above model as a basis, a finite element parametric study was developed for hybrid rectangular links for eccentrically braced frames. The parametric study was performed in two parts, the first part investigated links with various web and flange compactness ratios and both stiffened and unstiffened conditions for four link lengths covering the range of link behavior. The effect of web and flange compactness on a link's ability to achieve the target rotation prior to degradation from local buckling was of primary concern. Based on the results of the first part of the finite element study, recommendations for maximum compactness ratios and stiffener requirements were made and are given below.

Part 2 of the finite element parametric study considered links with compactness ratios near the proposed limits from Part 1, and investigated the use of different yield stresses for the webs and flanges of links. It was found that the proposed compactness ratio requirements were adequate for a range of steel yield stresses corresponding to commonly available steel grades. Additionally, link overstrength was studied using the results of analyses from both parts of the parametric study and it was found that a method for estimating link overstrength

proposed by others adequately estimated the overstrength of tubular links as a function of their normalized link length.

A testing program was then executed to verify the adequacy of the proposed design requirements for tubular links and validate the finite element results. The testing program included twelve primary links with haunch end connections that used three different cross-sections and four different normalized link lengths. Two of the cross-sections had compactness ratios near the proposed design limits and the third had relatively stocky webs and flanges. It was found that the proposed compactness limits were successful in preventing strength degradation due to local buckling prior to links achieving their target rotation. However, links with a normalized length at the transition point from shear to intermediate classification suffered flange fracture prior to achieving their target rotation. These links were investigated further as described below and two supplementary specimens with end connections more closely resembling those of the proof-of-concept specimen were fabricated.

Two possible causes for the early flange fractures observed for the links with a normalized length at the transition from shear to intermediate classification were given. The first possible cause was that the loading protocol used, which was from the 2002 AISC Seismic Provisions, was overly demanding and it was shown that if the links had been tested under the revised loading protocol of the 2005 AISC Seismic Provisions, these links may have achieved their target rotation. The second possible cause for the early flange fractures was the combined effect of overstrength and triaxial stress development. It was shown that links at this transition length are subjected to large values of shear and moment, exceeding plastic capacities in both cases, and that this in combination with the triaxial stresses that developed in the flanges because of the high restraint provided by the haunch end connection, could cause flange fracture.

The two supplementary links were also designed and tested to investigate the possible reasons for links at the transition length from shear to intermediate classification suffering flange fracture prior to achieving their target rotation. Both used an end connection similar

to the gusset and stiffener connection used in the proof-of-concept testing that possibly reduced the restraint in the flanges at the link ends. However, the first specimen tested still failed to achieve its target rotation, although the cumulative plastic rotation was improved. The second supplementary specimen was then tested using the loading protocol from the 2005 AISC Seismic Provisions. This link achieved the largest rotation of all links tested indicating that links with end connections that minimize, to the extent possible, the restraint against plastic flow in the flanges can achieve their target rotation when tested using the loading protocol of the 2005 AISC Seismic Provisions.

Based on the results of the analytical and experimental research performed in this study the following design requirements for tubular links for eccentrically braced frames have been proposed and are repeated here.

7.1.1 Link Strength

- The plastic shear, V_p, and moment, M_p, capacities of tubular links may be found, respectively, from:

$$V_p = \frac{2}{\sqrt{3}} F_{yw} t_w \left(d - 2t_f\right) \tag{7-1}$$

$$M_p = F_{yf} t_f \left(b - 2t_w\right)\left(d - t_f\right) + F_{yw} \frac{t_w d^2}{2} \tag{7-2}$$

  where F_{yw} and F_{yf} are the yield strengths of the webs and flanges respectively, t_w and t_f are the web and flange thicknesses, d is depth of the cross-section, and b is the width of the cross-section.

7.1.2 Link Length and Maximum Rotations

- The normalized link length, used to classify links and assign maximum rotations, is:

$$\rho = \frac{e}{\left(M_p / V_p\right)} \tag{7-3}$$

  where e is the actual link length.
- Links with $\rho \leq 1.6$ are classified as shear links . The maximum rotation demand for shear links should not exceed 0.08 rads.

- Link with $\rho > 2.6$ are classified as flexural links. The maximum rotation demand for flexural links should not exceed 0.02 rads.
- Links with $1.6 < \rho \leq 2.6$ are classified as intermediate links. The maximum rotation demand for intermediate links can be linearly interpolated from the values for shear and flexural links using ρ.

7.1.3 Compactness and Stiffener Requirements

- All links should have flanges satisfying:

$$b'/t_f \leq 0.64\sqrt{E_s/F_{yf}} \tag{7-4}$$

where b' is the clear flange width and E_s is Young's Modulus.

- Shear links should have webs satisfying:

$$d'/t_w \leq 1.67\sqrt{E_s/F_{yw}} \tag{7-5}$$

where d' is the clear web depth.

- Shear links should have web stiffeners if:

$$d'/t_w \geq 0.64\sqrt{E_s/F_{yw}} \tag{7-6}$$

otherwise, stiffeners are not required.

- Webs of intermediate and flexural links should satisfy:

$$d'/t_w \leq 0.64\sqrt{E_s/F_{yw}} \tag{7-7}$$

and no stiffeners are required.

- Stiffeners, when required for shear links, should have a maximum spacing, a, such that:

$$\frac{a}{t_w} + \frac{1}{8}\frac{d'}{t_w} = C_B \qquad (a \leq d) \tag{7-8}$$

where C_B is 20 for a maximum link rotation of 0.08 rads.

- The minimum cross-sectional area for web stiffeners, A_{st}, is:

$$A_{st} = \frac{F_{uw} t_w a}{0.828 F_{yst}} \left(1 - \frac{\frac{a}{d'}}{\sqrt{1 + \left(\frac{a}{d'} \right)^2}} \right) \tag{7-9}$$

where F_{uw} is the tensile strength of the web, F_{yst} is the yield strength of the stiffener and other terms are as previously defined.

- Other requirements for stiffeners are given in Berman and Bruneau (2005a).

7.1.4 Link Overstrength

- Design of framing members outside the link in eccentrically braced frames should consider the maximum possible shear force that could develop in the link. The maximum possible shear force, V_{ult}, is given by

$$V_{ult} = \Omega R_y V_p \tag{7-10}$$

where R_y is the ratio of mean to specified yield stress of the steel used and is given in the AISC Seismic Provisions, Ω is a cyclic hardening factor defined below, and V_p is the nominal plastic shear strength calculated as described below.

- The cyclic hardening factor, Ω, should vary with respect ρ as:

$$\begin{aligned} \Omega &= 1.6 & \rho &\le 1.6 \\ \Omega &= 1.6 - 0.56(\rho - 1.6) & 1.6 &< \rho \le 2.6 \\ \Omega &= 2.7/\rho & \rho &\ge 2.6 \end{aligned} \tag{7-11}$$

- V_p should be calculated using nominal material properties and (7-1), except for links with $\rho \le 1.6$ where the contribution of each flange to the plastic shear strength, V_f, should be added to the result of (7-1). The contribution of each flange to the plastic shear is given by:

$$V_f = \frac{F_{yf} b t_f^2}{2e} - \frac{F_{yf} t_w^2 e}{8b} \tag{7-12}$$

7.1.5 Link Connections

- Connections of eccentric braces to each end of the link can use a gusset and stiffener connection similar to that shown in figures 2-4 and 2-5 (i.e., those of the proof-of-concept test described in Berman and Bruneau, 2005a). Welds across the flange width should be kept as small as possible and the thicknesses of the gussets and stiffeners should be as small as possible while still satisfying strength requirements.

7.2 Conclusions

A new self-stabilizing tubular link for eccentrically braced frames has been developed. Links designed according the proposed requirements above were shown, experimentally and analytically, to have the ductility to achieve their target rotations under quasi-static cyclic loading as specified by the 2005 AISC loading protocol when end connections are used that do not overly restrain the plastic flow in the link flanges.

The compactness requirements in the AISC Seismic Provisions for hollow structural sections were not derived considering the use of these cross-sections as links in eccentrically braced frames. Therefore, web and flange compactness requirements have been proposed for tubular sections used in this manner. The proposed requirements for webs of tubular sections used as shear links allow a considerably larger compactness ratio than currently allowed by AISC as long as stiffeners are present. Proposed stiffener spacing for tubular links is also different from the current requirements for links utilizing wide-flange shapes in that they are only required for shear links, not intermediate and flexural links.

The proposed requirements for design of tubular links for eccentrically braced frames presented in this work are recommended for adoption in both building and bridge applications. They are appropriate for inclusion in the AISC Seismic Provisions for Steel Buildings and the NCHRP 12-49 Recommended LRFD Guidelines for the Seismic Design of Highway Bridges.

7.3 Recommendations for Further Research

7.3.1 Laterally Stable Links for EBFs

The predominant failure mode observed in the testing reported here was flange fracture, which was at least partly due to restraint against plastic flow and associated development of triaxial stresses in the flanges near the connections at the link end. Considering this failure mode, it would be advantageous to develop a link end connection (or link-to-eccentric brace connection) that reduces either the plastic flow demand in the flange at that location or reduces the restraint provided by the connection. Concepts similar to those developed for moment frame connections following the 1994 Northridge Earthquake may provide a starting point for development of such link end connections.

The development of low cycle fatigue formulations for all types of links for EBFs is a major area of research that warrants investigation. Such formulations could be used to compare estimated low cycle fatigue life with estimated low cycle fatigue demand, associated with seismic events, and assess the likelihood of fracture. Such a research program would have to consider the various detailing and associated failure mode possibilities for both tubular and WF links. While there is considerable experimental data available for EBF links, much of it is difficult to use in calibration of low cycle fatigue models because the tests were not conducting under constant amplitude cycling. A minimum of two constant deformation experiments, at different deformation amplitudes, would be required for each link detail type in order to calibrate Coffin-Manson style low cycle fatigue models. Results of such a research program could also serve as a framework for low cycle fatigue evaluation of other critical steel sub assemblages.

A detailed study of the triaxial restraint problem in the flanges at the links ends should also be conducted. Using solid finite element models, the problem of triaxial stress development and fracture could be explored in more detail and recommendations for alternative link end connections to minimize this problem could be made. Additionally, if tubular links with considerably thick plates (i.e., greater than 25 mm (1 in) thickness) and correspondingly large welds are to be used, an investigation of the fracture life for such configurations should

be performed. Considered in this investigation should also be strain rate effects as these might effect thicker plates and larger welds.

To further verify the adequacy of EBFs with self-stabilizing tubular links for use in bridge piers, earthquake simulation testing should be performed. Ideally, the testing would be carried out on a four-legged bridge pier with bi-directional shaking and EBFs in both orthogonal directions. This could also address any concerns about the eccentric braces causing torsion on the link under certain excitations.

7.3.2 Seismic Retrofit of Braced Steel Truss Bridge Piers

In addition to the further research on self-stabilizing links for EBFs, other retrofit strategies and their applications also should be studied, some of which are discussed in Berman and Bruneau (2005a). For instance, experimental evaluation of the supplemental retrofit strategy design procedure described in Berman and Bruneau (2005a) and developed further in Berman and Bruneau (2005b), should be performed to ensure that the buckling deformations of the existing braces can indeed be limited using that procedure. Of particular interest is the behavior of these systems when designed per Berman and Bruneau (2005b) and then subjected to ground motions. Therefore, shake table testing of supplemental systems is recommended.

Additionally, the application of various retrofit strategies to long span steel truss bridges should be studied in terms of global bridge response. Consideration for applying different retrofit strategies to different piers based on their height and stiffness should be given, since it is conceivable that in some cases two piers supporting the same bridge may be retrofitted using different strategies. The interaction of the different strategies on global bridge behavior should be of primary interest.

SECTION 8

REFERENCES

AISC (2001). *Manual of Steel Construction: Load and Resistance Factor Design, 3rd Ed*. American Institute of Steel Construction, Chicago, IL.

AISC (2002). *Seismic Provisions for Structural Steel Buildings*. American Institute of Steel Construction, Chicago, IL.

AISC (2005). *Seismic Provisions for Structural Steel Buildings*. American Institute of Steel Construction, Chicago, IL.

ASTM A370-03a. "Standard Test Methods and Definitions for Mechanical Testing of Steel Products." ASTM International, Materials Park, OH.

ASTM E606-92. "Standard Practice for Strain Controlled Fatigue Testing." ASTM International, Materials Park, OH.

ATC (1992). *Guidelines for Seismic Testing of Components of Steel Structures Report-24*, Applied Technology Council, Redwood City, CA.

ATC/MCEER. (2003). *NCHRP 12-49 Recommended LRFD Guidelines for the Seismic Design of Highway Bridges*, *Part I: Specifications*, ATC/MCEER Joint Venture Multidisciplinary Center for Earthquake Engineering Research: State University of New York at Buffalo, Buffalo, NY

Astaneh, A., and Cho, S.W. (1994). "Compression Behavior of Critical Members of the Golden Gate Bridge." *Proceedings of the Fifth US National Conference on Earthquake Engineering*, EERI, Vol. 2, p 713-722, Chicago, IL, July 10-14.

Astaneh, A. (1998). "Proof-Testing of Latticed Members and their Connections on the San Francisco-Oakland Bay Bridge." *Technical Report UCB/CEE-STEEL-98/03*, Department of Civil and Environmental Engineering, University of California Berkeley, Berkeley, CA.

Arce, G. (2002). "Impact of Higher Strength Steels on Local Buckling and Overstrength of Links in Eccentrically Braced Frames." M.S. Thesis, Department of Civil Engineering, University of Texas at Austin, Austin, TX.

Berman, J.W., and Bruneau, M. (2003). "Experimental Investigation of Light-Gauge Steel Plate Shear Walls for the Seismic Retrofit of Buildings." *Technical Report MCEER-03-0001*, Multidisciplinary Center for Earthquake Engineering Research, State University of New York at Buffalo, Buffalo, NY.

Berman, J.W., and Bruneau, M. (2005a). "Approaches for the Seismic Retrofit of Braced Steel Bridge Piers and Proof-of-Concept Testing of an Eccentrically Braced Frame with Tubular Link." *Technical Report MCEER-05-0004*, Multidisciplinary Center for Earthquake Engineering Research, State University of New York at Buffalo, Buffalo, NY.

Berman, J.W., and Bruneau, M. (2005b). "Supplemental System Retrofit Considerations for Braced Steel Bridge Piers." *Journal of Earthquake Engineering and Structural Dynamics* - Special Issue on Transportation Structures, 34(4 and 5), 497-517.

Bruneau, M., Uang, C.M., and Whittaker, A. (1998). *Ductile Design of Steel Structures*. McGraw-Hill, New York, NY.

Chen, W.F., Goto, Y., and Liew, J.Y.R, (1996). *Stability Design of Semi-Rigid Frames*, John Wiley & Sons, Inc., New York, NY.

Cook, N.E., (1983). "Strength of Flexibly-Connected Steel Frames Under Load-Histories," Ph.D. Dissertation, University of Colorado-Boulder, Boulder, CO.

Dafalias, Y.F., and Popov, E.P., (1976). "Plastic Internal Variables Formalism of Cyclic Plasticity", *Journal of Applied Mechanics*, ASCE, 43, 645-651.

Dusicka, P., Itani, A.M., and Buckle, I.G. (2002). "Cyclic Behavior of Shear Links and Tower Shaft Assembly of San Francisco-Oakland Bay Bridge Tower." *Technical Report CCEER 02-06*, Center for Civil Engineering Earthquake Research, University of Nevada Reno, Reno, NV.

Goto, Y., Suzuki, S., and Chen, W.F., (1991), "Analysis of Critical Behavior of Semi-Rigid Frames With or Without Load Histories in Connections", *International Journal of Solids and Structures*, 27(4), 467-483.

HKS (2001). *ABAQUS Standard User's Manual*. Hibbitt, Karlsson, and Sorensen, Inc., Pawtucket, RI.

Itani, A.M. (1997). "Cyclic Behavior of Richmond-San Rafael Tower Links." *Technical Report CCEER 97-4*, Center for Civil Engineering Earthquake Research, University of Nevada Reno, Reno, NV.

Itani, A., Vesco, T., and Dietrich, A. (1998). "Cyclic Behavior of "As-Built" Laced Members with End Gusset Plates on the San Francisco-Oakland Bay Bridge." *Technical Report CCEER 98-01*, Center for Civil Engineering Earthquake Research, University of Nevada, Reno.

Kaufmann, E.J., Metrovich, B., and Pense, A.W. (2001). "Characterization of Cyclic Inelastic Strain Behavior on Properties of A572 Gr. 50 and A913 Gr. 50 Rolled Sections" *ATLSS Report No. 01-13*, National Center for Engineering Research on Advanced Technology for Large Structural Systems, Lehigh University, Bethlehem, PA.

Kasai, K., and Popov, E.P. (1986). "Study of Seismically Resistant Eccentrically Braced Steel Frame Systes." *Report No. UCB/EERC-86/01*, Earthquake Engineering Research Center, College of Engineering, University of California Berkeley, Berkeley, CA.

Lee, K., and Bruneau, M. (2004). "Seismic Vulnerability Evaluation of Axially Loaded Steel Built-Up Laced Members." *Technical Report MCEER-04-0007*, Multidisciplinary Center for Earthquake Engineering Research, State University of New York at Buffalo, Buffalo, NY.

MathWorks (1999). *MatLab Function Reference*. The MathWorks, Inc., Natick, MA.

Mason, R.L., Gunst, R.F., and Hess, J.L. (2003). *Statistical Design and Analysis of Experiments: With Applications to Engineering and Science*. 2nd Ed. J. Wiley and Sons, New York, NY

Metris, Inc. (2005). K-Series cameras by Metris, Inc. www.metris.com.

Nakashima, M., Iwai, S., Iwata, M., Takeuchi, T., Konomi, S., Akazawa, T., and Sabuuri, K. (1994). "Energy Dissipation Behavior of Shear Panels Made of Low Yield Steel." *Earthquake Engineering and Structural Dynamics*, 23, 1299-1313.

Pollino, M., and Bruneau, M. (2004). "Seismic Retrofit of Bridge Steel Truss Piers Using a Controlled Rocking Approach." *Technical Report MCEER-04-0011*, Multidisciplinary Center for Earthquake Engineering Research, State University of New York at Buffalo, Buffalo, NY.

Richards, P., and Uang, C.M. (2002). "Evaluation of Rotation Capacity and Overstrength of Links in Eccentrically Braced Frames." *Report No. SSRP-2002/18*, Structural Systems Research Project, Department of Structural Engineering, University of California San Diego, La Jolla, CA.

Richards, P., and Uang, C.M. (2003). "Development of Testing Protocol for Short Links in Eccentrically Braced Frames." *Report No. SSRP-2003/08*, Structural Systems Research Project, Department of Structural Engineering, University of California San Diego, La Jolla, CA.

Ritchie, P., Kauhl, N., and Kulicki, J. (1999). "Critical Seismic Issues for Existing Steel Bridges." *Technical Report MCEER-99-0013*, Multidisciplinary Center for Earthquake Engineering Research, State University of New York at Buffalo, Buffalo, NY.

Uang, C.M., and Kleiser, M. (1997). "Cyclic Performance of As-Built Latticed Members for the San Francisco-Oakland Bay Bridge." *Report No. SSRP-97-01*, Department of Structural Engineering, University of California, San Diego.

APPENDIX A
LINK HYSTERESIS CURVES FROM THE FINITE ELEMENT PARAMETRIC STUDY

A.1 General

This Appendix contains the link shear force versus total link rotation hysteresis curves for all links in Parts 1 and 2 of the finite element parametric study described in Section 3. For the links from both Part 1 of the parametric study (figures C-1 to C-16), the dashed lines in the figures for each link correspond to the minimum of the plastic shear force, V_p, and the shear due to the plastic moment developing at the link ends, $V = 2M_p/e$. These values are calculated using the nominal yield stress of 345 MPa (50 ksi), not the actual yield stress 372 MPa (54 ksi), and therefore represent the values one would obtain in design. Each page of figures for the Part 1 links in this appendix represents a link cross-section, in other words each page has of figures has a constant web compactness, d'/t_w, and flange compactness, b'/t_f. Each row of plots on a page represents the normalized link lengths for those cross-sections and the columns represent the unstiffened and stiffened conditions as described in Section 3.

For the links of Part 2 of the parametric study (figures C-17 to C-25), each page of figures represents two link cross-section that was derived from the same combination of flange and web yield stresses as described in Section 8. The rows of figures for the Part 2 links indicate the normalized link length and the columns two separate the unstiffened and stiffened for a given combination of web and flange yield stresses. Recall that for Part 2 of the study the stiffened links had a web compactness of approximately $1.67\sqrt{E_s/F_{yw}}$, and the unstiffened links had a web compactness of approximately $0.64\sqrt{E_s/F_{yw}}$, which were the bounds in the

proposed design requirements of Section 3.5.4. As with the Part 1 links, the dashed lines in the Part 2 link hystereses indicate the minimum of V_p or $2M_p/e$ found using the nominal yield stresses.

Note that for some of the stiffened models, as the amplitude of buckling increased some convergence failures occurred. This was caused by large buckling displacements developing over a small rotation range. These instances resulted in some stiffened models not being analyzed for the full cyclic displacement history. However, where this is the case, the shear strength of those particular links had already dropped well below 80% of the maximum shear observed and therefore a limit plastic rotation could be calculated despite the convergence failure at larger rotations. In most cases the link hystereses are symmetric, however, there were a few links where the combination of web and flange buckling resulted in an unsymmetric hysteresis at large rotations. In these cases the loops were symmetric well past the limit rotation (i.e., the rotation at which the backbone curve drops below 80% of the maximum shear observed) and only became unsymmetric when large buckling deformations were observed in both the webs and flanges.

For all links presented in this appendix the hystereses are shown for the full analyses. Recall that no fracture model was incorporated in the analyses and therefore, with the exception of convergence failures, the analyses were run to rotations of approximately 0.2 rads. In many cases fracture would be expected prior to this level of rotation but not before the target rotations of 0.08 rads, 0.08 rads, 0.05 rads, and 0.02 rads for normalized link lengths, ρ, of 1.2, 1.6, 2.1, and 3.0 respectively.

A.2 Part 1 Link Hysteresis Curves

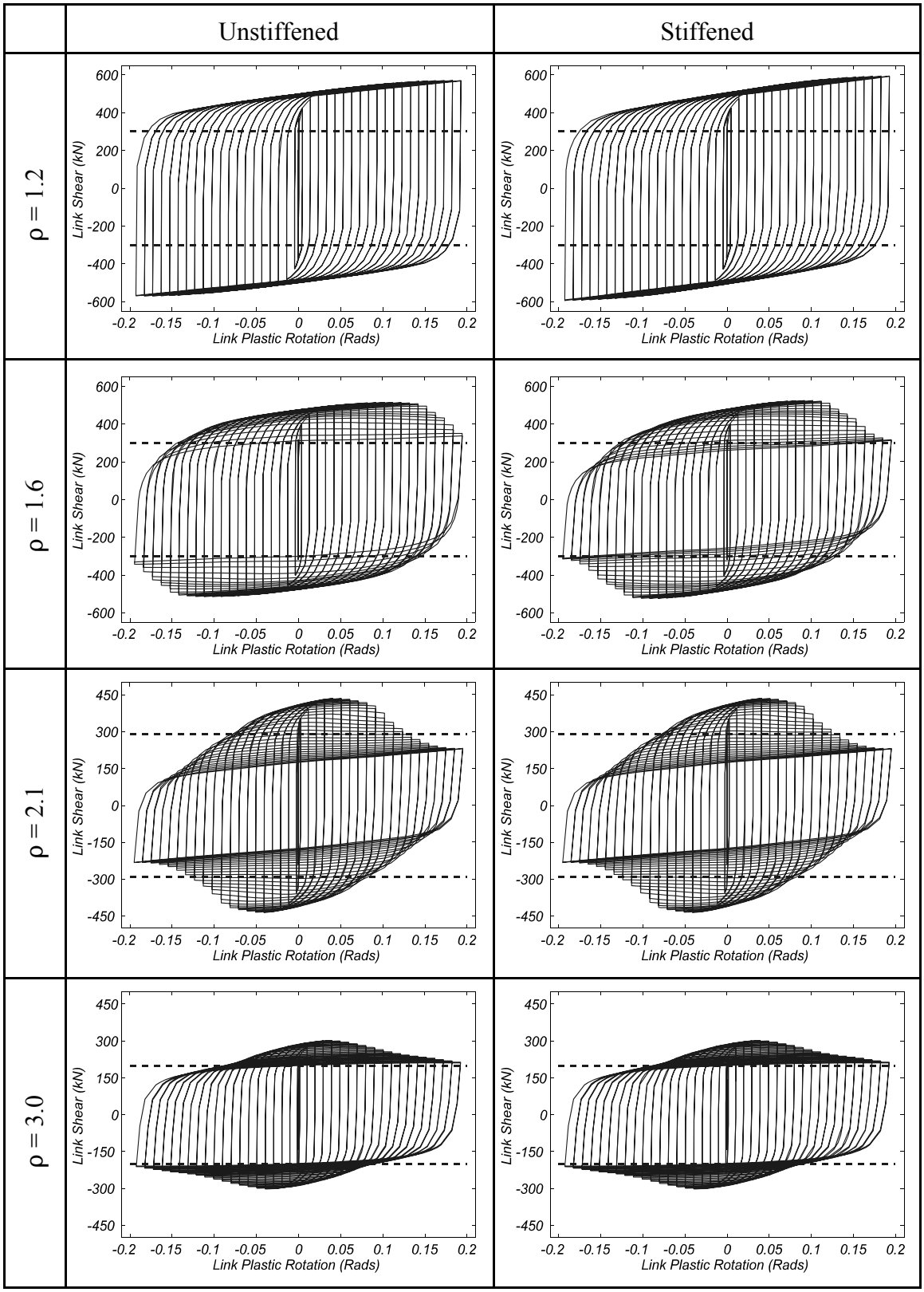

FIGURE A-1 Link Hystereses for Part 1 Links with $b'/t_f = 8.0$ and $d'/t_w = 12.0$

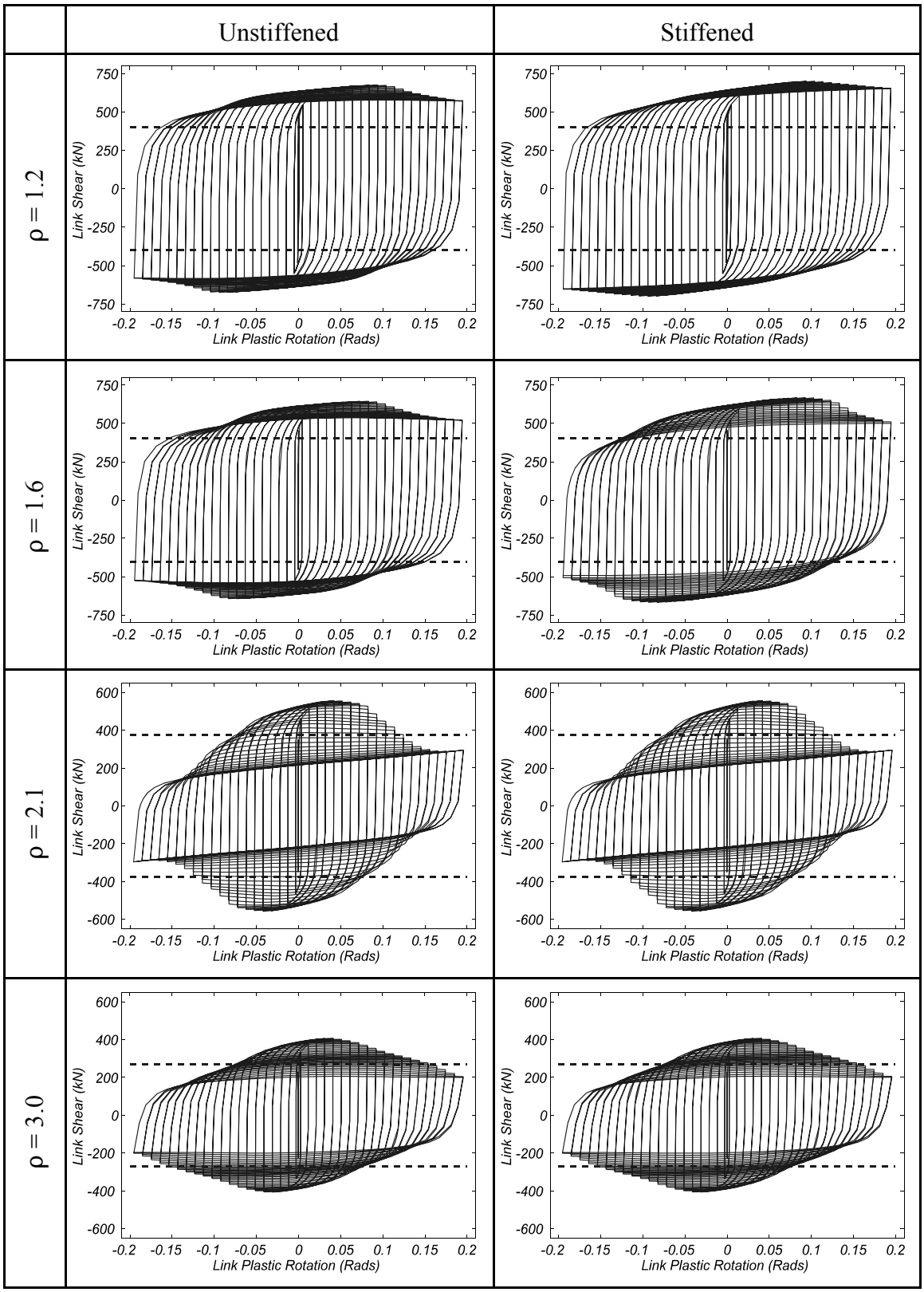

FIGURE A-2 Link Hystereses for Part 1 Links with $b'/t_f = 8.0$ and $d'/t_w = 16.0$

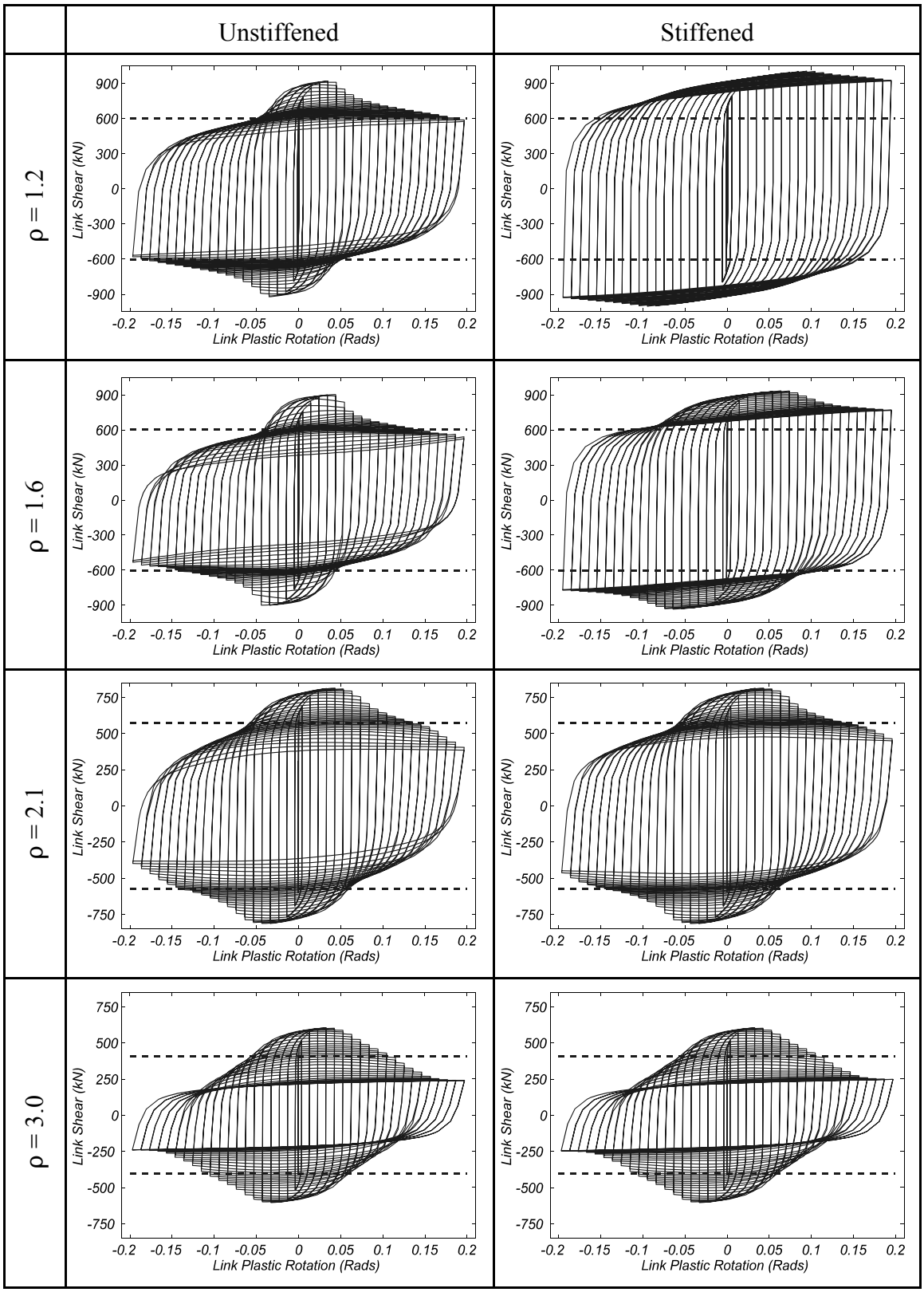

FIGURE A-3 Link Hystereses for Part 1 Links with $b'/t_f = 8.0$ and $d'/t_w = 24.0$

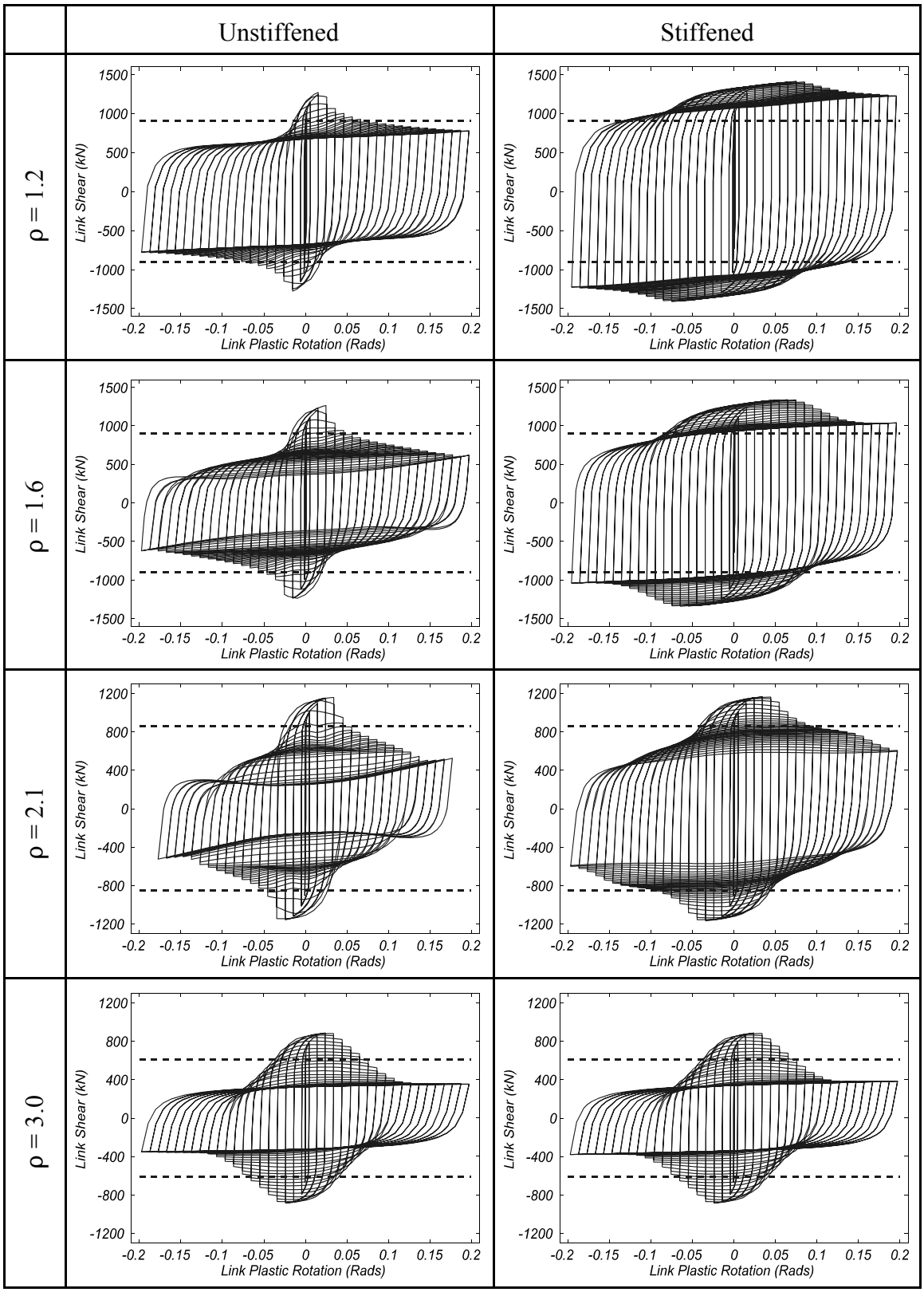

FIGURE A-4 Link Hystereses for Part 1 Links with $b'/t_f = 8.0$ and $d'/t_w = 36.0$

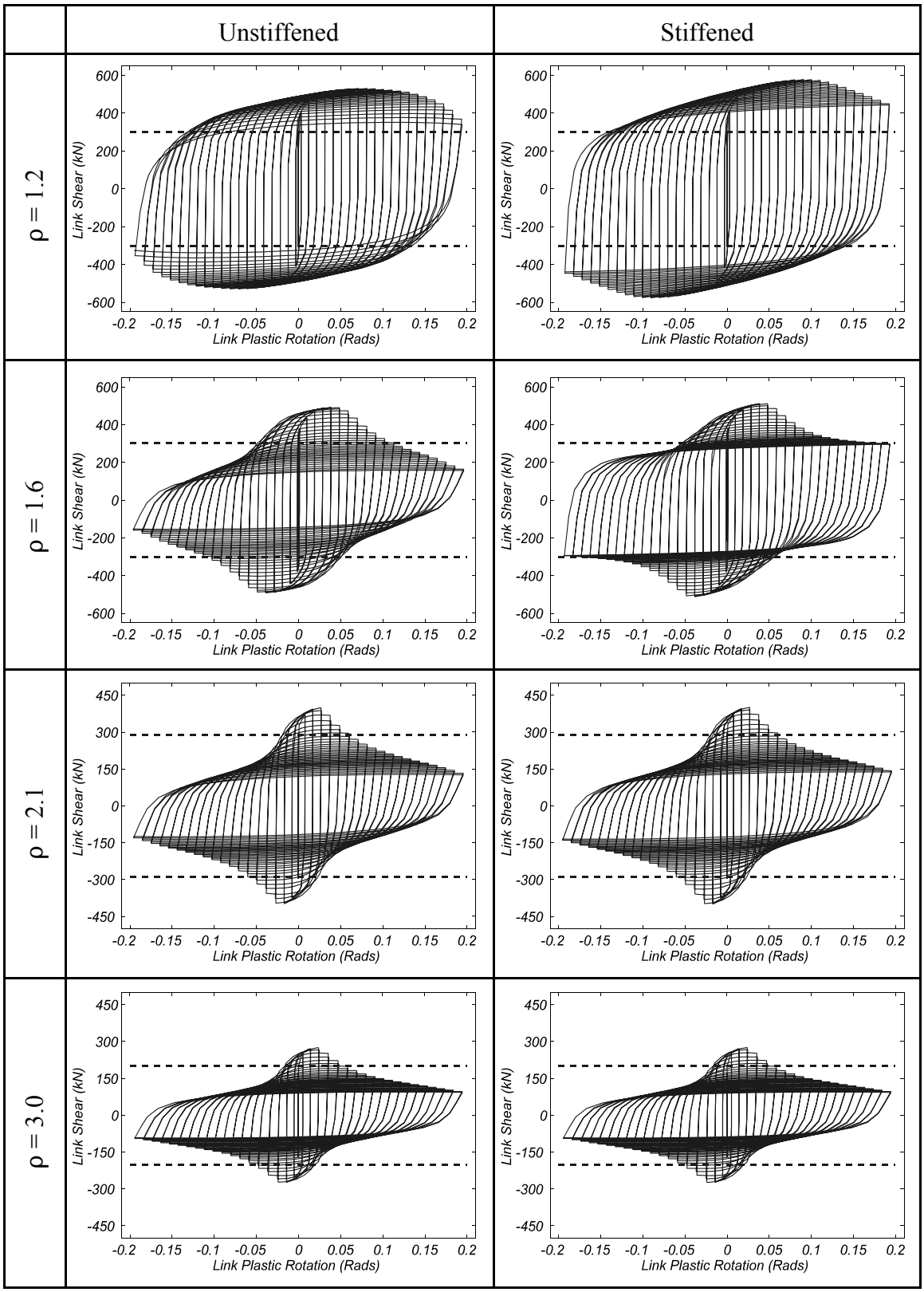

FIGURE A-5 Link Hystereses for Part 1 Links with $b'/t_f = 17.0$ and $d'/t_w = 12.0$

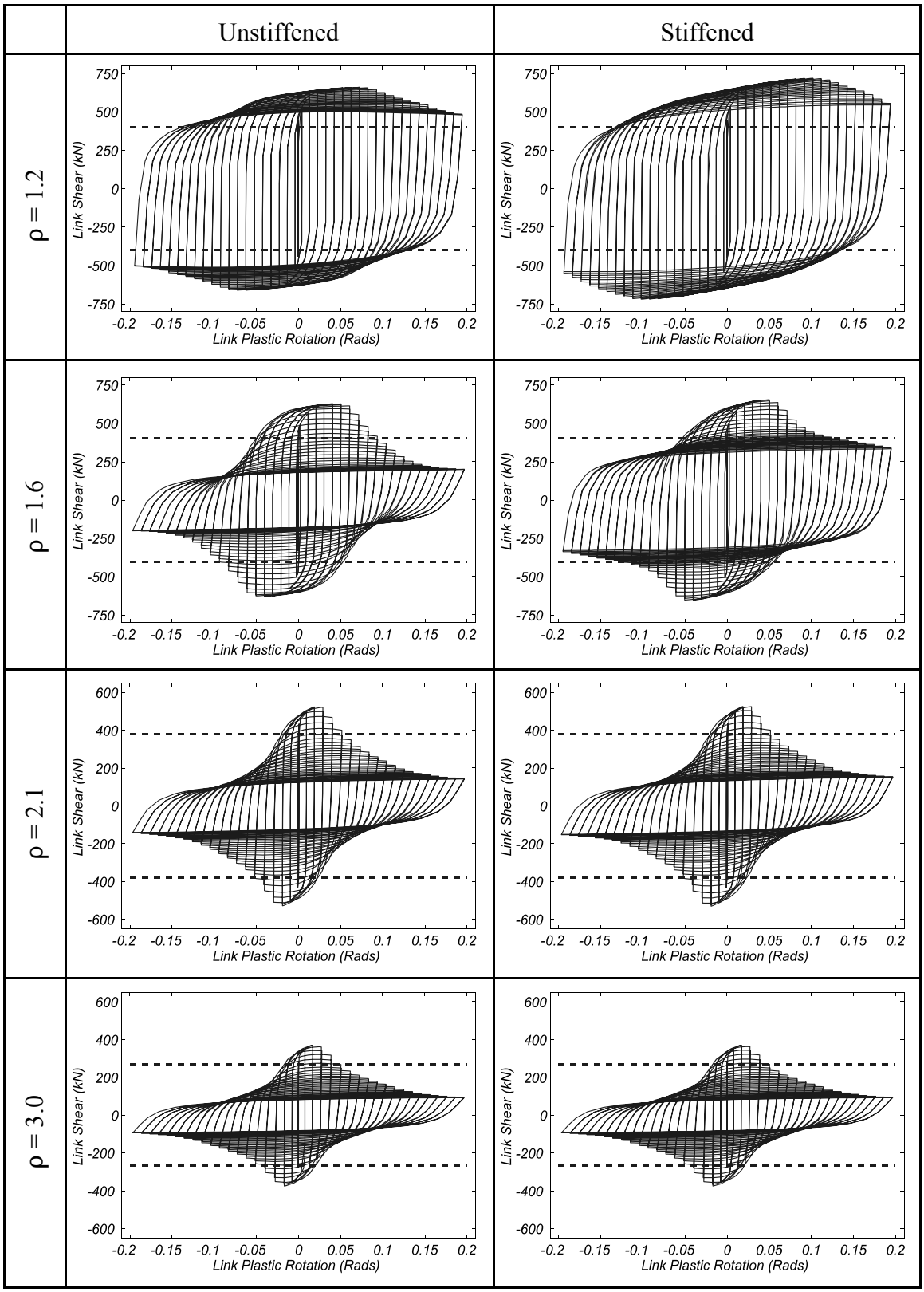

FIGURE A-6 Link Hystereses for Part 1 Links with $b'/t_f = 17.0$ and $d'/t_w = 16.0$

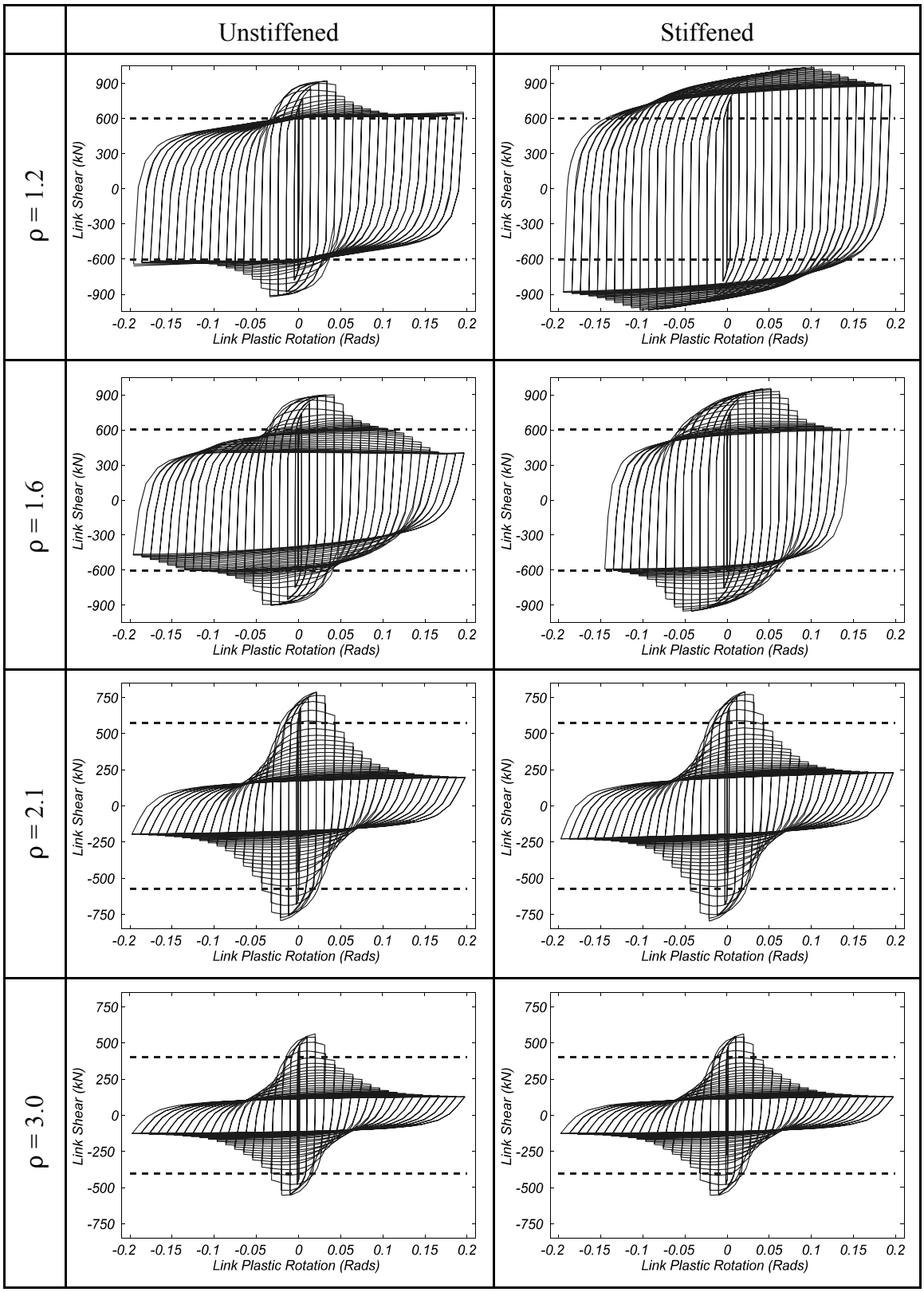

FIGURE A-7 Link Hystereses for Part 1 Links with $b'/t_f = 17.0$ and $d'/t_w = 24.0$

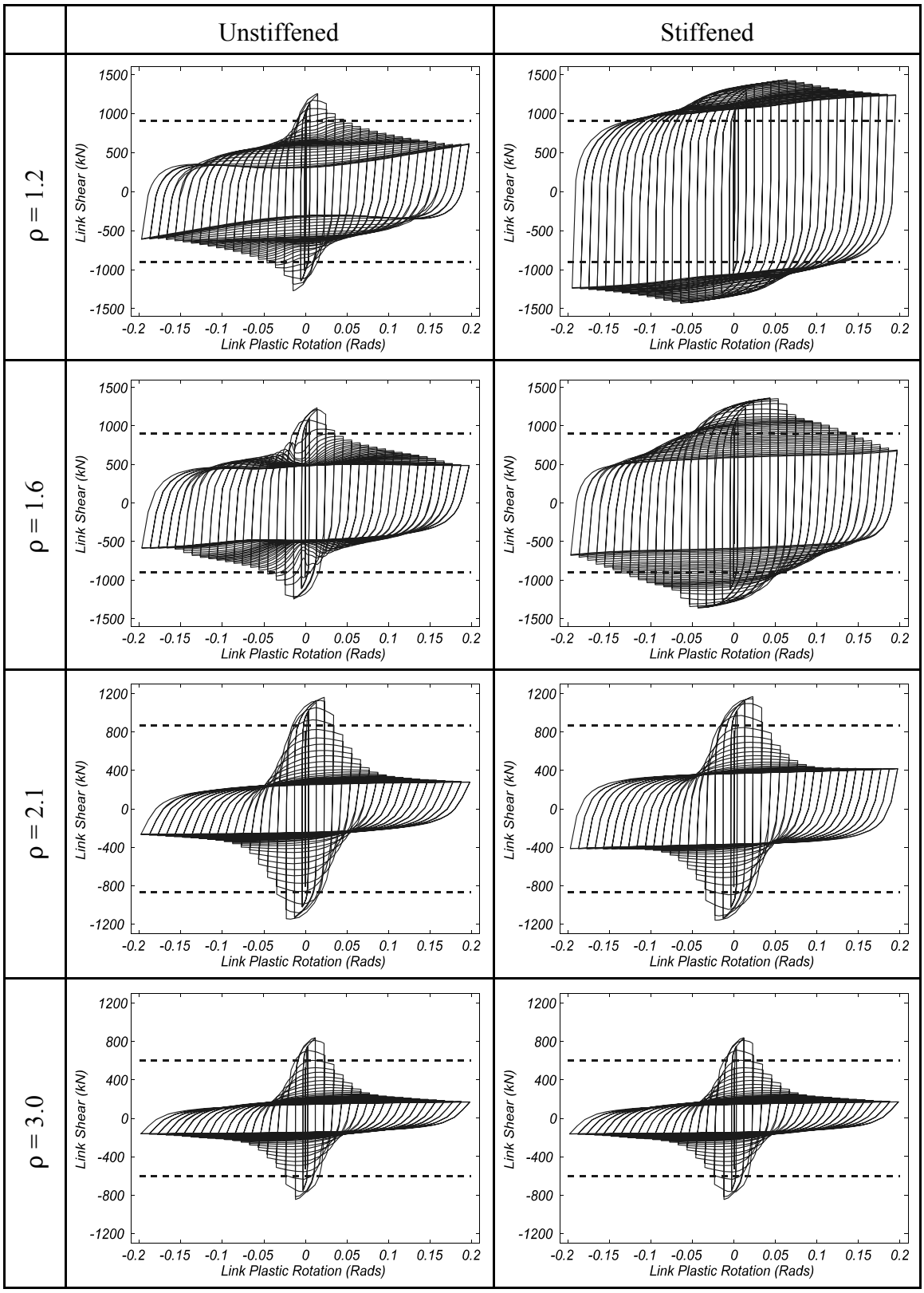

FIGURE A-8 Link Hystereses for Part 1 Links with $b'/t_f = 17.0$ and $d'/t_w = 36.0$

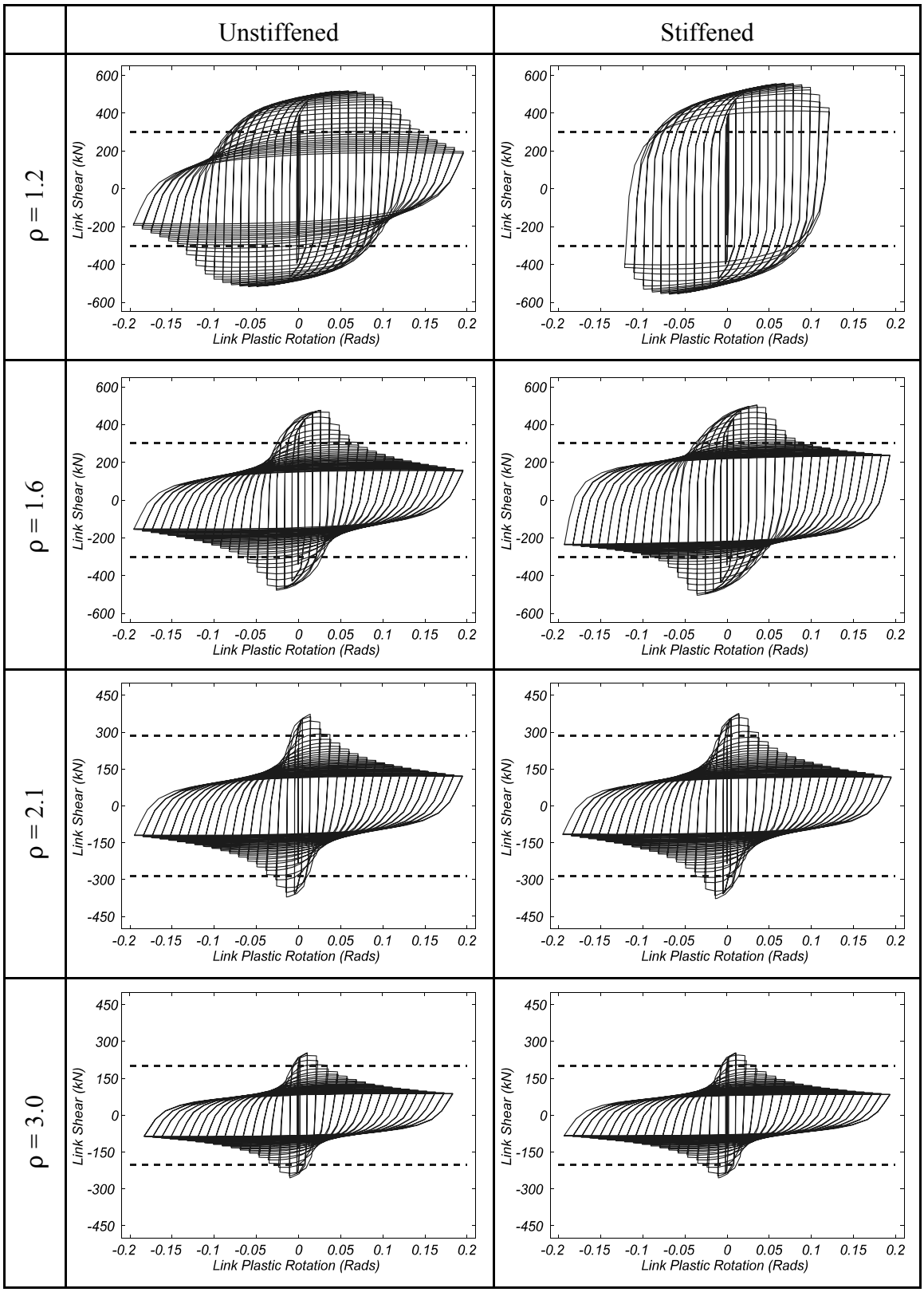

FIGURE A-9 Link Hystereses for Part 1 Links with $b'/t_f = 24.0$ and $d'/t_w = 12.0$

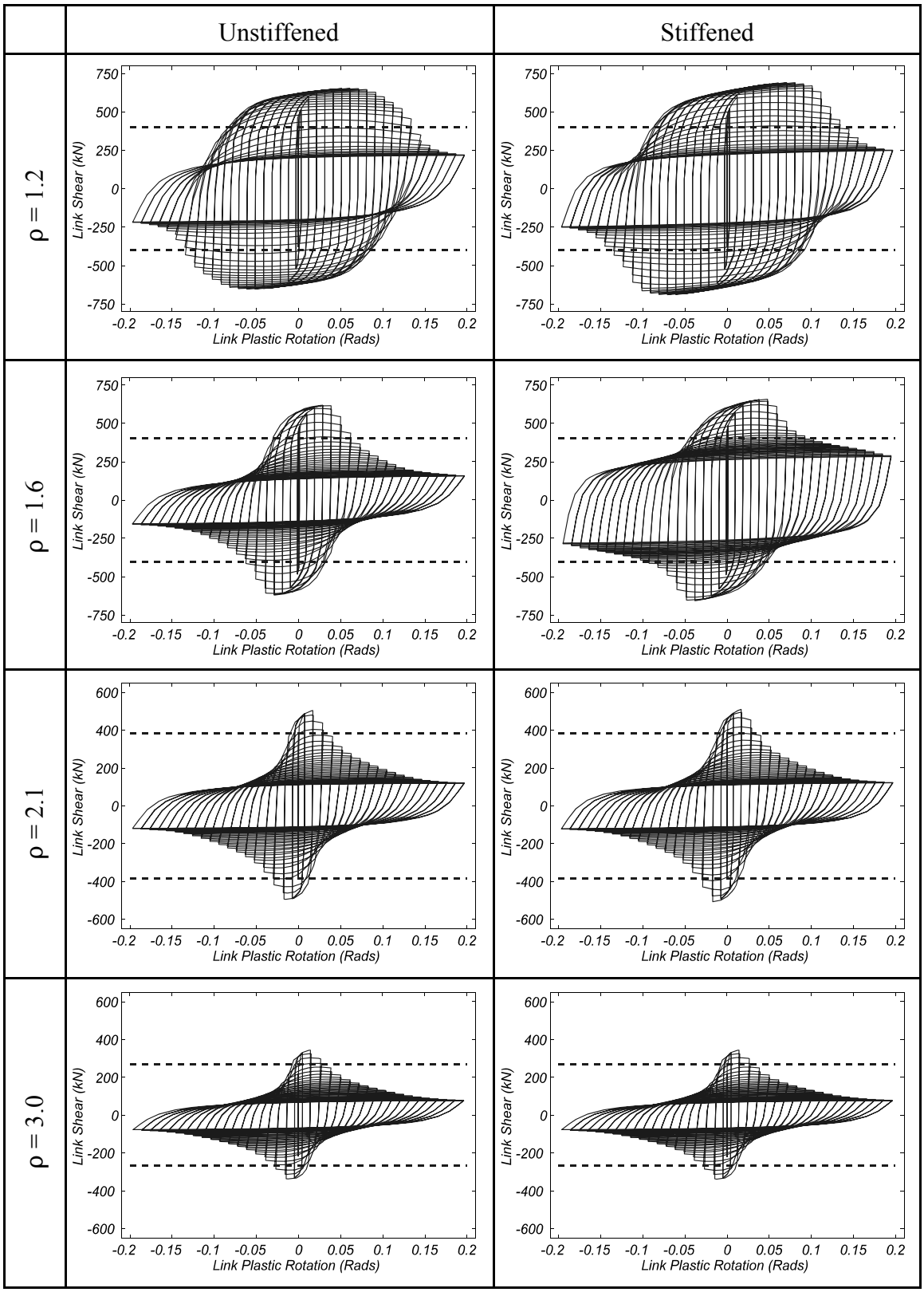

FIGURE A-10 Link Hystereses for Part 1 Links with $b'/t_f = 24.0$ and $d'/t_w = 16.0$

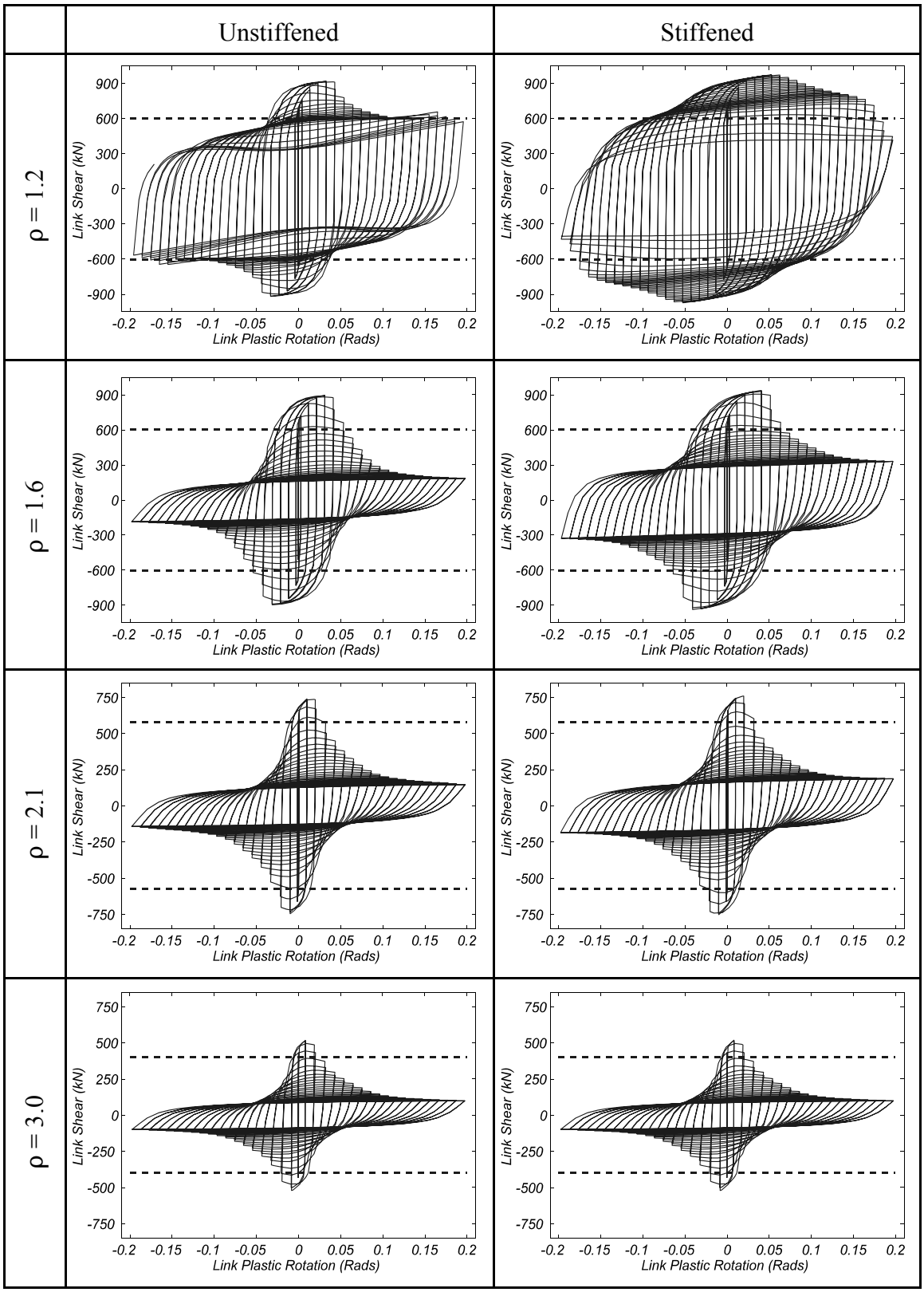

FIGURE A-11 Link Hystereses for Part 1 Links with $b'/t_f = 24.0$ and $d'/t_w = 24.0$

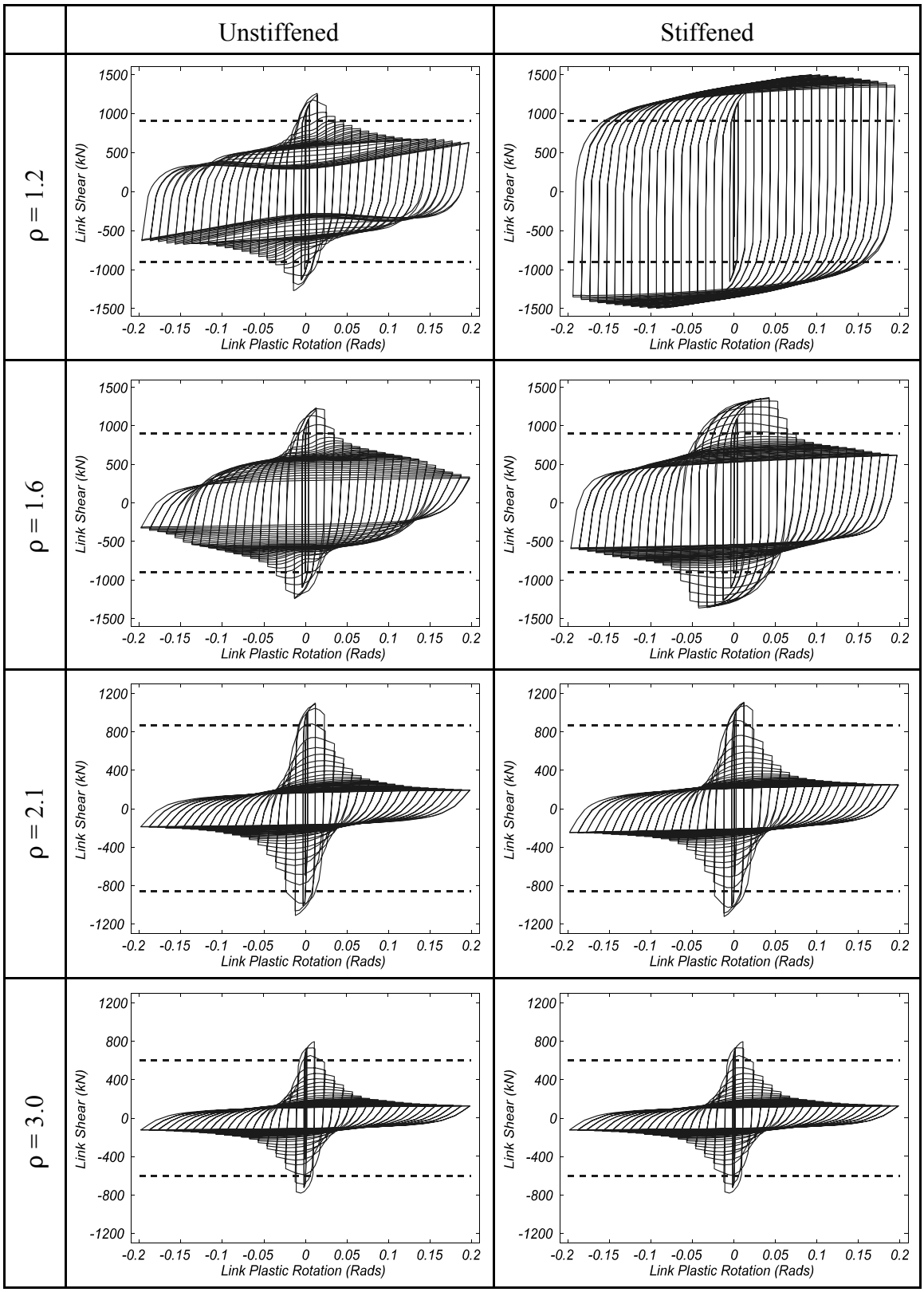

FIGURE A-12 Link Hystereses for Part 1 Links with $b'/t_f = 24.0$ and $d'/t_w = 36.0$

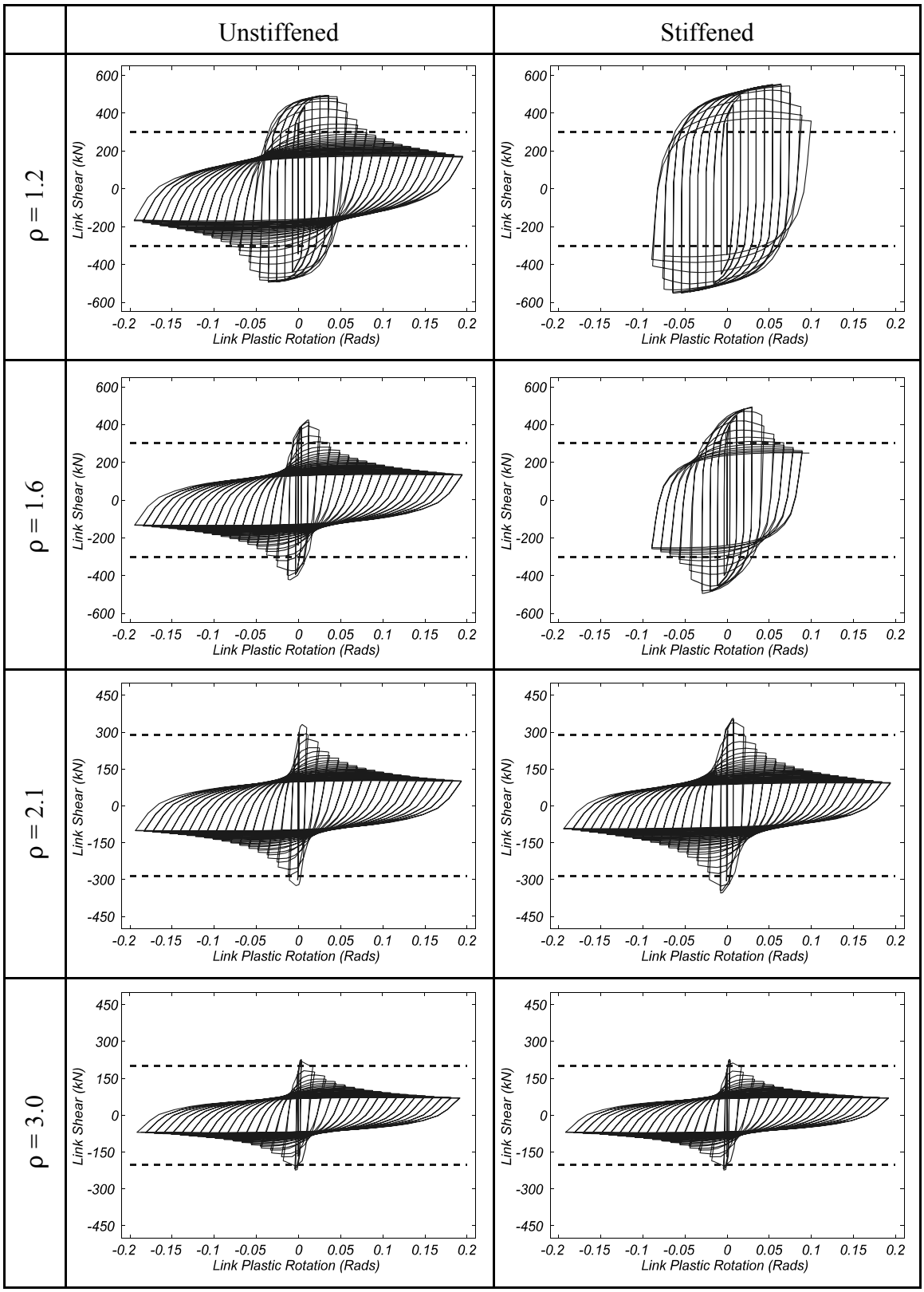

FIGURE A-13 Link Hystereses for Part 1 Links with $b'/t_f = 40.0$ and $d'/t_w = 12.0$

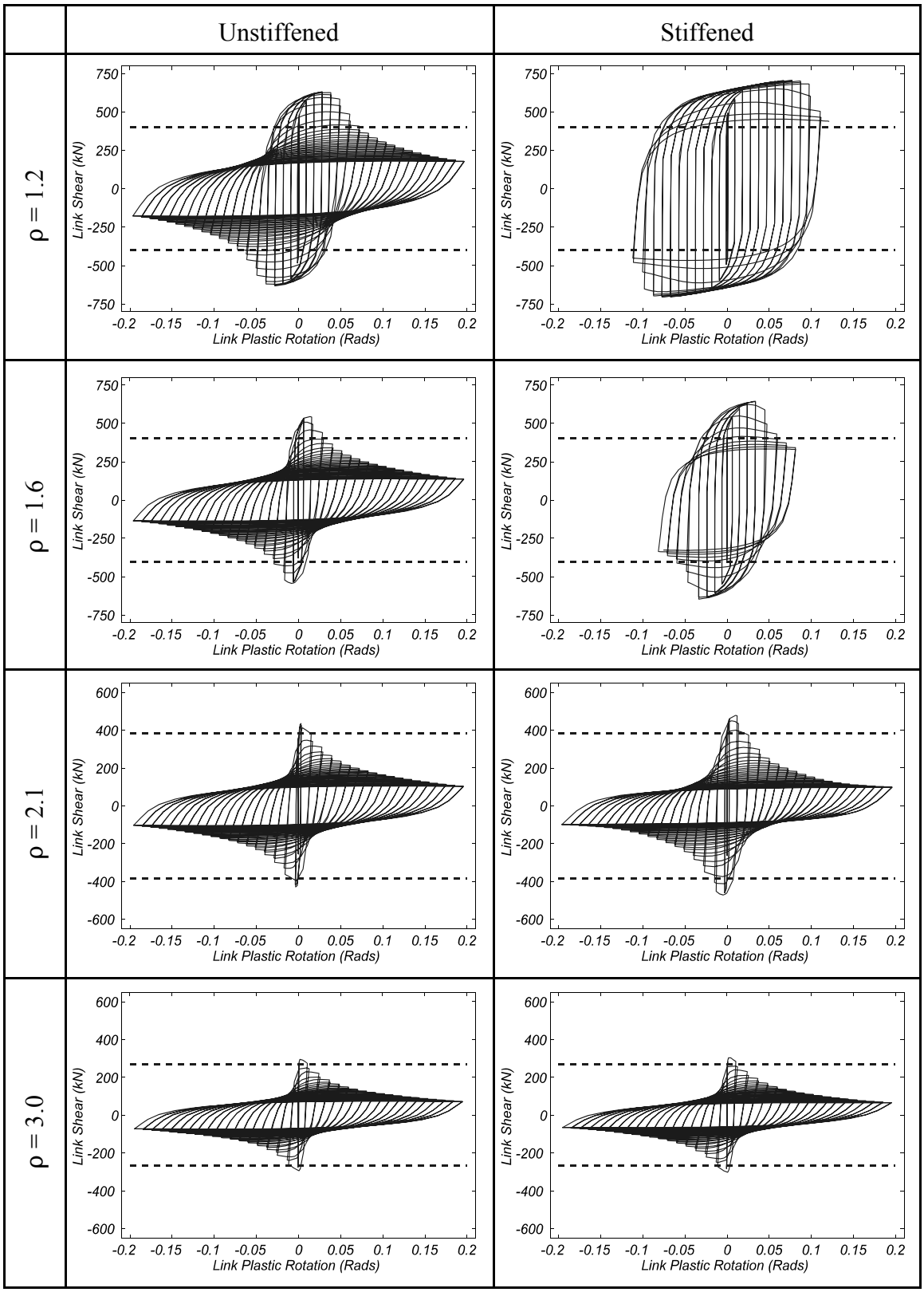

FIGURE A-14 Link Hystereses for Part 1 Links with $b'/t_f = 40.0$ and $d'/t_w = 16.0$

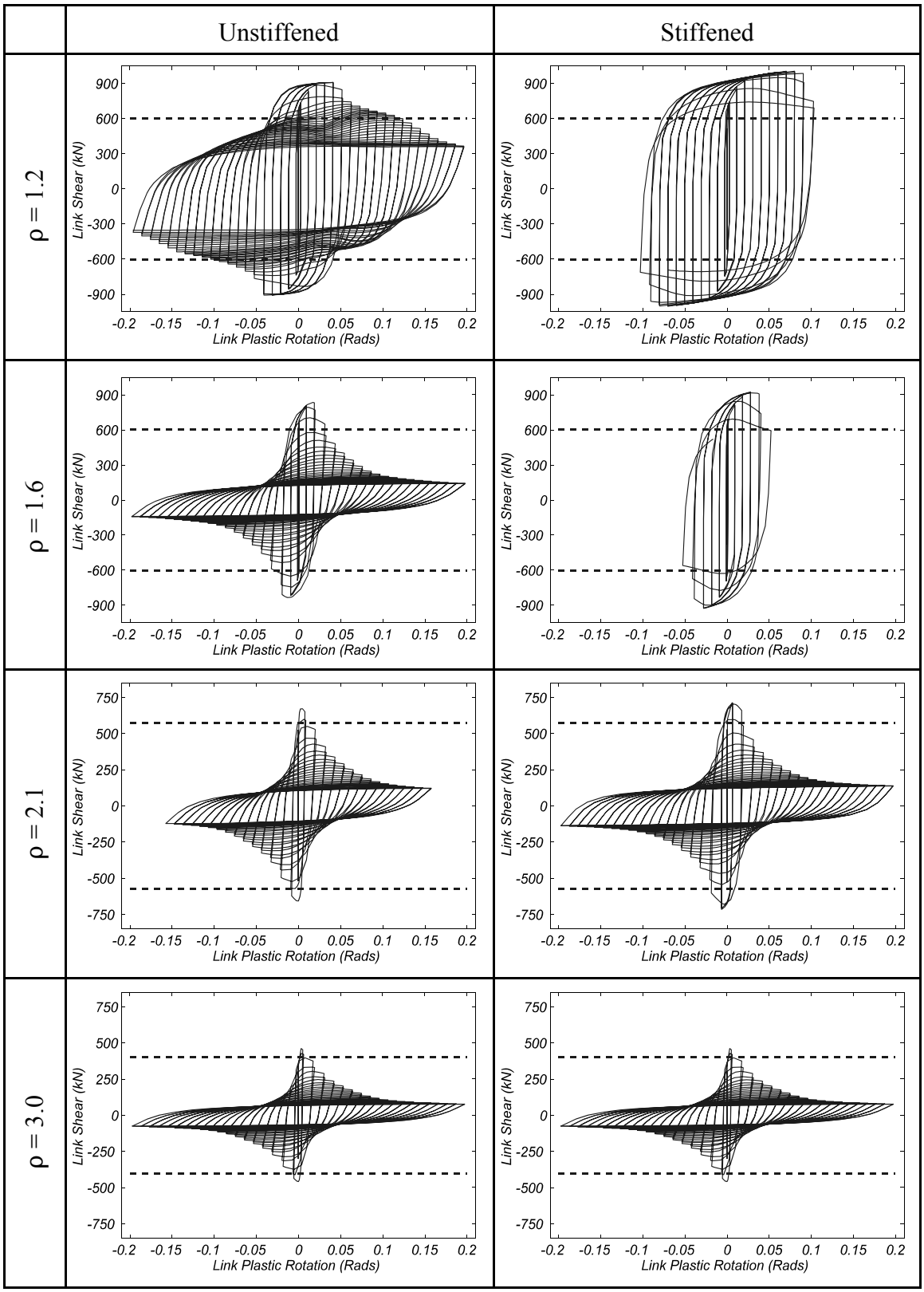

FIGURE A-15 Link Hystereses for Part 1 Links with $b'/t_f = 40.0$ and $d'/t_w = 24.0$

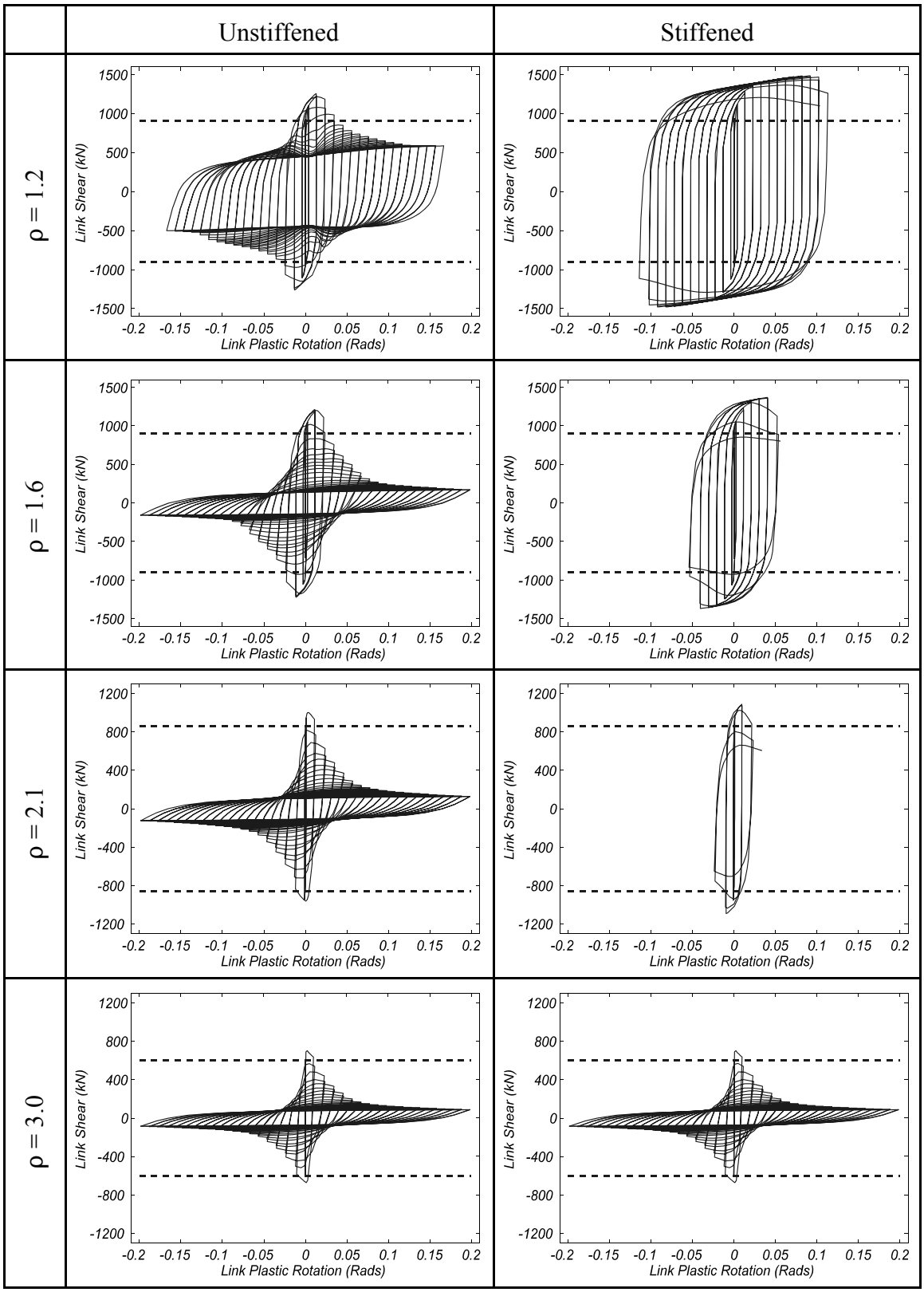

FIGURE A-16 Link Hystereses for Part 1 Links with $b'/t_f = 40.0$ and $d'/t_w = 36.0$

A.3 Part 2 Link Hysteresis Curves

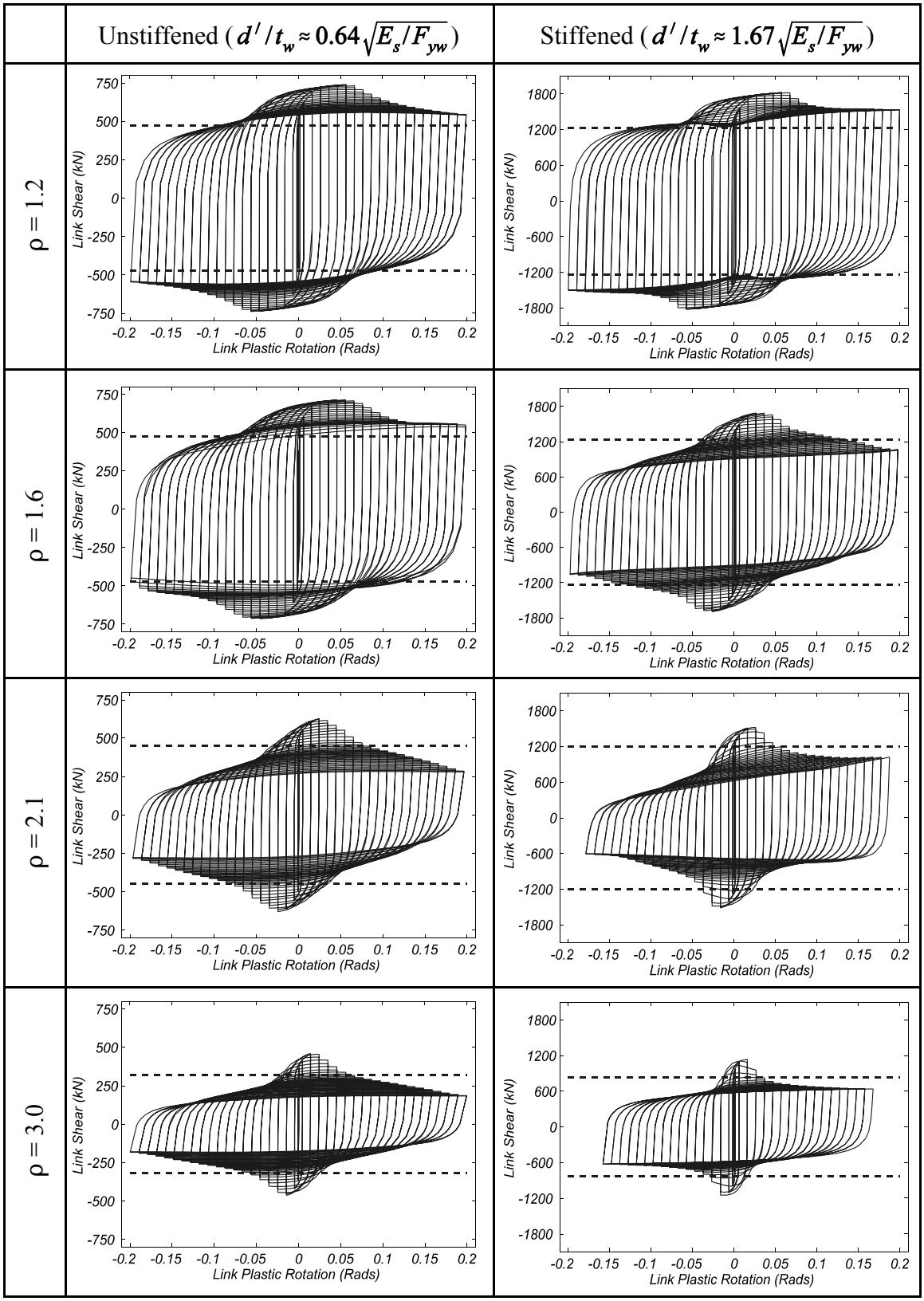

FIGURE A-17 Hystereses for Part 2 Links with F_{yf} = 250 MPa and F_{yw} = 250 MPa

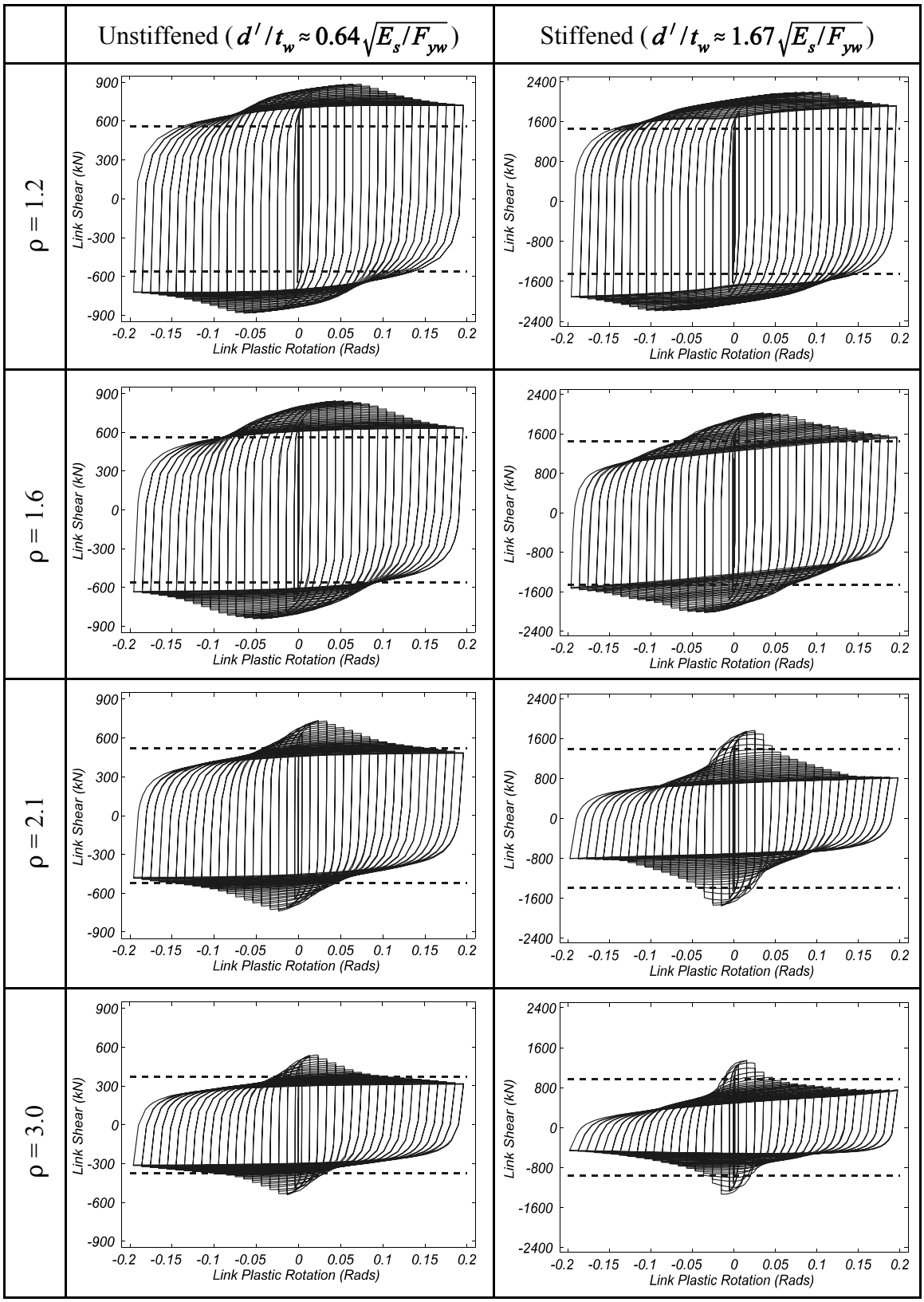

FIGURE A-18 Hystereses for Part 2 Links with F_{yf} = 250 MPa and F_{yw} = 345 MPa

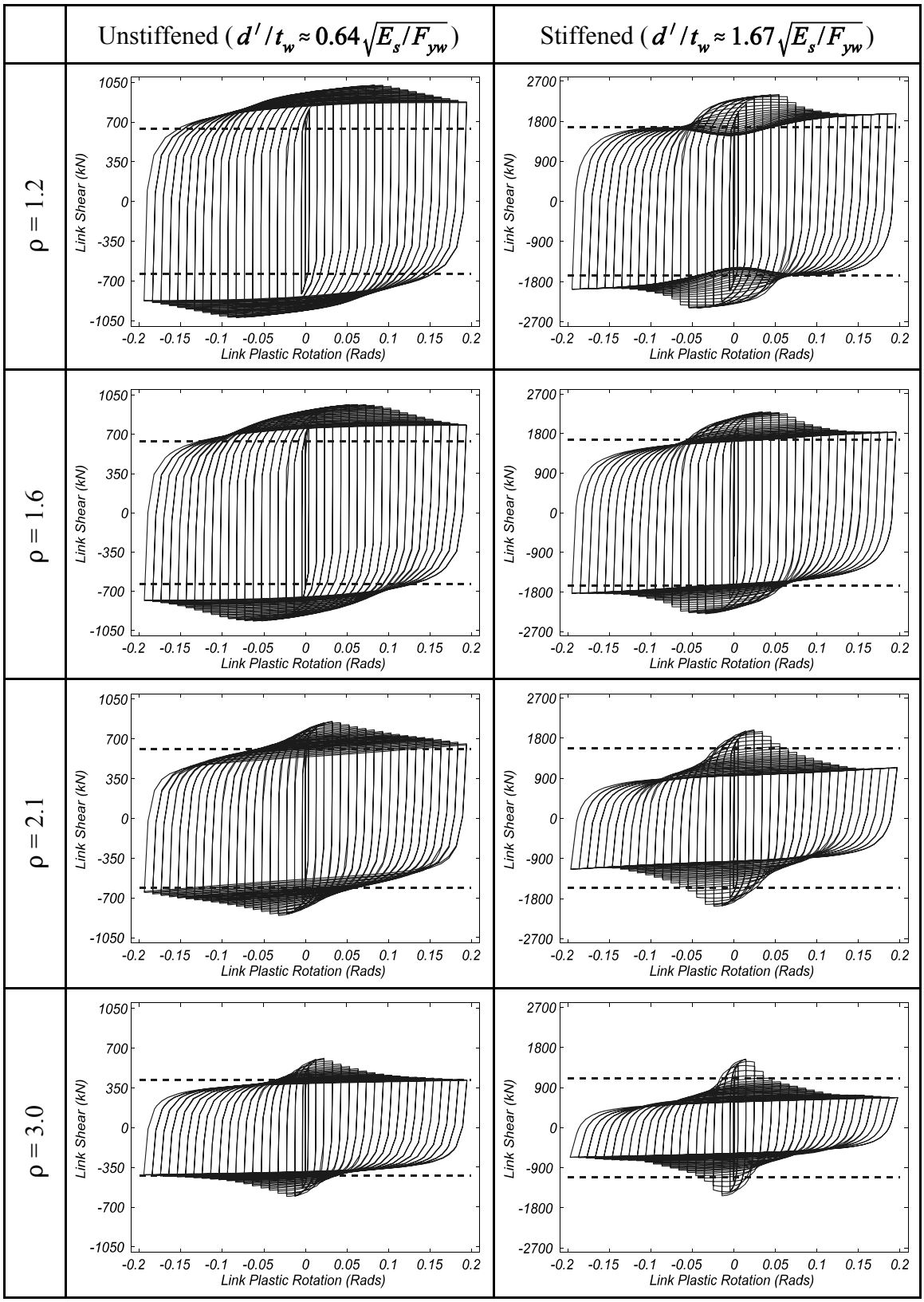

FIGURE A-19 Hystereses for Part 2 Links with F_{yf} = 250 MPa and F_{yw} = 450 MPa

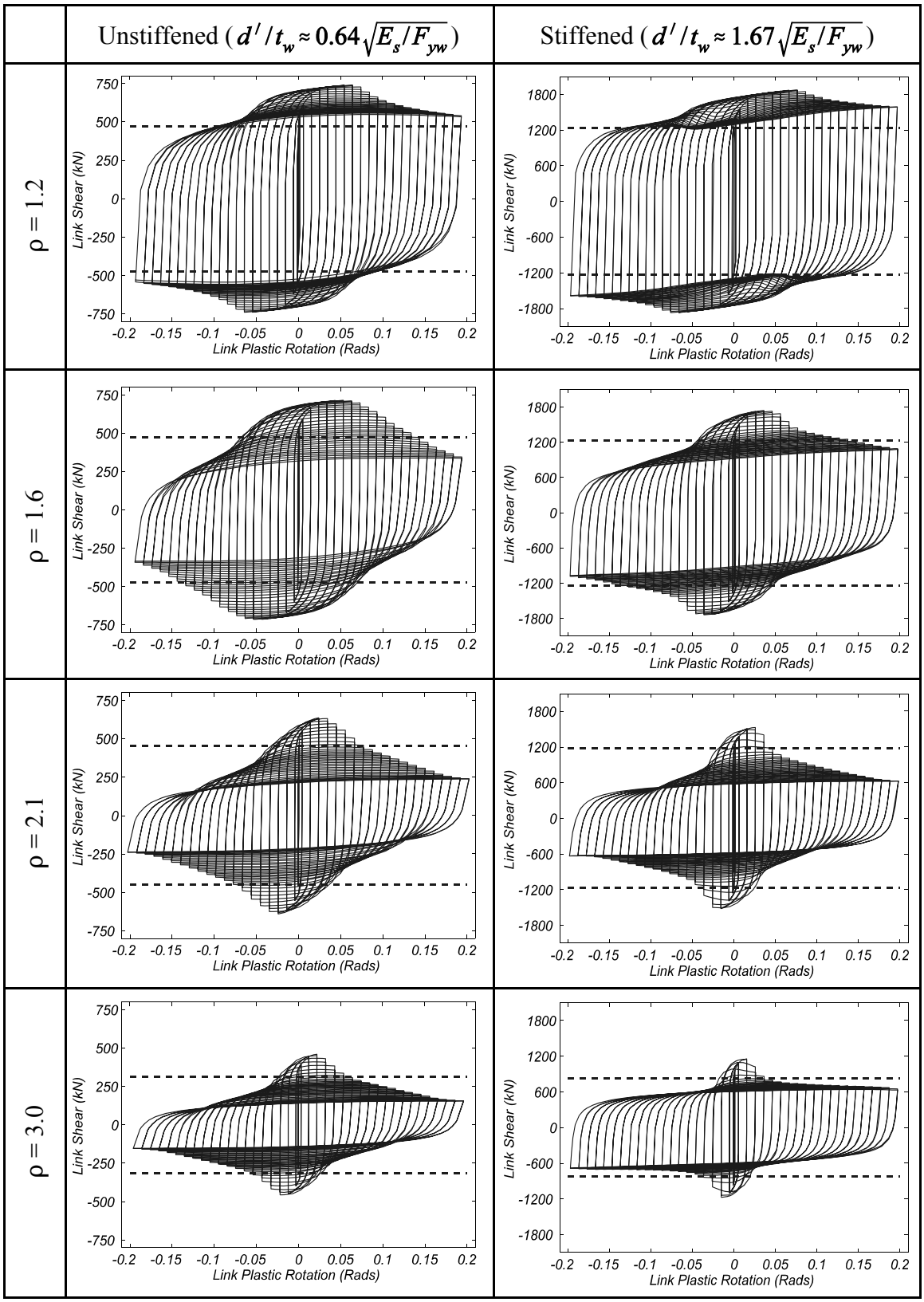

FIGURE A-20 Hystereses for Part 2 Links with F_{yf} = 345 MPa and F_{yw} = 250 MPa

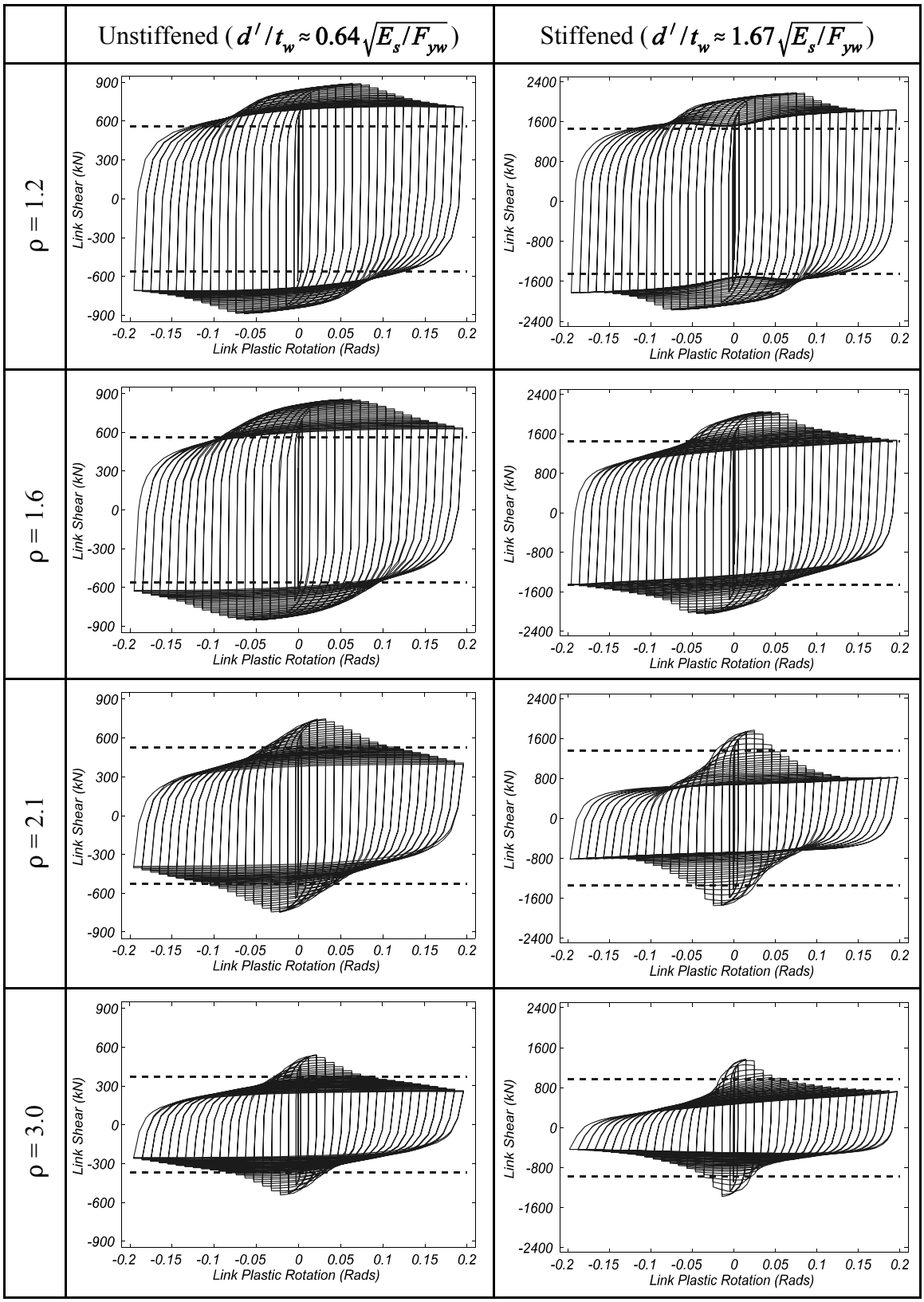

FIGURE A-21 Hystereses for Part 2 Links with F_{yf} = 345 MPa and F_{yw} = 345 MPa

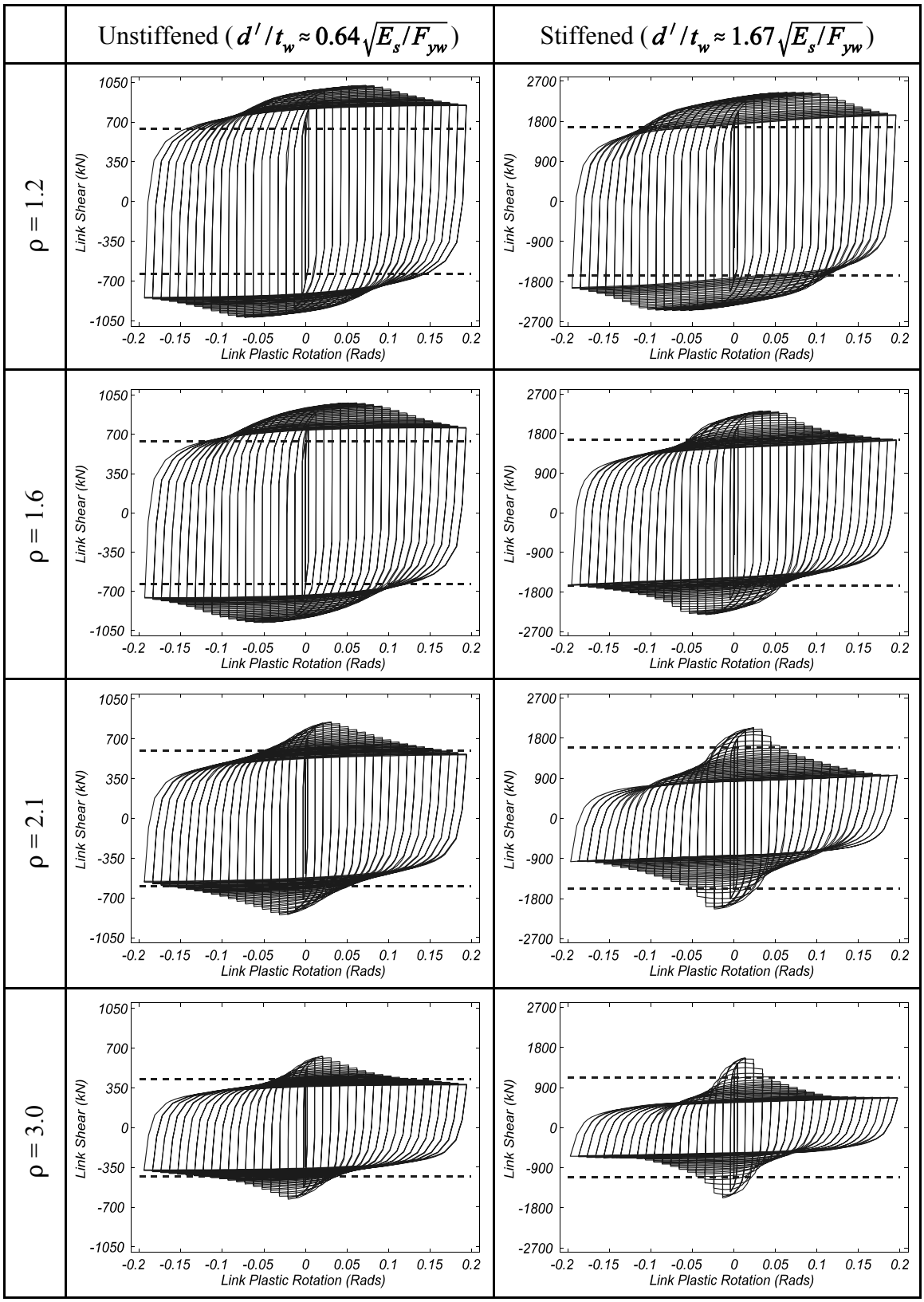

FIGURE A-22 Hystereses for Part 2 Links with F_{yf} = 345 MPa and F_{yw} = 450 MPa

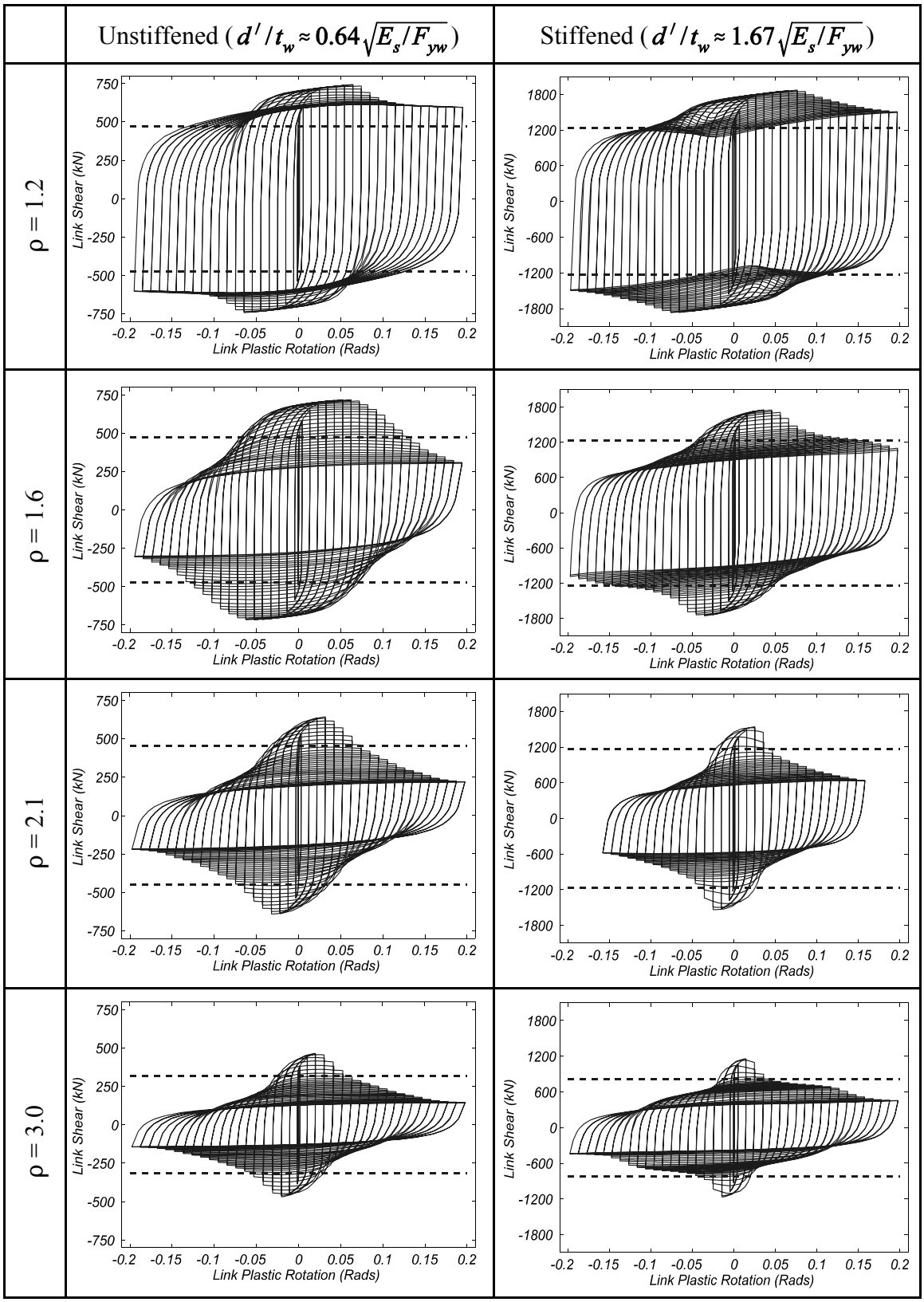

FIGURE A-23 Hystereses for Part 2 Links with F_{yf} = 450 MPa and F_{yw} = 250 MPa

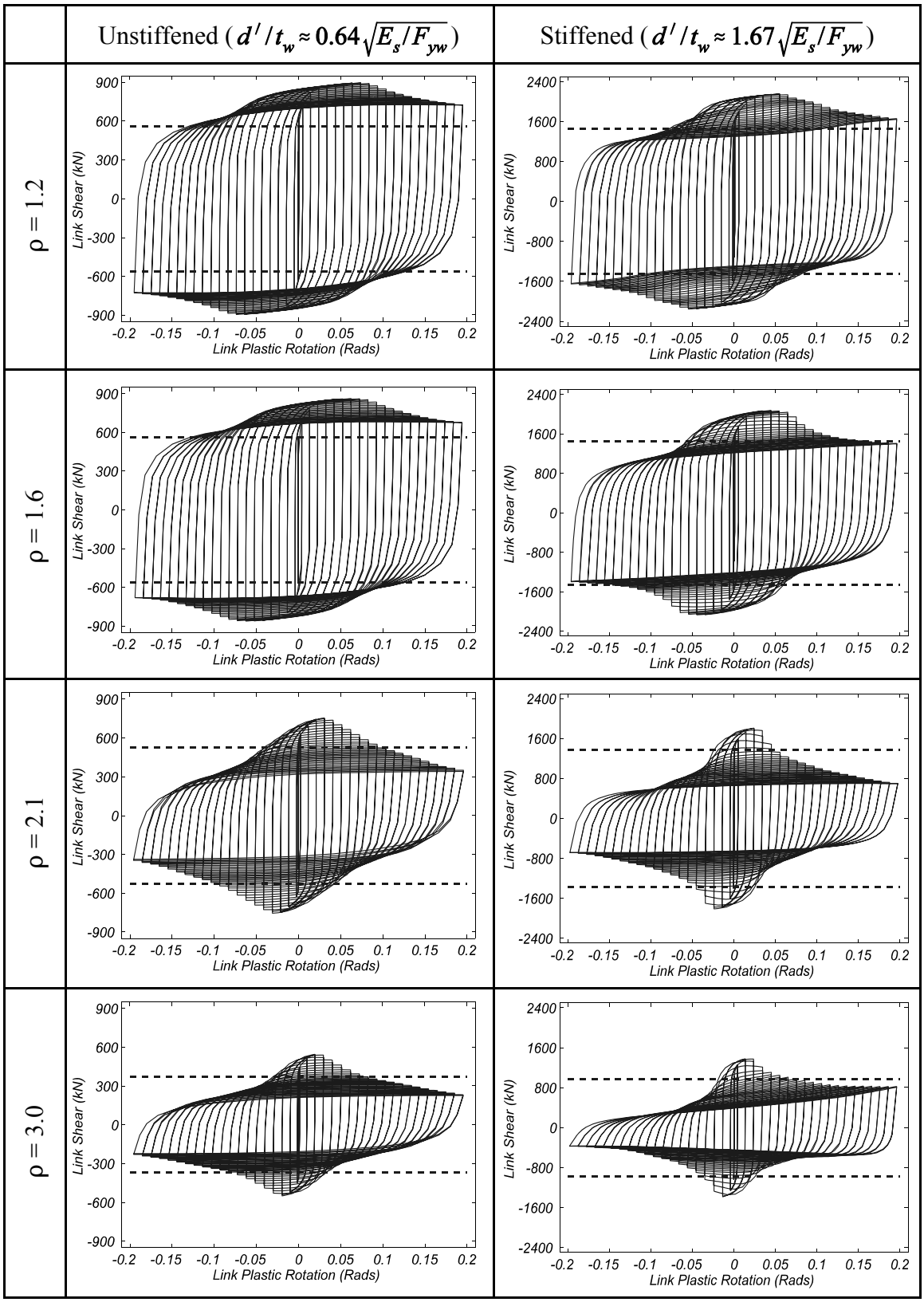

FIGURE A-24 Hystereses for Part 2 Links with F_{yf} = 450 MPa and F_{yw} = 345 MPa

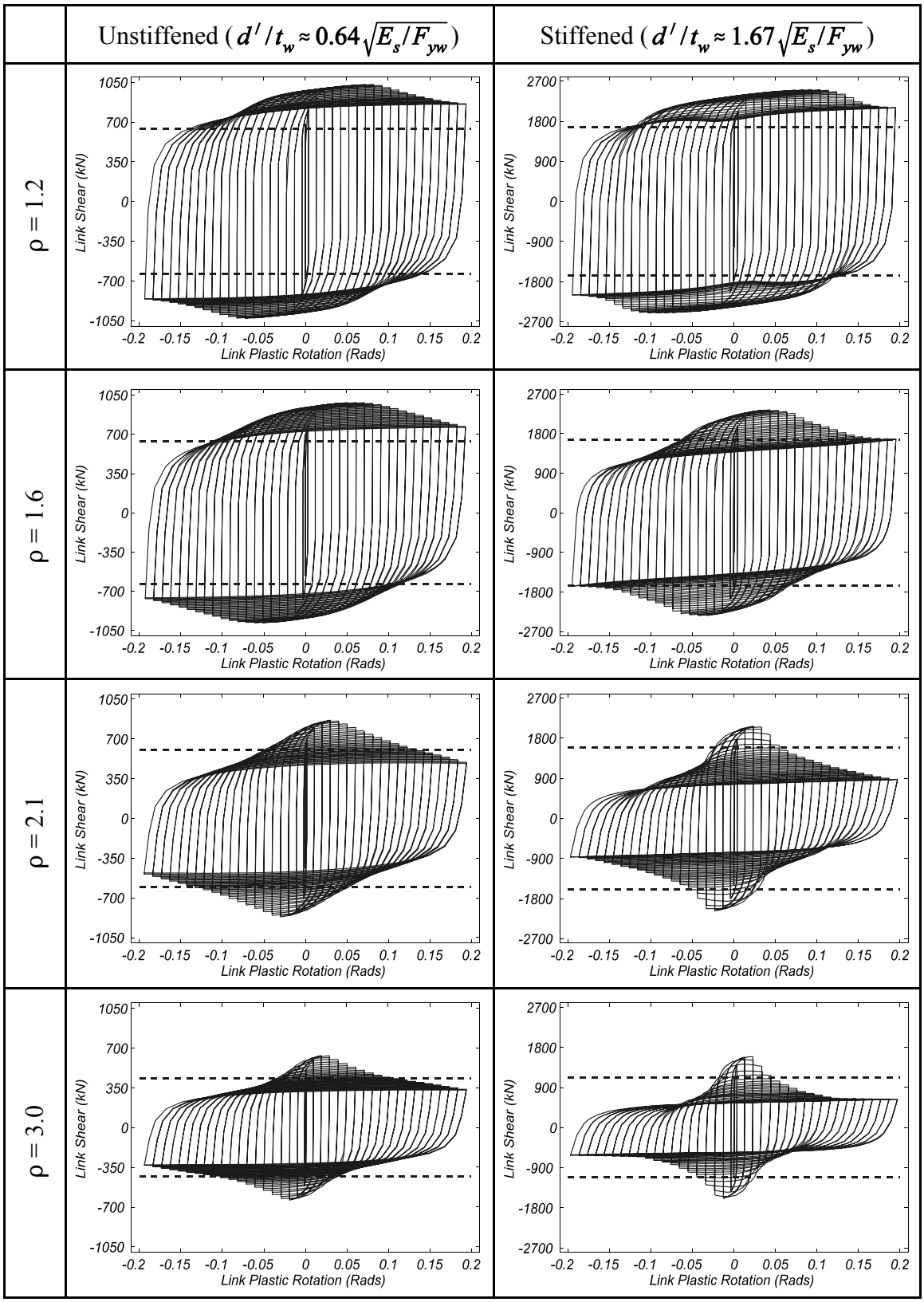

FIGURE A-25 Hystereses for Part 2 Links with F_{yf} = 450 MPa and F_{yw} = 450 MPa

APPENDIX B

ALTERNATIVE RECOMMENDED DESIGN REQUIREMENTS FOR HYBRID RECTANGULAR LINKS

The revised design requirements of Section 3.5.4 limit flange compactness ratios to less than $0.64\sqrt{E_s/F_{yf}}$. This was done for two reasons; for simplicity in that only one compactness criterion is provided for all links regardless of link length, and because all links satisfying both this limit and the web compactness limit met their target rotation. However, there were a number of short shear links (ρ = 1.2) in Part 1 of the parametric study with flange compactnesses of 24 and 40, which correspond to $1.00\sqrt{E_s/F_{yf}}$ and $1.66\sqrt{E_s/F_{yf}}$ respectively, that met their target rotations but would not be allowed under the revised requirements. Additionally, there were stiffened intermediate links with web compactness ratios exceeding $0.64\sqrt{E_s/F_{yw}}$ that almost reached their target rotation but would also not be allowed under the revised requirements. Finally, there were unstiffened flexural links with flange compactness ratios up to $1.00\sqrt{E_s/F_{yf}}$ that achieved their target rotation but likewise would be allowed under the revised requirements. It is therefore possible to give the designer more freedom by allowing the use of cross-section with compactness ratios in the above ranges as long as different target rotations are specified.

Consider figure B-1, which has limit plastic rotation versus normalized link length for selected links from Part 1 of the parametric study. Links shown are those that satisfy the revised design criteria for webs, along with stiffened links of intermediate length with web compactnesses up to $1.67\sqrt{E_s/F_{yw}}$. In other words, the links with $\rho \le 2.6$ included in figure B-1 have webs that are either stiffened if $0.64\sqrt{E_s/F_{yw}} \le d'/t_w \le 1.67\sqrt{E_s/F_{yw}}$ or are

unstiffened if $d'/t_w \le 0.64\sqrt{E_s/F_{yw}}$, and links with ρ > 2.6 shown in the figure have webs that satisfy $d'/t_w \le 0.64\sqrt{E_s/F_{yw}}$. Furthermore, the links in figure B-1 have been grouped according flange compactness.

From this figure, flange compactness appears to have a large effect on the limit plastic rotation of tubular links meeting the web criteria above. For instance, examining the limit plastic rotations shown in figure B-1 at a normalized length of 1.6, it is observed that links with a flange compactness ratio of 8 have significantly higher limit plastic rotations than those with compactness ratios of 17, 24, or 40. Similar observations can be made at lengths of 1.2, 2.1, and 3.0.

Based on these observations it is possible to shift the target rotation line, the solid line in figure B-1, so that larger flange compactness ratios can be used as long as the plastic rotation demand is limited to smaller values. For instance, consider moving the transition link lengths for shear-to-intermediate and intermediate-to-flexural from 1.6 to 1.25 and from 2.6 to 1.75, respectively. By doing so, all links with a flange compactness of 24 from figure B-1 would now meet their target rotation level as shown in figure B-2 including links having ρ = 2.1 with the larger web compactness ratios and stiffeners.

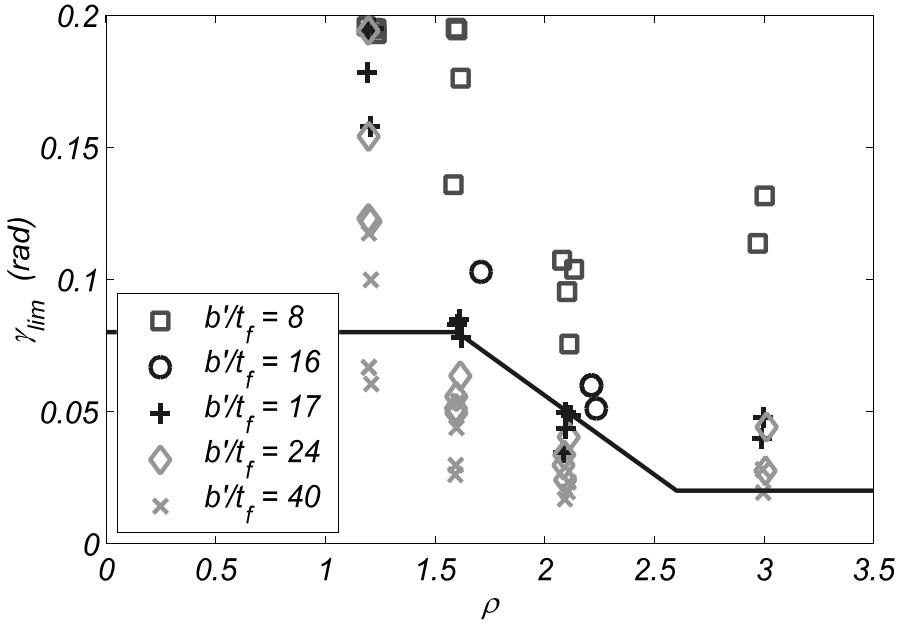

FIGURE B-1 Limit Plastic Rotation vs. Normalized Link Length for Selected Part 1 Links Sorted by Flange Compactness

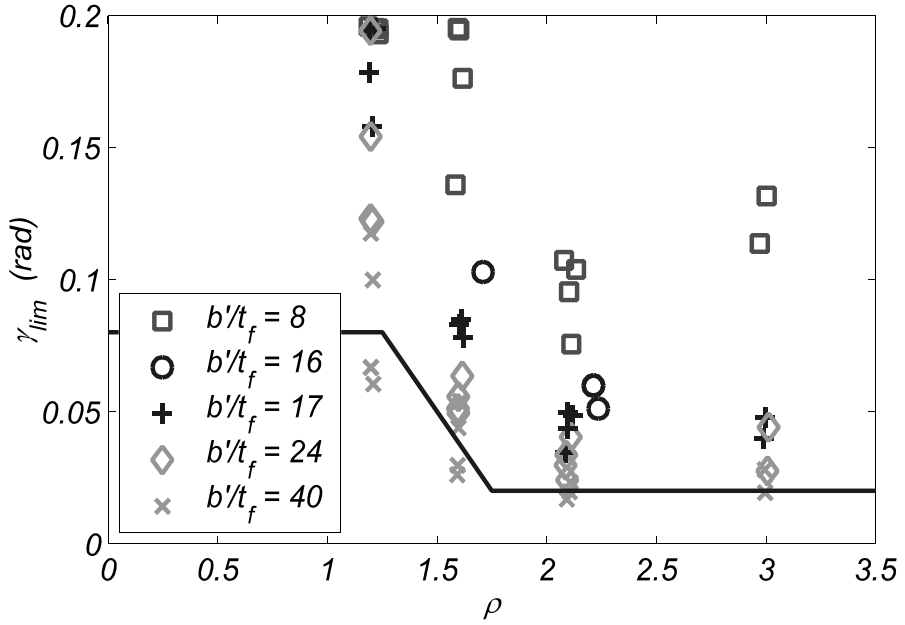

FIGURE B-2 Limit Plastic Rotation vs. Normalized Link Length for Selected Part 1 Links Sorted by Flange Compactness and Showing the Alternate Target Rotation Curve

Considering the above observations, the following alternative design requirements are proposed:

- For links with $b'/t_f \le 0.64\sqrt{E_s/F_{yf}}$ the requirements of Section 3.5.4 may be used, otherwise flanges should satisfy $b'/t_f \le 1.00\sqrt{E_s/F_{yf}}$ and the requirements below should be used.
- For links with ρ ≤ 2.6, no stiffeners are required if $d'/t_w \le 0.64\sqrt{E_s/F_{yw}}$ and if $0.64\sqrt{E_s/F_{yw}} \le d'/t_w \le 1.67\sqrt{E_s/F_{yw}}$ stiffeners shall be provided at a spacing, *a*, satisfying:

$$\frac{a}{t_w} + \frac{1}{8}\frac{d}{t_w} = C_B \qquad (a \le d) \tag{B-1}$$

  where C_B is 20 and 37 for ultimate limit link plastic rotations of 0.08 rads and 0.02 rads respectively.
- For links with ρ > 2.6, no stiffeners are required and webs must satisfy $d'/t_w \le 0.64\sqrt{E_s/F_{yw}}$.

- The plastic rotation demand for links with $\rho \leq 1.25$ should be limited to 0.08 rads, for links with $\rho > 1.75$ the plastic rotation demand should be limited to 0.02 rads, and for links in between, linear interpolation may be used to calculate the limit plastic rotation.

These requirements allow a wider range of link cross-sections but reduce the maximum design plastic rotation for the links. Therefore, it represents a tradeoff with the revised requirements given in Section 3.5.4.

Another option for changing the design requirements could have been to allow the use of larger flange compactness ratios only for the short shear links. Linearly interpolating between the two links having the lowest limit plastic rotation for a flange compactness ratio of 24 at lengths of 1.2 and 1.6 in figure B-1, indicates that if the normalized link length was kept below 1.45, links with flange compactness ratios of up to 24 ($\mathbf{1.00}\sqrt{E_s/F_{yf}}$) could be used along with the web requirements of Section 3.5.4. Modifying the revised design rules in this way would allow a wider range of cross-sections only for shear links with normalized length of less than 1.45, rather than the larger variation in cross-sections for a larger range in link lengths made possible by the reduced limit plastic rotations outlined in the bulleted list above. These examples of possible modifications to the revised design requirements proposed in Section 3.5.4 are for demonstration purposes only. However, for the remainder of this study, the proposed design requirements adopted are those of Section 3.5.4, mostly because they are in a format compatible with those currently used for WF links.

Multidisciplinary Center for Earthquake Engineering Research
List of Technical Reports

The Multidisciplinary Center for Earthquake Engineering Research (MCEER) publishes technical reports on a variety of subjects related to earthquake engineering written by authors funded through MCEER. These reports are available from both MCEER Publications and the National Technical Information Service (NTIS). Requests for reports should be directed to MCEER Publications, Multidisciplinary Center for Earthquake Engineering Research, State University of New York at Buffalo, Red Jacket Quadrangle, Buffalo, New York 14261. Reports can also be requested through NTIS, 5285 Port Royal Road, Springfield, Virginia 22161. NTIS accession numbers are shown in parenthesis, if available.

NCEER-87-0001 "First-Year Program in Research, Education and Technology Transfer," 3/5/87, (PB88-134275, A04, MF-A01).

NCEER-87-0002 "Experimental Evaluation of Instantaneous Optimal Algorithms for Structural Control," by R.C. Lin, T.T. Soong and A.M. Reinhorn, 4/20/87, (PB88-134341, A04, MF-A01).

NCEER-87-0003 "Experimentation Using the Earthquake Simulation Facilities at University at Buffalo," by A.M. Reinhorn and R.L. Ketter, to be published.

NCEER-87-0004 "The System Characteristics and Performance of a Shaking Table," by J.S. Hwang, K.C. Chang and G.C. Lee, 6/1/87, (PB88-134259, A03, MF-A01). This report is available only through NTIS (see address given above).

NCEER-87-0005 "A Finite Element Formulation for Nonlinear Viscoplastic Material Using a Q Model," by O. Gyebi and G. Dasgupta, 11/2/87, (PB88-213764, A08, MF-A01).

NCEER-87-0006 "Symbolic Manipulation Program (SMP) - Algebraic Codes for Two and Three Dimensional Finite Element Formulations," by X. Lee and G. Dasgupta, 11/9/87, (PB88-218522, A05, MF-A01).

NCEER-87-0007 "Instantaneous Optimal Control Laws for Tall Buildings Under Seismic Excitations," by J.N. Yang, A. Akbarpour and P. Ghaemmaghami, 6/10/87, (PB88-134333, A06, MF-A01). This report is only available through NTIS (see address given above).

NCEER-87-0008 "IDARC: Inelastic Damage Analysis of Reinforced Concrete Frame - Shear-Wall Structures," by Y.J. Park, A.M. Reinhorn and S.K. Kunnath, 7/20/87, (PB88-134325, A09, MF-A01). This report is only available through NTIS (see address given above).

NCEER-87-0009 "Liquefaction Potential for New York State: A Preliminary Report on Sites in Manhattan and Buffalo," by M. Budhu, V. Vijayakumar, R.F. Giese and L. Baumgras, 8/31/87, (PB88-163704, A03, MF-A01). This report is available only through NTIS (see address given above).

NCEER-87-0010 "Vertical and Torsional Vibration of Foundations in Inhomogeneous Media," by A.S. Veletsos and K.W. Dotson, 6/1/87, (PB88-134291, A03, MF-A01). This report is only available through NTIS (see address given above).

NCEER-87-0011 "Seismic Probabilistic Risk Assessment and Seismic Margins Studies for Nuclear Power Plants," by Howard H.M. Hwang, 6/15/87, (PB88-134267, A03, MF-A01). This report is only available through NTIS (see address given above).

NCEER-87-0012 "Parametric Studies of Frequency Response of Secondary Systems Under Ground-Acceleration Excitations," by Y. Yong and Y.K. Lin, 6/10/87, (PB88-134309, A03, MF-A01). This report is only available through NTIS (see address given above).

NCEER-87-0013 "Frequency Response of Secondary Systems Under Seismic Excitation," by J.A. HoLung, J. Cai and Y.K. Lin, 7/31/87, (PB88-134317, A05, MF-A01). This report is only available through NTIS (see address given above).

NCEER-87-0014 "Modelling Earthquake Ground Motions in Seismically Active Regions Using Parametric Time Series Methods," by G.W. Ellis and A.S. Cakmak, 8/25/87, (PB88-134283, A08, MF-A01). This report is only available through NTIS (see address given above).

NCEER-87-0015 "Detection and Assessment of Seismic Structural Damage," by E. DiPasquale and A.S. Cakmak, 8/25/87, (PB88-163712, A05, MF-A01). This report is only available through NTIS (see address given above).

NCEER-87-0016 "Pipeline Experiment at Parkfield, California," by J. Isenberg and E. Richardson, 9/15/87, (PB88-163720, A03, MF-A01). This report is available only through NTIS (see address given above).

NCEER-87-0017 "Digital Simulation of Seismic Ground Motion," by M. Shinozuka, G. Deodatis and T. Harada, 8/31/87, (PB88-155197, A04, MF-A01). This report is available only through NTIS (see address given above).

NCEER-87-0018 "Practical Considerations for Structural Control: System Uncertainty, System Time Delay and Truncation of Small Control Forces," J.N. Yang and A. Akbarpour, 8/10/87, (PB88-163738, A08, MF-A01). This report is only available through NTIS (see address given above).

NCEER-87-0019 "Modal Analysis of Nonclassically Damped Structural Systems Using Canonical Transformation," by J.N. Yang, S. Sarkani and F.X. Long, 9/27/87, (PB88-187851, A04, MF-A01).

NCEER-87-0020 "A Nonstationary Solution in Random Vibration Theory," by J.R. Red-Horse and P.D. Spanos, 11/3/87, (PB88-163746, A03, MF-A01).

NCEER-87-0021 "Horizontal Impedances for Radially Inhomogeneous Viscoelastic Soil Layers," by A.S. Veletsos and K.W. Dotson, 10/15/87, (PB88-150859, A04, MF-A01).

NCEER-87-0022 "Seismic Damage Assessment of Reinforced Concrete Members," by Y.S. Chung, C. Meyer and M. Shinozuka, 10/9/87, (PB88-150867, A05, MF-A01). This report is available only through NTIS (see address given above).

NCEER-87-0023 "Active Structural Control in Civil Engineering," by T.T. Soong, 11/11/87, (PB88-187778, A03, MF-A01).

NCEER-87-0024 "Vertical and Torsional Impedances for Radially Inhomogeneous Viscoelastic Soil Layers," by K.W. Dotson and A.S. Veletsos, 12/87, (PB88-187786, A03, MF-A01).

NCEER-87-0025 "Proceedings from the Symposium on Seismic Hazards, Ground Motions, Soil-Liquefaction and Engineering Practice in Eastern North America," October 20-22, 1987, edited by K.H. Jacob, 12/87, (PB88-188115, A23, MF-A01). This report is available only through NTIS (see address given above).

NCEER-87-0026 "Report on the Whittier-Narrows, California, Earthquake of October 1, 1987," by J. Pantelic and A. Reinhorn, 11/87, (PB88-187752, A03, MF-A01). This report is available only through NTIS (see address given above).

NCEER-87-0027 "Design of a Modular Program for Transient Nonlinear Analysis of Large 3-D Building Structures," by S. Srivastav and J.F. Abel, 12/30/87, (PB88-187950, A05, MF-A01). This report is only available through NTIS (see address given above).

NCEER-87-0028 "Second-Year Program in Research, Education and Technology Transfer," 3/8/88, (PB88-219480, A04, MF-A01).

NCEER-88-0001 "Workshop on Seismic Computer Analysis and Design of Buildings With Interactive Graphics," by W. McGuire, J.F. Abel and C.H. Conley, 1/18/88, (PB88-187760, A03, MF-A01). This report is only available through NTIS (see address given above).

NCEER-88-0002 "Optimal Control of Nonlinear Flexible Structures," by J.N. Yang, F.X. Long and D. Wong, 1/22/88, (PB88-213772, A06, MF-A01).

NCEER-88-0003 "Substructuring Techniques in the Time Domain for Primary-Secondary Structural Systems," by G.D. Manolis and G. Juhn, 2/10/88, (PB88-213780, A04, MF-A01).

NCEER-88-0004 "Iterative Seismic Analysis of Primary-Secondary Systems," by A. Singhal, L.D. Lutes and P.D. Spanos, 2/23/88, (PB88-213798, A04, MF-A01).

NCEER-88-0005 "Stochastic Finite Element Expansion for Random Media," by P.D. Spanos and R. Ghanem, 3/14/88, (PB88-213806, A03, MF-A01).

NCEER-88-0006 "Combining Structural Optimization and Structural Control," by F.Y. Cheng and C.P. Pantelides, 1/10/88, (PB88-213814, A05, MF-A01).

NCEER-88-0007 "Seismic Performance Assessment of Code-Designed Structures," by H.H-M. Hwang, J-W. Jaw and H-J. Shau, 3/20/88, (PB88-219423, A04, MF-A01). This report is only available through NTIS (see address given above).

NCEER-88-0008 "Reliability Analysis of Code-Designed Structures Under Natural Hazards," by H.H-M. Hwang, H. Ushiba and M. Shinozuka, 2/29/88, (PB88-229471, A07, MF-A01). This report is only available through NTIS (see address given above).

NCEER-88-0009 "Seismic Fragility Analysis of Shear Wall Structures," by J-W Jaw and H.H-M. Hwang, 4/30/88, (PB89-102867, A04, MF-A01).

NCEER-88-0010 "Base Isolation of a Multi-Story Building Under a Harmonic Ground Motion - A Comparison of Performances of Various Systems," by F-G Fan, G. Ahmadi and I.G. Tadjbakhsh, 5/18/88, (PB89-122238, A06, MF-A01). This report is only available through NTIS (see address given above).

NCEER-88-0011 "Seismic Floor Response Spectra for a Combined System by Green's Functions," by F.M. Lavelle, L.A. Bergman and P.D. Spanos, 5/1/88, (PB89-102875, A03, MF-A01).

NCEER-88-0012 "A New Solution Technique for Randomly Excited Hysteretic Structures," by G.Q. Cai and Y.K. Lin, 5/16/88, (PB89-102883, A03, MF-A01).

NCEER-88-0013 "A Study of Radiation Damping and Soil-Structure Interaction Effects in the Centrifuge," by K. Weissman, supervised by J.H. Prevost, 5/24/88, (PB89-144703, A06, MF-A01).

NCEER-88-0014 "Parameter Identification and Implementation of a Kinematic Plasticity Model for Frictional Soils," by J.H. Prevost and D.V. Griffiths, to be published.

NCEER-88-0015 "Two- and Three- Dimensional Dynamic Finite Element Analyses of the Long Valley Dam," by D.V. Griffiths and J.H. Prevost, 6/17/88, (PB89-144711, A04, MF-A01).

NCEER-88-0016 "Damage Assessment of Reinforced Concrete Structures in Eastern United States," by A.M. Reinhorn, M.J. Seidel, S.K. Kunnath and Y.J. Park, 6/15/88, (PB89-122220, A04, MF-A01). This report is only available through NTIS (see address given above).

NCEER-88-0017 "Dynamic Compliance of Vertically Loaded Strip Foundations in Multilayered Viscoelastic Soils," by S. Ahmad and A.S.M. Israil, 6/17/88, (PB89-102891, A04, MF-A01).

NCEER-88-0018 "An Experimental Study of Seismic Structural Response With Added Viscoelastic Dampers," by R.C. Lin, Z. Liang, T.T. Soong and R.H. Zhang, 6/30/88, (PB89-122212, A05, MF-A01). This report is available only through NTIS (see address given above).

NCEER-88-0019 "Experimental Investigation of Primary - Secondary System Interaction," by G.D. Manolis, G. Juhn and A.M. Reinhorn, 5/27/88, (PB89-122204, A04, MF-A01).

NCEER-88-0020 "A Response Spectrum Approach For Analysis of Nonclassically Damped Structures," by J.N. Yang, S. Sarkani and F.X. Long, 4/22/88, (PB89-102909, A04, MF-A01).

NCEER-88-0021 "Seismic Interaction of Structures and Soils: Stochastic Approach," by A.S. Veletsos and A.M. Prasad, 7/21/88, (PB89-122196, A04, MF-A01). This report is only available through NTIS (see address given above).

NCEER-88-0022 "Identification of the Serviceability Limit State and Detection of Seismic Structural Damage," by E. DiPasquale and A.S. Cakmak, 6/15/88, (PB89-122188, A05, MF-A01). This report is available only through NTIS (see address given above).

NCEER-88-0023 "Multi-Hazard Risk Analysis: Case of a Simple Offshore Structure," by B.K. Bhartia and E.H. Vanmarcke, 7/21/88, (PB89-145213, A05, MF-A01).

NCEER-88-0024 "Automated Seismic Design of Reinforced Concrete Buildings," by Y.S. Chung, C. Meyer and M. Shinozuka, 7/5/88, (PB89-122170, A06, MF-A01). This report is available only through NTIS (see address given above).

NCEER-88-0025 "Experimental Study of Active Control of MDOF Structures Under Seismic Excitations," by L.L. Chung, R.C. Lin, T.T. Soong and A.M. Reinhorn, 7/10/88, (PB89-122600, A04, MF-A01).

NCEER-88-0026 "Earthquake Simulation Tests of a Low-Rise Metal Structure," by J.S. Hwang, K.C. Chang, G.C. Lee and R.L. Ketter, 8/1/88, (PB89-102917, A04, MF-A01).

NCEER-88-0027 "Systems Study of Urban Response and Reconstruction Due to Catastrophic Earthquakes," by F. Kozin and H.K. Zhou, 9/22/88, (PB90-162348, A04, MF-A01).

NCEER-88-0028 "Seismic Fragility Analysis of Plane Frame Structures," by H.H-M. Hwang and Y.K. Low, 7/31/88, (PB89-131445, A06, MF-A01).

NCEER-88-0029 "Response Analysis of Stochastic Structures," by A. Kardara, C. Bucher and M. Shinozuka, 9/22/88, (PB89-174429, A04, MF-A01).

NCEER-88-0030 "Nonnormal Accelerations Due to Yielding in a Primary Structure," by D.C.K. Chen and L.D. Lutes, 9/19/88, (PB89-131437, A04, MF-A01).

NCEER-88-0031 "Design Approaches for Soil-Structure Interaction," by A.S. Veletsos, A.M. Prasad and Y. Tang, 12/30/88, (PB89-174437, A03, MF-A01). This report is available only through NTIS (see address given above).

NCEER-88-0032 "A Re-evaluation of Design Spectra for Seismic Damage Control," by C.J. Turkstra and A.G. Tallin, 11/7/88, (PB89-145221, A05, MF-A01).

NCEER-88-0033 "The Behavior and Design of Noncontact Lap Splices Subjected to Repeated Inelastic Tensile Loading," by V.E. Sagan, P. Gergely and R.N. White, 12/8/88, (PB89-163737, A08, MF-A01).

NCEER-88-0034 "Seismic Response of Pile Foundations," by S.M. Mamoon, P.K. Banerjee and S. Ahmad, 11/1/88, (PB89-145239, A04, MF-A01).

NCEER-88-0035 "Modeling of R/C Building Structures With Flexible Floor Diaphragms (IDARC2)," by A.M. Reinhorn, S.K. Kunnath and N. Panahshahi, 9/7/88, (PB89-207153, A07, MF-A01).

NCEER-88-0036 "Solution of the Dam-Reservoir Interaction Problem Using a Combination of FEM, BEM with Particular Integrals, Modal Analysis, and Substructuring," by C-S. Tsai, G.C. Lee and R.L. Ketter, 12/31/88, (PB89-207146, A04, MF-A01).

NCEER-88-0037 "Optimal Placement of Actuators for Structural Control," by F.Y. Cheng and C.P. Pantelides, 8/15/88, (PB89-162846, A05, MF-A01).

NCEER-88-0038 "Teflon Bearings in Aseismic Base Isolation: Experimental Studies and Mathematical Modeling," by A. Mokha, M.C. Constantinou and A.M. Reinhorn, 12/5/88, (PB89-218457, A10, MF-A01). This report is available only through NTIS (see address given above).

NCEER-88-0039 "Seismic Behavior of Flat Slab High-Rise Buildings in the New York City Area," by P. Weidlinger and M. Ettouney, 10/15/88, (PB90-145681, A04, MF-A01).

NCEER-88-0040 "Evaluation of the Earthquake Resistance of Existing Buildings in New York City," by P. Weidlinger and M. Ettouney, 10/15/88, to be published.

NCEER-88-0041 "Small-Scale Modeling Techniques for Reinforced Concrete Structures Subjected to Seismic Loads," by W. Kim, A. El-Attar and R.N. White, 11/22/88, (PB89-189625, A05, MF-A01).

NCEER-88-0042 "Modeling Strong Ground Motion from Multiple Event Earthquakes," by G.W. Ellis and A.S. Cakmak, 10/15/88, (PB89-174445, A03, MF-A01).

NCEER-88-0043 "Nonstationary Models of Seismic Ground Acceleration," by M. Grigoriu, S.E. Ruiz and E. Rosenblueth, 7/15/88, (PB89-189617, A04, MF-A01).

NCEER-88-0044 "SARCF User's Guide: Seismic Analysis of Reinforced Concrete Frames," by Y.S. Chung, C. Meyer and M. Shinozuka, 11/9/88, (PB89-174452, A08, MF-A01).

NCEER-88-0045 "First Expert Panel Meeting on Disaster Research and Planning," edited by J. Pantelic and J. Stoyle, 9/15/88, (PB89-174460, A05, MF-A01).

NCEER-88-0046 "Preliminary Studies of the Effect of Degrading Infill Walls on the Nonlinear Seismic Response of Steel Frames," by C.Z. Chrysostomou, P. Gergely and J.F. Abel, 12/19/88, (PB89-208383, A05, MF-A01).

NCEER-88-0047 "Reinforced Concrete Frame Component Testing Facility - Design, Construction, Instrumentation and Operation," by S.P. Pessiki, C. Conley, T. Bond, P. Gergely and R.N. White, 12/16/88, (PB89-174478, A04, MF-A01).

NCEER-89-0001 "Effects of Protective Cushion and Soil Compliancy on the Response of Equipment Within a Seismically Excited Building," by J.A. HoLung, 2/16/89, (PB89-207179, A04, MF-A01).

NCEER-89-0002 "Statistical Evaluation of Response Modification Factors for Reinforced Concrete Structures," by H.H-M. Hwang and J-W. Jaw, 2/17/89, (PB89-207187, A05, MF-A01).

NCEER-89-0003 "Hysteretic Columns Under Random Excitation," by G-Q. Cai and Y.K. Lin, 1/9/89, (PB89-196513, A03, MF-A01).

NCEER-89-0004 "Experimental Study of `Elephant Foot Bulge' Instability of Thin-Walled Metal Tanks," by Z-H. Jia and R.L. Ketter, 2/22/89, (PB89-207195, A03, MF-A01).

NCEER-89-0005 "Experiment on Performance of Buried Pipelines Across San Andreas Fault," by J. Isenberg, E. Richardson and T.D. O'Rourke, 3/10/89, (PB89-218440, A04, MF-A01). This report is available only through NTIS (see address given above).

NCEER-89-0006 "A Knowledge-Based Approach to Structural Design of Earthquake-Resistant Buildings," by M. Subramani, P. Gergely, C.H. Conley, J.F. Abel and A.H. Zaghw, 1/15/89, (PB89-218465, A06, MF-A01).

NCEER-89-0007 "Liquefaction Hazards and Their Effects on Buried Pipelines," by T.D. O'Rourke and P.A. Lane, 2/1/89, (PB89-218481, A09, MF-A01).

NCEER-89-0008 "Fundamentals of System Identification in Structural Dynamics," by H. Imai, C-B. Yun, O. Maruyama and M. Shinozuka, 1/26/89, (PB89-207211, A04, MF-A01).

NCEER-89-0009 "Effects of the 1985 Michoacan Earthquake on Water Systems and Other Buried Lifelines in Mexico," by A.G. Ayala and M.J. O'Rourke, 3/8/89, (PB89-207229, A06, MF-A01).

NCEER-89-R010 "NCEER Bibliography of Earthquake Education Materials," by K.E.K. Ross, Second Revision, 9/1/89, (PB90-125352, A05, MF-A01). This report is replaced by NCEER-92-0018.

NCEER-89-0011 "Inelastic Three-Dimensional Response Analysis of Reinforced Concrete Building Structures (IDARC-3D), Part I - Modeling," by S.K. Kunnath and A.M. Reinhorn, 4/17/89, (PB90-114612, A07, MF-A01). This report is available only through NTIS (see address given above).

NCEER-89-0012 "Recommended Modifications to ATC-14," by C.D. Poland and J.O. Malley, 4/12/89, (PB90-108648, A15, MF-A01).

NCEER-89-0013 "Repair and Strengthening of Beam-to-Column Connections Subjected to Earthquake Loading," by M. Corazao and A.J. Durrani, 2/28/89, (PB90-109885, A06, MF-A01).

NCEER-89-0014 "Program EXKAL2 for Identification of Structural Dynamic Systems," by O. Maruyama, C-B. Yun, M. Hoshiya and M. Shinozuka, 5/19/89, (PB90-109877, A09, MF-A01).

NCEER-89-0015 "Response of Frames With Bolted Semi-Rigid Connections, Part I - Experimental Study and Analytical Predictions," by P.J. DiCorso, A.M. Reinhorn, J.R. Dickerson, J.B. Radziminski and W.L. Harper, 6/1/89, to be published.

NCEER-89-0016 "ARMA Monte Carlo Simulation in Probabilistic Structural Analysis," by P.D. Spanos and M.P. Mignolet, 7/10/89, (PB90-109893, A03, MF-A01).

NCEER-89-P017 "Preliminary Proceedings from the Conference on Disaster Preparedness - The Place of Earthquake Education in Our Schools," Edited by K.E.K. Ross, 6/23/89, (PB90-108606, A03, MF-A01).

NCEER-89-0017 "Proceedings from the Conference on Disaster Preparedness - The Place of Earthquake Education in Our Schools," Edited by K.E.K. Ross, 12/31/89, (PB90-207895, A012, MF-A02). This report is available only through NTIS (see address given above).

NCEER-89-0018 "Multidimensional Models of Hysteretic Material Behavior for Vibration Analysis of Shape Memory Energy Absorbing Devices, by E.J. Graesser and F.A. Cozzarelli, 6/7/89, (PB90-164146, A04, MF-A01).

NCEER-89-0019 "Nonlinear Dynamic Analysis of Three-Dimensional Base Isolated Structures (3D-BASIS)," by S. Nagarajaiah, A.M. Reinhorn and M.C. Constantinou, 8/3/89, (PB90-161936, A06, MF-A01). This report has been replaced by NCEER-93-0011.

NCEER-89-0020 "Structural Control Considering Time-Rate of Control Forces and Control Rate Constraints," by F.Y. Cheng and C.P. Pantelides, 8/3/89, (PB90-120445, A04, MF-A01).

NCEER-89-0021 "Subsurface Conditions of Memphis and Shelby County," by K.W. Ng, T-S. Chang and H-H.M. Hwang, 7/26/89, (PB90-120437, A03, MF-A01).

NCEER-89-0022 "Seismic Wave Propagation Effects on Straight Jointed Buried Pipelines," by K. Elhmadi and M.J. O'Rourke, 8/24/89, (PB90-162322, A10, MF-A02).

NCEER-89-0023 "Workshop on Serviceability Analysis of Water Delivery Systems," edited by M. Grigoriu, 3/6/89, (PB90-127424, A03, MF-A01).

NCEER-89-0024 "Shaking Table Study of a 1/5 Scale Steel Frame Composed of Tapered Members," by K.C. Chang, J.S. Hwang and G.C. Lee, 9/18/89, (PB90-160169, A04, MF-A01).

NCEER-89-0025 "DYNA1D: A Computer Program for Nonlinear Seismic Site Response Analysis - Technical Documentation," by Jean H. Prevost, 9/14/89, (PB90-161944, A07, MF-A01). This report is available only through NTIS (see address given above).

NCEER-89-0026 "1:4 Scale Model Studies of Active Tendon Systems and Active Mass Dampers for Aseismic Protection," by A.M. Reinhorn, T.T. Soong, R.C. Lin, Y.P. Yang, Y. Fukao, H. Abe and M. Nakai, 9/15/89, (PB90-173246, A10, MF-A02). This report is available only through NTIS (see address given above).

NCEER-89-0027 "Scattering of Waves by Inclusions in a Nonhomogeneous Elastic Half Space Solved by Boundary Element Methods," by P.K. Hadley, A. Askar and A.S. Cakmak, 6/15/89, (PB90-145699, A07, MF-A01).

NCEER-89-0028 "Statistical Evaluation of Deflection Amplification Factors for Reinforced Concrete Structures," by H.H.M. Hwang, J-W. Jaw and A.L. Ch'ng, 8/31/89, (PB90-164633, A05, MF-A01).

NCEER-89-0029 "Bedrock Accelerations in Memphis Area Due to Large New Madrid Earthquakes," by H.H.M. Hwang, C.H.S. Chen and G. Yu, 11/7/89, (PB90-162330, A04, MF-A01).

NCEER-89-0030 "Seismic Behavior and Response Sensitivity of Secondary Structural Systems," by Y.Q. Chen and T.T. Soong, 10/23/89, (PB90-164658, A08, MF-A01).

NCEER-89-0031 "Random Vibration and Reliability Analysis of Primary-Secondary Structural Systems," by Y. Ibrahim, M. Grigoriu and T.T. Soong, 11/10/89, (PB90-161951, A04, MF-A01).

NCEER-89-0032 "Proceedings from the Second U.S. - Japan Workshop on Liquefaction, Large Ground Deformation and Their Effects on Lifelines, September 26-29, 1989," Edited by T.D. O'Rourke and M. Hamada, 12/1/89, (PB90-209388, A22, MF-A03).

NCEER-89-0033 "Deterministic Model for Seismic Damage Evaluation of Reinforced Concrete Structures," by J.M. Bracci, A.M. Reinhorn, J.B. Mander and S.K. Kunnath, 9/27/89, (PB91-108803, A06, MF-A01).

NCEER-89-0034 "On the Relation Between Local and Global Damage Indices," by E. DiPasquale and A.S. Cakmak, 8/15/89, (PB90-173865, A05, MF-A01).

NCEER-89-0035 "Cyclic Undrained Behavior of Nonplastic and Low Plasticity Silts," by A.J. Walker and H.E. Stewart, 7/26/89, (PB90-183518, A10, MF-A01).

NCEER-89-0036 "Liquefaction Potential of Surficial Deposits in the City of Buffalo, New York," by M. Budhu, R. Giese and L. Baumgrass, 1/17/89, (PB90-208455, A04, MF-A01).

NCEER-89-0037 "A Deterministic Assessment of Effects of Ground Motion Incoherence," by A.S. Veletsos and Y. Tang, 7/15/89, (PB90-164294, A03, MF-A01).

NCEER-89-0038 "Workshop on Ground Motion Parameters for Seismic Hazard Mapping," July 17-18, 1989, edited by R.V. Whitman, 12/1/89, (PB90-173923, A04, MF-A01).

NCEER-89-0039 "Seismic Effects on Elevated Transit Lines of the New York City Transit Authority," by C.J. Costantino, C.A. Miller and E. Heymsfield, 12/26/89, (PB90-207887, A06, MF-A01).

NCEER-89-0040 "Centrifugal Modeling of Dynamic Soil-Structure Interaction," by K. Weissman, Supervised by J.H. Prevost, 5/10/89, (PB90-207879, A07, MF-A01).

NCEER-89-0041 "Linearized Identification of Buildings With Cores for Seismic Vulnerability Assessment," by I-K. Ho and A.E. Aktan, 11/1/89, (PB90-251943, A07, MF-A01).

NCEER-90-0001 "Geotechnical and Lifeline Aspects of the October 17, 1989 Loma Prieta Earthquake in San Francisco," by T.D. O'Rourke, H.E. Stewart, F.T. Blackburn and T.S. Dickerman, 1/90, (PB90-208596, A05, MF-A01).

NCEER-90-0002 "Nonnormal Secondary Response Due to Yielding in a Primary Structure," by D.C.K. Chen and L.D. Lutes, 2/28/90, (PB90-251976, A07, MF-A01).

NCEER-90-0003 "Earthquake Education Materials for Grades K-12," by K.E.K. Ross, 4/16/90, (PB91-251984, A05, MF-A05). This report has been replaced by NCEER-92-0018.

NCEER-90-0004 "Catalog of Strong Motion Stations in Eastern North America," by R.W. Busby, 4/3/90, (PB90-251984, A05, MF-A01).

NCEER-90-0005 "NCEER Strong-Motion Data Base: A User Manual for the GeoBase Release (Version 1.0 for the Sun3)," by P. Friberg and K. Jacob, 3/31/90 (PB90-258062, A04, MF-A01).

NCEER-90-0006 "Seismic Hazard Along a Crude Oil Pipeline in the Event of an 1811-1812 Type New Madrid Earthquake," by H.H.M. Hwang and C-H.S. Chen, 4/16/90, (PB90-258054, A04, MF-A01).

NCEER-90-0007 "Site-Specific Response Spectra for Memphis Sheahan Pumping Station," by H.H.M. Hwang and C.S. Lee, 5/15/90, (PB91-108811, A05, MF-A01).

NCEER-90-0008 "Pilot Study on Seismic Vulnerability of Crude Oil Transmission Systems," by T. Ariman, R. Dobry, M. Grigoriu, F. Kozin, M. O'Rourke, T. O'Rourke and M. Shinozuka, 5/25/90, (PB91-108837, A06, MF-A01).

NCEER-90-0009 "A Program to Generate Site Dependent Time Histories: EQGEN," by G.W. Ellis, M. Srinivasan and A.S. Cakmak, 1/30/90, (PB91-108829, A04, MF-A01).

NCEER-90-0010 "Active Isolation for Seismic Protection of Operating Rooms," by M.E. Talbott, Supervised by M. Shinozuka, 6/8/9, (PB91-110205, A05, MF-A01).

NCEER-90-0011 "Program LINEARID for Identification of Linear Structural Dynamic Systems," by C-B. Yun and M. Shinozuka, 6/25/90, (PB91-110312, A08, MF-A01).

NCEER-90-0012 "Two-Dimensional Two-Phase Elasto-Plastic Seismic Response of Earth Dams," by A.N. Yiagos, Supervised by J.H. Prevost, 6/20/90, (PB91-110197, A13, MF-A02).

NCEER-90-0013 "Secondary Systems in Base-Isolated Structures: Experimental Investigation, Stochastic Response and Stochastic Sensitivity," by G.D. Manolis, G. Juhn, M.C. Constantinou and A.M. Reinhorn, 7/1/90, (PB91-110320, A08, MF-A01).

NCEER-90-0014 "Seismic Behavior of Lightly-Reinforced Concrete Column and Beam-Column Joint Details," by S.P. Pessiki, C.H. Conley, P. Gergely and R.N. White, 8/22/90, (PB91-108795, A11, MF-A02).

NCEER-90-0015 "Two Hybrid Control Systems for Building Structures Under Strong Earthquakes," by J.N. Yang and A. Danielians, 6/29/90, (PB91-125393, A04, MF-A01).

NCEER-90-0016 "Instantaneous Optimal Control with Acceleration and Velocity Feedback," by J.N. Yang and Z. Li, 6/29/90, (PB91-125401, A03, MF-A01).

NCEER-90-0017 "Reconnaissance Report on the Northern Iran Earthquake of June 21, 1990," by M. Mehrain, 10/4/90, (PB91-125377, A03, MF-A01).

NCEER-90-0018 "Evaluation of Liquefaction Potential in Memphis and Shelby County," by T.S. Chang, P.S. Tang, C.S. Lee and H. Hwang, 8/10/90, (PB91-125427, A09, MF-A01).

NCEER-90-0019 "Experimental and Analytical Study of a Combined Sliding Disc Bearing and Helical Steel Spring Isolation System," by M.C. Constantinou, A.S. Mokha and A.M. Reinhorn, 10/4/90, (PB91-125385, A06, MF-A01). This report is available only through NTIS (see address given above).

NCEER-90-0020 "Experimental Study and Analytical Prediction of Earthquake Response of a Sliding Isolation System with a Spherical Surface," by A.S. Mokha, M.C. Constantinou and A.M. Reinhorn, 10/11/90, (PB91-125419, A05, MF-A01).

NCEER-90-0021 "Dynamic Interaction Factors for Floating Pile Groups," by G. Gazetas, K. Fan, A. Kaynia and E. Kausel, 9/10/90, (PB91-170381, A05, MF-A01).

NCEER-90-0022 "Evaluation of Seismic Damage Indices for Reinforced Concrete Structures," by S. Rodriguez-Gomez and A.S. Cakmak, 9/30/90, PB91-171322, A06, MF-A01).

NCEER-90-0023 "Study of Site Response at a Selected Memphis Site," by H. Desai, S. Ahmad, E.S. Gazetas and M.R. Oh, 10/11/90, (PB91-196857, A03, MF-A01).

NCEER-90-0024 "A User's Guide to Strongmo: Version 1.0 of NCEER's Strong-Motion Data Access Tool for PCs and Terminals," by P.A. Friberg and C.A.T. Susch, 11/15/90, (PB91-171272, A03, MF-A01).

NCEER-90-0025 "A Three-Dimensional Analytical Study of Spatial Variability of Seismic Ground Motions," by L-L. Hong and A.H.-S. Ang, 10/30/90, (PB91-170399, A09, MF-A01).

NCEER-90-0026 "MUMOID User's Guide - A Program for the Identification of Modal Parameters," by S. Rodriguez-Gomez and E. DiPasquale, 9/30/90, (PB91-171298, A04, MF-A01).

NCEER-90-0027 "SARCF-II User's Guide - Seismic Analysis of Reinforced Concrete Frames," by S. Rodriguez-Gomez, Y.S. Chung and C. Meyer, 9/30/90, (PB91-171280, A05, MF-A01).

NCEER-90-0028 "Viscous Dampers: Testing, Modeling and Application in Vibration and Seismic Isolation," by N. Makris and M.C. Constantinou, 12/20/90 (PB91-190561, A06, MF-A01).

NCEER-90-0029 "Soil Effects on Earthquake Ground Motions in the Memphis Area," by H. Hwang, C.S. Lee, K.W. Ng and T.S. Chang, 8/2/90, (PB91-190751, A05, MF-A01).

NCEER-91-0001 "Proceedings from the Third Japan-U.S. Workshop on Earthquake Resistant Design of Lifeline Facilities and Countermeasures for Soil Liquefaction, December 17-19, 1990," edited by T.D. O'Rourke and M. Hamada, 2/1/91, (PB91-179259, A99, MF-A04).

NCEER-91-0002 "Physical Space Solutions of Non-Proportionally Damped Systems," by M. Tong, Z. Liang and G.C. Lee, 1/15/91, (PB91-179242, A04, MF-A01).

NCEER-91-0003 "Seismic Response of Single Piles and Pile Groups," by K. Fan and G. Gazetas, 1/10/91, (PB92-174994, A04, MF-A01).

NCEER-91-0004 "Damping of Structures: Part 1 - Theory of Complex Damping," by Z. Liang and G. Lee, 10/10/91, (PB92-197235, A12, MF-A03).

NCEER-91-0005 "3D-BASIS - Nonlinear Dynamic Analysis of Three Dimensional Base Isolated Structures: Part II," by S. Nagarajaiah, A.M. Reinhorn and M.C. Constantinou, 2/28/91, (PB91-190553, A07, MF-A01). This report has been replaced by NCEER-93-0011.

NCEER-91-0006 "A Multidimensional Hysteretic Model for Plasticity Deforming Metals in Energy Absorbing Devices," by E.J. Graesser and F.A. Cozzarelli, 4/9/91, (PB92-108364, A04, MF-A01).

NCEER-91-0007 "A Framework for Customizable Knowledge-Based Expert Systems with an Application to a KBES for Evaluating the Seismic Resistance of Existing Buildings," by E.G. Ibarra-Anaya and S.J. Fenves, 4/9/91, (PB91-210930, A08, MF-A01).

NCEER-91-0008 "Nonlinear Analysis of Steel Frames with Semi-Rigid Connections Using the Capacity Spectrum Method," by G.G. Deierlein, S-H. Hsieh, Y-J. Shen and J.F. Abel, 7/2/91, (PB92-113828, A05, MF-A01).

NCEER-91-0009 "Earthquake Education Materials for Grades K-12," by K.E.K. Ross, 4/30/91, (PB91-212142, A06, MF-A01). This report has been replaced by NCEER-92-0018.

NCEER-91-0010 "Phase Wave Velocities and Displacement Phase Differences in a Harmonically Oscillating Pile," by N. Makris and G. Gazetas, 7/8/91, (PB92-108356, A04, MF-A01).

NCEER-91-0011 "Dynamic Characteristics of a Full-Size Five-Story Steel Structure and a 2/5 Scale Model," by K.C. Chang, G.C. Yao, G.C. Lee, D.S. Hao and Y.C. Yeh," 7/2/91, (PB93-116648, A06, MF-A02).

NCEER-91-0012 "Seismic Response of a 2/5 Scale Steel Structure with Added Viscoelastic Dampers," by K.C. Chang, T.T. Soong, S-T. Oh and M.L. Lai, 5/17/91, (PB92-110816, A05, MF-A01).

NCEER-91-0013 "Earthquake Response of Retaining Walls; Full-Scale Testing and Computational Modeling," by S. Alampalli and A-W.M. Elgamal, 6/20/91, to be published.

NCEER-91-0014 "3D-BASIS-M: Nonlinear Dynamic Analysis of Multiple Building Base Isolated Structures," by P.C. Tsopelas, S. Nagarajaiah, M.C. Constantinou and A.M. Reinhorn, 5/28/91, (PB92-113885, A09, MF-A02).

NCEER-91-0015 "Evaluation of SEAOC Design Requirements for Sliding Isolated Structures," by D. Theodossiou and M.C. Constantinou, 6/10/91, (PB92-114602, A11, MF-A03).

NCEER-91-0016 "Closed-Loop Modal Testing of a 27-Story Reinforced Concrete Flat Plate-Core Building," by H.R. Somaprasad, T. Toksoy, H. Yoshiyuki and A.E. Aktan, 7/15/91, (PB92-129980, A07, MF-A02).

NCEER-91-0017 "Shake Table Test of a 1/6 Scale Two-Story Lightly Reinforced Concrete Building," by A.G. El-Attar, R.N. White and P. Gergely, 2/28/91, (PB92-222447, A06, MF-A02).

NCEER-91-0018 "Shake Table Test of a 1/8 Scale Three-Story Lightly Reinforced Concrete Building," by A.G. El-Attar, R.N. White and P. Gergely, 2/28/91, (PB93-116630, A08, MF-A02).

NCEER-91-0019 "Transfer Functions for Rigid Rectangular Foundations," by A.S. Veletsos, A.M. Prasad and W.H. Wu, 7/31/91, to be published.

NCEER-91-0020 "Hybrid Control of Seismic-Excited Nonlinear and Inelastic Structural Systems," by J.N. Yang, Z. Li and A. Danielians, 8/1/91, (PB92-143171, A06, MF-A02).

NCEER-91-0021 "The NCEER-91 Earthquake Catalog: Improved Intensity-Based Magnitudes and Recurrence Relations for U.S. Earthquakes East of New Madrid," by L. Seeber and J.G. Armbruster, 8/28/91, (PB92-176742, A06, MF-A02).

NCEER-91-0022 "Proceedings from the Implementation of Earthquake Planning and Education in Schools: The Need for Change - The Roles of the Changemakers," by K.E.K. Ross and F. Winslow, 7/23/91, (PB92-129998, A12, MF-A03).

NCEER-91-0023 "A Study of Reliability-Based Criteria for Seismic Design of Reinforced Concrete Frame Buildings," by H.H.M. Hwang and H-M. Hsu, 8/10/91, (PB92-140235, A09, MF-A02).

NCEER-91-0024 "Experimental Verification of a Number of Structural System Identification Algorithms," by R.G. Ghanem, H. Gavin and M. Shinozuka, 9/18/91, (PB92-176577, A18, MF-A04).

NCEER-91-0025 "Probabilistic Evaluation of Liquefaction Potential," by H.H.M. Hwang and C.S. Lee," 11/25/91, (PB92-143429, A05, MF-A01).

NCEER-91-0026 "Instantaneous Optimal Control for Linear, Nonlinear and Hysteretic Structures - Stable Controllers," by J.N. Yang and Z. Li, 11/15/91, (PB92-163807, A04, MF-A01).

NCEER-91-0027 "Experimental and Theoretical Study of a Sliding Isolation System for Bridges," by M.C. Constantinou, A. Kartoum, A.M. Reinhorn and P. Bradford, 11/15/91, (PB92-176973, A10, MF-A03).

NCEER-92-0001 "Case Studies of Liquefaction and Lifeline Performance During Past Earthquakes, Volume 1: Japanese Case Studies," Edited by M. Hamada and T. O'Rourke, 2/17/92, (PB92-197243, A18, MF-A04).

NCEER-92-0002 "Case Studies of Liquefaction and Lifeline Performance During Past Earthquakes, Volume 2: United States Case Studies," Edited by T. O'Rourke and M. Hamada, 2/17/92, (PB92-197250, A20, MF-A04).

NCEER-92-0003 "Issues in Earthquake Education," Edited by K. Ross, 2/3/92, (PB92-222389, A07, MF-A02).

NCEER-92-0004 "Proceedings from the First U.S. - Japan Workshop on Earthquake Protective Systems for Bridges," Edited by I.G. Buckle, 2/4/92, (PB94-142239, A99, MF-A06).

NCEER-92-0005 "Seismic Ground Motion from a Haskell-Type Source in a Multiple-Layered Half-Space," A.P. Theoharis, G. Deodatis and M. Shinozuka, 1/2/92, to be published.

NCEER-92-0006 "Proceedings from the Site Effects Workshop," Edited by R. Whitman, 2/29/92, (PB92-197201, A04, MF-A01).

NCEER-92-0007 "Engineering Evaluation of Permanent Ground Deformations Due to Seismically-Induced Liquefaction," by M.H. Baziar, R. Dobry and A-W.M. Elgamal, 3/24/92, (PB92-222421, A13, MF-A03).

NCEER-92-0008 "A Procedure for the Seismic Evaluation of Buildings in the Central and Eastern United States," by C.D. Poland and J.O. Malley, 4/2/92, (PB92-222439, A20, MF-A04).

NCEER-92-0009 "Experimental and Analytical Study of a Hybrid Isolation System Using Friction Controllable Sliding Bearings," by M.Q. Feng, S. Fujii and M. Shinozuka, 5/15/92, (PB93-150282, A06, MF-A02).

NCEER-92-0010 "Seismic Resistance of Slab-Column Connections in Existing Non-Ductile Flat-Plate Buildings," by A.J. Durrani and Y. Du, 5/18/92, (PB93-116812, A06, MF-A02).

NCEER-92-0011 "The Hysteretic and Dynamic Behavior of Brick Masonry Walls Upgraded by Ferrocement Coatings Under Cyclic Loading and Strong Simulated Ground Motion," by H. Lee and S.P. Prawel, 5/11/92, to be published.

NCEER-92-0012 "Study of Wire Rope Systems for Seismic Protection of Equipment in Buildings," by G.F. Demetriades, M.C. Constantinou and A.M. Reinhorn, 5/20/92, (PB93-116655, A08, MF-A02).

NCEER-92-0013 "Shape Memory Structural Dampers: Material Properties, Design and Seismic Testing," by P.R. Witting and F.A. Cozzarelli, 5/26/92, (PB93-116663, A05, MF-A01).

NCEER-92-0014 "Longitudinal Permanent Ground Deformation Effects on Buried Continuous Pipelines," by M.J. O'Rourke, and C. Nordberg, 6/15/92, (PB93-116671, A08, MF-A02).

NCEER-92-0015 "A Simulation Method for Stationary Gaussian Random Functions Based on the Sampling Theorem," by M. Grigoriu and S. Balopoulou, 6/11/92, (PB93-127496, A05, MF-A01).

NCEER-92-0016 "Gravity-Load-Designed Reinforced Concrete Buildings: Seismic Evaluation of Existing Construction and Detailing Strategies for Improved Seismic Resistance," by G.W. Hoffmann, S.K. Kunnath, A.M. Reinhorn and J.B. Mander, 7/15/92, (PB94-142007, A08, MF-A02).

NCEER-92-0017 "Observations on Water System and Pipeline Performance in the Limón Area of Costa Rica Due to the April 22, 1991 Earthquake," by M. O'Rourke and D. Ballantyne, 6/30/92, (PB93-126811, A06, MF-A02).

NCEER-92-0018 "Fourth Edition of Earthquake Education Materials for Grades K-12," Edited by K.E.K. Ross, 8/10/92, (PB93-114023, A07, MF-A02).

NCEER-92-0019 "Proceedings from the Fourth Japan-U.S. Workshop on Earthquake Resistant Design of Lifeline Facilities and Countermeasures for Soil Liquefaction," Edited by M. Hamada and T.D. O'Rourke, 8/12/92, (PB93-163939, A99, MF-E11).

NCEER-92-0020 "Active Bracing System: A Full Scale Implementation of Active Control," by A.M. Reinhorn, T.T. Soong, R.C. Lin, M.A. Riley, Y.P. Wang, S. Aizawa and M. Higashino, 8/14/92, (PB93-127512, A06, MF-A02).

NCEER-92-0021 "Empirical Analysis of Horizontal Ground Displacement Generated by Liquefaction-Induced Lateral Spreads," by S.F. Bartlett and T.L. Youd, 8/17/92, (PB93-188241, A06, MF-A02).

NCEER-92-0022 "IDARC Version 3.0: Inelastic Damage Analysis of Reinforced Concrete Structures," by S.K. Kunnath, A.M. Reinhorn and R.F. Lobo, 8/31/92, (PB93-227502, A07, MF-A02).

NCEER-92-0023 "A Semi-Empirical Analysis of Strong-Motion Peaks in Terms of Seismic Source, Propagation Path and Local Site Conditions, by M. Kamiyama, M.J. O'Rourke and R. Flores-Berrones, 9/9/92, (PB93-150266, A08, MF-A02).

NCEER-92-0024 "Seismic Behavior of Reinforced Concrete Frame Structures with Nonductile Details, Part I: Summary of Experimental Findings of Full Scale Beam-Column Joint Tests," by A. Beres, R.N. White and P. Gergely, 9/30/92, (PB93-227783, A05, MF-A01).

NCEER-92-0025 "Experimental Results of Repaired and Retrofitted Beam-Column Joint Tests in Lightly Reinforced Concrete Frame Buildings," by A. Beres, S. El-Borgi, R.N. White and P. Gergely, 10/29/92, (PB93-227791, A05, MF-A01).

NCEER-92-0026 "A Generalization of Optimal Control Theory: Linear and Nonlinear Structures," by J.N. Yang, Z. Li and S. Vongchavalitkul, 11/2/92, (PB93-188621, A05, MF-A01).

NCEER-92-0027 "Seismic Resistance of Reinforced Concrete Frame Structures Designed Only for Gravity Loads: Part I - Design and Properties of a One-Third Scale Model Structure," by J.M. Bracci, A.M. Reinhorn and J.B. Mander, 12/1/92, (PB94-104502, A08, MF-A02).

NCEER-92-0028 "Seismic Resistance of Reinforced Concrete Frame Structures Designed Only for Gravity Loads: Part II - Experimental Performance of Subassemblages," by L.E. Aycardi, J.B. Mander and A.M. Reinhorn, 12/1/92, (PB94-104510, A08, MF-A02).

NCEER-92-0029 "Seismic Resistance of Reinforced Concrete Frame Structures Designed Only for Gravity Loads: Part III - Experimental Performance and Analytical Study of a Structural Model," by J.M. Bracci, A.M. Reinhorn and J.B. Mander, 12/1/92, (PB93-227528, A09, MF-A01).

NCEER-92-0030 "Evaluation of Seismic Retrofit of Reinforced Concrete Frame Structures: Part I - Experimental Performance of Retrofitted Subassemblages," by D. Choudhuri, J.B. Mander and A.M. Reinhorn, 12/8/92, (PB93-198307, A07, MF-A02).

NCEER-92-0031 "Evaluation of Seismic Retrofit of Reinforced Concrete Frame Structures: Part II - Experimental Performance and Analytical Study of a Retrofitted Structural Model," by J.M. Bracci, A.M. Reinhorn and J.B. Mander, 12/8/92, (PB93-198315, A09, MF-A03).

NCEER-92-0032 "Experimental and Analytical Investigation of Seismic Response of Structures with Supplemental Fluid Viscous Dampers," by M.C. Constantinou and M.D. Symans, 12/21/92, (PB93-191435, A10, MF-A03). This report is available only through NTIS (see address given above).

NCEER-92-0033 "Reconnaissance Report on the Cairo, Egypt Earthquake of October 12, 1992," by M. Khater, 12/23/92, (PB93-188621, A03, MF-A01).

NCEER-92-0034 "Low-Level Dynamic Characteristics of Four Tall Flat-Plate Buildings in New York City," by H. Gavin, S. Yuan, J. Grossman, E. Pekelis and K. Jacob, 12/28/92, (PB93-188217, A07, MF-A02).

NCEER-93-0001 "An Experimental Study on the Seismic Performance of Brick-Infilled Steel Frames With and Without Retrofit," by J.B. Mander, B. Nair, K. Wojtkowski and J. Ma, 1/29/93, (PB93-227510, A07, MF-A02).

NCEER-93-0002 "Social Accounting for Disaster Preparedness and Recovery Planning," by S. Cole, E. Pantoja and V. Razak, 2/22/93, (PB94-142114, A12, MF-A03).

NCEER-93-0003 "Assessment of 1991 NEHRP Provisions for Nonstructural Components and Recommended Revisions," by T.T. Soong, G. Chen, Z. Wu, R-H. Zhang and M. Grigoriu, 3/1/93, (PB93-188639, A06, MF-A02).

NCEER-93-0004 "Evaluation of Static and Response Spectrum Analysis Procedures of SEAOC/UBC for Seismic Isolated Structures," by C.W. Winters and M.C. Constantinou, 3/23/93, (PB93-198299, A10, MF-A03).

NCEER-93-0005 "Earthquakes in the Northeast - Are We Ignoring the Hazard? A Workshop on Earthquake Science and Safety for Educators," edited by K.E.K. Ross, 4/2/93, (PB94-103066, A09, MF-A02).

NCEER-93-0006 "Inelastic Response of Reinforced Concrete Structures with Viscoelastic Braces," by R.F. Lobo, J.M. Bracci, K.L. Shen, A.M. Reinhorn and T.T. Soong, 4/5/93, (PB93-227486, A05, MF-A02).

NCEER-93-0007 "Seismic Testing of Installation Methods for Computers and Data Processing Equipment," by K. Kosar, T.T. Soong, K.L. Shen, J.A. HoLung and Y.K. Lin, 4/12/93, (PB93-198299, A07, MF-A02).

NCEER-93-0008 "Retrofit of Reinforced Concrete Frames Using Added Dampers," by A. Reinhorn, M. Constantinou and C. Li, to be published.

NCEER-93-0009 "Seismic Behavior and Design Guidelines for Steel Frame Structures with Added Viscoelastic Dampers," by K.C. Chang, M.L. Lai, T.T. Soong, D.S. Hao and Y.C. Yeh, 5/1/93, (PB94-141959, A07, MF-A02).

NCEER-93-0010 "Seismic Performance of Shear-Critical Reinforced Concrete Bridge Piers," by J.B. Mander, S.M. Waheed, M.T.A. Chaudhary and S.S. Chen, 5/12/93, (PB93-227494, A08, MF-A02).

NCEER-93-0011 "3D-BASIS-TABS: Computer Program for Nonlinear Dynamic Analysis of Three Dimensional Base Isolated Structures," by S. Nagarajaiah, C. Li, A.M. Reinhorn and M.C. Constantinou, 8/2/93, (PB94-141819, A09, MF-A02).

NCEER-93-0012 "Effects of Hydrocarbon Spills from an Oil Pipeline Break on Ground Water," by O.J. Helweg and H.H.M. Hwang, 8/3/93, (PB94-141942, A06, MF-A02).

NCEER-93-0013 "Simplified Procedures for Seismic Design of Nonstructural Components and Assessment of Current Code Provisions," by M.P. Singh, L.E. Suarez, E.E. Matheu and G.O. Maldonado, 8/4/93, (PB94-141827, A09, MF-A02).

NCEER-93-0014 "An Energy Approach to Seismic Analysis and Design of Secondary Systems," by G. Chen and T.T. Soong, 8/6/93, (PB94-142767, A11, MF-A03).

NCEER-93-0015 "Proceedings from School Sites: Becoming Prepared for Earthquakes - Commemorating the Third Anniversary of the Loma Prieta Earthquake," Edited by F.E. Winslow and K.E.K. Ross, 8/16/93, (PB94-154275, A16, MF-A02).

NCEER-93-0016 "Reconnaissance Report of Damage to Historic Monuments in Cairo, Egypt Following the October 12, 1992 Dahshur Earthquake," by D. Sykora, D. Look, G. Croci, E. Karaesmen and E. Karaesmen, 8/19/93, (PB94-142221, A08, MF-A02).

NCEER-93-0017 "The Island of Guam Earthquake of August 8, 1993," by S.W. Swan and S.K. Harris, 9/30/93, (PB94-141843, A04, MF-A01).

NCEER-93-0018 "Engineering Aspects of the October 12, 1992 Egyptian Earthquake," by A.W. Elgamal, M. Amer, K. Adalier and A. Abul-Fadl, 10/7/93, (PB94-141983, A05, MF-A01).

NCEER-93-0019 "Development of an Earthquake Motion Simulator and its Application in Dynamic Centrifuge Testing," by I. Krstelj, Supervised by J.H. Prevost, 10/23/93, (PB94-181773, A-10, MF-A03).

NCEER-93-0020 "NCEER-Taisei Corporation Research Program on Sliding Seismic Isolation Systems for Bridges: Experimental and Analytical Study of a Friction Pendulum System (FPS)," by M.C. Constantinou, P. Tsopelas, Y-S. Kim and S. Okamoto, 11/1/93, (PB94-142775, A08, MF-A02).

NCEER-93-0021 "Finite Element Modeling of Elastomeric Seismic Isolation Bearings," by L.J. Billings, Supervised by R. Shepherd, 11/8/93, to be published.

NCEER-93-0022 "Seismic Vulnerability of Equipment in Critical Facilities: Life-Safety and Operational Consequences," by K. Porter, G.S. Johnson, M.M. Zadeh, C. Scawthorn and S. Eder, 11/24/93, (PB94-181765, A16, MF-A03).

NCEER-93-0023 "Hokkaido Nansei-oki, Japan Earthquake of July 12, 1993, by P.I. Yanev and C.R. Scawthorn, 12/23/93, (PB94-181500, A07, MF-A01).

NCEER-94-0001 "An Evaluation of Seismic Serviceability of Water Supply Networks with Application to the San Francisco Auxiliary Water Supply System," by I. Markov, Supervised by M. Grigoriu and T. O'Rourke, 1/21/94, (PB94-204013, A07, MF-A02).

NCEER-94-0002 "NCEER-Taisei Corporation Research Program on Sliding Seismic Isolation Systems for Bridges: Experimental and Analytical Study of Systems Consisting of Sliding Bearings, Rubber Restoring Force Devices and Fluid Dampers," Volumes I and II, by P. Tsopelas, S. Okamoto, M.C. Constantinou, D. Ozaki and S. Fujii, 2/4/94, (PB94-181740, A09, MF-A02 and PB94-181757, A12, MF-A03).

NCEER-94-0003 "A Markov Model for Local and Global Damage Indices in Seismic Analysis," by S. Rahman and M. Grigoriu, 2/18/94, (PB94-206000, A12, MF-A03).

NCEER-94-0004 "Proceedings from the NCEER Workshop on Seismic Response of Masonry Infills," edited by D.P. Abrams, 3/1/94, (PB94-180783, A07, MF-A02).

NCEER-94-0005 "The Northridge, California Earthquake of January 17, 1994: General Reconnaissance Report," edited by J.D. Goltz, 3/11/94, (PB94-193943, A10, MF-A03).

NCEER-94-0006 "Seismic Energy Based Fatigue Damage Analysis of Bridge Columns: Part I - Evaluation of Seismic Capacity," by G.A. Chang and J.B. Mander, 3/14/94, (PB94-219185, A11, MF-A03).

NCEER-94-0007 "Seismic Isolation of Multi-Story Frame Structures Using Spherical Sliding Isolation Systems," by T.M. Al-Hussaini, V.A. Zayas and M.C. Constantinou, 3/17/94, (PB94-193745, A09, MF-A02).

NCEER-94-0008 "The Northridge, California Earthquake of January 17, 1994: Performance of Highway Bridges," edited by I.G. Buckle, 3/24/94, (PB94-193851, A06, MF-A02).

NCEER-94-0009 "Proceedings of the Third U.S.-Japan Workshop on Earthquake Protective Systems for Bridges," edited by I.G. Buckle and I. Friedland, 3/31/94, (PB94-195815, A99, MF-A06).

NCEER-94-0010 "3D-BASIS-ME: Computer Program for Nonlinear Dynamic Analysis of Seismically Isolated Single and Multiple Structures and Liquid Storage Tanks," by P.C. Tsopelas, M.C. Constantinou and A.M. Reinhorn, 4/12/94, (PB94-204922, A09, MF-A02).

NCEER-94-0011 "The Northridge, California Earthquake of January 17, 1994: Performance of Gas Transmission Pipelines," by T.D. O'Rourke and M.C. Palmer, 5/16/94, (PB94-204989, A05, MF-A01).

NCEER-94-0012 "Feasibility Study of Replacement Procedures and Earthquake Performance Related to Gas Transmission Pipelines," by T.D. O'Rourke and M.C. Palmer, 5/25/94, (PB94-206638, A09, MF-A02).

NCEER-94-0013 "Seismic Energy Based Fatigue Damage Analysis of Bridge Columns: Part II - Evaluation of Seismic Demand," by G.A. Chang and J.B. Mander, 6/1/94, (PB95-18106, A08, MF-A02).

NCEER-94-0014 "NCEER-Taisei Corporation Research Program on Sliding Seismic Isolation Systems for Bridges: Experimental and Analytical Study of a System Consisting of Sliding Bearings and Fluid Restoring Force/Damping Devices," by P. Tsopelas and M.C. Constantinou, 6/13/94, (PB94-219144, A10, MF-A03).

NCEER-94-0015 "Generation of Hazard-Consistent Fragility Curves for Seismic Loss Estimation Studies," by H. Hwang and J-R. Huo, 6/14/94, (PB95-181996, A09, MF-A02).

NCEER-94-0016 "Seismic Study of Building Frames with Added Energy-Absorbing Devices," by W.S. Pong, C.S. Tsai and G.C. Lee, 6/20/94, (PB94-219136, A10, A03).

NCEER-94-0017 "Sliding Mode Control for Seismic-Excited Linear and Nonlinear Civil Engineering Structures," by J. Yang, J. Wu, A. Agrawal and Z. Li, 6/21/94, (PB95-138483, A06, MF-A02).

NCEER-94-0018 "3D-BASIS-TABS Version 2.0: Computer Program for Nonlinear Dynamic Analysis of Three Dimensional Base Isolated Structures," by A.M. Reinhorn, S. Nagarajaiah, M.C. Constantinou, P. Tsopelas and R. Li, 6/22/94, (PB95-182176, A08, MF-A02).

NCEER-94-0019 "Proceedings of the International Workshop on Civil Infrastructure Systems: Application of Intelligent Systems and Advanced Materials on Bridge Systems," Edited by G.C. Lee and K.C. Chang, 7/18/94, (PB95-252474, A20, MF-A04).

NCEER-94-0020 "Study of Seismic Isolation Systems for Computer Floors," by V. Lambrou and M.C. Constantinou, 7/19/94, (PB95-138533, A10, MF-A03).

NCEER-94-0021 "Proceedings of the U.S.-Italian Workshop on Guidelines for Seismic Evaluation and Rehabilitation of Unreinforced Masonry Buildings," Edited by D.P. Abrams and G.M. Calvi, 7/20/94, (PB95-138749, A13, MF-A03).

NCEER-94-0022 "NCEER-Taisei Corporation Research Program on Sliding Seismic Isolation Systems for Bridges: Experimental and Analytical Study of a System Consisting of Lubricated PTFE Sliding Bearings and Mild Steel Dampers," by P. Tsopelas and M.C. Constantinou, 7/22/94, (PB95-182184, A08, MF-A02).

NCEER-94-0023 “Development of Reliability-Based Design Criteria for Buildings Under Seismic Load,” by Y.K. Wen, H. Hwang and M. Shinozuka, 8/1/94, (PB95-211934, A08, MF-A02).

NCEER-94-0024 “Experimental Verification of Acceleration Feedback Control Strategies for an Active Tendon System,” by S.J. Dyke, B.F. Spencer, Jr., P. Quast, M.K. Sain, D.C. Kaspari, Jr. and T.T. Soong, 8/29/94, (PB95-212320, A05, MF-A01).

NCEER-94-0025 “Seismic Retrofitting Manual for Highway Bridges,” Edited by I.G. Buckle and I.F. Friedland, published by the Federal Highway Administration (PB95-212676, A15, MF-A03).

NCEER-94-0026 “Proceedings from the Fifth U.S.-Japan Workshop on Earthquake Resistant Design of Lifeline Facilities and Countermeasures Against Soil Liquefaction,” Edited by T.D. O’Rourke and M. Hamada, 11/7/94, (PB95-220802, A99, MF-E08).

NCEER-95-0001 “Experimental and Analytical Investigation of Seismic Retrofit of Structures with Supplemental Damping: Part 1 - Fluid Viscous Damping Devices,” by A.M. Reinhorn, C. Li and M.C. Constantinou, 1/3/95, (PB95-266599, A09, MF-A02).

NCEER-95-0002 “Experimental and Analytical Study of Low-Cycle Fatigue Behavior of Semi-Rigid Top-And-Seat Angle Connections,” by G. Pekcan, J.B. Mander and S.S. Chen, 1/5/95, (PB95-220042, A07, MF-A02).

NCEER-95-0003 “NCEER-ATC Joint Study on Fragility of Buildings,” by T. Anagnos, C. Rojahn and A.S. Kiremidjian, 1/20/95, (PB95-220026, A06, MF-A02).

NCEER-95-0004 “Nonlinear Control Algorithms for Peak Response Reduction,” by Z. Wu, T.T. Soong, V. Gattulli and R.C. Lin, 2/16/95, (PB95-220349, A05, MF-A01).

NCEER-95-0005 “Pipeline Replacement Feasibility Study: A Methodology for Minimizing Seismic and Corrosion Risks to Underground Natural Gas Pipelines,” by R.T. Eguchi, H.A. Seligson and D.G. Honegger, 3/2/95, (PB95-252326, A06, MF-A02).

NCEER-95-0006 “Evaluation of Seismic Performance of an 11-Story Frame Building During the 1994 Northridge Earthquake,” by F. Naeim, R. DiSulio, K. Benuska, A. Reinhorn and C. Li, to be published.

NCEER-95-0007 “Prioritization of Bridges for Seismic Retrofitting,” by N. Basöz and A.S. Kiremidjian, 4/24/95, (PB95-252300, A08, MF-A02).

NCEER-95-0008 “Method for Developing Motion Damage Relationships for Reinforced Concrete Frames,” by A. Singhal and A.S. Kiremidjian, 5/11/95, (PB95-266607, A06, MF-A02).

NCEER-95-0009 “Experimental and Analytical Investigation of Seismic Retrofit of Structures with Supplemental Damping: Part II - Friction Devices,” by C. Li and A.M. Reinhorn, 7/6/95, (PB96-128087, A11, MF-A03).

NCEER-95-0010 “Experimental Performance and Analytical Study of a Non-Ductile Reinforced Concrete Frame Structure Retrofitted with Elastomeric Spring Dampers,” by G. Pekcan, J.B. Mander and S.S. Chen, 7/14/95, (PB96-137161, A08, MF-A02).

NCEER-95-0011 “Development and Experimental Study of Semi-Active Fluid Damping Devices for Seismic Protection of Structures,” by M.D. Symans and M.C. Constantinou, 8/3/95, (PB96-136940, A23, MF-A04).

NCEER-95-0012 “Real-Time Structural Parameter Modification (RSPM): Development of Innervated Structures,” by Z. Liang, M. Tong and G.C. Lee, 4/11/95, (PB96-137153, A06, MF-A01).

NCEER-95-0013 “Experimental and Analytical Investigation of Seismic Retrofit of Structures with Supplemental Damping: Part III - Viscous Damping Walls,” by A.M. Reinhorn and C. Li, 10/1/95, (PB96-176409, A11, MF-A03).

NCEER-95-0014 “Seismic Fragility Analysis of Equipment and Structures in a Memphis Electric Substation,” by J-R. Huo and H.H.M. Hwang, 8/10/95, (PB96-128087, A09, MF-A02).

NCEER-95-0015 “The Hanshin-Awaji Earthquake of January 17, 1995: Performance of Lifelines,” Edited by M. Shinozuka, 11/3/95, (PB96-176383, A15, MF-A03).

NCEER-95-0016 “Highway Culvert Performance During Earthquakes,” by T.L. Youd and C.J. Beckman, available as NCEER-96-0015.

NCEER-95-0017 “The Hanshin-Awaji Earthquake of January 17, 1995: Performance of Highway Bridges,” Edited by I.G. Buckle, 12/1/95, to be published.

NCEER-95-0018 “Modeling of Masonry Infill Panels for Structural Analysis,” by A.M. Reinhorn, A. Madan, R.E. Valles, Y. Reichmann and J.B. Mander, 12/8/95, (PB97-110886, MF-A01, A06).

NCEER-95-0019 “Optimal Polynomial Control for Linear and Nonlinear Structures,” by A.K. Agrawal and J.N. Yang, 12/11/95, (PB96-168737, A07, MF-A02).

NCEER-95-0020 "Retrofit of Non-Ductile Reinforced Concrete Frames Using Friction Dampers," by R.S. Rao, P. Gergely and R.N. White, 12/22/95, (PB97-133508, A10, MF-A02).

NCEER-95-0021 "Parametric Results for Seismic Response of Pile-Supported Bridge Bents," by G. Mylonakis, A. Nikolaou and G. Gazetas, 12/22/95, (PB97-100242, A12, MF-A03).

NCEER-95-0022 "Kinematic Bending Moments in Seismically Stressed Piles," by A. Nikolaou, G. Mylonakis and G. Gazetas, 12/23/95, (PB97-113914, MF-A03, A13).

NCEER-96-0001 "Dynamic Response of Unreinforced Masonry Buildings with Flexible Diaphragms," by A.C. Costley and D.P. Abrams," 10/10/96, (PB97-133573, MF-A03, A15).

NCEER-96-0002 "State of the Art Review: Foundations and Retaining Structures," by I. Po Lam, to be published.

NCEER-96-0003 "Ductility of Rectangular Reinforced Concrete Bridge Columns with Moderate Confinement," by N. Wehbe, M. Saiidi, D. Sanders and B. Douglas, 11/7/96, (PB97-133557, A06, MF-A02).

NCEER-96-0004 "Proceedings of the Long-Span Bridge Seismic Research Workshop," edited by I.G. Buckle and I.M. Friedland, to be published.

NCEER-96-0005 "Establish Representative Pier Types for Comprehensive Study: Eastern United States," by J. Kulicki and Z. Prucz, 5/28/96, (PB98-119217, A07, MF-A02).

NCEER-96-0006 "Establish Representative Pier Types for Comprehensive Study: Western United States," by R. Imbsen, R.A. Schamber and T.A. Osterkamp, 5/28/96, (PB98-118607, A07, MF-A02).

NCEER-96-0007 "Nonlinear Control Techniques for Dynamical Systems with Uncertain Parameters," by R.G. Ghanem and M.I. Bujakov, 5/27/96, (PB97-100259, A17, MF-A03).

NCEER-96-0008 "Seismic Evaluation of a 30-Year Old Non-Ductile Highway Bridge Pier and Its Retrofit," by J.B. Mander, B. Mahmoodzadegan, S. Bhadra and S.S. Chen, 5/31/96, (PB97-110902, MF-A03, A10).

NCEER-96-0009 "Seismic Performance of a Model Reinforced Concrete Bridge Pier Before and After Retrofit," by J.B. Mander, J.H. Kim and C.A. Ligozio, 5/31/96, (PB97-110910, MF-A02, A10).

NCEER-96-0010 "IDARC2D Version 4.0: A Computer Program for the Inelastic Damage Analysis of Buildings," by R.E. Valles, A.M. Reinhorn, S.K. Kunnath, C. Li and A. Madan, 6/3/96, (PB97-100234, A17, MF-A03).

NCEER-96-0011 "Estimation of the Economic Impact of Multiple Lifeline Disruption: Memphis Light, Gas and Water Division Case Study," by S.E. Chang, H.A. Seligson and R.T. Eguchi, 8/16/96, (PB97-133490, A11, MF-A03).

NCEER-96-0012 "Proceedings from the Sixth Japan-U.S. Workshop on Earthquake Resistant Design of Lifeline Facilities and Countermeasures Against Soil Liquefaction, Edited by M. Hamada and T. O'Rourke, 9/11/96, (PB97-133581, A99, MF-A06).

NCEER-96-0013 "Chemical Hazards, Mitigation and Preparedness in Areas of High Seismic Risk: A Methodology for Estimating the Risk of Post-Earthquake Hazardous Materials Release," by H.A. Seligson, R.T. Eguchi, K.J. Tierney and K. Richmond, 11/7/96, (PB97-133565, MF-A02, A08).

NCEER-96-0014 "Response of Steel Bridge Bearings to Reversed Cyclic Loading," by J.B. Mander, D-K. Kim, S.S. Chen and G.J. Premus, 11/13/96, (PB97-140735, A12, MF-A03).

NCEER-96-0015 "Highway Culvert Performance During Past Earthquakes," by T.L. Youd and C.J. Beckman, 11/25/96, (PB97-133532, A06, MF-A01).

NCEER-97-0001 "Evaluation, Prevention and Mitigation of Pounding Effects in Building Structures," by R.E. Valles and A.M. Reinhorn, 2/20/97, (PB97-159552, A14, MF-A03).

NCEER-97-0002 "Seismic Design Criteria for Bridges and Other Highway Structures," by C. Rojahn, R. Mayes, D.G. Anderson, J. Clark, J.H. Hom, R.V. Nutt and M.J. O'Rourke, 4/30/97, (PB97-194658, A06, MF-A03).

NCEER-97-0003 “Proceedings of the U.S.-Italian Workshop on Seismic Evaluation and Retrofit,” Edited by D.P. Abrams and G.M. Calvi, 3/19/97, (PB97-194666, A13, MF-A03).

NCEER-97-0004 "Investigation of Seismic Response of Buildings with Linear and Nonlinear Fluid Viscous Dampers," by A.A. Seleemah and M.C. Constantinou, 5/21/97, (PB98-109002, A15, MF-A03).

NCEER-97-0005 "Proceedings of the Workshop on Earthquake Engineering Frontiers in Transportation Facilities," edited by G.C. Lee and I.M. Friedland, 8/29/97, (PB98-128911, A25, MR-A04).

NCEER-97-0006 "Cumulative Seismic Damage of Reinforced Concrete Bridge Piers," by S.K. Kunnath, A. El-Bahy, A. Taylor and W. Stone, 9/2/97, (PB98-108814, A11, MF-A03).

NCEER-97-0007 "Structural Details to Accommodate Seismic Movements of Highway Bridges and Retaining Walls," by R.A. Imbsen, R.A. Schamber, E. Thorkildsen, A. Kartoum, B.T. Martin, T.N. Rosser and J.M. Kulicki, 9/3/97, (PB98-108996, A09, MF-A02).

NCEER-97-0008 "A Method for Earthquake Motion-Damage Relationships with Application to Reinforced Concrete Frames," by A. Singhal and A.S. Kiremidjian, 9/10/97, (PB98-108988, A13, MF-A03).

NCEER-97-0009 "Seismic Analysis and Design of Bridge Abutments Considering Sliding and Rotation," by K. Fishman and R. Richards, Jr., 9/15/97, (PB98-108897, A06, MF-A02).

NCEER-97-0010 "Proceedings of the FHWA/NCEER Workshop on the National Representation of Seismic Ground Motion for New and Existing Highway Facilities," edited by I.M. Friedland, M.S. Power and R.L. Mayes, 9/22/97, (PB98-128903, A21, MF-A04).

NCEER-97-0011 "Seismic Analysis for Design or Retrofit of Gravity Bridge Abutments," by K.L. Fishman, R. Richards, Jr. and R.C. Divito, 10/2/97, (PB98-128937, A08, MF-A02).

NCEER-97-0012 "Evaluation of Simplified Methods of Analysis for Yielding Structures," by P. Tsopelas, M.C. Constantinou, C.A. Kircher and A.S. Whittaker, 10/31/97, (PB98-128929, A10, MF-A03).

NCEER-97-0013 "Seismic Design of Bridge Columns Based on Control and Repairability of Damage," by C-T. Cheng and J.B. Mander, 12/8/97, (PB98-144249, A11, MF-A03).

NCEER-97-0014 "Seismic Resistance of Bridge Piers Based on Damage Avoidance Design," by J.B. Mander and C-T. Cheng, 12/10/97, (PB98-144223, A09, MF-A02).

NCEER-97-0015 “Seismic Response of Nominally Symmetric Systems with Strength Uncertainty,” by S. Balopoulou and M. Grigoriu, 12/23/97, (PB98-153422, A11, MF-A03).

NCEER-97-0016 “Evaluation of Seismic Retrofit Methods for Reinforced Concrete Bridge Columns,” by T.J. Wipf, F.W. Klaiber and F.M. Russo, 12/28/97, (PB98-144215, A12, MF-A03).

NCEER-97-0017 “Seismic Fragility of Existing Conventional Reinforced Concrete Highway Bridges,” by C.L. Mullen and A.S. Cakmak, 12/30/97, (PB98-153406, A08, MF-A02).

NCEER-97-0018 “Loss Asssessment of Memphis Buildings,” edited by D.P. Abrams and M. Shinozuka, 12/31/97, (PB98-144231, A13, MF-A03).

NCEER-97-0019 “Seismic Evaluation of Frames with Infill Walls Using Quasi-static Experiments,” by K.M. Mosalam, R.N. White and P. Gergely, 12/31/97, (PB98-153455, A07, MF-A02).

NCEER-97-0020 “Seismic Evaluation of Frames with Infill Walls Using Pseudo-dynamic Experiments,” by K.M. Mosalam, R.N. White and P. Gergely, 12/31/97, (PB98-153430, A07, MF-A02).

NCEER-97-0021 “Computational Strategies for Frames with Infill Walls: Discrete and Smeared Crack Analyses and Seismic Fragility,” by K.M. Mosalam, R.N. White and P. Gergely, 12/31/97, (PB98-153414, A10, MF-A02).

NCEER-97-0022 "Proceedings of the NCEER Workshop on Evaluation of Liquefaction Resistance of Soils," edited by T.L. Youd and I.M. Idriss, 12/31/97, (PB98-155617, A15, MF-A03).

MCEER-98-0001 "Extraction of Nonlinear Hysteretic Properties of Seismically Isolated Bridges from Quick-Release Field Tests," by Q. Chen, B.M. Douglas, E.M. Maragakis and I.G. Buckle, 5/26/98, (PB99-118838, A06, MF-A01).

MCEER-98-0002 "Methodologies for Evaluating the Importance of Highway Bridges," by A. Thomas, S. Eshenaur and J. Kulicki, 5/29/98, (PB99-118846, A10, MF-A02).

MCEER-98-0003 "Capacity Design of Bridge Piers and the Analysis of Overstrength," by J.B. Mander, A. Dutta and P. Goel, 6/1/98, (PB99-118853, A09, MF-A02).

MCEER-98-0004 "Evaluation of Bridge Damage Data from the Loma Prieta and Northridge, California Earthquakes," by N. Basoz and A. Kiremidjian, 6/2/98, (PB99-118861, A15, MF-A03).

MCEER-98-0005 "Screening Guide for Rapid Assessment of Liquefaction Hazard at Highway Bridge Sites," by T. L. Youd, 6/16/98, (PB99-118879, A06, not available on microfiche).

MCEER-98-0006 "Structural Steel and Steel/Concrete Interface Details for Bridges," by P. Ritchie, N. Kauhl and J. Kulicki, 7/13/98, (PB99-118945, A06, MF-A01).

MCEER-98-0007 "Capacity Design and Fatigue Analysis of Confined Concrete Columns," by A. Dutta and J.B. Mander, 7/14/98, (PB99-118960, A14, MF-A03).

MCEER-98-0008 "Proceedings of the Workshop on Performance Criteria for Telecommunication Services Under Earthquake Conditions," edited by A.J. Schiff, 7/15/98, (PB99-118952, A08, MF-A02).

MCEER-98-0009 "Fatigue Analysis of Unconfined Concrete Columns," by J.B. Mander, A. Dutta and J.H. Kim, 9/12/98, (PB99-123655, A10, MF-A02).

MCEER-98-0010 "Centrifuge Modeling of Cyclic Lateral Response of Pile-Cap Systems and Seat-Type Abutments in Dry Sands," by A.D. Gadre and R. Dobry, 10/2/98, (PB99-123606, A13, MF-A03).

MCEER-98-0011 "IDARC-BRIDGE: A Computational Platform for Seismic Damage Assessment of Bridge Structures," by A.M. Reinhorn, V. Simeonov, G. Mylonakis and Y. Reichman, 10/2/98, (PB99-162919, A15, MF-A03).

MCEER-98-0012 "Experimental Investigation of the Dynamic Response of Two Bridges Before and After Retrofitting with Elastomeric Bearings," by D.A. Wendichansky, S.S. Chen and J.B. Mander, 10/2/98, (PB99-162927, A15, MF-A03).

MCEER-98-0013 "Design Procedures for Hinge Restrainers and Hinge Sear Width for Multiple-Frame Bridges," by R. Des Roches and G.L. Fenves, 11/3/98, (PB99-140477, A13, MF-A03).

MCEER-98-0014 "Response Modification Factors for Seismically Isolated Bridges," by M.C. Constantinou and J.K. Quarshie, 11/3/98, (PB99-140485, A14, MF-A03).

MCEER-98-0015 "Proceedings of the U.S.-Italy Workshop on Seismic Protective Systems for Bridges," edited by I.M. Friedland and M.C. Constantinou, 11/3/98, (PB2000-101711, A22, MF-A04).

MCEER-98-0016 "Appropriate Seismic Reliability for Critical Equipment Systems: Recommendations Based on Regional Analysis of Financial and Life Loss," by K. Porter, C. Scawthorn, C. Taylor and N. Blais, 11/10/98, (PB99-157265, A08, MF-A02).

MCEER-98-0017 "Proceedings of the U.S. Japan Joint Seminar on Civil Infrastructure Systems Research," edited by M. Shinozuka and A. Rose, 11/12/98, (PB99-156713, A16, MF-A03).

MCEER-98-0018 "Modeling of Pile Footings and Drilled Shafts for Seismic Design," by I. PoLam, M. Kapuskar and D. Chaudhuri, 12/21/98, (PB99-157257, A09, MF-A02).

MCEER-99-0001 "Seismic Evaluation of a Masonry Infilled Reinforced Concrete Frame by Pseudodynamic Testing," by S.G. Buonopane and R.N. White, 2/16/99, (PB99-162851, A09, MF-A02).

MCEER-99-0002 "Response History Analysis of Structures with Seismic Isolation and Energy Dissipation Systems: Verification Examples for Program SAP2000," by J. Scheller and M.C. Constantinou, 2/22/99, (PB99-162869, A08, MF-A02).

MCEER-99-0003 "Experimental Study on the Seismic Design and Retrofit of Bridge Columns Including Axial Load Effects," by A. Dutta, T. Kokorina and J.B. Mander, 2/22/99, (PB99-162877, A09, MF-A02).

MCEER-99-0004 "Experimental Study of Bridge Elastomeric and Other Isolation and Energy Dissipation Systems with Emphasis on Uplift Prevention and High Velocity Near-source Seismic Excitation," by A. Kasalanati and M. C. Constantinou, 2/26/99, (PB99-162885, A12, MF-A03).

MCEER-99-0005 "Truss Modeling of Reinforced Concrete Shear-flexure Behavior," by J.H. Kim and J.B. Mander, 3/8/99, (PB99-163693, A12, MF-A03).

MCEER-99-0006 "Experimental Investigation and Computational Modeling of Seismic Response of a 1:4 Scale Model Steel Structure with a Load Balancing Supplemental Damping System," by G. Pekcan, J.B. Mander and S.S. Chen, 4/2/99, (PB99-162893, A11, MF-A03).

MCEER-99-0007 "Effect of Vertical Ground Motions on the Structural Response of Highway Bridges," by M.R. Button, C.J. Cronin and R.L. Mayes, 4/10/99, (PB2000-101411, A10, MF-A03).

MCEER-99-0008 "Seismic Reliability Assessment of Critical Facilities: A Handbook, Supporting Documentation, and Model Code Provisions," by G.S. Johnson, R.E. Sheppard, M.D. Quilici, S.J. Eder and C.R. Scawthorn, 4/12/99, (PB2000-101701, A18, MF-A04).

MCEER-99-0009 "Impact Assessment of Selected MCEER Highway Project Research on the Seismic Design of Highway Structures," by C. Rojahn, R. Mayes, D.G. Anderson, J.H. Clark, D'Appolonia Engineering, S. Gloyd and R.V. Nutt, 4/14/99, (PB99-162901, A10, MF-A02).

MCEER-99-0010 "Site Factors and Site Categories in Seismic Codes," by R. Dobry, R. Ramos and M.S. Power, 7/19/99, (PB2000-101705, A08, MF-A02).

MCEER-99-0011 "Restrainer Design Procedures for Multi-Span Simply-Supported Bridges," by M.J. Randall, M. Saiidi, E. Maragakis and T. Isakovic, 7/20/99, (PB2000-101702, A10, MF-A02).

MCEER-99-0012 "Property Modification Factors for Seismic Isolation Bearings," by M.C. Constantinou, P. Tsopelas, A. Kasalanati and E. Wolff, 7/20/99, (PB2000-103387, A11, MF-A03).

MCEER-99-0013 "Critical Seismic Issues for Existing Steel Bridges," by P. Ritchie, N. Kauhl and J. Kulicki, 7/20/99, (PB2000-101697, A09, MF-A02).

MCEER-99-0014 "Nonstructural Damage Database," by A. Kao, T.T. Soong and A. Vender, 7/24/99, (PB2000-101407, A06, MF-A01).

MCEER-99-0015 "Guide to Remedial Measures for Liquefaction Mitigation at Existing Highway Bridge Sites," by H.G. Cooke and J. K. Mitchell, 7/26/99, (PB2000-101703, A11, MF-A03).

MCEER-99-0016 "Proceedings of the MCEER Workshop on Ground Motion Methodologies for the Eastern United States," edited by N. Abrahamson and A. Becker, 8/11/99, (PB2000-103385, A07, MF-A02).

MCEER-99-0017 "Quindío, Colombia Earthquake of January 25, 1999: Reconnaissance Report," by A.P. Asfura and P.J. Flores, 10/4/99, (PB2000-106893, A06, MF-A01).

MCEER-99-0018 "Hysteretic Models for Cyclic Behavior of Deteriorating Inelastic Structures," by M.V. Sivaselvan and A.M. Reinhorn, 11/5/99, (PB2000-103386, A08, MF-A02).

MCEER-99-0019 "Proceedings of the 7th U.S.- Japan Workshop on Earthquake Resistant Design of Lifeline Facilities and Countermeasures Against Soil Liquefaction," edited by T.D. O'Rourke, J.P. Bardet and M. Hamada, 11/19/99, (PB2000-103354, A99, MF-A06).

MCEER-99-0020 "Development of Measurement Capability for Micro-Vibration Evaluations with Application to Chip Fabrication Facilities," by G.C. Lee, Z. Liang, J.W. Song, J.D. Shen and W.C. Liu, 12/1/99, (PB2000-105993, A08, MF-A02).

MCEER-99-0021 "Design and Retrofit Methodology for Building Structures with Supplemental Energy Dissipating Systems," by G. Pekcan, J.B. Mander and S.S. Chen, 12/31/99, (PB2000-105994, A11, MF-A03).

MCEER-00-0001 "The Marmara, Turkey Earthquake of August 17, 1999: Reconnaissance Report," edited by C. Scawthorn; with major contributions by M. Bruneau, R. Eguchi, T. Holzer, G. Johnson, J. Mander, J. Mitchell, W. Mitchell, A. Papageorgiou, C. Scaethorn, and G. Webb, 3/23/00, (PB2000-106200, A11, MF-A03).

MCEER-00-0002 "Proceedings of the MCEER Workshop for Seismic Hazard Mitigation of Health Care Facilities," edited by G.C. Lee, M. Ettouney, M. Grigoriu, J. Hauer and J. Nigg, 3/29/00, (PB2000-106892, A08, MF-A02).

MCEER-00-0003 "The Chi-Chi, Taiwan Earthquake of September 21, 1999: Reconnaissance Report," edited by G.C. Lee and C.H. Loh, with major contributions by G.C. Lee, M. Bruneau, I.G. Buckle, S.E. Chang, P.J. Flores, T.D. O'Rourke, M. Shinozuka, T.T. Soong, C-H. Loh, K-C. Chang, Z-J. Chen, J-S. Hwang, M-L. Lin, G-Y. Liu, K-C. Tsai, G.C. Yao and C-L. Yen, 4/30/00, (PB2001-100980, A10, MF-A02).

MCEER-00-0004 "Seismic Retrofit of End-Sway Frames of Steel Deck-Truss Bridges with a Supplemental Tendon System: Experimental and Analytical Investigation," by G. Pekcan, J.B. Mander and S.S. Chen, 7/1/00, (PB2001-100982, A10, MF-A02).

MCEER-00-0005 "Sliding Fragility of Unrestrained Equipment in Critical Facilities," by W.H. Chong and T.T. Soong, 7/5/00, (PB2001-100983, A08, MF-A02).

MCEER-00-0006 "Seismic Response of Reinforced Concrete Bridge Pier Walls in the Weak Direction," by N. Abo-Shadi, M. Saiidi and D. Sanders, 7/17/00, (PB2001-100981, A17, MF-A03).

MCEER-00-0007 "Low-Cycle Fatigue Behavior of Longitudinal Reinforcement in Reinforced Concrete Bridge Columns," by J. Brown and S.K. Kunnath, 7/23/00, (PB2001-104392, A08, MF-A02).

MCEER-00-0008 "Soil Structure Interaction of Bridges for Seismic Analysis," I. PoLam and H. Law, 9/25/00, (PB2001-105397, A08, MF-A02).

MCEER-00-0009 "Proceedings of the First MCEER Workshop on Mitigation of Earthquake Disaster by Advanced Technologies (MEDAT-1), edited by M. Shinozuka, D.J. Inman and T.D. O'Rourke, 11/10/00, (PB2001-105399, A14, MF-A03).

MCEER-00-0010 "Development and Evaluation of Simplified Procedures for Analysis and Design of Buildings with Passive Energy Dissipation Systems," by O.M. Ramirez, M.C. Constantinou, C.A. Kircher, A.S. Whittaker, M.W. Johnson, J.D. Gomez and C. Chrysostomou, 11/16/01, (PB2001-105523, A23, MF-A04).

MCEER-00-0011 "Dynamic Soil-Foundation-Structure Interaction Analyses of Large Caissons," by C-Y. Chang, C-M. Mok, Z-L. Wang, R. Settgast, F. Waggoner, M.A. Ketchum, H.M. Gonnermann and C-C. Chin, 12/30/00, (PB2001-104373, A07, MF-A02).

MCEER-00-0012 "Experimental Evaluation of Seismic Performance of Bridge Restrainers," by A.G. Vlassis, E.M. Maragakis and M. Saiid Saiidi, 12/30/00, (PB2001-104354, A09, MF-A02).

MCEER-00-0013 "Effect of Spatial Variation of Ground Motion on Highway Structures," by M. Shinozuka, V. Saxena and G. Deodatis, 12/31/00, (PB2001-108755, A13, MF-A03).

MCEER-00-0014 "A Risk-Based Methodology for Assessing the Seismic Performance of Highway Systems," by S.D. Werner, C.E. Taylor, J.E. Moore, II, J.S. Walton and S. Cho, 12/31/00, (PB2001-108756, A14, MF-A03).

MCEER-01-0001 "Experimental Investigation of P-Delta Effects to Collapse During Earthquakes," by D. Vian and M. Bruneau, 6/25/01, (PB2002-100534, A17, MF-A03).

MCEER-01-0002 "Proceedings of the Second MCEER Workshop on Mitigation of Earthquake Disaster by Advanced Technologies (MEDAT-2)," edited by M. Bruneau and D.J. Inman, 7/23/01, (PB2002-100434, A16, MF-A03).

MCEER-01-0003 "Sensitivity Analysis of Dynamic Systems Subjected to Seismic Loads," by C. Roth and M. Grigoriu, 9/18/01, (PB2003-100884, A12, MF-A03).

MCEER-01-0004 "Overcoming Obstacles to Implementing Earthquake Hazard Mitigation Policies: Stage 1 Report," by D.J. Alesch and W.J. Petak, 12/17/01, (PB2002-107949, A07, MF-A02).

MCEER-01-0005 "Updating Real-Time Earthquake Loss Estimates: Methods, Problems and Insights," by C.E. Taylor, S.E. Chang and R.T. Eguchi, 12/17/01, (PB2002-107948, A05, MF-A01).

MCEER-01-0006 "Experimental Investigation and Retrofit of Steel Pile Foundations and Pile Bents Under Cyclic Lateral Loadings," by A. Shama, J. Mander, B. Blabac and S. Chen, 12/31/01, (PB2002-107950, A13, MF-A03).

MCEER-02-0001 "Assessment of Performance of Bolu Viaduct in the 1999 Duzce Earthquake in Turkey" by P.C. Roussis, M.C. Constantinou, M. Erdik, E. Durukal and M. Dicleli, 5/8/02, (PB2003-100883, A08, MF-A02).

MCEER-02-0002 "Seismic Behavior of Rail Counterweight Systems of Elevators in Buildings," by M.P. Singh, Rildova and L.E. Suarez, 5/27/02. (PB2003-100882, A11, MF-A03).

MCEER-02-0003 "Development of Analysis and Design Procedures for Spread Footings," by G. Mylonakis, G. Gazetas, S. Nikolaou and A. Chauncey, 10/02/02, (PB2004-101636, A13, MF-A03, CD-A13).

MCEER-02-0004 "Bare-Earth Algorithms for Use with SAR and LIDAR Digital Elevation Models," by C.K. Huyck, R.T. Eguchi and B. Houshmand, 10/16/02, (PB2004-101637, A07, CD-A07).

MCEER-02-0005 "Review of Energy Dissipation of Compression Members in Concentrically Braced Frames," by K.Lee and M. Bruneau, 10/18/02, (PB2004-101638, A10, CD-A10).

MCEER-03-0001 "Experimental Investigation of Light-Gauge Steel Plate Shear Walls for the Seismic Retrofit of Buildings" by J. Berman and M. Bruneau, 5/2/03, (PB2004-101622, A10, MF-A03, CD-A10).

MCEER-03-0002 "Statistical Analysis of Fragility Curves," by M. Shinozuka, M.Q. Feng, H. Kim, T. Uzawa and T. Ueda, 6/16/03, (PB2004-101849, A09, CD-A09).

MCEER-03-0003 "Proceedings of the Eighth U.S.-Japan Workshop on Earthquake Resistant Design f Lifeline Facilities and Countermeasures Against Liquefaction," edited by M. Hamada, J.P. Bardet and T.D. O'Rourke, 6/30/03, (PB2004-104386, A99, CD-A99).

MCEER-03-0004 "Proceedings of the PRC-US Workshop on Seismic Analysis and Design of Special Bridges," edited by L.C. Fan and G.C. Lee, 7/15/03, (PB2004-104387, A14, CD-A14).

MCEER-03-0005 "Urban Disaster Recovery: A Framework and Simulation Model," by S.B. Miles and S.E. Chang, 7/25/03, (PB2004-104388, A07, CD-A07).

MCEER-03-0006 "Behavior of Underground Piping Joints Due to Static and Dynamic Loading," by R.D. Meis, M. Maragakis and R. Siddharthan, 11/17/03, (PB2005-102194, A13, MF-A03, CD-A00).

MCEER-03-0007 "Seismic Vulnerability of Timber Bridges and Timber Substructures," by A.A. Shama, J.B. Mander, I.M. Friedland and D.R. Allicock, 12/15/03.

MCEER-04-0001 "Experimental Study of Seismic Isolation Systems with Emphasis on Secondary System Response and Verification of Accuracy of Dynamic Response History Analysis Methods," by E. Wolff and M. Constantinou, 1/16/04 (PB2005-102195, A99, MF-E08, CD-A00).

MCEER-04-0002 "Tension, Compression and Cyclic Testing of Engineered Cementitious Composite Materials," by K. Kesner and S.L. Billington, 3/1/04, (PB2005-102196, A08, CD-A08).

MCEER-04-0003 "Cyclic Testing of Braces Laterally Restrained by Steel Studs to Enhance Performance During Earthquakes," by O.C. Celik, J.W. Berman and M. Bruneau, 3/16/04, (PB2005-102197, A13, MF-A03, CD-A00).

MCEER-04-0004 "Methodologies for Post Earthquake Building Damage Detection Using SAR and Optical Remote Sensing: Application to the August 17, 1999 Marmara, Turkey Earthquake," by C.K. Huyck, B.J. Adams, S. Cho, R.T. Eguchi, B. Mansouri and B. Houshmand, 6/15/04, (PB2005-104888, A10, CD-A00).

MCEER-04-0005 "Nonlinear Structural Analysis Towards Collapse Simulation: A Dynamical Systems Approach," by M.V. Sivaselvan and A.M. Reinhorn, 6/16/04, (PB2005-104889, A11, MF-A03, CD-A00).

MCEER-04-0006 "Proceedings of the Second PRC-US Workshop on Seismic Analysis and Design of Special Bridges," edited by G.C. Lee and L.C. Fan, 6/25/04, (PB2005-104890, A16, CD-A00).

MCEER-04-0007 "Seismic Vulnerability Evaluation of Axially Loaded Steel Built-up Laced Members," by K. Lee and M. Bruneau, 6/30/04, (PB2005-104891, A16, CD-A00).

MCEER-04-0008 "Evaluation of Accuracy of Simplified Methods of Analysis and Design of Buildings with Damping Systems for Near-Fault and for Soft-Soil Seismic Motions," by E.A. Pavlou and M.C. Constantinou, 8/16/04, (PB2005-104892, A08, MF-A02, CD-A00).

MCEER-04-0009 "Assessment of Geotechnical Issues in Acute Care Facilities in California," by M. Lew, T.D. O'Rourke, R. Dobry and M. Koch, 9/15/04, (PB2005-104893, A08, CD-A00).

MCEER-04-0010 "Scissor-Jack-Damper Energy Dissipation System," by A.N. Sigaher-Boyle and M.C. Constantinou, 12/1/04 (PB2005-108221).

MCEER-04-0011 "Seismic Retrofit of Bridge Steel Truss Piers Using a Controlled Rocking Approach," by M. Pollino and M. Bruneau, 12/20/04 (PB2006-105795).

MCEER-05-0001 "Experimental and Analytical Studies of Structures Seismically Isolated with an Uplift-Restraint Isolation System," by P.C. Roussis and M.C. Constantinou, 1/10/05 (PB2005-108222).

MCEER-05-0002 "A Versatile Experimentation Model for Study of Structures Near Collapse Applied to Seismic Evaluation of Irregular Structures," by D. Kusumastuti, A.M. Reinhorn and A. Rutenberg, 3/31/05 (PB2006-101523).

MCEER-05-0003 "Proceedings of the Third PRC-US Workshop on Seismic Analysis and Design of Special Bridges," edited by L.C. Fan and G.C. Lee, 4/20/05, (PB2006-105796).

MCEER-05-0004 "Approaches for the Seismic Retrofit of Braced Steel Bridge Piers and Proof-of-Concept Testing of an Eccentrically Braced Frame with Tubular Link," by J.W. Berman and M. Bruneau, 4/21/05 (PB2006-101524).

MCEER-05-0005 "Simulation of Strong Ground Motions for Seismic Fragility Evaluation of Nonstructural Components in Hospitals," by A. Wanitkorkul and A. Filiatrault, 5/26/05 (PB2006-500027).

MCEER-05-0006 "Seismic Safety in California Hospitals: Assessing an Attempt to Accelerate the Replacement or Seismic Retrofit of Older Hospital Facilities," by D.J. Alesch, L.A. Arendt and W.J. Petak, 6/6/05 (PB2006-105794).

MCEER-05-0007 "Development of Seismic Strengthening and Retrofit Strategies for Critical Facilities Using Engineered Cementitious Composite Materials," by K. Kesner and S.L. Billington, 8/29/05.

MCEER-05-0008 "Experimental and Analytical Studies of Base Isolation Systems for Seismic Protection of Power Transformers," by N. Murota, M.Q. Feng and G-Y. Liu, 9/30/05.

MCEER-05-0009 "3D-BASIS-ME-MB: Computer Program for Nonlinear Dynamic Analysis of Seismically Isolated Structures," by P.C. Tsopelas, P.C. Roussis, M.C. Constantinou, R. Buchanan and A.M. Reinhorn, 10/3/05.

MCEER-05-0010 “Steel Plate Shear Walls for Seismic Design and Retrofit of Building Structures,” by D. Vian and M. Bruneau, 12/15/05.

MCEER-05-0011 “The Performance-Based Design Paradigm,” by M.J. Astrella and A. Whittaker, 12/15/05.

MCEER-06-0001 “Seismic Fragility of Suspended Ceiling Systems,” H. Badillo-Almaraz, A.S. Whittaker, A.M. Reinhorn and G.P. Cimellaro, 2/4/06.

MCEER-06-00002 “Multi-Dimensional Fragility of Structures,” by G.P. Cimellaro, A.M. Reinhorn and M. Bruneau, 3/1/06.

MCEER-06-0003 “Built-Up Shear Links as Energy Dissipators for Seismic Protection of Bridges,” by P. Dusicka, A.M. Itani and I.G. Buckle, 3/15/06.

MCEER-06-0004 “Analytical Investigation of the Structural Fuse Concept,” by R.E. Vargas and M. Bruneau, 3/16/06.

MCEER-06-0005 “Experimental Investigation of the Structural Fuse Concept,” by R.E. Vargas and M. Bruneau, 3/17/06.

MCEER-06-0006 “Further Development of Tubular Eccentrically Braced Frame Links for the Seismic Retrofit of Braced Steel Truss Bridge Piers,” by J.W. Berman and M. Bruneau, 3/27/06.

MULTIDISCIPLINARY CENTER FOR EARTHQUAKE ENGINEERING RESEARCH

A National Center of Excellence in Advanced Technology Applications

University at Buffalo, State University of New York
Red Jacket Quadrangle ▪ Buffalo, New York 14261
Phone: (716) 645-3391 ▪ Fax: (716) 645-3399
E-mail: *mceer@mceermail.buffalo.edu* ▪ WWW Site *http://mceer.buffalo.edu*

University at Buffalo *The State University of New York*

ISSN 1520-295X